Evolution of soil moisture and analysis of fluvial altimetry using GNSS-R

Minh Cuong Ha

THÈSE

En vue de l'obtention du

DOCTORAT DE L'UNIVERSITÉ DE TOULOUSE

Délivré par : *l'Université Toulouse 3 Paul Sabatier (UT3 Paul Sabatier)*

Présentée et soutenue le *18/06/2018* **par :**

MINH CUONG HA

Evolution of soil moisture and analysis of fluvial altimetry using GNSS-R
Évolution de l'humidité des sols et analyse de l'altimétrie fluviale par GNSS-R

JURY

GUILLAUME RAMILLIEN	Directeur de Recherche CNRS (GET)	Président du jury
JOSÉ DARROZES	MC UPS (GET)	Directeur de thèse
MURIEL LLUBES	MC UPS (GET)	Codirecteur de thèse
ANDREA WALPERSDORF	Physicienne UGA (ISTerre)	Rapporteur 1
JOSÉ ANTONIO GRANDE GIL	Professeur UHU (ETSI)	Rapporteur 2
PIERRE-LOUIS FRISON	MC UPEM	Rapporteur 3
MYRIAM SCHMUTZ	Professeur INP Bordeaux (ENSEGID)	Examinateur
MANUELA GRIPPA	Physicienne adjointe CNAP (GET)	Invité

École doctorale et spécialité :
SDU2E : Sciences de la Terre et des Planètes Solides

Unité de Recherche :
Géoscience Environnement Toulouse(UMR 5563)

Directeur(s) de Thèse :
José DARROZES et *Murriel LLUBES*

Rapporteurs :
Andrea WALPERSDORF, *José Antonio GRANDE GIL* et *Pierre-Louis FRISON*

Résumé:

L'eau fait partie intégrante de la vie sur notre planète et joue un rôle important dans les études pour évaluer l'impact du changement climatique. La recherche des ressources en eau est donc très importante pour la communauté scientifique du "climat" non seulement en surveillant de près le budget régional et mondial des ressources en eau, mais aussi pour comprendre les changements dans la fréquence et l'intensité des événements météorologiques ponctuels. Cela est particulièrement vrai pour les phénomènes météorologiques extrêmes, qui ont de grands impacts socio-économiques. L'impact des tempêtes tropicales plus ou plus intenses, des méga-neiges ou des coupes de poussières est l'un des principaux domaines de la recherche climatique.

Le but de mon travail de recherche est de fournir des moyens d'évaluer l'impact des changements climatiques sur les ressources en eau et de trouver des outils flexibles permettant une gestion durable de l'eau.

Des études récentes ont montré que l'on peut tirer parti des ondes émises en continu par les constellations du système mondial de navigation par satellite (GNSS) pour mesurer l'humidité du sol. Cette technique de télédétection opportuniste, connue sous le nom de réflectométrie GNSS (GNSS-R), consiste à comparer l'interférence des ondes réfléchies par le sol et celles provenant directement des satellites. Dans ma thèse, je me suis concentré sur la base GNSS-R sur le rapport signal-sur-bruit (SNR) enregistré par un récepteur GNSS conventionnel avec une unique antenne pour récupérer les variations d'humidité du sol. Beaucoup d'études ont montré l'efficacité de la méthode sur les sols argileux, et j'ai démontré dans ma thèse qu'elle était tout aussi efficace sur les sols sableux à condition d'appliquer la méthode du déroulement de phase. Cette méthode que je propose a été appliquée avec succès pour déterminer les variations locales d'humidité du sol: (1) 100% du sable dans le terrain de jeu de volleyball (Toulouse, France); et (2) >85% de sable dans la zone critique sahélienne de Dahra (Sénégal).

En outre, la mesure précise et continue des niveaux d'eau des rivières est un élément important de la gestion des ressources en eau, afin d'obtenir une estimation continue du débit de la rivière dans le monde. La précision de la technique GNSS-R pour l'altimétrie fluviale est son pas d'échantillonnage élevé permet de suivre les événements hydrologiques extrêmes. Deux méthodes, les moindres carrés et la technique "Larson", ont été appliquées avec succès pour déterminer les variations des hauteurs au Vietnam: (1) sur la fleuve Rouge (21 ° 2'44.04 "N, 105 ° 51'48.86" E) où les événements et changements morphologiques associés aux événements hydrologiques (tempête tropicale) en 2016; et (2) sur le delta du Mékong (9 ° 31'38.63 "N, 106 ° 12'2.01" E) où les eaux continentales interagissent avec les eaux océanique.

Mon travail montre que le GNSS-R est une alternative puissante et un complément significatif aux techniques actuelles de mesure de la gestion des ressources en eau en établissant un lien entre les différentes résolutions temporelles et spatiales actuellement obtenues par les outils conventionnels (*in-situ* capteurs, télédétection radar, etc.). Cette technique présente le grand avantage d'être basic sur le réseau pérenne du constatation GNSS et peut donc être utilisé sur n'importe quelle station GNSS. Par conséquent, en implantant une chaîne de traitement SNR, on peut automatiquement suivre les variations des environnementaux fondamentaux, i.e. la hauteur de la rivière, la pente locale de la surface de l'eau, les zones inondées, les variations d'humidité du sol et même la hauteur de végétation.

Mots clés: GNSS-R, Télédétection, Rapport signal sur bruit, SNR, Altimétrie, Humidité du sol, Phase de déballage, Cycle de l'eau, Inondation, Changement climatique, Réflectométrie, Multi-trajets, GNSS, GPS, GLONASS.

Abstract :

Water is an integral part of life on our planet and it plays an important role in climatic changes. Water resources research is, therefore, very important for the climate communities to not only closely monitor the regional and global water supply budget, but to also understand changes in frequency of occurrence and strength of individual weather events. This is especially true for extreme weather events, which have great societal and economic impacts. Whether we will have more or more intense tropical storms, mega-snow events, or dust-bowls in the near or far future climate. This is one of the key focus areas of climate research.

The aim of my PhD work is to provide some answers to assess the impact of future climate change threats on water resources. And we are trying to find the adaptive tools needed for sustainable water resources management.

In an effort to optimize water resource management, it is crucial to improve soil moisture situation awareness. With the advent of remote sensing, soil moisture is systematically monitored at the global scale but at the expense of the temporal and/or spatial resolution. Recent studies suggested to take advantage of continuously emitted waves by the Global Navigation Satellite System (GNSS) constellations, to retrieve soil moisture. This opportunistic remote sensing technique, known as GNSS Reflectometry (GNSS-R), consists in comparing the interference of reflected waves by the ground and those which come directly from satellites. In my thesis, I focused on GNSS-R technique base on the signal-to-noise ratio (SNR) recorded by conventional GNSS receiver with single antenna to retrieve soil moisture variations. Previous studies show the efficiency of this methodology for clay soil and I demonstrate for the first time, it's efficiency for sandy soil using Unwrapping phase method. This method that I propose has been successfully applied to determine local soil moisture variations of : (1) 100% of sand in Volleyball playground (Toulouse, France); and (2) >85% of sand in the Sahelian critical zone of Dahra (Senegal).

In addition, accurate and continuous measurement of river water levels is an important element in water resource management, to obtain an ongoing estimate of the river's flow around the world. The accuracy of GNSS-R technique for river altimetry is useful for detection of extreme hydrological events and to show the competition between continental and oceanic water near coastal area. The two methods, Least Square and "Larson" methods, has been successfully applied to determine local variations in Vietnam of: (1) the Red river (21°02'44.04"N, 105°51'48.86"E) to identify flood events and morphological changes associated to the hydrological events (tropical storm) in 2016; and (2) the Mekong river delta (9°31'38.63"N, 106°12'2.01"E) where continental water interacts with oceanic water.

My work shows that GNSS-R is a powerful alternative and a significant complement to the current measurement techniques for managing water resource by establishing a link between the different temporal and spatial resolutions currently achieved by conventional tools (*in-situ* sensors, remote sensing radar, etc.). This technique has a great advantage based on already-developed and sustainable GNSS satellites networks, and can be applied to any GNSS geodetic station. Therefore, by installing a processing chain of the SNR acquisitions, we are able to monitor various environmental parameters i.e. height river, local slope of water surface, flooded areas, soil moisture variations and even vegetation/plant height.

Keywords: GNSS-R, Remote sensing, Signal-to-Noise Ratio, SNR, Altimetry, Soil moisture, Unwrapping phase, Water cycle, Flood, Climate change, Reflected signals, Multipaths, GNSS, GPS, GLONASS.

List of Acronyms

- **AMSR** Advanced Microwave Scanning Radiometer
- **AVHRR** Advanced Very High-Resolution Radiometer
- **BASINS** Better Assessment Science Integrating Point and Nonpoint Sources
- **CCI** Climate Change Initiative
- **CDMA** Code Division Multiple Access
- **CICERO** Community Initiative for Cellular Earth Remote Observation
- **CNES** Centre National d'Études Spatiales
- **CORS** Continuously Operating Reference Station
- **CRWU** Climate Ready Water Utilities
- **CYGNSS** Cyclone Global Navigation Satellite System
- **CoRTAD** Coral Reef Temperature Anomaly Database
- **EGNOS** European Geostationary Navigation Overlay Service
- **EGRET** Exploration and Graphics for RivEr Trends
- **ENSO** El Niño/Southern Oscillation
- **ENVISAT** Environmental Satellite
- **EOS** Earth Observing System
- **ERS** European Remote-Sensing Satellite
- **ESA** European Space Agency
- **ESA** European Space Agency
- **GET** Géosciences Environnement Toulouse
- **GNSS** Global Navigation Satellite System
- **GNSS-R** Global Navigation Satellite System Reflectometry
- **GPM** Global Precipitation Measurement
- **GPS** Global Positioning System

- **GRACE** Gravity Recovery and Climate Experiment
- **GWOS** Global Wetland Observing System
- **HELP** Hydrology for the Environment, Life and Policy
- **IGS** International GNSS Service
- **IPPC** Intergovernmental Panel on Climate Change
- **IPT** Interference Pattern Technical
- **IRNSS** Indian Regional Navigation Satellite System
- **ISRO** Indian Space Research Organisation
- **ISRO** Indian Space Research Organization
- **InSAR** Interferometric Synthetic Aperture Radar
- **LBAS** Local Based Augmentation System
- **LEO** Low Earth Orbit satellites
- **LHCP** Left Hand Circularly Polarized
- **MODIS** Moderate Resolution Imaging Spectroradiometer
- **MSAS** Multi-Functional Satellite-based Augmentation System
- **NASA** National Aeronautics and Space Administration
- **NCDC** National Climatic Data Center
- **NDPES** National Pollutant Discharge Elimination System
- **NERC** Natural Environment Research Council
- **NMRI** Normalized Microwave Reflection Index
- **NOAA** National Oceanic and Atmospheric Administration
- **NOC** National Oceanography Centre
- **NWP** Numerical Weather Prediction
- **PARIS- IOD** ESA PARIS In Orbit Demonstrator mission
- **PRN** Pseudo-Random Noise

- **PUB** Prediction of Ungauged Basins
- **QZSS** Quasi-Zenith Satellite System
- **RHCP** Right Hand Circularly Polarized
- **RO** Radio Occultation
- **RTK** Real Time Kinematic
- **SAR** Synthetic Aperture Radar
- **SARAL** Satellite with ARgos and ALtiKa
- **SDU2E** Sciences de l'Univers, de l'Environnement et de l'Espace
- **SE** Satellite Elevation
- **SM** Soil Moisture
- **SMAP** Soil Moisture Active Passive
- **SMEX** Soil Moisture Experiment
- **SMOS** Soil Moisture and Ocean Salinity
- **SNAS** Chinese Satellite Navigation Augmentation System
- **SNR** Signal to Noise Ratio
- **SSH** Sea Surface Heights
- **SST** Sea Surface Temperature
- **SSTL** Surrey Satellite Technology Ltd
- **SWC** National Storm Water Calculator
- **SWE** Snow Water Equivalent
- **T/P** TOPEX/Poseidon satellite
- **TEC** Total Electron Content
- **TIROS-N** Advanced Television Infrared Observation Satellite
- **TMDLs** Total Maximum Daily Loads
- **TRMM** Tropical Rainfall Measuring Mission

- **USDA/SCAN** United States Department of Agriculture/Soil Climate Analysis Network
- **VSM** Volumetric Soil Moisture
- **WAAS** Wide Area Augmentation System
- **WAM** West African Monsoon
- **WCT** Weather and Climate Toolkit
- **WRTDS** Weighted Regressions on Time, Discharge, and Season

Acknowledgements

There are some say that doing research is particularly difficult, others say it's not, but no one dares say that you do not have to spend a lot of time and effort doing a thesis, and that the accomplishment ends up arriving one day. For me, being a PhD student, it was really long and intense efforts. I arrived in France with many gaps, in terms of knowledge, work experience. It was also necessary to overcome the shortcomings caused by living abroad, without my relatives, far from my home, but it was very lucky for me to have very kindly and friendly help of the people who work at GET and the Vietnamese friends who have been living and studying here at this early arriving time.

And it's true that a thesis is primarily a personal project, but after a few years of thesis, I'm aware that my project would not have succeeded without the help and sometimes involuntary support of a very large number of people. The use would therefore, that tribute be paid to all those people who, directly or indirectly, helped to the success of this project. And for my part, the people to thank are numerous. I would like to say to them my total gratitude in the following lines. I am already apologizing to those who will not be quoted in this text and who would have deserved it in many ways.

First of all, two people to whom I would like to express my most sincere gratitude are my thesis advisors, José Darrozes, whose direction and support has been most appreciated and without whom, this work would not have been possible, and Murriel Llubes, for her support and extremely useful advices during these years of intense work. *"Không thầy, đố mày làm nên"*, as this well-known Vietnamese proverb says: " impossible to succeed in life without teachers ". Thank you very much, I have had a lot of fun over the last years and you have always been supportive, enthusiastic, and available to help and answer questions.

I would also like to sincerely thank the rapporteurs of my thesis, Professors Andréa Walpersdorf, José Antonio Grande Gil and Pierre-Louis Frison for having given time for a careful and detailed reading of my manuscript as well as for their encouraging and constructive comments. I would also like to thank the examiners, Myriam Schmutz and Manuela Grippa for agreeing to participate in my thesis jury.

A special thanks to Remote Sensing and GNSS-R group research of GET: Guillaume Ramillien, Fréderic Frappart, Nicolas Roussel and Grégory Dufrechou. Thank you very much for the knowledge, experience and advice that are very important and useful in my doctoral dissertation research.

I would also like to thank the GET laboratory and all the members of its Executive Board. I would like to thank Michel Grégoire, Étienne Ruellan, Olivier Vanderaghe and Laurence Marlat. A big thank you in particular to Carine Baritaud who has helped me a lots with administrative procedures. I would also like to thank the management of the SDU2E Doctoral School for their support.

A big thank to all my doctoral colleagues and especially those with whom I shared

my office and who supported me a lots in French, living abroad experiences, cultures... during the thesis: Michel, Bérangé and Augustin .Thank you, Friday lunches sometimes allow me to relieve stress with interesting stories.

I would like to thank people from MISTRALE project whose helped me with the development, GNSS-R experiences and made possible the success of most of the experimental campaigns presented in this work. I would also like to thank the people involved in the Soil-TakeCare project for very interesting campaigns in Cartagena (Spain) and Estarreja (Portugal) for research on environmental pollution.

Thank you very much to all my Vietnamese friends and family who supported me and kept me going even in the toughest moments. Particularly, to my parents Ha Minh-Hung and Nhu Thi-Xuan, and my younger sister Lien, who with your example of life-long effort and perseverance gave me the best encouragement I could have.

And finally, most importantly, my family, my lovely wife Vu Phuong-Lan and my sweet angel Ha Bao Lam. Thank you very much! I can not possibly express with words all my gratitude for you, knowing that this entire section would not be enough to write to you my appreciation and gratitude. Thanks for always by my side during this time and that made this Thesis possible.

Xin chân thành cảm ơn!
Big thank!
Grand merci!

Remerciements

Certains disent que faire de la recherche est particulièrement difficile, d'autres disent que non, mais personne n'ose dire que vous n'avez pas à consacrer beaucoup de temps et d'efforts à faire une thèse et que l'accomplissement finit par arriver un jour. Pour moi, en tant qu'étudiant au doctorat, les efforts étaient longs et intenses. Je suis arrivé en France avec beaucoup de lacunes, en termes de connaissances, d'expérience de travail. Il fallait aussi surmonter les imperfections causées par la vie à l'étranger, sans ma famille, loin de chez moi, mais j'ai eu beaucoup de chance d'avoir une aide très aimable et amicale des gens qui travaillent au GET et des amis vietnamiens qui ont été vivre et étudier ici à cette heure d'arrivée précoce.

Et c'est vrai qu'une thèse est avant tout un projet personnel, mais après quelques années de thèse, je suis conscient que mon projet n'aurait pas réussi sans l'aide et parfois le soutien involontaire d'un très grand nombre de personnes. L'usage serait donc de rendre hommage à tous ceux qui, directement ou indirectement, ont contribué au succès de ce projet. Et pour ma part, les gens à remercier sont nombreux. Je voudrais leur dire ma totale gratitude dans les lignes suivantes. Je m'excuse déjà auprès de ceux qui ne seront pas cités dans ce texte et qui l'auraient mérité de bien des façons.

Tout d'abord, deux personnes à qui je voudrais exprimer ma plus sincère gratitude sont mes directeurs de thèse, José Darrozes, dont la direction et le soutien ont été très appréciés et sans qui, ce travail n'aurait pas été possible, et Murriel Llubes, pour son soutien et ses conseils extrêmement utiles durant ces années de travail intense. *"Không thầy, đố mày làm nên"*, comme le dit ce proverbe vietnamien très connu: " mpossible de réussir dans la vie sans professeurs ". Merci beaucoup, je me suis beaucoup amusé ces dernières années et vous avez toujours été d'un grand soutien, enthousiaste et disponible pour aider et répondre à toutes mes questions.

Je voudrais également remercier sincèrement les rapporteurs de ma thèse, le professeur ... pour avoir donné le temps de lire attentivement et en détail mon manuscrit ainsi que pour leurs commentaires encourageants et constructifs. Je voudrais également remercier les examinateurs, le professeur ... d'avoir accepté de participer à mon jury de thèse.

Un très grand merci à tous les membres de l'équipe de la télédeétection et GNSS-R du GET: Guillaume Ramillien, Frédéric Frappart, Nicolas Roussel et Grégory Dufrechou. Merci beaucoup pour les connaissances, l'expérience et les conseils qui sont très importants et utiles dans mes recherches doctorales.

Je voudrais également remercier le laboratoire GET et tous les membres de son Conseil d'administration. Je tiens à remercier Michel Grégoire, Étienne Ruellan, Olivier Vanderaghe et Laurence Marlat. Un grand merci en particulier à Carine Baritaud qui m'a beaucoup aidé avec les procédures administratives. Je voudrais également remercier la direction de l'école doctorale SDU2E pour son soutien.

Un grand merci à tous mes collègues doctorants et surtout à ceux avec qui j'ai partagé

mon bureau et qui m'ont soutenu beaucoup en français, vivant à l'étranger des expériences, des cultures ... pendant ma thèse: Michel, Bérangé et Augustin .Merci, les déjeuners du vendredi permettez-moi de soulager le stress avec des histoires intéressantes.

Je tiens à remercier les personnes du projet MISTRALE qui m'ont aidé avec le développement, les expériences GNSS-R et ont rendu possible le succès de la plupart des campagnes expérimentales présentées dans ce travail. Je voudrais également remercier les personnes impliquées dans le projet Soil-TakeCare pour des campagnes très intéressantes à Carthagène (Espagne) et Estarreja (Portugal) pour la recherche sur la pollution de l'environnement.

Merci beaucoup à tous mes amis et ma famille vietnamiens qui m'ont soutenu et m'ont permis d'aller même dans les moments les plus difficiles. En particulier, à mes parents, Ha Minh-Hung et Nhu Thi-Xuan, et à ma petit sœur Lien, qui, avec votre exemple d'effort et de persévérance, m'a donné les meilleurs encouragements possibles.

Et enfin, le plus important, ma famille, ma charmante épouse Vu Phuong-Lan et mon doux ange Ha Bao Lam. Merci beaucoup! Je ne peux pas exprimer avec des mots toute ma gratitude pour vous, sachant que toute cette section ne serait pas suffisante pour vous écrire mon appréciation et gratitude. Merci pour toujours à mes côtés pendant ce temps et cela a rendu possible cette thèse.

Xin chân thành cảm ơn!
Big thank!
Grand merci!

Contents

Contents **Page No.**

Chapter I
INTRODUCTION

Contents

Pourquoi les études du cycle de l'eau sont-elles importantes?

- **Cycle de l'eau**

  L'eau fait partie intégrante de la vie de notre planète et, comme nous le savons, 70% de la surface de la Terre est couverte par les océans. L'eau change constamment d'état et on la retrouve sous trois phases (liquide, vapeur et glace). Les processus associés au cycle de l'eau peuvent se dérouler en un clin d'œil ou sur des millions d'années (Source: `http://water.usgs.gov/edu/watercycle.html`, 10 août 2015). Les déplacements de l'eau sous ses différentes formes, sur et/ou sous la surface de la Terre, et les changements perpétuels de phase sont les ingrédients essentiels du cycle planétaire de l'eau (Fig. I.3). D'après la loi de conservation de masse, la masse d'eau sur Terre est constante dans le temps mais sa répartition dans les principaux réservoirs : glace, eau douce, eau saline et atmosphère est variable selon un large éventail de variables climatiques. Ce cycle naturel est un circuit fermé dans lesquels la Terre fournit à l'atmosphère de la vapeur d'eau qui, par condensation, revient ensuite via des phases liquides (pluie, brouillard) et/ou solides (neige, grêle) vers le globe (Leite and Peixoto, 1995). Les phénomènes naturels qui composent le cycle de l'eau sont:

  - le transfert d'eau du globe vers l'atmosphère en phase gazeuse par l'évaporation de l'eau liquide et/ou solide des mers, lacs, rivières, sols etc. et l'évapotranspiration des plantes;
  - le transport de l'eau dans ses phases gazeuse et solide ou liquide (nuages) par la circulation générale atmosphérique;
  - la condensation partielle de la vapeur d'eau dans de petites gouttelettes et/ou de petits cristaux de glace qui restent en suspension dans l'atmosphère et forment les nuages;
  - transfert de l'eau dans ses phases solides ou liquides de l'atmosphère vers le globe par précipitation des hydrométéores et dépôt à la surface;
  - le ruissellement, l'écoulement et le stockage de surface : l'infiltration de l'eau dans le sous-sol et son absorption par les racines planes, le ruissellement et l'écoulement vers les cours d'eau puis vers les lacs et/ou la mer les océans et le stockage de l'eau dans les nappes phréatiques.

  Puis ce cycle recommence. Le cycle de l'eau implique l'échange d'énergie, ce qui entraîne des changements de température. Par exemple, lorsque l'eau s'évapore, elle absorbe l'énergie de son environnement et refroidit l'environnement. Quand elle se condense, elle libère de l'énergie et réchauffe l'environnement. Ces échanges thermiques influencent fortement la zone critique mais aussi le climat.

- **Effets du changement du climat global**

  Le système hydrologique est potentiellement très sensible aux changements climatiques. Les changements dans les précipitations affectent l'ampleur et le moment de l'inondation ainsi que la fréquence et l'intensité des inondations et des sécheresses. Les changements de température entraînent des changements dans l'évapotranspiration, l'humidité des sols et l'infiltration vers les eaux souterraines. Des phénomènes globaux comme El Niño / Oscillation australe (ENSO) contribue à des variations saisonnières et interannuelles de la température et des précipitations qui compliquent l'analyse du changement climatique à plus long terme dans les régions du Pacifique. Les anomalies climatiques (c'est-à-dire les écarts par rapport à la norme) associées aux extrêmes ENSO varient à la fois en termes de magnitude et de distribution spatiale. Par exemple, la phase chaude persistante d'ENSO de 1990 à 1995 (qui provoque des sécheresses et des inondations dans de nombreuses zones) était inhabituelle dans le contexte des dernières années (Trenberth and Hoar, 1996). Bien qu'il n'y ait pas de relation claire entre l'augmentation des températures mondiales et la survenance de la phase chaude/froide liées à ENSO, ce phénomène climatique affecte le contenu et la nature du cycle global de l'eau (Grimm and Tedeschi, 2009). Cela est particulièrement vrai aux niveaux local et régional. Toutes les principales analyses du changement climatique jusqu'à ce jour ont conclu que si la température augmente en raison de l'augmentation des gaz à effet de serre, le cycle global de l'eau devrait être amélioré et une augmentation des précipitations et de l'humidité du sol se produira, en particulier dans les hautes altitudes, surtout pendant l'hiver (GIEC, 1996). Tous ces changements sont associés à des mécanismes physiques identifiables.

- **Changements de l'usage des terres**

  L'utilisation des terres, les variations de la couverture terrestre, influencent de manière significative les processus hydrologiques et biogéochimiques des bassins versants. Ces changements peuvent modifier l'interception, l'évapotranspiration, l'infiltration, l'humidité du sol, l'équilibre hydrique et le cycle biogéochimique du carbone, de l'azote et d'autres éléments (Talib and Randhir, 2017). Les changements dans les modèles de la couverture des terres peuvent avoir un impact direct sur les flux d'énergie et de masse. Par exemple, lorsque de grandes superficies de forêts sont défrichées, la transpiration réduite entraîne une réduction de la formation des nuages, une diminution des précipitations et une augmentation du dessèchement. Les changements observés dans les zones de défrichées des surfaces continentales induisent un réchauffement ou un refroidissement local tels que l'albédo (réflectivité) augmentent, la température de surface diminue. La désertification peut se produire lorsque le surpâturage remplace la savane et altère ainsi

les bilans de surface et l'albédo et modifie les schémas régionaux de circulation des précipitations. Le surpâturage entraîne une augmentation des émissions qui, à son tour, provoquent un refroidissement radiatif et une diminution des précipitations (Salati and Vose, 1986). Les forêts, et en particulier les forêts tropicales, jouent un rôle important dans le cycle mondial de l'eau. Les sols forestiers sont pour partie responsables de l'évaporation dans les forêts. L'élimination des forêts réduira donc, non seulement, l'évaporation liés aux arbres, mais réduira aussi l'évaporation des sols forestiers. La diminution locale de l'évaporation qui en résulte a des conséquences mondiales sur les précipitations, les ressources en eau et même la sécurité alimentaire. La déforestation empêche l'eau de retourner dans l'atmosphère, entraînant des changements d'un certain nombre de caractéristiques du bassin versant où elle se développe. La récolte de bois ou le changement de l'usage des terres peuvent entraîner une aggravation de la pénurie et accroître l'ampleur des inondations. Un développement accru des plaines inondables et des bassins de drainage peut également modifier le débit d'eau en bloquant les flux d'eau et en augmentant la largeur, la profondeur ou la vitesse des eaux de crue. Les étangs, les lacs, les réservoirs et les autres puits du bassin versant empêchent ou modifient aussi l'écoulement des eaux vers l'aval.

Couvrir de grandes surfaces de sol avec de l'asphalte et d'autres surfaces imperméables, comme en témoignent les tendances mondiales à l'urbanisation et à l'étalement urbain, conduit à une augmentation du ruissellement et empêche le réapprovisionnement des réservoirs d'eau souterraine, affectant ainsi le cycle global de l'eau. L'eau tombant sous forme de précipitations (pluie/neige/grêle) dans une région peut provenir d'une région éloignée, ou être due à l'humidité recyclée provenant de l'évaporation de la région. Les régimes de vent, la topographie et la couverture du sol dans le monde jouent tous un rôle dans les schémas de recyclage de l'eau et dans la distribution des ressources hydriques mondiales. Les changements dans l'utilisation des terres, tels que l'irrigation, les barrages et la déforestation, peuvent modifier les schémas d'évaporation d'une région, ce qui peut aussi affecter la qualité de l'eau (van der Ent et al., 2010).

Outils permettant l'analyse du cycle de l'eau

L'eau est peut-être la composante la plus importante de tout écosystème. De l'eau est stockée profondément dans la terre. D'autre part, l'eau de surface est la source qui soutient la vie sur terre. Dans de nombreux cas, l'eau structure également l'habitat physique d'un écosystème. Les ours polaires, par exemple, dépendent de la glace océanique pour chasser et capturer avec succès les phoques. Les rivières, les lacs et les autres parties de l'eau divisent les environnements dans des habitats différents, définissant efficacement où certains organismes peuvent vivre et d'autres pas (Corenblit et al., 2007, 2011). De plus, la majeure partie de la vie sur Terre vit en réalité complètement submergée dans les eaux

océaniques. L'eau est vraiment un facteur fondamental dans le développement de tous les écosystèmes (Fig. I.2). Dans un large contexte, les sciences de la météorologie et de l'océanographie décrivent des parties d'une série de processus physiques globaux impliquant l'eau qui sont aussi des composantes majeures de la science de l'hydrologie. Les géologues décrivent une autre partie des processus physiques en abordant le mouvement des eaux souterraines de la planète. Les hydrologues sont intéressés à obtenir des informations mesurables et des connaissances continues sur le cycle de l'eau. Il est également important de mesurer la quantité d'eau impliquée dans le stade de transition qui se produit lorsque l'eau se déplace d'un processus à l'autre. L'hydrologie est donc une science vaste qui utilise des informations provenant d'un large éventail d'autres sciences et les intègre pour quantifier les déplacements de l'eau. Les outils fondamentaux de l'hydrologie s'appuient sur des techniques scientifiques issues des mathématiques, de la physique, de l'ingénierie, de la chimie, de la géologie et de la biologie. L'hydrologie est donc l'une des disciplines interdisciplinaires qui constituent la base du développement et de la gestion des ressources en eaux. Une meilleure connaissance des états hydrologiques de surface

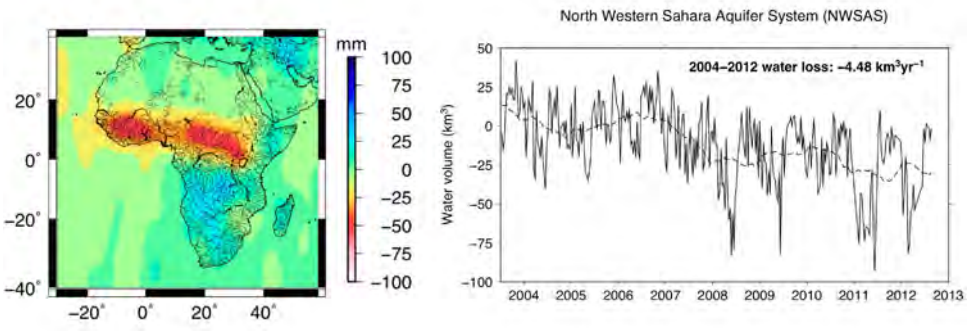

Figure I.1 – Suivi des changements d'eau de grands bassins par gravimétrie satellitaire, notons qu'au cours de la période 2004-2012 une tendance linéaire décroissante est clairement visible et elle correspond à une perte d'eau de $4.5 \mathrm{km}^2 \mathrm{yr}^{-1}$ ce qui se corrèle bien avec les données de surveillance in situ de l'aquifère sahraoui nord-occidental et est interprétée comme étant un pompage anthropique excessif de cet aquifère (Ramillien et al., 2014).

et des flux, ainsi que de leur variabilité spatio-temporelle à travers différentes échelles, est un objectif important dans de nombreuses études hydrologiques (Maurer et al., 2001; Roads et al., 2003). À cette fin, les approches traditionnelles ponctuelles, telles que les observations *in-situ* Ropelewski and Yarosh (1998), la modélisation guidée par les observations au sol (Mitchell et al., 2004) ou l'extraction directe à partir de données de télédétection (McCabe et al., 2005), deviennent inadéquats. Pour améliorer cette situation, des recherches sont menées par un certain nombre de groupes dans le but d'utiliser et de combiner autant de produits de données que possible dans un cadre intégré de manière à améliorer l'estimation des états et des flux du cycle de l'eau. Cette intégration

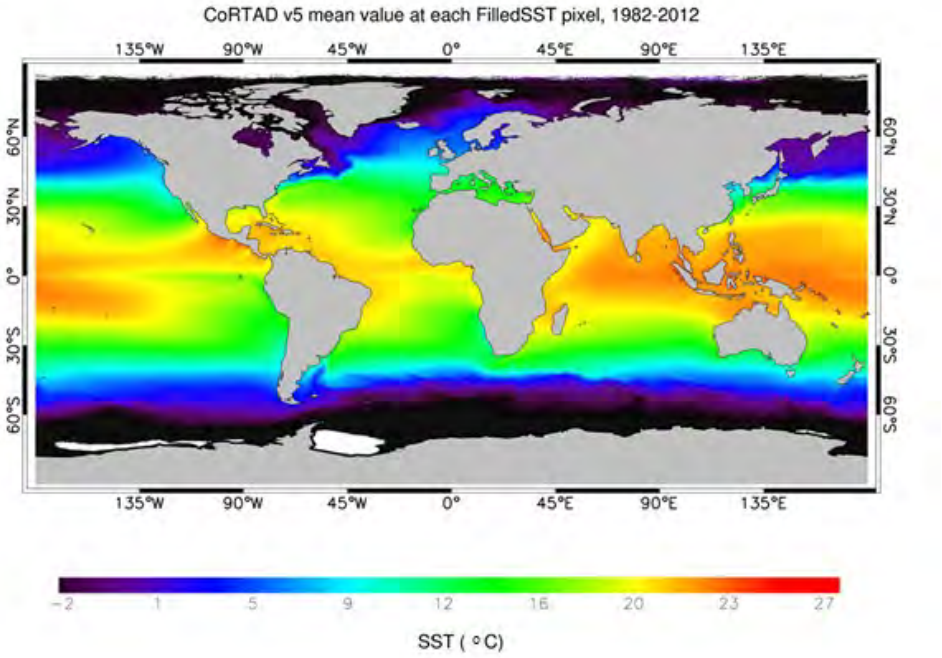

Figure I.2 – La base de données sur les anomalies de température des récifs coralliens (CoRTAD) est une collection de cartes de température de surface de la mer et de contraintes thermiques connexes, développée spécifiquement pour les applications de coraux sans correspondance aux autres écosystèmes. La base CoRTAD Version 5 contient des données SST de résolution globale d'environ 4 km sur une échelle de temps hebdomadaire de 1982 à 2012. Les données SST sont dérivées du capteur spatial AVHRR (Advanced Very High Resolution Radiometer).

des données et des modèles est appelée assimilation de données ou fusion de données (McLaughlin, 2002). Récemment, les données de télédétection jouent un rôle de plus en plus important dans cet effort. La raison principale est que les données de télédétection fournissent des observations à grande échelle et systématiques de la surface terrestre de manière cohérente dans le monde entier. De plus, les progrès dans les capteurs, le développement d'algorithmes de récupération et les augmentations considérables de la distribution de données libres, du stockage et du traitement des données ont grandement encouragé l'utilisation des données de télédétection en hydrologie (Pan et al., 2008). Le cycle de l'eau est généralement divisé en deux compartiments principaux: le premier est constitué des eaux océaniques (§ I.2.1) et le second concerne les eaux continentales (§ I.2.2).

Organisation du manuscrit

Après ce **premier chapitre** d'introduction générale et qui montre l'importance du cycle de l'eau, le travail présenté dans ce manuscrit se découpe en 5 chapitres:

- Dans le **deuxième chapitre**, je présenterai l'état de l'art de cette technique de télédétection opportuniste que l'on appelle le GNSS-R et je rappellerai succinctement avant les bases des systèmes GNSS.

- Dans le **troisième chapitre**, je présenterai une nouvelle approche du GNSS-R pour récupérer les variations d'humidité des sols sableux en utilisant le déroulement de la phase du SNR avec deux exemples:

  - L'un expérimental et assez simple puisque constitué de 100% de sable à iso granulométrie. Ce site, qui correspond au terrain de Beach Volley de l'université Paul Sabatier, a servi à la mise au point et au test de la méthodologie.
  - Le second est un exemple naturel présentant un sol riche en sable de quartz ($\sim$ 80%) mais aussi d'argile, de matière organique expériences il s'agit du site de Dahra au Sénégal.

  .

- Dans le **quatrième chapitre**, je présenterai le potentiel et la précision atteinte par la technique GNSS-R pour l'altimétrie fluviale pour détecter des événements hydrologiques extrêmes. Là encore deux sites ont été utilisés et pour avoir suffisamment de points de réflexion lors de nos expérimentations nous nous sommes placés dans des deltas. Autre intérêt des deltas c'est qu'ils sont sujets à de fortes variations des niveaux à cause des interactions entre les crues continentales et les marées océaniques, ces deltas sont:

  - le delta du fleuve Rouge et

– celui du Mékong, tous deux situés au Vietnam.

.

- Je termine ce travail dans un **cinquième chapitre** où je fais un bref résumé des principaux résultats obtenus dans ce manuscrit et où je présente également les différentes perspectives offertes par ce travail de thèse.

I.1 Why studies of the water cycle are important?

I.1.1 Water cycle

Water is an integral part of life on this planet, and as we know, 70 % of the Earth's surface is covered by oceans. It is always changing states between three phases (liquid, vapor, and ice) with these processes happening in the blink of an eye and over millions of years (Source: http://water.usgs.gov/edu/watercycle.html Accessed 10 Aug 2015). The movement of water in its different forms, continuous movement of water on, above and below the surface of the Earth, and the perpetual water phase changes are essential ingredients of the planetary water cycle (Fig. I.3). After the law of conservation of mass, the water mass on Earth remains fairly constant over time but the partitioning of the water into the major reservoirs of ice, fresh water, saline water and atmospheric water is variable depending on a wide range of climatic variables.

The water cycle is a closed circulation of the water in its three phases (solid, liquid and gaseous) inside the climate system. It is closed sequence of natural phenomena, in which the globe provides the atmosphere with water vapor that afterwards returns in liquid or solid phases to the globe (Leite and Peixoto, 1995). The natural phenomena that make up the water cycle are:

- the transfer of water from the globe to the atmosphere in its gaseous phase by the evaporation of liquid or solid water of the seas, lakes, river, etc. and the evapotranspiration of plants at the surface;
- water transport in its gaseous and solid or liquid phases (clouds) by the general circulation of atmosphere;
- partial condensation of water vapor in small droplets and ice crystals that remain in suspension in the atmosphere, making the clouds;
- water transfer in its solid or liquid phases from atmosphere to the globe by hydrometeor precipitation and deposition at the surface;
- runoff and storage at the surface, water infiltration at the subsurface and absorption by plan roots, the intensification of rivers on their way to the sea or lakes, and underground water storage (phreatic deposits).

And then this cycle starts again. The water cycle involves the exchange of energy, which leads to temperature changes. For instance, when water evaporates, it takes up energy from its surroundings and cools the environment. When it condenses, it releases energy and warms the environment. These heat exchanges influence strongly the critical zone but also climate.

The physical processes governing the water and energy cycles are extremely complicated, involving scales ranging from the planetary to the microscopic one. Any alterations in atmospheric gaseous composition (water vapor, carbon dioxide, ozone, etc.), particulates (desert dust, smoke, urban smog, etc.), or clouds (coverage and brightness) can disturb the radiative heat balance and result in chain reactions in the water cycle. It is very important for the climate community to not only closely monitor the regional and global water budget, but to also understand changes in frequency of occurrence and strength of individual weather events. This is especially true of extreme weather events, which have great societal and economic impacts. Whether we will have more or more intense tropical storms, mega-snow events, or dust-bowls in the near or far future climate is one of the key focus areas of climate research.

As we can see from figure I.1, the water cycle consists of an aerial branch, which transports water vapor, liquid and solid water of clouds by the general circulation of the atmosphere, and a terrestrial branch formed by the surface and subterranean run-off. The role of the terrestrial hydrosphere in the Earth's climate system can be described by climate-related variables, such as radiation, precipitation, evapotranspiration, soil moisture, clouds, water vapor, surface water and run-off, etc. Measurements of these quantities are required to better understand the global climate and its variability, both spatially and temporally, and to help advance our understanding of the coupling between the terrestrial and atmospheric branches of the water cycle, and how this coupling may influence climate variability and predictability. In order to enhance the prediction of global water cycle variations, understanding of hydrological processes and its close linkage with the energy cycle is fundamental. Here, a number of key questions are addressed:

- **How can we quantify the water cycle processes (storages and fluxes, as well as land-atmosphere, surface-groundwater, water-ecosystem and land-oceans interactions)?**

- **How can we assess the impacts of and the vulnerabilities to future climate change in water resources and what is the potential to adaptation in water resources management?**

- **What tools can be further developed/improved to predict the water cycle components (to measure, simulate and predict water cycle quantity and quality in space and time)?**

Observations from space and *in situ* of water cycle components and their interactions with ecosystems, climate and human activities provide opportunities to address most of the above questions.

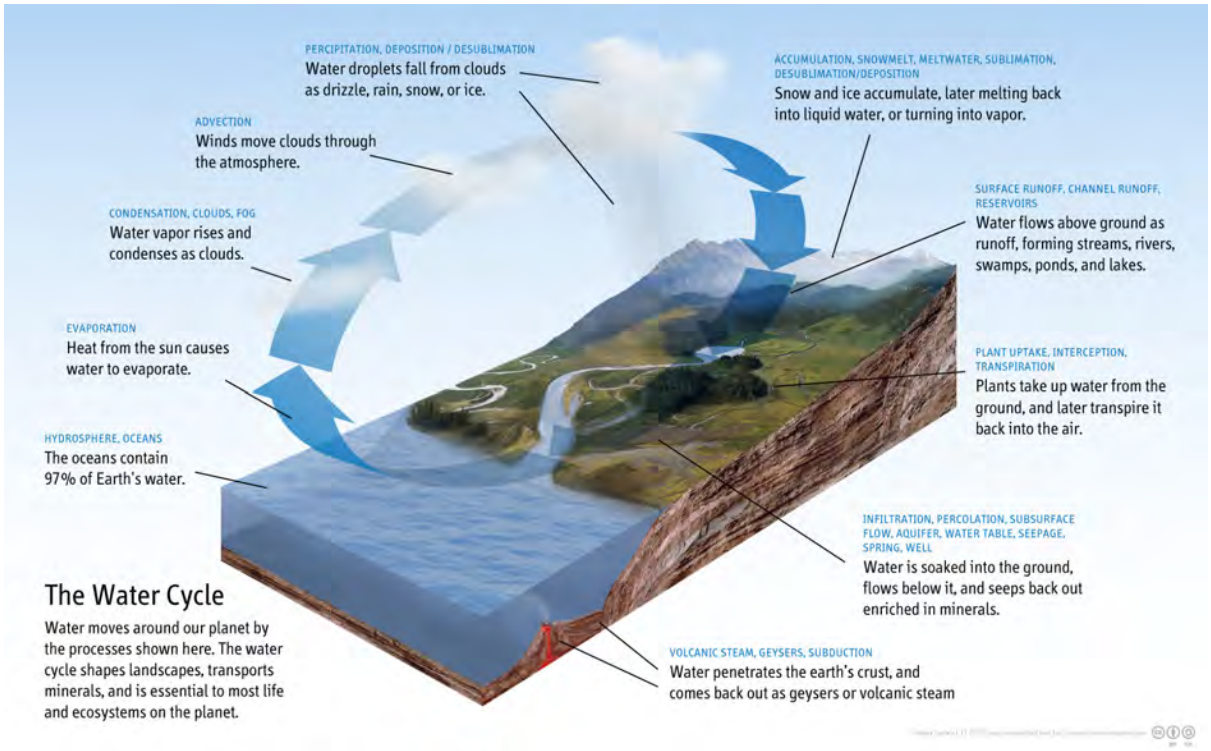

Figure I.3 – Diagram of the Water Cycle (v1.11). The water cycle shapes landscapes, transports minerals, and is essential to most life and ecosystem on the planet. It describes the pilgrimage of water as water molecules make their way from the Earth's surface to the atmosphere, and back again. This gigantic system, powered by energy from the sun, is a continuous exchange of moisture between the oceans, the atmosphere, and the land (from Edhu Tal, 2016).

I.1.2 Factors Affecting Water Cycle

The water cycle is being affected by human activities, such as water resource exploitation, urbanization, and deforestation. All these controls the distribution of water and the cycles. Below we will consider three of these factors: human consumption, effects of global climate, land use changes, etc.

I.1.2.1 Human Consumption

We are becoming increasingly aware of our impacts on nature, but unfortunately many of the things we do have become so ingrained in our way of life that it is hard to change. Numerous human activities can impact on the water cycle: constructing dams, pumping water for farming, deforestation and the burning of fossil fuels. Every time humans interrupt the natural water cycle there will be an effect. We can summarize this interruption of water in two ways:

- Withdrawals: We take water out of the system to irrigate crops (Fig. I.4), to provide us with drinking water and to carry out many of our industrial processes (*e.g.* agri-food industry).
- Discharges: We add substances to the water, intentionally or not, as pollutants from increased agricultural needs and from increased economic activity (*e.g.* waste from sewage treatment plants).

I.1.2.2 Effects of Changing Global Climate

The hydrologic system is potentially very sensitive to climate changes. Changes in precipitation affect the magnitude and timing of runoff and the frequency and intensity of floods and droughts. Changes in temperature results in changes in evapotranspiration, soil moisture, and infiltration.

The El Niño/Southern Oscillation (ENSO) phenomenon contributes seasonal-to-interannual variations in temperature and precipitation that complicate longer-term climate change analysis in Pacific parts of the world. Climate anomalies (i.e., departures from the norm) associated with ENSO extremes vary both in magnitude and spatial distribution. For example, the 1990 to 1995 persistent warm-phase of ENSO (which causes droughts and floods in many areas) was unusual in the context of the last 120 years (Trenberth and Hoar, 1996). Although a relationship has not been found between increasing global temperatures and the occurrence of warm/cold-phase of ENSO events, this climate phenomenon will certainly affect the content and nature of the global water cycle (Grimm and Tedeschi, 2009). This is especially true at the local and regional levels. All major climate change analyses to date have concluded that if temperature does increase as a result of increased greenhouse gases, the global mean water cycle will be enhanced

and increased precipitation and soil moisture will occur, especially in high latitudes especially during the winter (IPCC, 1996). All these changes are associated with identifiable physical mechanisms.

I.1.2.3 Land Use Changes

Land use, land cover can significantly influence the hydrologic balance and biogeochemical processes of watershed systems. These changes can alter interception, evapotranspiration, infiltration, soil moisture, water balance, and biogeochemical cycling of carbon, nitrogen, and other elements (Talib and Randhir, 2017). Changes in land cover patterns can directly impact energy and mass fluxes. For example, when large areas of forests are cleared, reduced transpiration results in reduced cloud formation, less rainfall, and increased drying. Changes in land cover can alter the reflectance of the Earth's surface and induce local warming or cooling such as albedo (reflectivity) increases, surface temperature declines. Desertification can occur when overgrazing of savanna vegetation alters surface albedo and surface water budgets, and thus changes the regional circulation and precipitation patterns. Overgrazing can also increase the amount of suspended dust that, in turn, cause radiative cooling and a decline in precipitation (Salati and Vose, 1986).

Forests, and tropical forests in particular, play an important role in the global water cycle. The forest floors are for a large part responsible for evaporation in forests. Removal of forests will thus not only reduce the evaporation from the trees, but will also reduce the evaporation from the forest floor. The resulting local decrease of evaporation is very likely to have global consequences for rainfall, water resources and food security. Deforestation keeps water from returning to the atmosphere, resulting in changes in a number of characteristics of the watershed. Harvesting of timber or changing land use from farmland to housing developments can also increase runoff and cause the magnitude of flooding to be increased.

More development in flood plains and drainage basins can also damage the pattern of water flow by blocking the flow of water and increasing the width, depth, or velocity of flood waters. Ponds, lakes, reservoirs, and other sinks in the watershed also prevent or alter runoff from continuing downstream. Covering land surfaces with asphalt and other impervious surfaces, as evidenced by worldwide trends toward urbanization and urban sprawl, both increase runoff and inhibit replenishment of the ground water reservoirs, and thus affects the overall water cycle.

The water falling as precipitation (rain/snow/hail) in one region may have originated from a butterfly effect in a distant region, or that it may be recycled moisture that originated as evaporation within the region. Global wind patterns, topography, and land cover all play a role in moisture recycling patterns and the distribution of global water resources. Land use changes such as irrigation, dams, and deforestation can alter evaporation patterns in a region, potentially affecting water resources in distant regions

(van der Ent et al., 2010).

I.2 Tools permitting the analysis of the water cycle

Water is perhaps the most important component of any ecosystem. Some water is stored deep in the earth. Surface water, on the other hand, is the source that sustains life on land. In many cases, water also structures the physical habitat of an ecosystem. Polar bears, for example, rely on ocean ice in order to successfully hunt and capture seals. Rivers, lakes, and other bodies of water divide environments into different habitats, effectively defining where some organisms can live and others cannot (Corenblit et al., 2007, 2011). What's more, most of the life on Earth actually lives completely submerged in the waters of the oceans. Water is truly a powerful factor in all ecosystems (Fig. I.5). In a broad context, the sciences of meteorology and oceanography describe parts of a

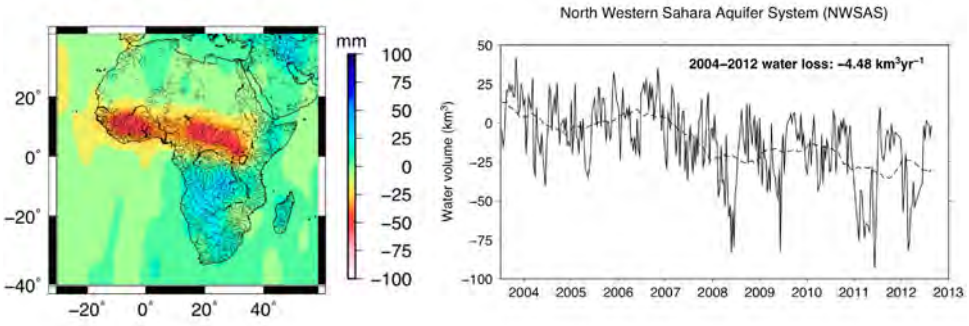

Figure I.4 – Monitoring of water changes of large watersheds by GRACE gravimetry, noted that over the period 2004-2012 the decreasing linear trend showing a loss $\sim 4.5 \text{km}^2\text{yr}^{-1}$ corresponds to the monitoring data of the North Western Saharan aquifer and it is interpreted by excessive pumping (Ramillien et al., 2014).

series of global physical processes involving water that are also major components of the science of hydrology. Geologists describe another part of the physical processes by addressing groundwater movement within the planet's subterranean features. Hydrologists are interested in obtaining measurable information and knowledge about the water cycle. Also important is the measurement of the amount of water involved in the transitional stages that occur as the water moves from one process within the cycle to other processes. Hydrology, therefore, is a broad science that utilizes information from a wide range of other sciences and integrates them to quantify the movement of water. The fundamental tools of hydrology are based in supporting scientific techniques that originated in mathematics, physics, engineering, chemistry, geology, and biology. Hydrology, therefore, is one of the interdisciplinary sciences that is the basis for water resources development and

water resources management.

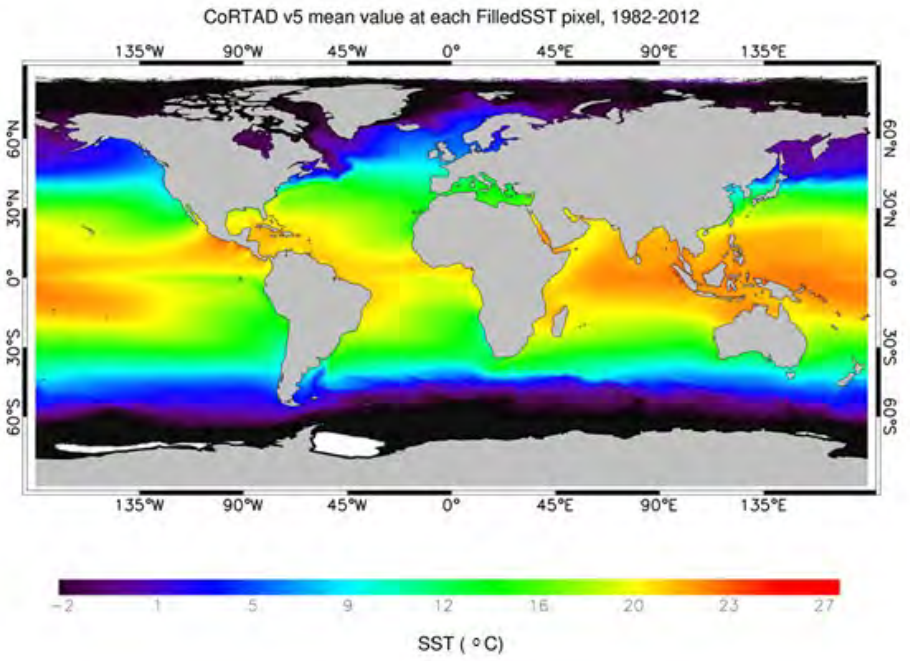

Figure I.5 – The Coral Reef Temperature Anomaly Database (CoRTAD) is a collection of sea surface temperature (SST) map and related thermal stress metrics, developed specifically for coral reef ecosystem applications but relevant to other ecosystems as well. The CoRTAD Version 5 contains global, approximately 4 km resolution SST data on a weekly time scale from 1982 through 2012. The SST data are derived from the Advanced Very High-Resolution Radiometer (AVHRR) sensor.

An improved knowledge of the land surface hydrologic states and fluxes, and of their spatial and temporal variability across different scales, is an important goal in many hydrologic studies (Maurer et al., 2001; Roads et al., 2003). To this end, isolated traditional approaches, such as *in-situ* observations (Ropelewski and Yarosh, 1998), ground observations driven modelling (Mitchell et al., 2004), or direct retrievals from remotely sensed variables (McCabe et al., 2005), become inadequate. To improve this situation, research is being carried out by a number of groups with the goal to utilize and combine as many data products as possible within an integrated framework in a manner to improve the estimation of the water cycle states and fluxes. This integration of data and models is referred to as data assimilations or data fusion (McLaughlin, 2002). Recently, remote sensing data are playing an increasingly important role in such efforts. The main reason is that remote sensing data provides large-scale, systematic land surface observations consistently over the globe. Moreover, advancements in sensors, development of improved retrieval algorithms and tremendous increases in data distribution, storage and processing has greatly promoted the use of remote sensing data in hydrology (Pan et al.,

2008). Water cycle is usually divided in two main compartments: the first one point out the oceanic water (§I.2.1) and the second one highlight the continental water (§I.2.2).

I.2.1 Ocean Water cycle

From the major components of the water cycle (§I.1.1) have been briefly summarized we can turn to some of the modern tools used to study these processes. The emphasis will be on the satellite-based sensors and accompanying models that the National Aeronautics and Space Administration (NASA) and National Oceanic and Atmospheric Administration (NOAA) have launched since the mid-1970s.

Over the years, several NASA missions have studied the effects associated with the global water cycle including El Niño and La Niña, such as changes in sea surface temperature, cloud cover, ocean surface winds, and rainfall. These studies are augmented by data from operational satellites of NOAA. For examples:

- Initial efforts at mapping sea surface temperature and cloud cover were conducted using data from NASA's Nimbus series of satellites. Also, this series included the first ocean color scanner (Coastal Zone Color Scanner), which provided the first estimates of phytoplankton productivity (chlorophyll concentrations) from space.

- The Advanced Very High Resolution Radiometer (AVHRR) instrument flown on NOAA's TIROS-N weather satellite in 1978 and on the NOAA-6 satellite in 1979 greatly enhanced the accurate measurements of factors related to climate variability (*e.g.* Fig. I.5). Still further increases were added to the AVHRR instrument and on subsequent NOAA satellites.

- Sea Surface using radar altimeters – JASON-1, 2, 3; ENVISAT, ERS, SARAL, Sentinel 3 and TOPEX-POSEIDON (*e.g.* Fig. I.6): Satellite altimetry is a radar technique providing the topography of the Earth surface based on the measurement of the distance between the satellite and the surface derived from the two-way travel time of an electromagnetic wave emitted by the altimeter (or altimeter range) and the precise knowledge of the satellite orbit (Chelton et al., 2001; Biancamaria et al., 2017). For environmental applications, short repeat period is necessary, the recent generation of satellite altimeter tried to improve this parameter (Fig. I.7). The primary objectives of radar altimetry from satellites were to measure the marine geoid and monitor the dynamics topography of the sea surface (Vu et al. (2018), submitted) over the open ocean and the coastal areas (Fig. I.8).

Currently, there are many NASA missions that are simultaneously measuring a myriad of Earth's water cycle variables; ocean/sea salinity or temperature (Fig. I.5) or tides (Fig. I.6) or height (Fig. I.7), Evaporation, Condensation, Precipitation, Groundwater Flow, Ice Accumulation, and Run-off. NASA's water cycle research missions can be grouped into

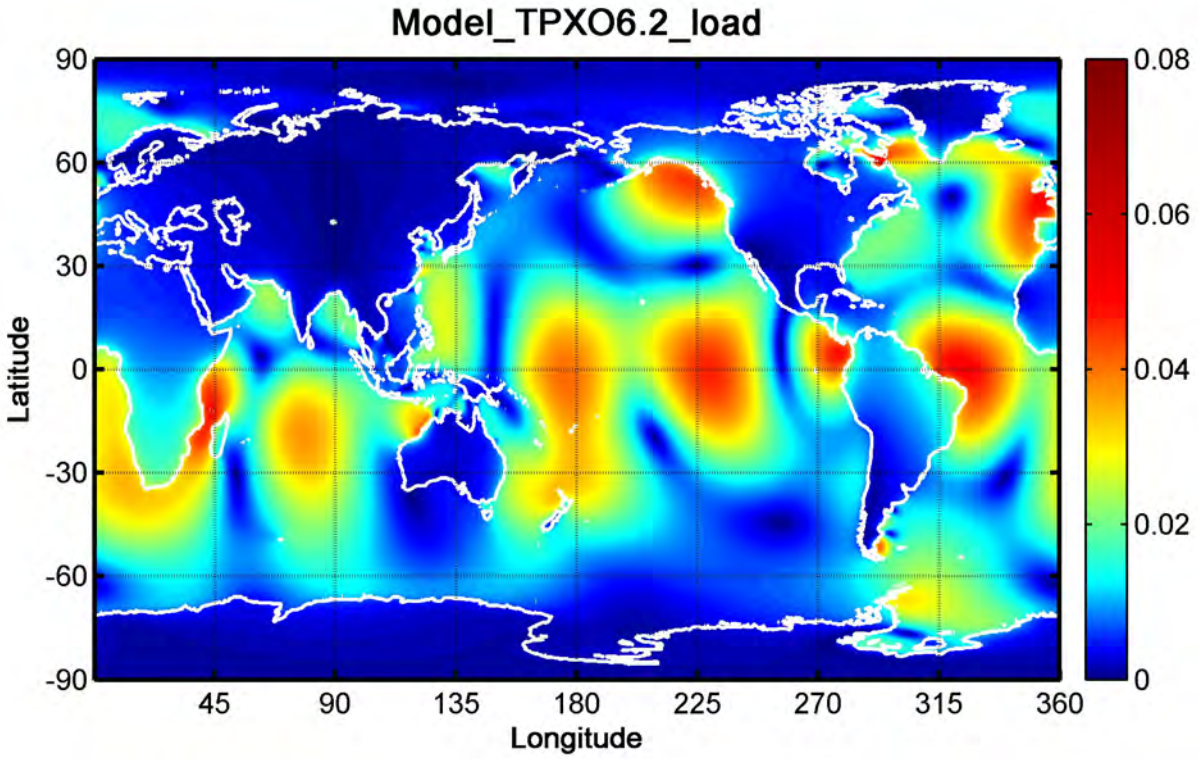

Figure I.6 – The ocean tide map for the principle lunar tide (M2) load tide height amplitude (m) from TPXO6.2_load. The principal assimilated data set is TOPEX/Poseidon (T/P) satellite radar altimetry.

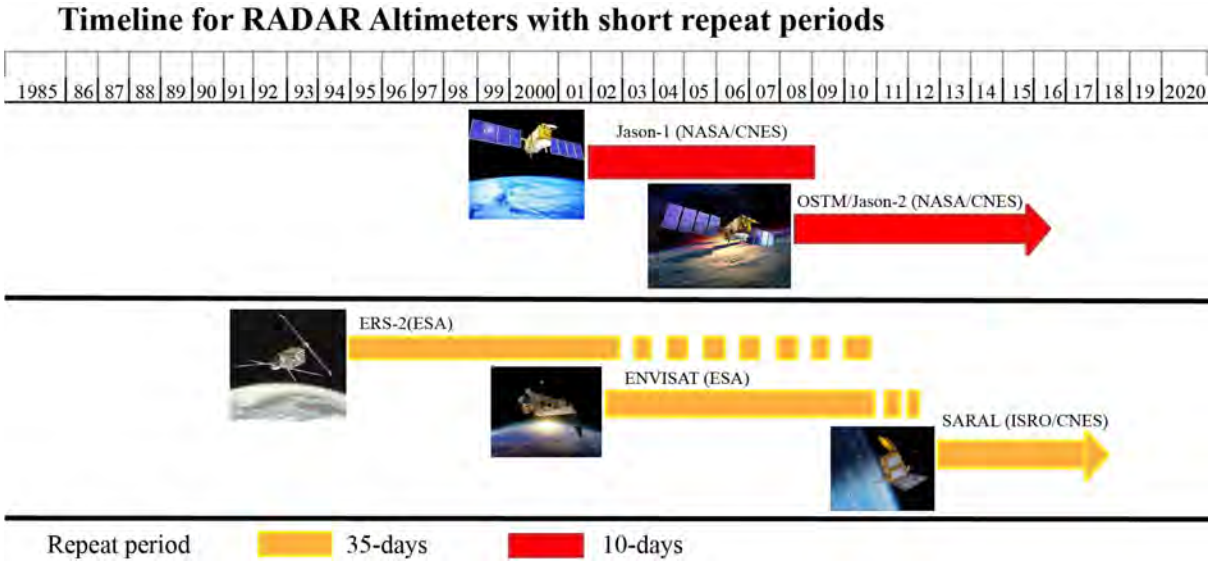

Figure I.7 – Timeline for Radar altimeters with short repeat period used for the analyses of coastal performance (modified from Birkett and Beckley (2010); Vu et al. (2018)).

3 major categories; Water Cycle, Energy Cycle, and Water and Energy Cycle Missions. NASA's goal is to improve/nurture the following global measurements: precipitation (P), evaporation (E), P-E and the land hydrologic state, such as soil-water, freeze/thaw and snow. Therefore, an experimental global water and energy cycle observation system combining environmental satellites and potential new exploratory missions – i.e. advanced remote sensing systems for solid precipitation, soil moisture, and ground water storage – may be feasible. These proposed approaches are tantalizing, for knowledge of global fresh water availability under the effects of climate change is of increasing importance as the human population grows. Space measurements provide the only means of systematically observing the full Earth while maintaining the measurement accuracies needed to assess global variability.

I.2.2 Continental Water Cycle

The continental hydrologic cycle involves both land surface and its interaction in the critical zone in all phases via liquid and frozen precipitation, infiltration and recharge, surface run-off and snow-melt, stream/river flow, and evapotranspiration. These different transport mechanisms are interconnected and strongly affected by the land-atmosphere dynamics and surface heterogeneity in soil type, topography, and vegetation. Numerous international programs, such as:

- Prediction of Ungauged Basins (PUB) and Hydrology for the Environment, Life and Policy (HELP), which focus on the lack of rain gauge data within single watersheds, have been instrumented in bringing worldwide attention to the lack of ground observations.

- The advent of the Earth Observing System (EOS) era in the 1990s, NASA, ESA, and JAXA have launched numerous space-borne sensors to study the various components of the terrestrial water cycle.

There are some uses/sensor/missions to estimate and monitor components of the water cycle that can be used to expand the knowledge in quantifying the spatial and temporal variations in the continental water cycle:

- Precipitation – Tropical Rainfall Measuring Mission (TRMM): Satellite estimates of precipitation are key to understanding the global water cycle with high temporal resolution. It can address particular challenges in analyzing precipitation over land, including understanding rain/no-rain classification, making retrievals over complex terrain, integration of model information (which is important in areas where satellites have trouble making retrievals), and inter-calibration of all precipitation-relevant satellites.

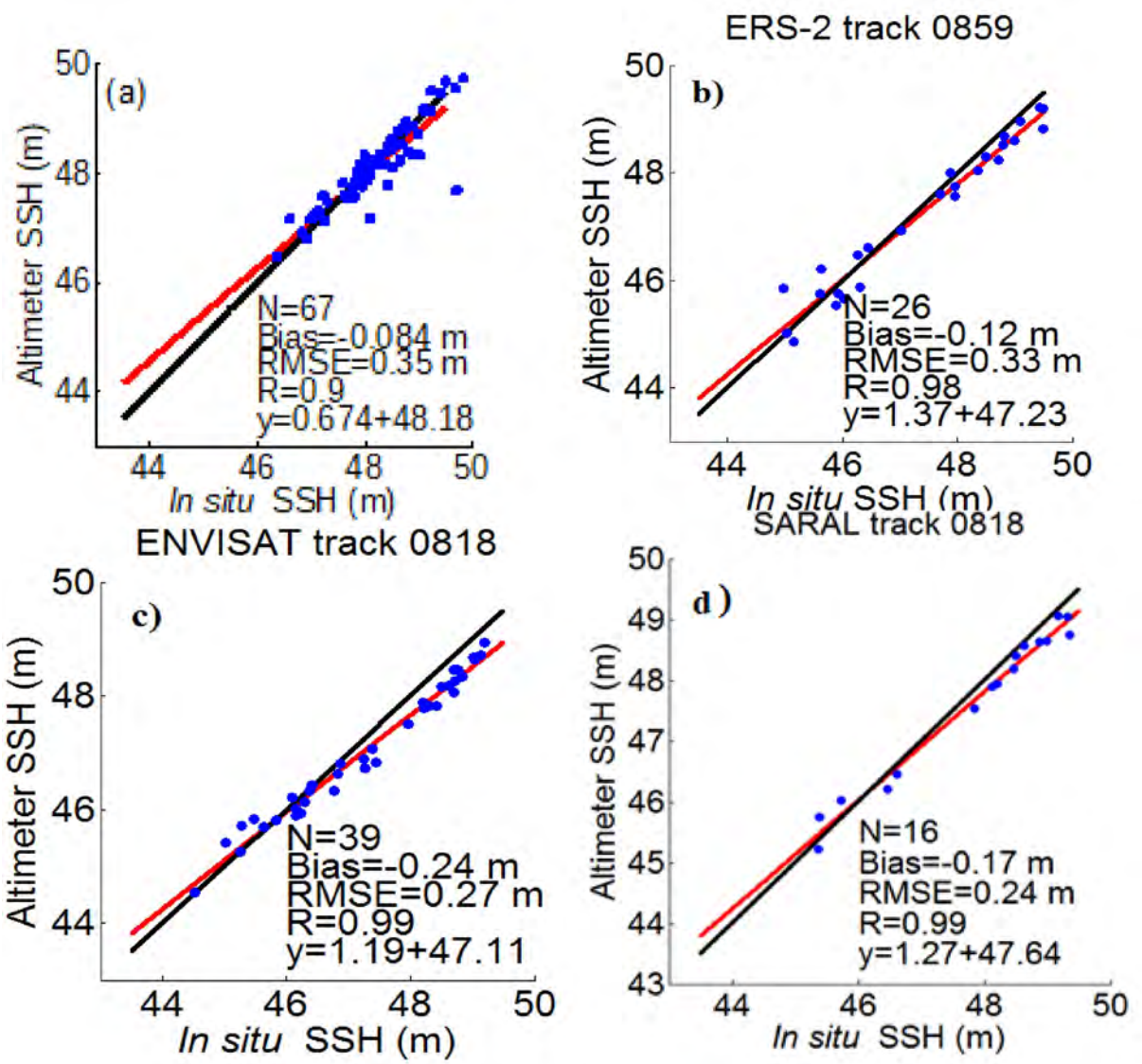

Figure I.8 – Coastal performances between in situ (tide gauge) and altimeter based SSH in La Rochelle using different satellites: a) JASON-2 descending track 70; b) ERS2, descending track 0859; c) ENVISAT descending track 818, d) SARAL descending track 218. (modified from Vu et al. (2018)).

- Evapotranspiration (ET) and sensible heat flux – Moderate Resolution Imaging Spectroradiometer (MODIS): is required at many different spatial and temporal scales in climate, weather, hydrology, and agricultural research and applications. Satellite remote sensing is viewed as one of the only technologies that can be used with land surface models to derive ET from field to global scales, particularly in regions with little or no ground resources available.

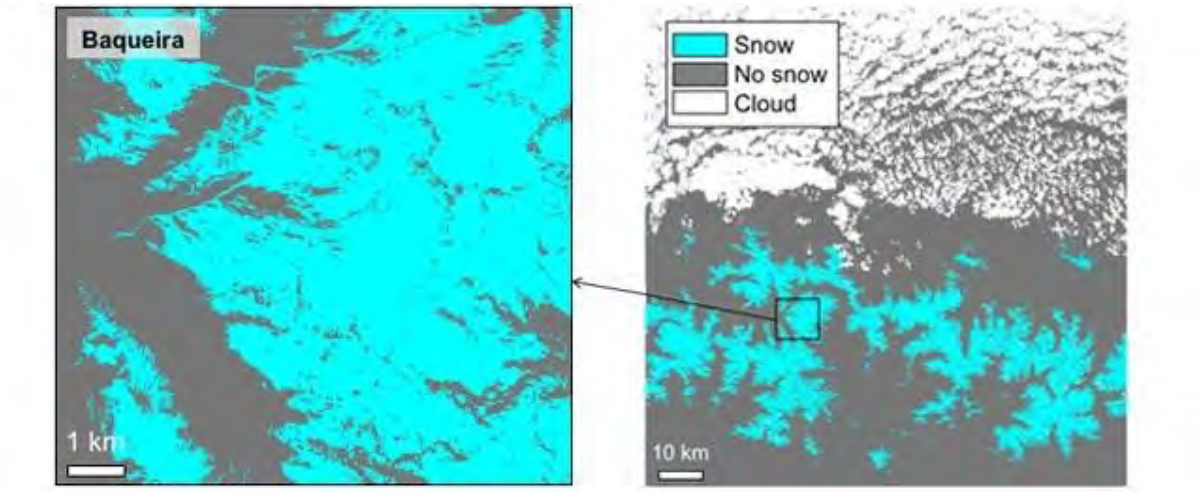

Figure I.9 – Snow map in the Pyrenees on 16 April 2017. The Theia snow product indicates the snow presence or absence on the land surface every fifth day if there is no cloud. This 20 m resolution product is derived from Sentinel-2 L2A images.

- Surface water - JASON-1, 2, 3 and TOPEX-POSEIDON: Water flux throughout the world's rivers, lakes, and wetlands is one of the longest monitored components in terrestrial water balance science. The diversity of satellite sensors now available provide invaluable complementary observations, such as water storage change estimates at the basin scale or spatially distributed geomorphological parameters.

- Snow: Water stored in snow cover is one of the main components of water balance in many parts of the world. The large spatial variability of snow characteristics, particularly in mountains, makes remote sensing a very important alternative to ground snow observations (Fig I.9).

- Soil moisture (SM) constitutes only about 0.005 % of global water resources but it is a key variable controlling numerous processes, the interactions in the critical zone and feedback loops within the climate system. A particular aspect of soil moisture is that controls and governs the surface energy balance, the partitioning between latent and sensible heat and between infiltration and run-off (Blumberg and Freilikher, 2001). In terms of precision agriculture another interesting point is

its ability to monitor and map soil moisture from satellite. The major Earth Observation satellites dedicated to monitoring soil moisture are: Advanced Microwave Scanning Radiometer (AMSR), Soil Moisture Active Passive (SMAP), Soil Moisture and Ocean Salinity (SMOS): Soil moisture near the surface is a relatively new field of remote sensing study. Recent advances in satellite remote sensing have pushed the envelope in the science of soil moisture estimation, improving estimates for modelling and applications. Climate Data Records of soil moisture are fundamental for improving our understanding of long-term dynamics in the coupled water, energy, and carbon cycles over land. To respond to this need, in 2012 the European Space Agency (ESA) released the first multi-decadal, global satellite-observed soil moisture (SM) dataset as part of its Climate Change Initiative (CCI) program. This product, named ESA CCI SM, combines various single-sensor using active and passive microwave soil moisture imagery products into a COMBINED active + passive microwave product (Fig. I.10). Very often, due to weather conditions, the data received from optical sensors could not be used. The radar data give the opportunity to deliver this information. Experimental and theoretical investigations carried out by many scientists worldwide have shown that microwave backscattering from land surfaces is sensitive to vegetation features (Helm et al., 2007; Helm, 2008; Marchan-Hernandez et al., 2010; Kebiao et al., 2008; Larson et al., 2008b; Germain et al., 2004; Gleason et al., 2005). The dielectric characteristics of vegetation material are indeed strongly influenced by moisture content over a wide range of the microwave spectrum. The space based SAR and InSAR observations provide worldwide coverage, even in presence of clouds, of proxies for soil moisture variations and vegetation water content, for various scales, derived from amplitude and phase content of radar imagery (Fig. I.10 and Fig. I.12).

- Surface water - JASON-1, 2, 3 and TOPEX-POSEIDON: Water flux throughout the world's rivers, lakes, and wetlands is one of the longest monitored components in terrestrial water balance science and more generally in the global water cycle. The diversity of satellite sensors now available provide invaluable complementary observations, such as water storage change estimates at the basin scale or spatially distributed geomorphological parameters.

- Groundwater is a more complex variable to study with remote sensing techniques, the most efficient mission was pioneered by GRACE: Gravity Recovery and Climate Experiment launch in 2002. Groundwater comprises more than half of the world's drinking water and a large portion of the water used to irrigate crops. However, groundwater data are scarce in most of the world, making remotely sensed groundwater information that much more valuable. GRACE measures the change in total column water mass (Fig I.2) at continental scales (Tapley et al. (2004); Ramillien

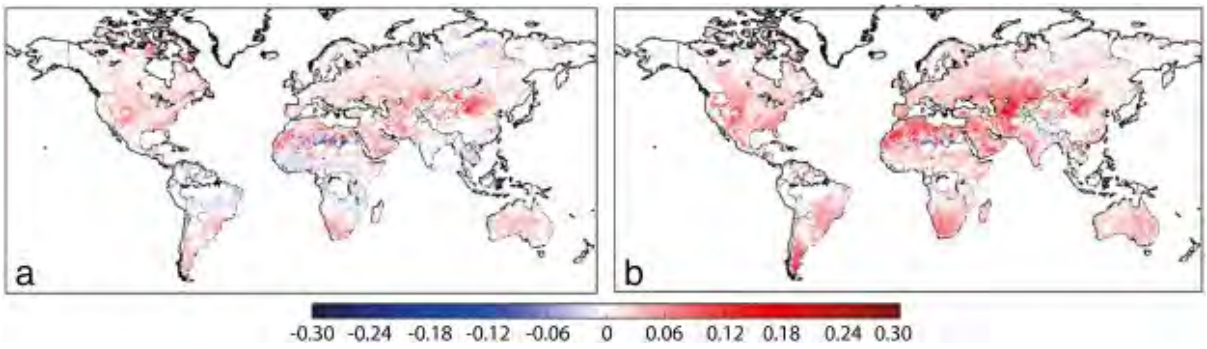

Figure I.10 – Differences in correlations of a) absolute soil moisture values and b) anomalies differences between ESA Climate Change Initiative (CCI) Soil Moisture (SM) COMBINED v02.2 and soil moisture from the first layer of soil of two offline experiments over 1979–2014. Experiment GE8F has a first layer of soil of 1 cm depth (0–1 cm), GA89 of 7 cm depth (0–7 cm). Differences are only shown for pixels that provide significant correlations ($p < 0.05$) for both experiments. Pixels where the correlation level is very low are not met have been left blank. (From Dorigo et al. (2017)).

et al. (2014)).

Currently, research satellites/sensors are aimed at measuring specific components and/or processes of the global energy and water cycles. In fact, historically, space agencies have created separate teams by sensor, focused on the retrieval and/or validation of individual water and energy cycle products. When satellite retrieved surface water and energy budget variables are combined with *in-situ* data like river discharge, budget closure is rarely if ever achieved, demonstrating a basic inconsistency among the retrieved variables (Pan and Wood, 2006). Identifying and diagnosing the degree of hydro meteorological closure in land surface and atmospheric models is a critical and often overlooked component of modeling studies, and is likely a symptom of the focus on separate sensing programs.

I.2.3 Existing tools for water cycle research

There is a range of tools available to help science community to analyze and assess impacts of a changing climate on the water cycle. These tools provide users with convenient data access capabilities, common data transformation utilities, and analysis methods for data and related information.

- *Better Assessment Science Integrating Point and Nonpoint Sources* (BASINS) is a multipurpose environmental analysis system designed to help regional, state, and local agencies perform watershed- and water quality-based studies. It is a useful tool for those interested in watershed management, development of total maximum daily loads (TMDLs), coastal zone management, nonpoint source programs, water

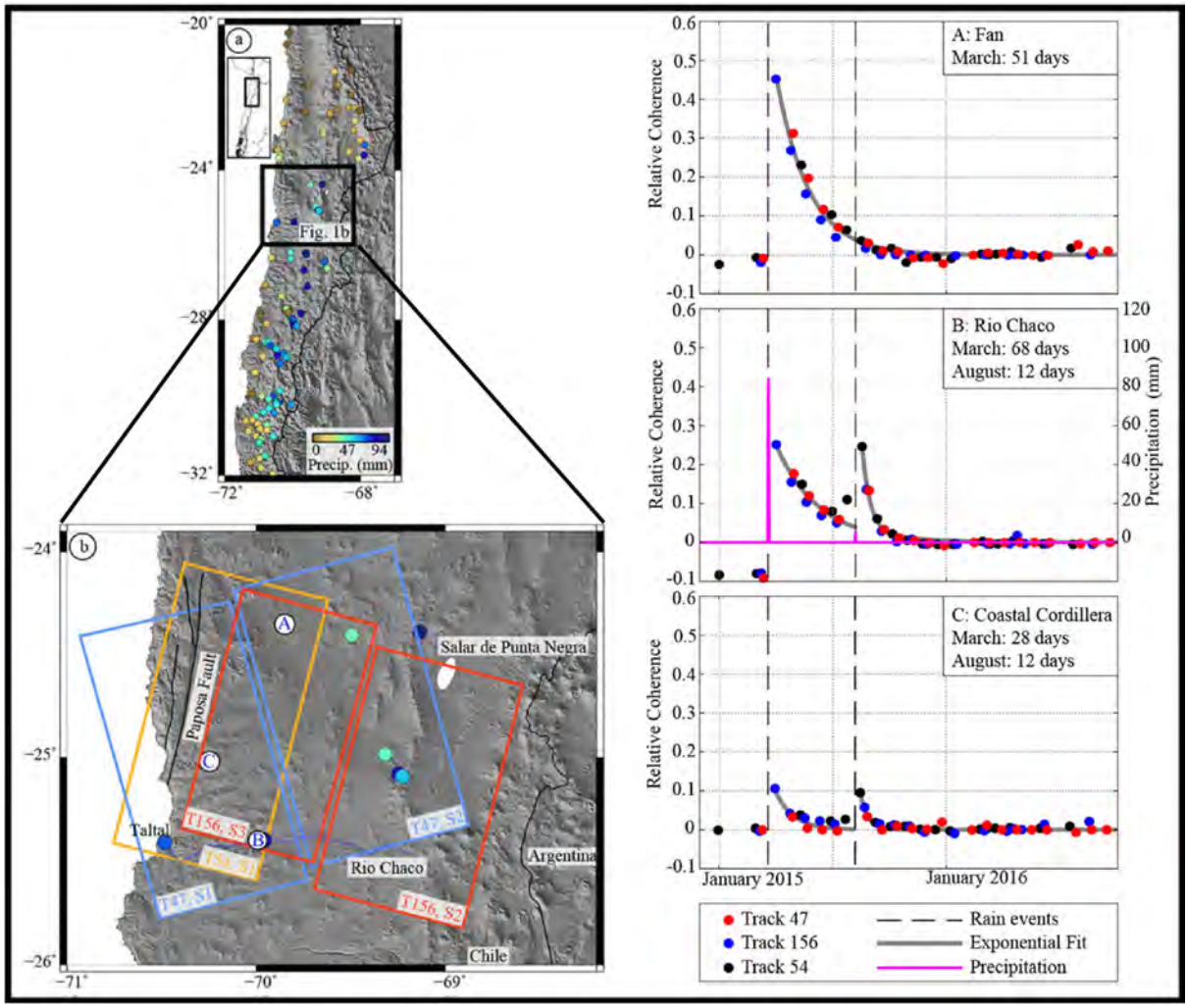

Figure I.11 – a) March 2015 precipitations from in-situ gauges; b) study location map of the Sentinel 1A tracks with the location of the time series (A, B, C) presented in the right graph; c) graph of relative INSAR coherence as a function of time. Time series results (noted A, B, C) from three independent INSAR tracks (colored dots). This example shows the exponential decay of the ground moisture (grey exponential fit) after a rain fall event (dashed grey line). (Modified from CP Scott (2017))

quality modeling, and National Pollutant Discharge Elimination System (NDPES) permitting.

- *EPA's Climate Ready Water Utilities* (CRWU) initiative assists the water sector, which includes drinking water, wastewater, and storm water utilities, in addressing climate change impacts. The impacts of events such as Hurricane Sandy pose challenges to water sector utilities. Extreme weather events, sea level rise, shifting precipitation patterns and temperature variability, all intensified by climate change, have significant implications for the sustainability of the water sector. By planning for, assessing and adapting to these challenges, the water sector can fulfill their public health and environmental missions and begin the process of becoming climate ready.

- *Exploration and Graphics for RivEr Trends* (EGRET): An R-package for the analysis of long-term changes in water quality and streamflow, including the water-quality method Weighted Regressions on Time, Discharge, and Season (WRTDS). It is a method of analysis for long-term surface water quality data. It is intended for use with data sets of more than about 200 observations of water quality over a time span of about 20 years or more.

- *The Federal Support Toolbox for integrated Water Resources* is a USACE initiative that started in 2005 prior to Building Strong Collaborative Relationships for a Sustainable Water Future project. It is supported by multiple stakeholders participating in the project who are interested in its capability to deepen knowledge and understanding, build capabilities and foster collaboration opportunities – especially integrated water resources management.

- *The Geo Data Portal* helps scientists and decision makers construct ensembles and compare climate hind casts and future projections for particular spatial areas. It helps with data management for modeling and assessing the impacts of future climate conditions.

- *Global Precipitation Measurement Education Tools:* this website, presented by NASA's Global Precipitation Measurement (GPM) mission, provides students and educators with resources to learn about Earth's water cycle, weather and climate, and the technology and societal applications of studying them.

- *EPA's National Storm Water Calculator* (SWC) is a desktop application that estimates the annual amount of rainwater and frequency of runoff from a specific site anywhere in the United States (including Puerto Rico). Estimates are based on local soil conditions, land cover, and historic rainfall records. It is designed to be used

by anyone interested in reducing runoff from a property, including site developers, landscape architects, urban planners, and homeowners.

- *National Water Census Data Portal:* The National Water Census Data Platform, enables integration and delivery of water budget information alongside other data of interest to managers, such as water use data or ecological assessment criteria.

- *NOAA's Weather and Climate Toolkit* (WCT) is free, platform independent software distributed from NOAA's National Climatic Data Center (NCDC). The WCT allows the visualization and data export of weather and climate data, including Radar, Satellite and Model data. The WCT provides tools for background maps, animations and basic filtering.

I.3 GNSS-R for water cycle studies

As demonstrated by *in-situ* or remote sensing technics continuous (high temporal resolution) measurement with high spatial resolution is a real challenging goal for monitoring Earth's water cycle.This task not yet completely solved by the above mentioned observation techniques. In the recent years, a new Earth observing systems have grown considerably and it's base on the use of Global Navigation Satellite System (GNSS) signals for remote sensing. With the development of GNSS, including the Global Positioning System (GPS) in the United States, the Russian GLONASS, the European Galileo, the Japanese QZSS, the Indian IRNSS and the Chinese Beidou, as a satellite microwave (L-band) technique with signals through the Earth's atmosphere, more and wider applications and new potentials are explored and utilized to measure environmental parameters quantifying essential surface conditions for the understanding of the water cycle. The versatility and availability of GNSS reflected and refracted signals can image the Earth's surface environments as a new, highly precise, continuous, all-weather and near-real-time remote sensing tool. The refracted signals from GNSS Radio Occultation (GNSS-RO) satellites together with ground GNSS observations can provide many information/parameters for water cycles studies such as the high-resolution tropospheric water vapor, temperature and pressure, tropopause parameters and ionospheric total electron content (TEC) and electron density profile as well. The GNSS reflected signals from the ocean and land surface could determine the ocean height (Martin-Neira, 1993; Wagner and Klokočník, 2003; Germain et al., 2004; Kostelecký et al., 2005; Rius et al., 2002, 2012; Roussel et al., 2015b), wind speed and wind direction (Komjathy et al., 2004; You et al., 2004; Gleason et al., 2005; Thompson et al., 2005) of ocean surface, and from land surface could retrieve soil moisture (Zavorotny and Voronovich, 2000; Roussel et al., 2016), ice and snow thickness (Komjathy et al., 2000a; Zavorotny and Zuffada, 2002).

In this section, I will address some objectives and results of GNSS-RO and GNSS-R

remote sensing in the atmosphere, oceans, land and hydrology as well as new opportunities for studying water cycle. For the fundamental details of this opportunistic remote sensing technique, I will introduce in the Chapter 2 “State of the art of GNSS-R” of my manuscript.

I.3.1 GNSS-R atmospheric studies

The traditional atmospheric observing instruments, such as the water vapor radiometer (WVR), ionosonde, incoherent scatter radars (ISR), topside sounders onboard satellites, in situ rocket and satellite observations (Cloud-Aerosol Lidar and Infrared Pathfinder Satellite Observation well known as CALIPSO), are expensive and also partly restricted to either the bottom side ionosphere or the lower part of the topside ionosphere. While GPS satellites in high altitude orbits (∼20,200 km) are capable of providing details on the structure of the entire ionosphere, even the plasma-sphere. Therefore, GPS has been widely applied in atmospheric sounding, meteorology, climatology and space weather.

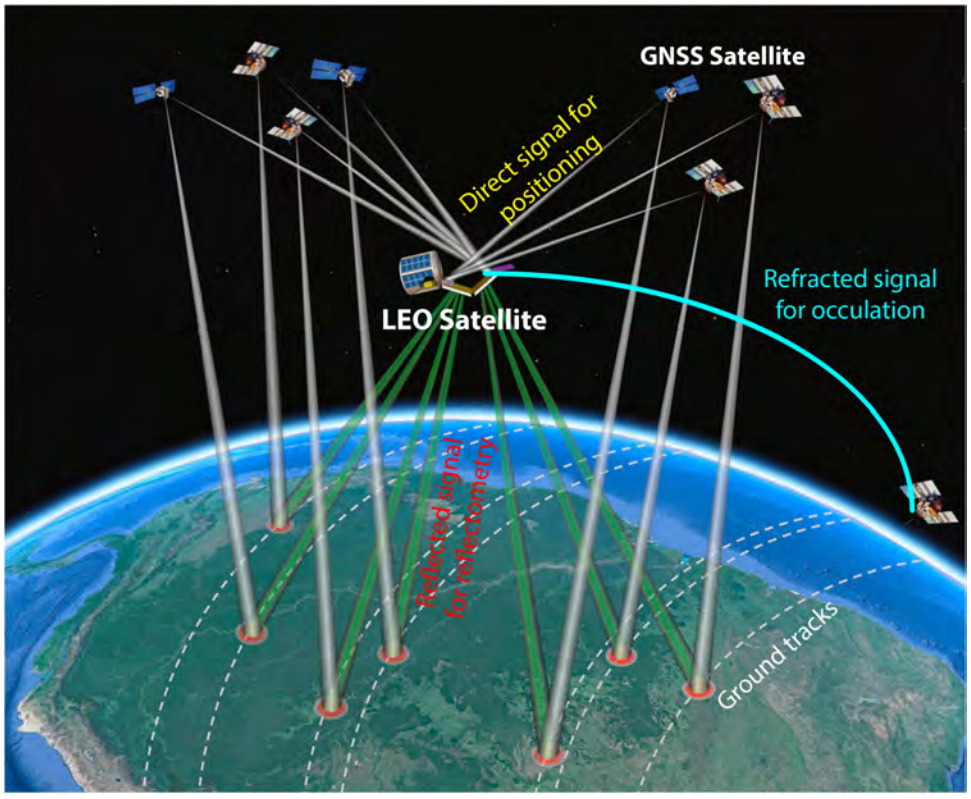

Figure I.12 – Illustration of the geometry of the direct, reflected and refracted GNSS signals and their use for different applications.

Due to the atmospheric refraction, GPS signals propagate through the Earth atmosphere along a slightly curved path and with slightly retarded speeds. For a long time, the

delay of GNSS signals in the troposphere and ionosphere was considered as a nuisance, an error source, and now, with the use of GNSS receivers installed on low Earth orbit (LEO) satellites (Figure I.12) to measure the GNSS-RO signals coupled with ground-based atmospheric sounding techniques that use Continuously Operating Reference Station (CORS) networks, GNSS signals has been used to determine the useful atmospheric parameters. These parameters including tropospheric water vapor, temperature and pressure, and ionospheric total electron content (TEC) and electron density profile which were consistent with traditional instruments observations at comparable accuracies (Schmidt et al. (2005); Schmidt et al. (2008); Jin et al. (2006); Jin et al. (2007)). Nowadays, a number of GNSS-RO missions have been successfully launched for atmospheric, ionospheric detection and climate change/water cycle related studies, such as:

- *The US/ Argentina SAC-C, German CHAMP* (CHAllenging Minisatellite Payload): with the RO on measurements onboard the spacecraft and the infrastructure developed on ground, CHAMP had become a pilot mission for the pre-operational use of space-borne GPS observations for atmospheric and ionospheric research and applications in weather prediction and space weather monitoring;

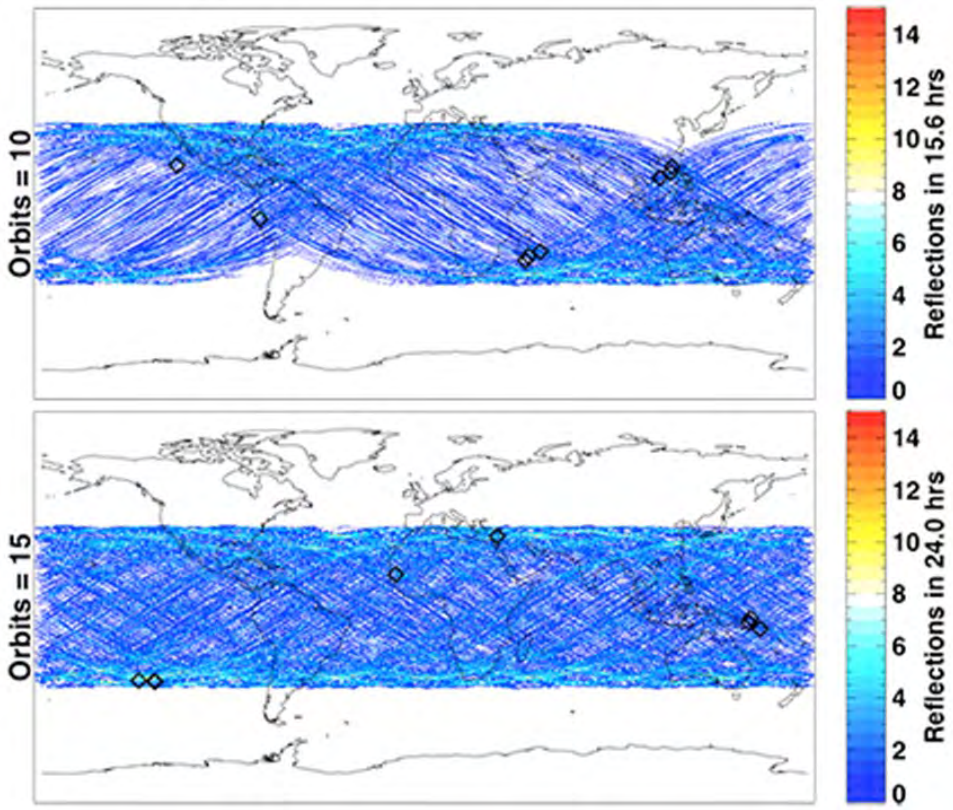

Figure I.13 – CYGNSS coverage (From Calculating Coverage Statistics with CYGNSS - Earth observatory - NASA).

- *Climate Community Initiative for Continuing Earth Radio Occultation* (CICERO) is a follow-on mission to the COSMIC as a self-supporting enterprise for the greater GNSS-RO science and wider user communities who will share in its design, evolution, and success (www.geooptics.com). The CICERO project changes the way to collect and disseminate Earth observational data with 100 microsatellites in Low-Earth Orbit (LEO) performing GNSS atmospheric radio occultation (GNSS-RO) and GNSS Surface Reflection (GNSS-SR) measurements. The CICERO constellation is designed with lower cost of acquiring data essential to understand our planet and expands the possibilities for obtaining new types of data from space. The plan is to initially launch 20 satellites with follow-on launches to reach a sustained array of 100 spacecrafts. The full CICERO constellations are expected to deliver nearly 100,000 atmospheric profiles per a day (Thomas Yunck and Lenz, 2007). Meanwhile, since CICERO has GNSS Surface Reflection (GNSS-SR), it is expected to detect more detailed Earth's surface characteristics and time-varying evolutions;

- *NASA's Cyclone Global Navigation Satellite System* (CYGNSS): CYGNSS was launched into low Earth orbit on December 15, 2016 (Fig. I.13) and it's a constellation of eight micro-satellites designed to measure surface winds in and near the inner core of hurricanes, including regions beneath the eye wall and intense inner rain bands that could not previously be measured from space. The CYGNSS-measured wind fields, when combined with precipitation fields (*e.g.*, produced by the Global Precipitation Measurement [GPM] core satellite and its constellation of precipitation imagers - including the upcoming NASA TROPICS Mission), will provide coupled observations of moist atmospheric thermodynamics and ocean surface response, enabling new insights into hurricane inner core dynamics and energetics.

The main objective of the RO technique (Fig. I.12) for retrieval of atmospheric profiles provided by these missions is to improve numerical weather prediction (NWP) models, especially over polar and oceanic regions where data coverage is crude.

I.3.2 GNSS-R ocean studies

In the recent, the exploitation of Global Navigation Satellite Systems (GNSS) signals for purposes other than navigation and positioning has been conceived and assessed both theoretically and experimentally (Zavorotny et al., 2014). GNSS-Reflectometry (GNSS-R) is a promising remote sensing tool that fulfills the requirements for high spatial coverage, short temporal revisit time, and low cost and low weight as GNSS-R sensors are passive systems equipped with very simple and low-cost instrumentation. The GNSS satellites are constantly broadcasting radio signals to the Earth. However, part of the signals is reflected back from the rough Earth's surface. The delay of the GPS reflected signal with respect to the rough surface could provide information on the differential

paths between direct and reflected signals. Together with information on the receiver antenna position and the medium, the delay measurements associated with the properties of the reflecting surface can be used to produce the surface roughness parameters and to determine surface characteristics. For example, the measurements of GPS reflected signals from the ocean surface could retrieve the ocean surface height, wind speed, wind direction, and even sea ice conditions.

I.3.2.1 Determining ocean surface height

More than 20 years ago Martin-Neira (1993) have proposed the new opportunist application GNSS-R for altimetry. A large amount of studies has been carrying out like Fabra et al. (2012). In altimetry, the main parameter is the vertical height of the reflecting surface, either in absolute terms (*e.g.*, with respect to the center of the Earth) or in relative terms (*e.g.*, with respect to the ellipsoid). Given that the GNSS-R measured surface height will be an averaged value across this area, area which increased with the antenna height (Löfgren et al., 2015; Liu et al., 2017). But one GNSS-R receiver can potentially track up to 40 reflections regarding only GPS and GLONASS constellations (D'Addio et al., 2014). Therefore, the spatio-temporal resolution compared, to others altimetric remote sensing techniques, is significantly improved. The altimetric retrieval techniques are presented in Yu et al. (2014) and Hajj and Zuffada (2003), whereas Yu et al. (2014) suggests to perform altimetry on multiple waveforms at different Doppler frequencies of the full DMM and Hajj and Zuffada (2003) presents an approach that requires neither surface roughness information nor models. The new signals like Galileo signal (E1, E5, and E6) have also been tested for altimetric applications and compared to GPS L1 and L5 signals (Pascual et al., 2014a,b).

Sea surface height (SSH) is constantly changing. Throughout earth's history the sea surface height varied drastically and this ongoing process has a significant impact on life in coastal areas. Therefore, there is a need for constant monitoring of those fluctuations. Nowadays there are primary two approaches for monitoring and measuring sea surface height, mareographs and satellite altimetry. There are many forms of mareographs: floating mareographs, acoustic mareographs, radar mareographs and pressure-based systems, each of these systems carries out the measuring process in a slightly different manner. The mareographs provide data with high accuracy though they suffer from the disadvantage that the punctual measurements do only allow drawing conclusions about the sea surface height in the near vicinity of the tide graph.

Satellite altimetry is a method developed to overcome this problem but with a lesser temporal resolution. The principle of the satellite altimetry based on altimeters emit signals to Earth, and receive the echo from the sea surface, after its reflection. The sea height is represented by the distance satellite - surface and the satellite's position relative to an arbitrary reference surface (the reference ellipsoid). Some location systems like

Doris enable to determine the satellite's position at a high accuracy. We have also to take into account the disturbance suffered by the wave radar. The measurement of these disturbances (by others instruments, or by using multiple frequencies), or their estimation with models, can correct the altimetry measurement.

This satellite altimetry requires dedicated transmitters and receivers with large directional antennae top to achieve high resolution, while GPS as a bistatic radar system, requires only a receiver, not a transmitter, and can receive global, continuous, near-real-time and all-weather signals from global covering GPS satellites. Although the satellite radar technique measures sea surface height at high spatial resolution along its ground track, the cross-track distance is usually quite large (*e.g.*, about the order of 300 km for TOPEX/Poseidon). The GPS reflected signals from the ocean surface can measure the ocean surface height with high temporal-spatial resolution. The tested results of Martin-Neira et al. (2001) in the determining the sea surface height using GPS reflected signals showed a good consistency at the level of about 2 cm in very calm sea state with independent TOPEX/Poseidon data. using Interference Pattern Technique (IPT) of GNSS reflected signals from the ocean surface (Fig. I.14) could compensate these defects of existing techniques near coastal areas, *e.g.*, radar altimetry.

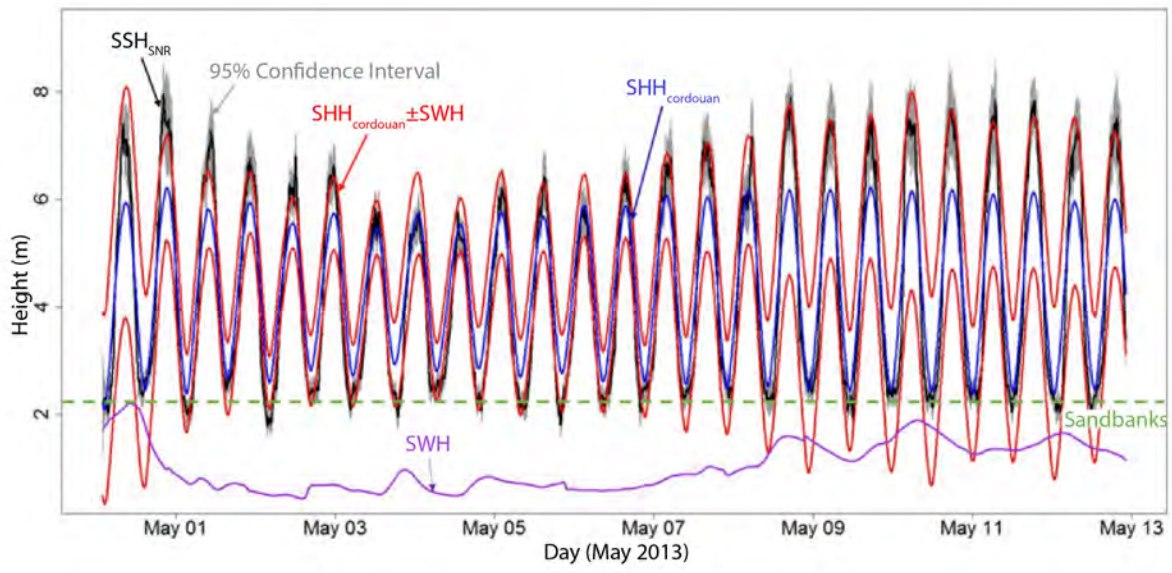

Figure I.14 – Raw (black) SNR-based tide measurements compared with Cordouan tide records (blue) plus SWH values (red) obtained from Wave-Watch III model. Grey area is the 95% Confidence Interval. IPT was improved by LSIM (Roussel et al., 2015b).

I.3.2.2 Monitoring the ocean surface winds

GPS technique in a bistatic radar configuration also can measure the wind vector parameters on the sea surface. The key issue is to extract information from the GPS reflected signal. The primary measurement is the received power from the GPS reflected signal for a variety of delays and Doppler values in a glistening zone surrounding a nominal specular reflection point (Garrison and Katzberg, 1997; Clifford et al., 1998). Therefore, the GPS reflected signal power measurements can measure the ocean surface wind speed and direction (*e.g.* Lin et al. (1999); Komjathy et al. (2000b); Garrison et al. (2002); Cardellach et al. (2003); Thompson et al. (2005); Clarizia and Ruf (2017)).

The NASA-Langley Research Center have shown that using the Delay Mapping Receiver (DMR) with the L1 GPS signal at 1575.42 MHz can also estimates the wind speeds and directions on the ocean surface with high accuracy. The estimated wind speed using surface-reflected GPS data is consistent with independent wind speed measurements derived from the TOPEX/Poseidon altimetry satellite and balloon measurements at the level of 2 m/s. In addition, the surface wind speed retrievals from GPS reflected signals have been shown to be consistent with other independent techniques such as scatterometers, flight level winds, microwave radiometers, and dropsondes (Katzberg et al., 2006a; Katzberg and Dunion, 2009).

The National Oceanography Centre (NOC) has developed the first ever global wind speed products based on reflected GPS signals, using data from the UK TechDemoSat-1 satellite. The measuring principle relies on detecting navigation signals after reflection from the ocean surface, where a calm ocean will give a clean reflection, whilst a rough ocean surface will reduce and spread out the reflected signal. The NOC have developed algorithms that estimate the ocean roughness and wind speed from these reflected navigation signals. This achievement is the result of over fifteen years of partnership between Surrey Satellite Technology Ltd (SSTL) and NOC, sponsored by Innovate UK, the European Space Agency, the UK Centre for Earth Observation Instrumentation and the Natural Environment Research Council (NERC). With support from the European Space Agency and SSTL, the NOC developed the processing chain that transforms reflected signals measured on the satellite to delay-Doppler maps and Levels 2 wind speed products. This data has been released on the website www.merrbys.org. The TechDemoSat-1 mission continues to transform our understanding of spaceborne GNSS-R by providing the opportunity to improve signal calibration and to explore the characteristics of the reflected signals and develop new algorithms and applications.

I.3.2.3 Sounding the sea ice conditions

Due to complex and varying conditions of sea ice, an inaccessible environment and persistent cloud covering, it is very difficult to monitor sea ice conditions with conventional

instruments. Thus, measuring sea ice conditions mainly relies on satellite radar techniques. However, no single sensor is capable of providing the essential range of observations (Livingstone et al., 1987; Rubashkin S.G., 1993). Characterization of sea ice salinity (Rodriguez-Alvarez et al., 2012) and ice thickness are a key parameter for classification and characterization of sea ice masses. Similar to sea surface wind speed retrieval, model fitting between the theoretical and measured delay waveforms can be used to determine the roughness of an ice surface (Komjathy et al., 2000a). In the transition from newly formed sea ice to older and thicker ice, a gradual decrease was observed in bulk salinity and an increase in surface roughness. Roughness may also be inferred by investigating the characteristics of the phase or coherence of the interferometric signal (Rivas et al., 2010). Permittivity of sea ice is another important parameter which can be estimated by GNSS-R. All of these data are also important parameters which influence the temperature and circulation pattern of both the ocean/continent and atmosphere and thus can be used for analyses of the Earth's climate change.

The GPS reflectometry can measure the sea ice conditions as a new technique. Komjathy et al. (2000a) analyzed the aircraft experiment of GPS reflections from Arctic sea ice and over the ice pack near Barrow, Alaska, USA. Correlations from comparisons between RADARSAT backscatter and GPS forward scattered data indicate that the GPS reflected signals could provide useful information on sea ice conditions. The reflected signal shape was quite consistent for the moderate altitudes of the airborne GPS receiver and the peak power changed significantly along the flight track. This behaviour of the reflected signal showed clearly the sensitivity to ice condition, indicating that the GPS reflected signals can be used to determine the ice features. In addition, as the effective dielectric constant of ice depends on various factors, such as the ice composition, density, age, origin, salinity, temperature, morphology (Shokr, 1998), the internal ice states can be determined with the reflection coefficient over a frozen sea surface by the effective dielectric constant of ice and the dielectric constant of the underlying water under some conditions (Melling, 1998).

In recent, GNSS signals reflected from ice were correctly identified (Fig. I.15) and measured using the UK DMC experiment on February, 4th 2005 over the Kuskowkwim Bay Alaska (Gleason, 2005; Alonso-Arroyo et al., 2017). Earth-reflected Global Positioning System (GPS) L-band signals exploited by GNSS-R systems deeply penetrate in ice, allowing for analysis of snowpack internal structures and characteristics, such as thickness and accumulation rates (Wiehl M. and R., 2003). In contrast with the typical Ku- and C-bands used in ice sheets analysis from SAR data, the low frequency GNSS signals can penetrate up to 100 meters in the ice, allowing for ice investigation on the millennium scale.

In the future, GPS reflected signals might provide more detailed information and internal states of sea ice, including the floe ridges, frost flowers, broken ice, and fine-scale

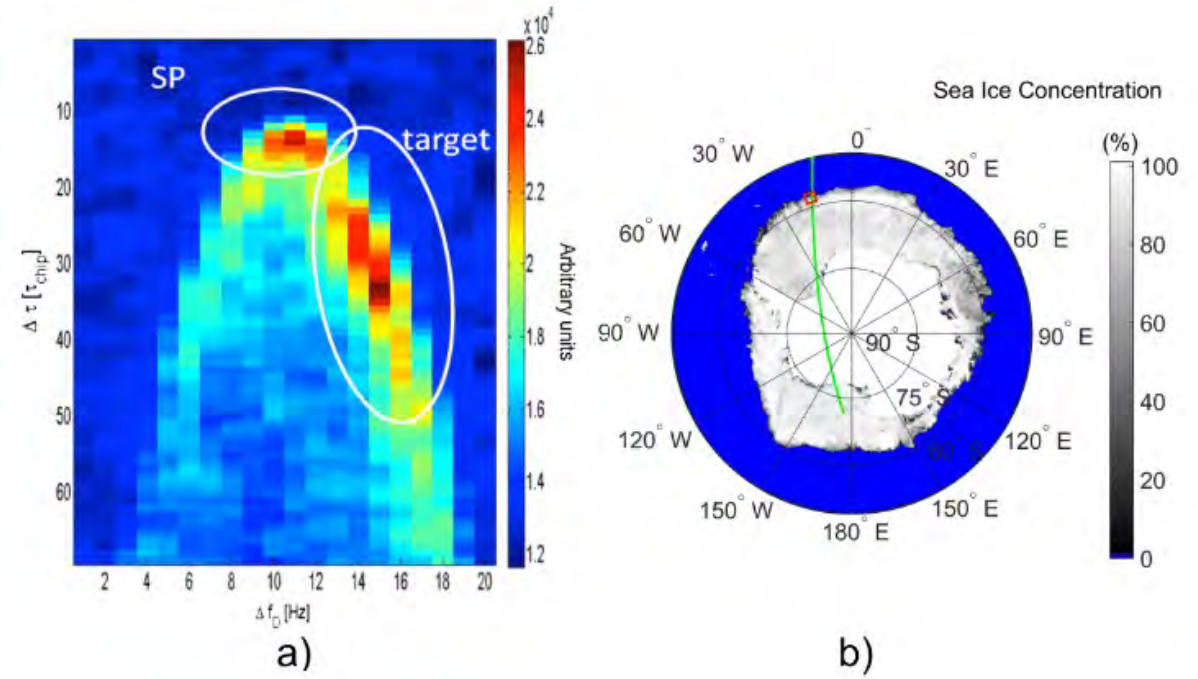

Figure I.15 – TDS-1 DDM image acquired on 2014-10-31 at 09:44:48 over an ice infested area (a). The stronger scattering areas related to specular point (SP) and sea ice are enclosed within white ellipses labeled as SP and target, respectively. Ice concentration map relevant to Antarctica obtained processing SSMI data (b). The area of interest and the TDS-1 track are highlighted by the red rectangle and the green line, respectively. (From Schiavulli et al. (2017))

roughness at the snow-ice interface. Therefore, the reflected GPS signals have a high potential and applications in sensing and investigating the sea ice state, particularly for inaccessible and atrocious sea ice cover.

I.3.3 GNSS land/hydrology studies

Stored moisture in soil and snow is another important factor in the water cycle. Quantifying the spatio-temporal distribution of moisture is important for environmentally oriented research and for decision making in agriculture and hazard management. As the Alps provide long-term water storage for a large part of Central Europe, they provide a particularly relevant example. The weather in the Alps (*e.g.*, warm temperatures in spring time, sustained precipitation on saturated soils) can cause flooding. In summer, melt water originating from the Alps can mitigate drought conditions downstream. Determination of moisture in soil and snow in the alpine context is therefore very important for local and downstream policy making and water resources management, which critically depends on understanding meteorological and hydrological processes in the complex alpine terrain. This includes the processes of heat and moisture transport in the atmospheric boundary layer and the interactions at the well-known Critical zone.

I.3.3.1 Monitoring lake and wetland

Within the global water and energy cycles, it is critical to identify and understand interrelations of water cycles and the critical zone phenomenon involving precipitation, soil moisture change, interactions between atmosphere, vegetation and soil, freeze/thaw state, inundation, stream flow, and run-off together with wetlands dynamics and cycles of CH_4 and CO_2 (Paustian et al., 2006) emission change and water storage capacity change. Hydrologic alterations including wetland filling or drainage can impact water impoundments or release from continental drainage basins and significantly affect global sea level (Gornitz et al., 1997; Sahagian, 2000).

For the conventional geodetic instruments, it is difficult to monitor pounds, small rivers/lakes. While cross-track distance of satellite radar altimetry is usually large, the spatial resolution is fairly low to monitor small (Jin and Komjathy, 2010). GNSS reflected signals could detect characteristics of small Earth's surface, such as the pound/lake. Treuhaft et al. (2001) measured the surface height of the Crater Lake in Central Oregon with 2-cm precision in 1 second using the GPS signals reflected from the surface of Crater Lake. In addition, the strength of this signal is also a good discriminator between wet and dry ground areas and therefore could be applied to coastal and wetland mapping (Garrison and Katzberg, 2000).

Monitoring wetland dynamics with a high temporal resolution and a global coverage is critical to fill an important Earth sciences information gap and thereby advance

the capability to address science issues in global cycles. A GNSS-R constellation like CYGGNSS (launch in December 2016) is also capable of radio occultation measurements could be part of a system for observing the global water cycle. In particular, GNSS-RO, based on the refraction of GNSS signals passing through the atmosphere, has been shown to provide highly accurate water vapor profiles from the mid-troposphere to the surface (Kursinski and Gebhardt, 2014), with sub-kilometer vertical resolution (Kursinski et al., 2000). These profiles have been used to probe the internal humidity structure of tropical cyclones (Vergados et al., 2013), improve understanding of infrared retrievals under cloudy conditions (Vergados et al., 2014), and advance our understanding of how tropical humidity is related to large-scale atmospheric circulation patterns such as the Hadley cell (Vergados et al., 2015). These circulations can affect the global atmospheric dynamics and thus the global CH_4 distribution. Furthermore, measurements of intense precipitation and other hydrometeors are expected from polarimetric GNSS-RO observations, a concept to be tested from a spaceborne experiment (Cardellach et al., 2015). This would represent an additional piece of the water cycle being measured by GNSS-based techniques.

Wetland information that GNSS-R can contribute to direct societal benefit applications and policy implementation in an array of ecosystem functions where wetlands must be preserved or restored (Dorsey, 2015). GNSS-R would support the mapping of inundation patterns in much higher temporal detail, at both pan-basin and sub-basin scales and allow detection of key events such as maximum inundation stages (which vary in timing and location across the basins) and irregular episodic flooding due to rain. In view of The Global Wetland Observing System (GWOS), GNSS-R data would provide valuable inputs on a regular and global basis and be a main contributor to the Convention.

I.3.3.2 Measuring soil moisture

The soil moisture content is important for hydrology, climatology, and agriculture (Jackson et al., 1996). Since soil moisture determines water availability at the surface, and therefore, controls the partitioning of the incoming radiation into the latent and sensible heat flux, it is one of the main controls of the land-atmosphere feedbacks and a key component in the water cycle. Understanding these processes is also essential for predicting natural hazards like i) landslides where the increase of soil moisture induce an increase of weight that can trigger the landslide; ii) droughts, and iii) floods. In the agricultural context, the level of moisture in soil is an important element affecting plantation and plant growth. Hence, monitoring this attribute over the surface of an irrigated system facilitates correct and timely irrigation for consistently high yields, while avoiding application of excessive water prevents leaching of nitrates below depths of root penetration and depriving them of the needed oxygen.

Single point measurements sensors commonly used for moisture include:

- Frequency domain sensor such as a capacitance sensor;
- Neutron moisture gauges, uses the moderator properties of water for neutrons;
- Neutron moisture gauges, uses the moderator properties of water for neutrons.

For time domain transmission (TDT) and time domain reflectometry (TDR), we used the dielectric properties of soil and water to measure the soil moisture. Water has a high dielectric constant; a higher water concentration causes a higher average dielectric constant for the soil. The average dielectric constant can be sensed by measuring the speed of propagation along a buried transmission line (Stacheder et al., 2009).

For Heat dissipation sensor: Heat dissipation probe provides an indirect measurement of soil suction on the basis of different thermal conductivity properties of soil components and the heat dissipation rate is sensitive to soil water content. Farmers use soil moisture information, from one/few single point sensors or worse, rely on the nearest hydrological or meteorological station that can be at more than ten kilometers away, to adapt their farming practices (Spellman, 2017).

In this way, on water logging and flooding side, an important aspect is to monitor the soil moisture content to understand when excess rainfall will cause water logging and/or flooding. Again, the spatial extent is difficult to measure as most tools are *in-situ* sensors at a coarse grid. Remote sensing tools are used but their spatial resolution or their temporal one can be coarse. This is a challenging point because when you have an accurate spatial resolution you have a low temporal one with a revisiting time of few weeks and reversely so it is difficult to provide the right image at the right time.

In the past, the soil moisture was also inferred using passive radiometers and/or active remote sensing radiometers sensors (*e.g.*, Njoku and Entekhabi (1996); Ulaby et al. (1996); Mancini et al. (1999); Jackson (2001); Jackson et al. (2002)). However, these remote sensing techniques are more expensive. The GNSS signal forward scattered from a land surface is similar to scattering from an ocean surface (Garrison and Katzberg, 2000), while the main differences are in the spatially and temporally varying dielectric constant, surface roughness, and possible vegetation cover. Masters et al. (2000, 2004) obtained soil moisture the Central Plains Experimental Range of Colombia, with the peak power of the GNSS reflections. Katzberg et al. (2006b) and many others have successfully estimated soil reflectivity and dielectric constant with GNSS reflected signals.

The power level of the GNSS reflected signal from the land contains various important information *i.e.* soil moisture, dielectric constant, surface roughness, and possible vegetation cover (Masters et al., 2004). Some experiments, using GNSS reflected signals, have demonstrate that it could be used for soil moisture retrieval (Fig. I.16). For example, Katzberg et al. (2006b) obtained the soil reflectivity and dielectric constant using a GPS reflectometer installed on an HC130 aircraft during the Soil Moisture Experiment 2002 (SMEX02) near Ames, Iowa (USA), which were consistent with results found for

other microwave techniques operating at L-band. In addition, the multi-path from ground GNSS networks is possibly related to the near-surface soil moisture. Larson et al. (2008b) found nearly consistent fluctuations in near-surface soil moisture from the ground using only GPS multi-path, comparable with soil moisture fluctuations in the top 5 cm of soil measured from conventional sensors. However, GPS multipath signals are very complex due to various factors, *e.g.*, vegetable, foliage, and glass debris. To retrieve the soil moisture parameters, it is necessary to further remove the other factors' effects. Additionally, simulations have been performed by Ferrazzoli et al. (2011) which have opened up the possibility of sensing forest biomass using GNSS reflections. This is another area where validation data is needed to further assess the feasibility of this application.

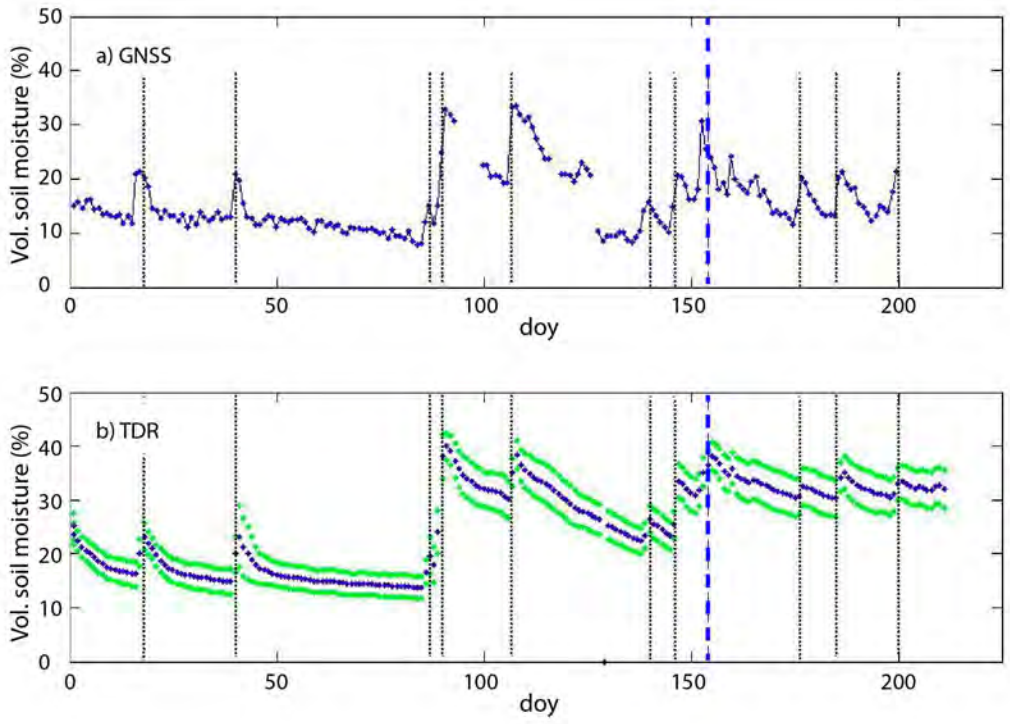

Figure I.16 – Volumetric soil moisture variations at Sutherland a) from GNSS data and b) from TDR sensors. Vertical lines show precipitation events for rain (black dots line) and snow (blue dashed line) (From Vey et al. (2016a)).

I.3.3.3 Vegetation water content

When the soil is covered with vegetation, the bistatic scattering around the specular direction is essentially influenced by the power attenuation of reflected signal (Ferrazzoli et al., 2000)with stronger attenuation when plant biomass increase. So, many authors considered as vegetation, *i.e.* Small et al. (2014) develop a method of forest imaging

vegetation water content (VWC, Figure I.17) from the multipath variation in the signal received at a permanent geodetic receiver. The Normalized Microwave Reflection Index (NMRI), developed by Small et al. (2014), remove the first order terrain effects and produce an observable sensitive to VWC.

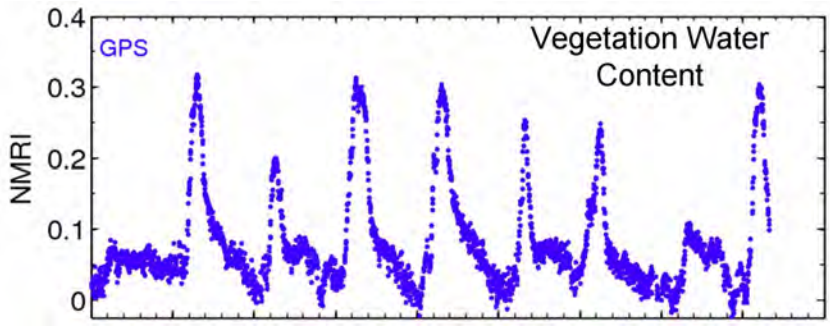

Figure I.17 – Vegetation Water Content derived from GNSS-R measurements (time versus NMRI).

I.3.3.4 Measuring land snow/ice thickness (cryospheric sensing)

Snow is a critical storage component in the hydrologic cycle and an important component of the climate system; however, current *in-situ* observations of snow distribution are sparse. Snow Water Equivalent (SWE), snow height (HS), and height of new snow (HNS) are vital parameters in cryospheric sciences such as snow hydrology, as well as in avalanche hazard and snow climatology. In addition, snow cover determines albedo and is therefore also important in land-atmosphere feedbacks for the critical zone. In the forecast of avalanche hazard, particularly for wet snow avalanches, important decisions must be made based on these parameters describing the development of the snowpack and its variability with slope angle, aspect, and altitude (Lehning and Fierz, 2008; Schirmer et al., 2010). In snow hydrology, if the spatial distribution of SWE and HS is measured over entire catchments, we can obtain an estimation of the total stored water resources (Grünewald et al., 2010; Wirz et al., 2011). This information is extremely valuable for hydroelectric companies, water supply companies, and risk assessment (Blanchet et al., 2009; Blanchet and Lehning, 2010).

However, *in-situ* observations of snow distribution are sparse, and remotely sensed products are not enough precise and only available at a coarse spatial scale, *e.g.*, the U.S. Snowpack Telemetry (SNOTEL) network (Serreze et al., 1999) or french CES "surface enneigée" from THEIA pole.

Mid to high-latitude or high elevation continental snow constitute of low density snow or dry snow with little wet content, or sub-surface layers of Antarctica's dry snow are rather transparent to L-band signals. This property of the L-bands has been employed

(Eisen et al., 2008) to retrieve the deep layering of large ice sheet like the Antarctic plateau. Some studies on modelling like Wiehl M. and R. (2003) show the potential of GNSS-R technique to determine parameters like the accumulation rates of snow. Some other studies used linear polarization antennas to quantify the number and location of the interference notches and solve for the layer thickness of the snow (Rodriguez-Alvarez et al., 2012). As the ice thickness is related to the amplitude of the reflected signal as a function of the incidence angle or relative amplitudes between different polarizations (Lowe et al., 2002a), the snow/ice thickness can be retrieved from the GPS reflected signals. In addition, the change in snow depth is also monitored using the corresponding multi-path modulation of the ground GPS signal. The tested results for two springs 2009 snowstorms in Colorado showed strong agreement between GPS snow depth estimates, field measurements, and nearby ultrasonic snow depth sensors (Larson et al., 2009).

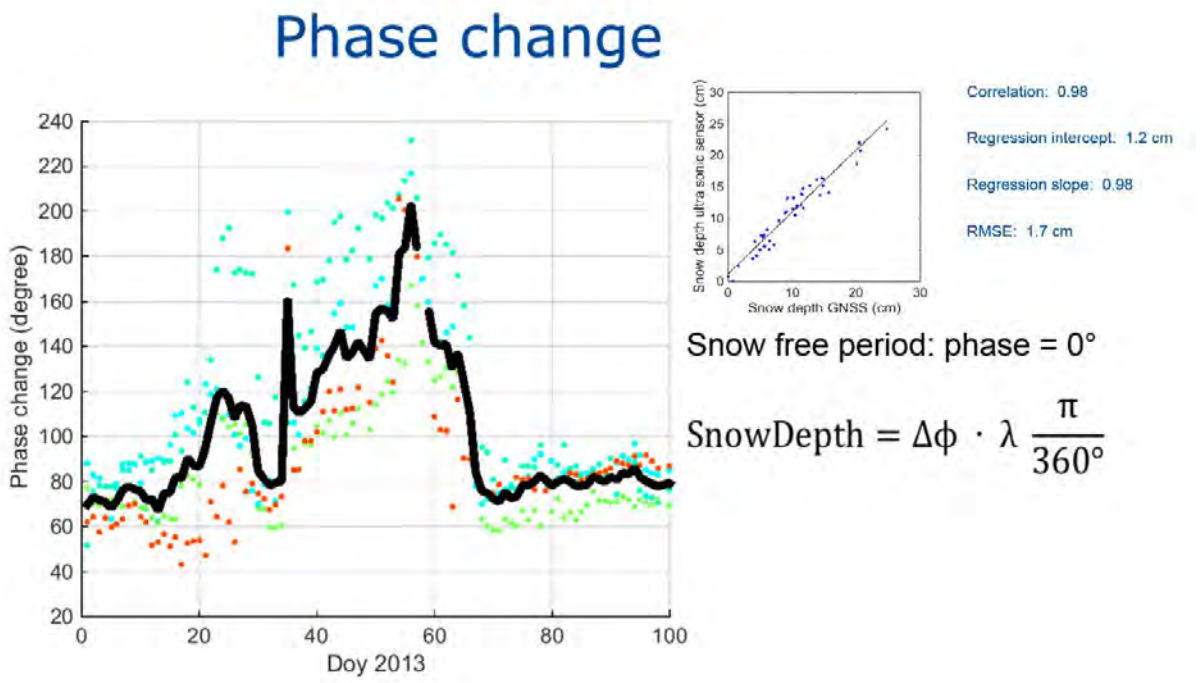

Figure I.18 – Snow depth estimation using the variation of the SNR_r phase, linear correlation between snow depth GNSS- R and the ultra-sonic *in-situ* sensor, modified from (Vey et al., 2016b).

As for others applications, three main parameters of sea/continental ice (i.e. thickness, surface roughness and ice permittivity) can be retrieved with GNSS-R (Larson et al., 2009; Gutmann et al., 2012). These parameters can be combined to help characterize different ice types including new ice, young ice, thin first-year ice, etc. The estimated precision is at a few cm levels.

The IPT, Larson et al. (2015) can be applied to in situ networks like H_2O network (Larson, 2015) in a very impressive way to increase the measurements. Ones, Larson

et al. (2010); Vey et al. (2016a), demonstrated that the height is a noisy measurement and with outliers (Fig. I.18). An improved methodology used a fixed reflector height and modelling a sinusoidal adjustment. In so doing, we can estimate the SNR_r phase and thus convert phase into snow depth. Same results are also obtained in Rodriguez-Alvarez et al. (2012) with a dedicated GNSS-R receiver (GOLD-RTR) using a linear polarization.

I.4 Organization of the manuscript

After this **first chapter** which takes the place of general introduction, the work presented in this manuscript is organized in 5 chapters:

- In the **second chapter** I will present the state of the art of GNSS-R opportunistic remote sensing technique from fundamental of the GNSS system to existence of GNSS-R measurement technique.
- In the **third chapter**, I will present the new GNSS-R approach to retrieve soil moisture variations using Unwrapping SNR phase in case of sandy soil with two examples:(Volleyball field, Dahra experiments)
  - The first experimental and quite simple since constituted of 100% sand with iso granulometry. This site, which corresponds to the Volleyball field located at Paul Sabatier University, was used to develop and test the methodology.
  - The second is a natural example with soil rich in quartz sand ($\sim$ 80%) but also clay, located in the field experiment of Dahra in Senegal.

  .
- In the **Fourth chapter**, I will present the potential and accuracy of GNSS-R technique for river altimetry based on the SNR signal for detection of extreme hydrological events: Red River Delta and Mekong Delta (Vietnam). The interest of these two deltas is that are subjected to dramatic changes in water levels due to the interactions between the continental floods and the oceanic tides.

I close my remarks with a **fifth chapter** which allows me to make a short summary of the main results obtained in this manuscript and I also present the different perspectives offered by this thesis work.

Chapter II

STATE OF THE ART OF GNSS-R

Contents

Looking at all remote sensing systems, the system with the largest and most widely used constellation in the world is obviously the Global Navigation Satellite System (GNSS). Indeed, it is used by anyone obtaining its Position, Velocity and time (PVT) from

GNSS constellations (GPS, GALILEO, GLONASS, BEIDOU/COMPASS etc.). This system has shown the quality of these performances in geodesy, but also meteorology and many fields of geophysics. However, this remote sensing tool has gained new impetus with the use of often undesirable signals for conventional GNSS methods: reflected signals. This opportunistic method is therefore an evolution of GNSS and has been called GNSS reflectometry or GNSS-R. There are many GNSS-R issues, because with the launch of new satellites (GALILEO, BEIDOU / COMPASS for example), the quality and density of source signals is improving day by day with the increase in the number of satellites in orbit. It represents an undeniable complementary with other dedicated remote sensing systems since it allows the monitoring of natural environmental phenomena with a high temporal frequency and a worldwide cover. Then, as we shall see, it allows the monitoring of a large number of environmental problems: altimetric monitoring of ocean waters, coastal zones, inland waters but it is also likely to give other important information such as soil moisture, snow depth, mapping of flooded areas. This is certainly one of the main advantages of this method, born of the accidental reflection of a GNSS radius on sea surface (Auber et al., 1994) but now used on wide variety of surfaces (soil, water, snow, vegetation, detection of targets for example: boat, oil slick, etc.). Early experimental studies using GPS signal reflections date back to the early 1990s, Martin-Neira (1993) suggests using backscattered signals to determine tidal height variations. Experimental tests carried out by Katzberg and Garrison (1996) show that it is possible to use these low-energy signals on Low Earth Orbit satellites (LEO) to follow Ionospheric delays on ocean areas. Since then, environmental applications have diversified. The temporal variations of the water level are currently being monitored throughout the world (Larson et al., 2013, 2017; Löfgren et al., 2014; Shah and Garrison, 2014; Lestarquit et al., 2016), soil moisture (Larson et al., 2008b, 2010; Roussel et al., 2015a, 2016; Chew et al., 2016; Zhang et al., 2017), snow depth (Larson et al., 2009; Cardellach et al., 2012; Jin and Najibi, 2014) and even biomass (Egido et al., 2014; Motte et al., 2016). After a few reminders concerning the GPS and the various GNSS constellations, we will discuss the structures of the signals delivered by these constellations and we will see how they are used to make positioning either by measuring the code that modulates the carrier or by measuring the phase of the carrier. Then we focus on the opportunistic signals of GNSS Reflectometry. We will see how to measure them with specialized receivers for reflectometry or with standard receivers used for positioning. We will then present the fundamental concepts of the different methods of measuring the observable provided by the reflectometry.

II.1 What is GNSS

II.1.1 Principle of GNSS

The first constellation of GNSS satellites began in the 1970s (Seeber, 1993): The Global Positioning System (GPS), better known under the GPS acronym, was originally developed as part of a collaboration within NATO funded by the US Army (US DoD). The main objective of the system is to benefit from complete planetary coverage for an unlimited number of simultaneous users (passive system). This system works regardless of climatic conditions. The GPS system answers 3 main questions: What is the time? What is my position? What is my speed? The GPS system has three distinct segments (Duquenne et al., 2005):

- The spatial segment which consists of a set of satellites;
- The control segment that controls the system;
- The user segment which is made up of all civilian and military users of the system.

II.1.1.1 The spatial segment

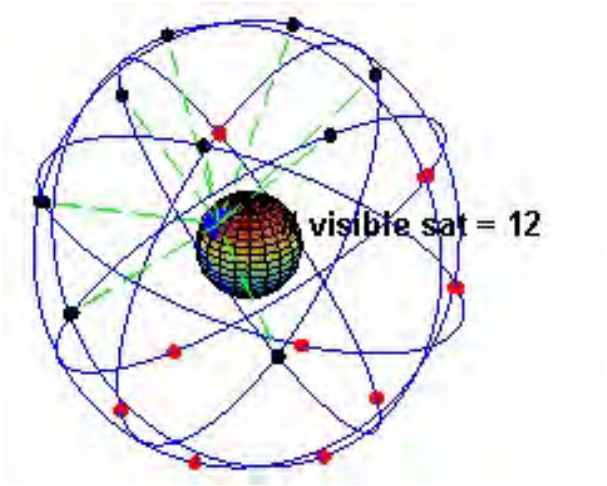

Figure II.1 – Spatial GPS segment with its 6 orbital planes. This geometry allows a worldwide cover with at least 4 satellites in visibility.

Initially, the GPS system consisted of 24 satellites (Fig. II.1) distributed on 6 orbital planes $\approx 55°$ / equator with a period of revolution ≈ 12 h, flight altitude ≈ 20.200 km. The south and north poles have to lowest coverage due to a lack of satellites (Fig. II.2). The different types of satellite used by the GPS system are divided into different blocks:

- Block I: 11 satellites (1978 to 1985), were designed to validate the concept;

- lock II and IIA: 28 launched (early 1989), the first operational version of the system began in 1993. Their initial lifetime was 7.5 years. The block IIA brought an improvement to the clocks (2 cesium clocks and 2 rubidium clocks);

- The IIR and IIR-M blocks: replace the previous blocks, they have a lifespan $\approx$ 10 year, the 12 satellites of the IIR block are able to communicate with each other. They have a modernized version: the IIR-M block, consisting of 9 satellites, which inaugurates the new civilian frequency L2C (first satellite launched in 2005) and the new military code M;

- The IIF block: with its 12 satellites, it presents the latest improvements of the GPS system with the appearance of the frequency L5 (1^{st} satellite launched in 2010).

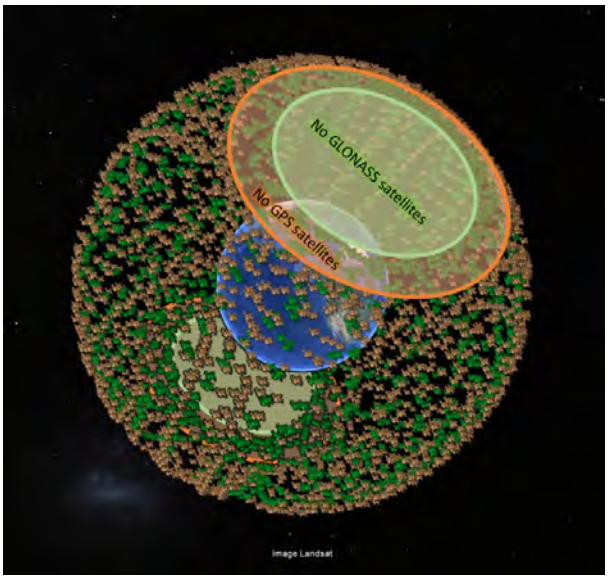

Figure II.2 – Coverage density of the two oldest GNSS constellations: the US GPS system (orange) and the Soviet GLONASS system (green). However, there is a lack of coverage at the poles, this hole is more important for the GPS system than for the GLONASS system. On this representation are represented the different positions, during a day, of the set of satellites of each constellation, the time step between two positions is fifteen minutes. N.B.: the distance from Earth (blue sphere) to satellite is not to scale.

II.1.1.2 The control segment

It consists of 5 ground stations located in Hawaii, Ascension Island, Diego Garcia, Kwajalein (Marshall Islands) and Colorado Springs (Master Control Station). The stations continuously record the GPS signals, perform meteorological measurements and send the data to the Colorado Springs station (Fig. II.3).

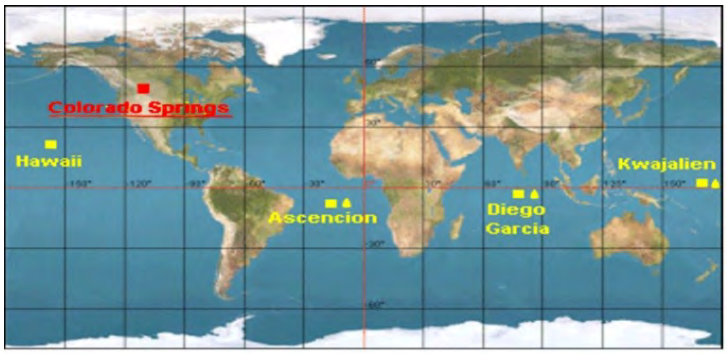

Figure II.3 – Location ground stations, they are located on a line near the equator except for the main station of Colorado Spring. (▲: ground antenna, ■, ■: tracking station). Modified from the Federal Aviation Administration (FAA, USA).

II.1.1.3 The user segment

This is the user community who, based on information from satellites and using the GPS receiver, will find their space-time position. It includes the various existing GPS receivers, both civil and military, that are used for sea/river, road and air navigation.

In particular, national and international organizations maintaining their own permanent GNSS networks consisting of ground stations, such as the International GNSS Service (IGS) or the Permanent GNSS Network (PGN), set up and maintained by the French National Geographic Institute (IGN) in France. A specific French network, known as “Réseau GNSS Pernament” (RGP), is also maintained by the IGN. These organizations collect and process data from the various GNSS constellations before redistributing them to users.

II.1.2 Description and structure of the GPS system

The GNSS signal is, expressed in terms of electromagnetic spectrum, a microwave signal (Fig. II.4) in L-band ($\sim$ 20cm wavelength) generated and diffused continuously by the various GNSS satellite constellations. This L-band signal has several advantages:

- the signals are not disturbed by solar and Earth radiation;
- they can penetrate cloud layers (“all weather” signal);
- they functioning day and night;
- the receivers are passive, meaning that they simply receive the signal which is continuously transmitted by the satellites and can therefore accommodate an "infinite number" of users without saturating the system.

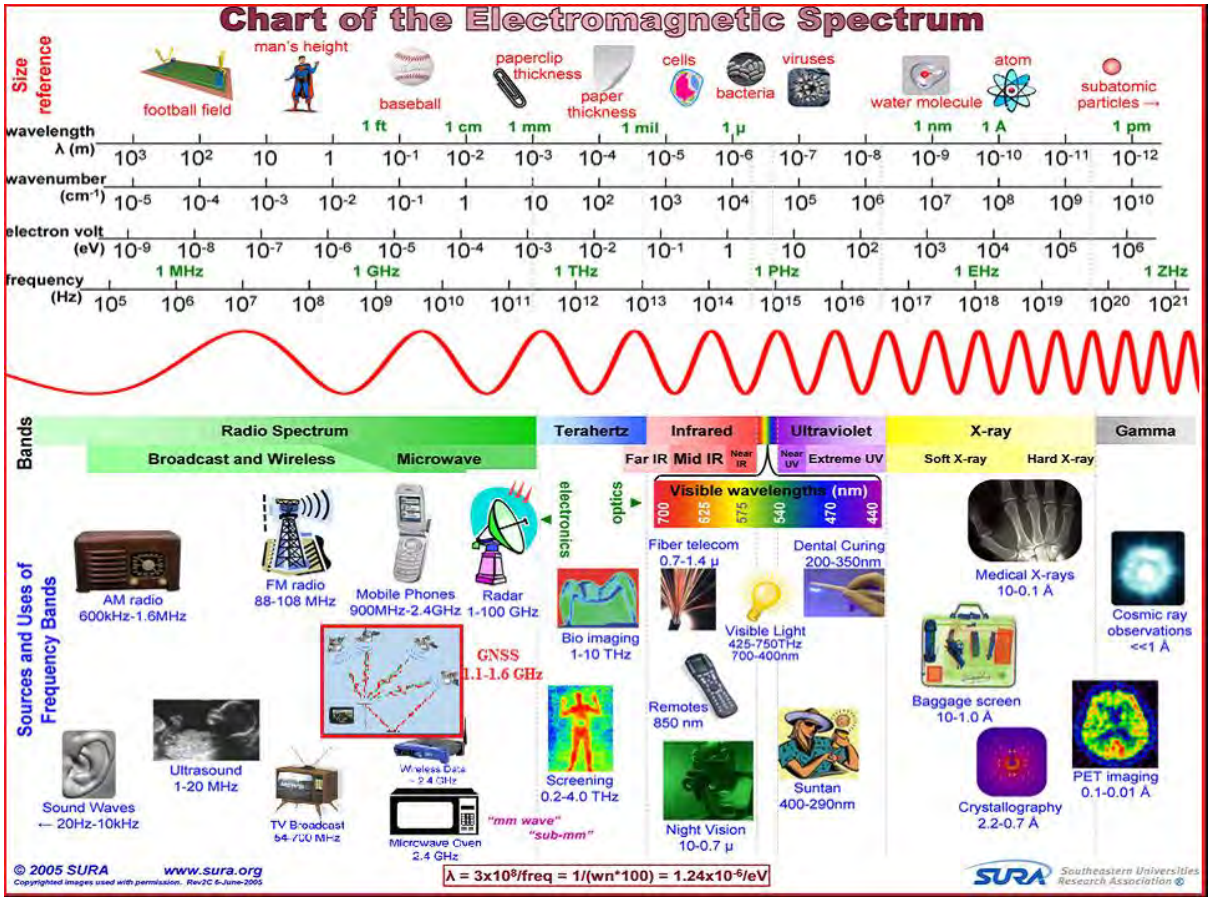

Figure II.4 – Electromagnetic spectrum and its applications (modified from SURA chart, 2005), red window corresponds to GNSS spectrum.

The GPS constellation pioneered have now spread to other constellations. Recognition of this fact has led us to describe first GPS signals. The GPS signal is based on a fundamental frequency of 10.23 MHz and from this frequency, the two main frequencies are obtained by modulation: *f1* of 1575.42 MHz and *f2* of 1227.60 MHz and with the GPS modernization, a third frequency *f5* was introduced at 1176.45 MHz. The GPS satellites transmit multiple coded signals, either for civilian or military purposes. The civil modulation corresponds to the *C/A* code (Coarse Acquisition Code is one of the signals broadcast on the L1 carrier), with a sequence resulting from the modulo-2 addition of the pseudo-random binary *C/A* code at 1 Mega-chips per second and with a period of 1ms (figure II.5). The *P* code (for "precise") at 10.23 Mega-chips per second with a period of 1 week. These different modulation codes have the following characteristics:

- Pseudo-random noise (PRN) codes or "Gold codes" (Gold, 1967), which is made of two types of codes (Groves, 2008): The *C/A* code (Fig. II.5) allows each satellite to be identified and the *P* code is reserved for military applications. These codes are based on the “Code Division Multiple Access” (CDMA) technique, for sending information by spectrum diffusion, which is an effective response to the multipath problems that are specific to mobile signals. More generally, this type of communications is particularly suitable for the GNSS signals with a low signal-to-noise ratio (SNR);

- A 12.5 minutes navigation message giving the satellite's condition, GNSS time, the gap between the GNSS time and Coordinated Universal Time (UTC), the satellite ephemeris, the almanacs of different satellites (accuracy of the orbital parameters is less than the ephemeris), weather information and other relevant parameters for calculation of the final position of the receiver. A total of 25 frames, 1500 bits each, are transmitted at a rate of 50 bits per second (bps).

II.1.2.1 PRN Codes

If we consider A "Pseudo Random Noise" code (PRN) as a random sequence of n pulses generated at a given frequency, and with an amplitude of a_n, equal to +1 or -1 with the same probability. For a pulse duration T_c, which corresponds to the inverse of the frequency, the signal sequence is written:

$$S(t) = \sum_{n=-\infty}^{+\infty} a_n \Pi(\frac{t - nT_c}{T_c}) \tag{II.1}$$

The individual pulse of the random sequence is called a chip. The auto-correlation

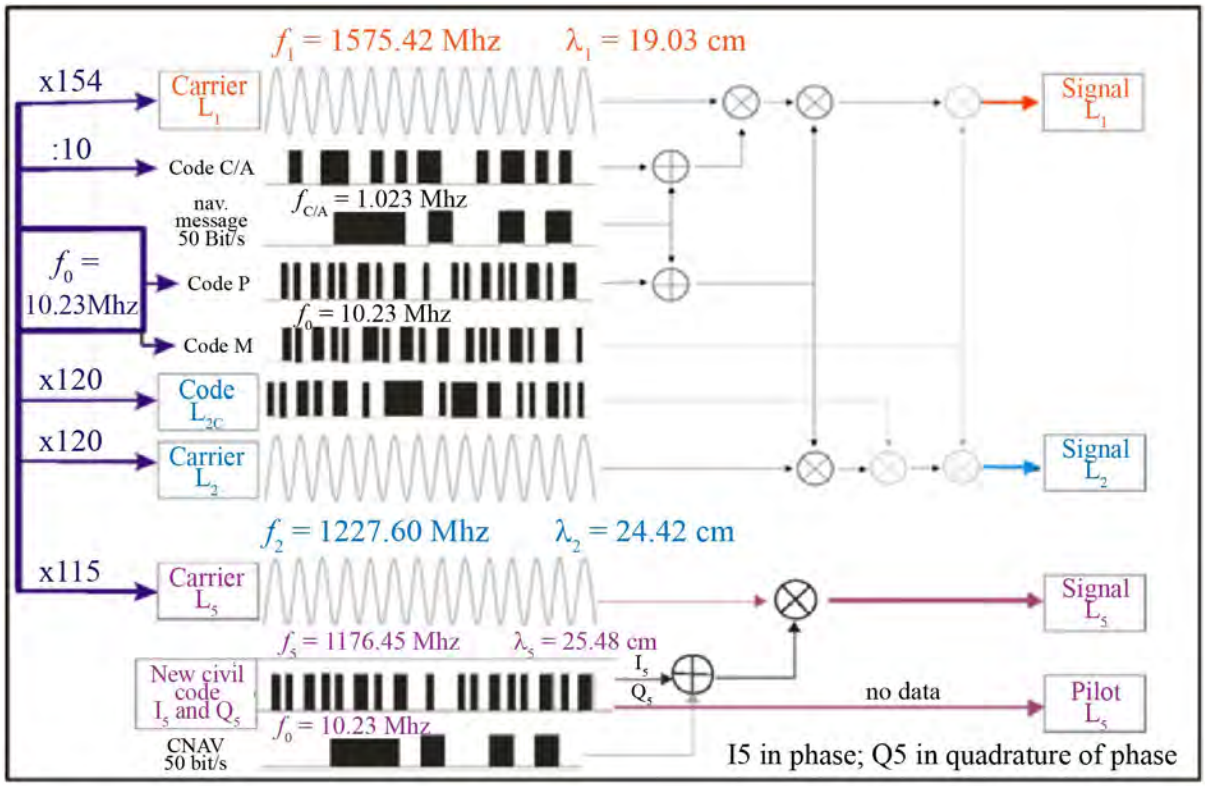

Figure II.5 – Structure of the modernized L-band GPS signals, the M-code is a new version of previous military P(Y) code. For Block IIR-M, IIF, and subsequent blocks, the L2C signal, scheduled to be the first of the modernized civil GPS signals. It will provide greater accuracy and robustness and faster signal acquisition than the current L1 C/A-code signal. It is combination of C/A and two additional PRN ranging codes will be transmitted: L2 Civil Moderate (L2 CM) code and the L2 Civil Long (L2 CL) code.

function R_p of this infinite sequence can be represented by a triangle Λ_{τ_c}:

$$R_p(\tau) \approx \Lambda_{\tau_c} = \begin{cases} -\frac{|\tau|}{\tau_c} & \text{when } \mid \tau \mid < \tau_c \\ 0 & \text{otherwise} \end{cases} \quad \text{(II.2)}$$

with τ is the time interval.

As illustrated in equation II.2, increasing the frequency of chips induces a final triangle correlation for which the base is narrower and therefore final correlation is more accurate. Two types of PRN codes are used to broadcast GPS signals: The *C/A* code (Coarse Acquisition) and the code *P* (Precise).

The *C/A* code is used for civil applications, it has a frequency of 1.023MHz and it is in "Open Access". The length of this code is 1,023 chips, generated with a clock of 1023MHz and a spectral bandwidth of 2046MHz. The *C/A* code is unique for each GPS satellite, this PRN code correlation has similar properties to the white Gaussian noise. That is to say a high auto-correlation to uniquely identifying each of the satellites and a low cross-correlation, which because of the finite length of the *C/A* code, is not zero, but is low enough for the proposed navigation applications. And thus, allows a single receiver to receive signals from different GPS satellites simultaneously without significant interference between them. It only modulates on the carrier L_1, which has a frequency equal to 154 times the fundamental frequency f_0 at 1575.42MHz.

The *P* code, which is reserved for the military, has a frequency that is equal to the fundamental frequency at 10.23MHz. It has a period of 7 days ($\sim$ 720 Gbytes). It modulates the frequencies of carriers L_1 and L_2 (120 x f_0 at 1227.60 MHz). When it is encrypted by the *W* code of the military (in wartime), it gives a new code called code *P(Y)*.

The GPS signals are generated synchronous to each other in order to have a common reference time for solving positioning equations. The signals are transmitted in Right Hand Circular Polarized (RHCP), so the polarization rotation caused by the ionosphere does not affect signal reception. Circular polarization means that the end of the vector of the electric field vector is a circle in a plane perpendicular to the wave propagation direction. We speak of right polarization if the circle, over time, is built in a clockwise direction, and the polarization direction is inversed for left polarization or Left Hand Circular Polarized (LHCP).

II.1.2.2 The signals from the L1 band

The signal S_1 of the carrier L_1 is modulated by the codes *C/A* and *P(Y)*, respectively in phase *(I)* and quadrature of phase *(Q)*. The navigation message is superimposed on these two codes. The analytical expression of the signal S_1 transmitted on L_1 with the

carrier frequency f_1 for a given satellite is written:

$$S_1(t) = \sqrt{2P_{C/A,L_1}}D(t)C/A(t)\cos(2\pi f_1 t + \varphi_{L_1}) + \sqrt{2P_{P(Y),L_1}}D(t)P(t)\sin(2\pi f_1 t + \varphi_{L_1}) \quad \text{(II.3)}$$

where:

- $P_{C/A,L_1}$ and $P_{P(Y),L_1}$ are the powers transmitted in L_1 for the two codes C/A and $P(Y)$;
- $D(t)$ is the transmission message;
- $C/A(t)$ and $P(t)$ are the binary sequences of the codes C/A and $P(Y)$.

The PRN codes and the navigation message are synchronized since they are based on the same reference clock.

II.1.2.3 The signals from the L2 band

The signal S_2 of the carrier L_2 is only modulated by the code $P(Y)$. It is written:

$$S_12(t) = \sqrt{2P_{P(Y),L_2}}P(t)\cos(2\pi f_2 t + \varphi_{L_2}) \quad \text{(II.4)}$$

with:

- $P_{P(Y),L_2}$ is the transmission power for L_2;
- $P(t)$ the sequence of the $P(Y)$ code.

There is no data transmitted on the frequency L_2 ($D(t)$ absent, formula II.3).

II.1.2.4 Modernization of the GPS system

The GPS system is seeking to perpetuate, so it is essential to make it evolve according to technological progress, the appearance of new constellations and / or new applications. In the early time, developments were guided by technological progress, as evidenced by the various blocs that have been launched. The emergence of new applications for civil aviation for example and the arrival of competing constellations (for example GLONASS, GALILEO, BEIDOU) have led to deeper changes such as the emergence of new civil codes and (IIR-M block) and a new carrier. In addition, so-called augmentation systems, which seek to improve the accuracy of the system (§ II.1.6), rely on ground stations and a few satellites to provide corrections to reduce errors in GNSS systems.

The new L2C Civil Code

The new civil signal (Fig. II.5), which modulates the L_2 carrier, makes it possible to correct the ionospheric effects by combining the measurements of pseudo-distances

obtained on L2C with the measurements of the *C/A* code obtained on L_1. The main difference between the L2C code and the *C/A* code, except for a different carrier frequency, is that for the civil part of the L2C signal, there are two codes multiplexed between them (the military part of the signal is close to that of L_1). One of these codes, called "Code Moderate" (CM clocked at 511 kHz), which is multiplexed with the navigation message while the other code known as "Code Long" (CL clocked at 511 kHz), is not. These codes have a longer period than the *C/A* code, with a period of 1ms. The *CL* code has a period of 1.5 seconds and the *CM* code of 20ms.

The S2C signal [II.5] that transmits at frequency f2 for the L2 band for a given satellite is:

$$S_{2C}(t) = \sqrt{2P_{P,L_2}}D(t)P(t)\cos(2\pi f_2 t+\varphi_{L_2})+\sqrt{2P_{C/A,L_2}}[D(t)CM(t)\oplus CL(t)]\cos(2\pi f_2 t+\varphi_{L_2}) \quad \text{(II.5)}$$

with $\oplus$ modulo-2 addition, which corresponds to the multiplexing operator of civil codes (Azmani, 2010).

The new carrier L5 and its civil code

In addition to having a different carrier frequency (Fig. II.5), the S5 signal of the L_5 carrier (1,176.45MHz) [II.6] is modulated by a third civil code (Azmani, 2010). This code was designed for "life safety" applications in civil aviation. The S5 signal is modulated by a Quadrature Phase Shift Keying modulation (QPSK) with a component in phase I5 = $NH_{10}I$, which contains the navigation information and the quadrature component Q5 = $NH_{20}Q$ (period of 20ms) that contains no data and is called the "pilot signal" in figure II.5:

$$S_5(t) = \sqrt{2P_{C/A,L_5}}D(t)NH_{10}I_5(t)\cos(2\pi f_5 t + \varphi_{L_5}) + \sqrt{2P_{P,L_5}}NH_{20}Q_5\sin(2\pi f_5 t + \varphi_{L_5}) \quad \text{(II.6)}$$

where NH_{10} and NH_{20} are the Neumann-Hoffman multiplexing codes of I5 and Q5 at 10ms and 20ms, respectively.

II.1.3 Description and structure of the GALILIO system

The European satellite navigation system GALILEO is designed on a civilian basis, while integrating the necessary security protections. Starting in the 1990s, the project really began to develop from March 26, 2002, when the Council of Ministers of the European Union Transport validated the GALILEO program's development phase. The first validation satellite IOVE-A (GALILEO In Orbit Validation Element, II.2) was launched at the end of 2005, before being joined by a second IOVE-B in April 2008. These two satellites (IOVE- A and IOVE-B in an almost operational orbit of 23222 km) demonstrated the interoperability of GALILEO and GPS systems, for example: the possibility of substituting a system for the user, transparent to the user, other. The first four GALILEO

operational satellites were then launched in October 2011 and 2012. GALILEO is being developed by the European Space Agency (ESA) and will consist of a constellation of 30 satellites placed on three orbital planes spaced at 120° apart and inclined to 56° with respect to the equator, with an altitude of 23616 km and a revolution period of the satellites of 14 h 21 min. In the same way as the GPS system, GALILEO uses the CDMA to distinguish the satellites from each other, and also transmits in L-band to the following main carriers:

- E_1 (=L_1): $f = 1575.42$ MHz, $\lambda = 19.03$ cm;
- E_{5a}: $f = 1176.45$ MHz, $\lambda = 25.48$ cm;
- E_{5b}: $f = 1207.14$ MHz, $\lambda = 24.83$ cm;
- E_6: $f = 1278.75$ MHz, $\lambda = 23.4$ cm.

The GALILEO system is based on the Binary Offset Carrier code (BOC) and its variants CBOC and AltBOC, which have various advantages compared to the traditional BPSK: it's allow to separates energy from the signal on both sides of the carrier, the carrier, which has the advantage not to overlapping the signal energy directly over existing signals while using the same carrier. This also favors the transmission of the signal over a wide bandwidth, which translates to a correlation function with a narrow peak where there is:

a) better correlation;

b) a lower sensitivity to thermal noise;

c) reduced multipath (Fig. II.6).

In operational phase, GALILEO will offer 5 services (Enderle, 2009) with more or less restricted access to:

1. Open Service (OS), completely open, free service, for the standard modes of maritime and land navigation systems, has the standard and precise working mode. Guaranteed accuracy in horizontal plane is 4m, while in vertical plane it is 8m;
2. Commercial Service (CS), commercial approach, the introduction of two additional encrypted signals, the level of accuracy is sufficient for precision agriculture, surveying measurements, etc. Continuity of service is guaranteed. Accuracy of spatial coordinate's determination in the CS mode is at centimeter level;
3. Safety of Life (SoL) has all the functionality of OS services, users are authorized, and the continuity of service is guaranteed, suitable for navigation in air, land and maritime trans-port. Guaranteed accuracy in horizontal plane is 4m, while in vertical plane it is 8m;

4. Public Regulated Service (PRS), authorized access, encryption signals for PVT, with high priority of continuous service use, strategic and secure infrastructure. Guaranteed accu-racy in horizontal plane is 6.5m, while in vertical plane it is 12m;

5. Search and Rescue (SAR), the current localization of emergency calls, rescue operations, etc. Authorized services have the access.

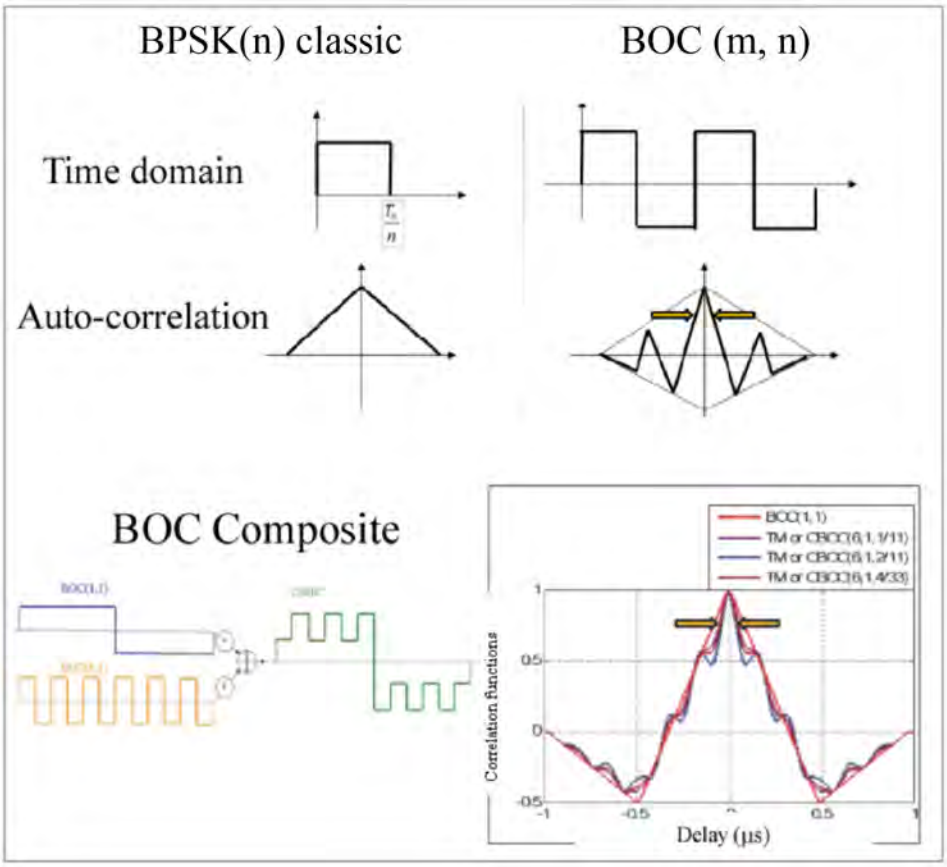

Figure II.6 – Difference between BPSK, BOC and CBOC (BOC composite) modulation codes; n is the number of chips and m is the multiplier coefficient for obtaining the frequency of the sub-carrier from the reference frequency of the C/A code: $f_{C/A} = 1.023$MHz. The yellow arrows indicate the tightening of the auto-correlation function, compared with BPSK or BOC of the CBOC or the American equivalent of the TMBOC of the GPS. For the CBOC/TMBOC, several composite signals were generated using various values of n and m for the first and the second BOC signal (JA, 2008).

II.1.4 Description and structure of the GLONASS system

The other perfectly operational constellation, the GLONASS constellation, is the one developed by Soviet Union. It began in 1976 to achieve its objectives only in 2001. Since 2001, many new satellites have been launched and the constellation has been providing global geo-positioning since 2011. The constellation is currently nominated with 24 satellites distributed over three inclined orbital planes of 64.8°. The orbital inclination, higher than the GPS orbits, allows satellites to pass more on polar areas than GPS (Bernhard Hofmann-Wellenhof, 2001). The quasi-circular orbits are located at an altitude of 19100 km above the earth's surface, and their period of revolution is 11 h 15 min 44 s with a repetition of 8 sidereal days (one sidereal day = 23h56min). One of the special features of the Russian system is that it uses CDMA multiple access on the L_3 band (the first satellite launched in 2010). For the L_1 and L_2 bands, the PRN codes are the same for all satellites. A C/A code is modulated on the carrier L_1, and a P code on the carrier L_1 and L_2. To identify satellites, the GLONASS system uses a variant that directly modulates the carrier known as Frequency Division Multiple Access (FDMA, Table II.2). The satellites are identified by their own frequency, which makes it possible, in theory, for GLONASS system more resilient to interference signals. Frequencies on L_1 and L_2 can be defined as follows:

$$f_{L1} = 1601MHz + k0.5625Mhz \tag{II.7}$$

$$f_{L2} = 1246MHz + k0.4375Mhz \tag{II.8}$$

with k is the number of the channels used, this number has evolved over time: until 1998, k varied from 0 to 12, then from 1998 to 2005 it was modified to vary between -7 and 12 and finally since 2005 the final configuration uses only 12 values from -7 and 4 and two channels are in reserve: the 5 and 6 can be used exceptionally (Table II.1). The ratio f_1/f_2 is constant and equal to 9/7.

The recent evolution of the system will see the appearance of a new L_5 carrier with frequency $f_5 = 1176.45$MHz and $\lambda = 25.48$cm.

II.1.5 Other constellations

II.1.5.1 COMPASS-BeiDou

Wishing also to overcome the dependence on the US GPS, the Chinese authorities began very quickly establish a regional free system: BeiDou-1. This system, initiated in the early 1990s, was realized by the launch of two first BeiDou-1A and BeiDou-1B satellites in 2000. This system has the originality to rely on four geostationary satellites (three operational and one reserve) and one mobile In medium orbit. This system, which is only regional (covers only China), requires emission from the user segment, and is therefore very limited in relation to the GPS system, whose users are only passive receivers.

TABLE II.1 – Correspondence between channel number and sub-band for GLONASS L_1 and L_2 carriers.

Channel number	Nominal frequency of sub-band L_1 (MHz)	Nominal frequency of sub-band L_2 (MHz)
6	1605.3750	1248.6250
5	1604.8125	1248.1875
4	1604.2500	1247.7500
3	1603.6875	1247.3125
2	1603.1250	1246.8750
1	1602.5625	1246.4375
0	1602.0000	1246.0000
-1	1601.4375	1245.5625
-2	1600.8750	1245.1250
-3	1600.3125	1244.6875
-4	1599.7500	1244.2500
-5	1599.1875	1243.8125
-6	1598.6250	1243.3750
-7	1598.0625	1242.9375

The Chinese authorities then decided to complete this geographically limited regional system by launching the BeiDou-2 project, also known as COMPASS (Chong, 2009). This comprehensive system includes a nominal constellation of 35 satellites:

◇ 5 Geostationary Earth Orbit satellites (GEO) for retroactive compatibility with BeiDou-1, at an altitude of about 35786 km;

◇ 30 non-geostationary satellites: 27 in the Medium Earth Orbit (MEO) at an altitude of 21150 km, in the same way as other GNSS satellites, and 3 in the Inclined GeoSynchronous Orbits (IGSO).

The period of revolution of the 27 MOE satellites is 12 h 53 min and their orbital planes are inclined at 55.5 ° with respect to the equator (ILRS, 2012).

The current COMPASS constellation consists of 5 GEO satellites, 5 IGSO satellites and 4 MEO satellites (Liu, 2013).

The BEIDOU system offers two services:

- Authorized Service (AS), a public service with a precision of less than 10 m, has been operational since 14 January 2013;
- Service reserved, precision unknown.

The signal structure (Table II.2) is quite similar to other systems with CDMA transmission and BOC, MBOC and TMBOC modulations and the new QKSP. The signal is transmitted on L bands following (Liu, 2013):

▷ B_1: $f = 1561.10$ MHz, $\lambda = 19.20$ cm;

▷ $B_{1\text{-}2}$: $f = 1589.74$ MHz, $\lambda = 18.86$ cm;

▷ B_2: $f = 1207.14$ MHz, $\lambda = 24.83$ cm;

▷ B_3: $f = 1268.52$ MHz, $\lambda = 23.63$ cm.

II.1.5.2 Quasi-Zenith Satellite System (QZSS)

Quasi-Zenith Satellite System (QZSS) is a regional satellite positioning system (the "Toundra" orbit flying over Japan and Australia) being developed by the Japanese space agency JAXA. Quasi-Zenith Satellite (QZS) can refer to both satellites in Quasi-Zenith Orbits QZO and geostationary orbits (GEO). For that reason, the name “QZO satellite” is used when it is necessary to specifically refer to satellites in QZO. Satellite positioning systems use satellite signals to calculate position information. The QZSS is sometimes called the “Japanese GPS”.

QZSS include 6 signals:

1. L1C/A frequencies using the C/A code and L1C (1575.42 MHz), which are positioning complement to GPS;

2. L2C (1227.6 MHz): positioning complement to GPS;

3. L1-SAIF and L1Sb(1575.42 MHz): used by the augmentation system (see in SBAS) for accurate, real-time and sub-meter (Crisis Messaging Service);

4. L5 and L5S (1176.45 MHz): using for positioning complement to GPS and for the augmentation experiment use;

5. The LEX carrier L6 (1278.75 MHz) is a high-precision (3cm) signal compatible with GALILEO's E6 signal;

6. S-band (2 Ghz) using for Safety Messaging Service.

II.1.5.3 Indian Regional Navigation Satellite System (IRNSS)

The Indian Regional Navigation Satellite System (IRNSS) with an operational name of NAVIC (NAVigation with Indian Constellation), is also a regional satellite navigation system under development. Its regional coverage is focused on India and its periphery up to a distance $\sim$ 2,000 km from its borders.

The system consists of a constellation of seven satellites and a support ground segment. Three of the satellites in the constellation are located in geostationary orbit (GEO) at 32.5° East, 83° East, and 131.5° East longitude. The other four are inclined geosynchronous orbit (GSO). Two of the GSOs cross the equator at 55° East and two at 111.75° East. The four GSO satellites will appear to be moving in the form of an "8". In addition, various ground-based systems will control, track orbits, check integration and send radio signals to the satellites. The land-based Master Control Center (MCC) will run navigational software.

NAVIC signals will consist of:

i. A Standard Positioning Service (SPS) carried on L5 at 1176.45 MHz and will be modulated by a 1 MHz BPSK signal;

ii. Precision Service (PS) carried on S-band at 2492,028 MHz using BOC.

II.1.6 The Positioning measurement

It is possible with the GNSS system to position itself in two different ways according to the capacities of the receivers. Commercially mono-frequency receivers (L_1) use positioning by measuring the code; the more sophisticated receivers, more expensive as the bi- or tri-frequencies use the measurement of the phase much more accurate to position.

II.1.6.1 Code measurement

The basic principle of positioning by code measurement is the observation of the distances between the satellites and the receiver of unknown position which may be on the ground, on a ship or on an aircraft (Bernhard Hofmann-Wellenhof, 2001). The position of the satellites is determined roughly by the control segment (ephemerides and almanacs). The precise orbits are recalculated by the International GNSS Service (IGS) after the passage of the satellites. The distance measurement between the receiver and a satellite is represented by a wave front situated at a distance d from the satellite. This wave front is materialized in space by a sphere whose center is the satellite j and on which is located the receiver i theoretically, three satellites are therefore necessary to obtain the point of intersection of the three spheres (in fact two points exist but one of them is not on Earth). To obtain the distance D_i^j separating the receiver i and a satellite j, which must be visible, we multiply the wave propagation time Δt_i^j by the wave propagation velocity c (velocity of light). Thus, we get:

$$D_i^j = c\Delta t_i^j \tag{II.9}$$

While in theory it is simple to measure, it does raise certain issues: How can the propagation delay be measured? Which satellite is sending the signal? This is why the GPS receivers have a satellite tracking function which identifies the satellite by the PRN code (by reading the C/A code on the L_1) from the transmitting satellite and then generates the replica of the identified the GPS satellite and delays that replica until it is aligned/correlated with the satellite signal, this alignment delay then corresponds to the propagation time Δt_i^j with the synchronization error, which is actually why we speak it actually of measuring “pseudo-distance". Indeed, in practice, all the time are in absolute GPS time corresponding to January 6, 1980 at 00h UTC. Therefore, for proper positioning, it is necessary to calculate this satellite / receiver offset:

$$\Delta t_i^j = t_{Ri} - t_E^j \tag{II.10}$$

where:

- $t_{Ri} = t_R + \delta t_i$ is the arrival time of the wave at receiver i in receiver time and which depends on the absolute arrival time t_R and the clock offset of the receiver with respect to the absolute time δt_i;

- $t_E^j = t_E + \delta t^j$ is the time of transmission by the satellite j in satellite time which depends on the absolute transmission time t_E and the satellite clock offset relative to the absolute time δt^j.

The equation II.10 expressed in absolute time is written:

$$\Delta t_i^j = t_R - t_E + (\delta t^j - \delta t_i) \tag{II.11}$$

The measurement of the pseudo-distance (PSD), derived from equation II.9, is therefore:

$$PSD_i^j = c(t_R - t_E) + c(\delta t^j - \delta t_i) = \rho_i^j + c(t_R - t_E) \tag{II.12}$$

with ρ_i^j is the geometric distance between satellite j and receiver i.

We can see that there are four unknowns in the equation II.12. The first unknown is the time t_{Ri} and then we look at the coordinates (X, Y and Z). It should be noted that with three satellites a positioning is possible in 2D simply: t, X, Y. This relation underlies a propagation in the vacuum of the wave. This is no longer true when it comes into the atmosphere. In order to achieve geodetic accuracy, other corrections should also be taken into account. For example, the apparent extension of the satellite receiver distance due to the troposphere crossing (δ_{tropo}) should be corrected and the perturbation of signal due to the dispersion nature of the ionosphere (ionospheric delay δ_{iono}, depending on the frequency f of the signal). It is also necessary to take into account an ε term containing all the other factors that can disturb the signal (relativistic effect, multiple reflections of the electromagnetic signal before reception, etc.). The measurement of the pseudo-distance will therefore become:

$$PSD_i^j = \rho_i^j + c(t_R - t_E) + \delta_{tropo} + \delta_{iono} + \varepsilon \tag{II.13}$$

All these errors mean that the precision of the pseudo-distance measurement is metric. If one wants to obtain a centimeter precision, the commercial receivers should have an estimate of the time to 10^{-10} and therefore a precise clock at least 10^{-10} s which would greatly increase the cost. When it is desired to make precise measurements, it is preferable to measure the phase which corresponds to the number of cycles carried out by the carrier since its emission. So, the positioning by measuring code that is typically used for navigation systems in vehicles or on mobile phones. It has unfortunately very limited precision (a few meters, even a few tens of meters). The performances of this type of measurements are generally optimized by downstream application of a Kalman filter. This filter assumes a correlation between the successive measurements and conditions the calculated position. This geographical conditioning is also based on the existing and known road network.

II.1.6.2 The measurement of the phase

Here again, we go through a satellite identification phase. The modulation (code and navigation message) is removed from the main frequency of the considered carrier. The

phase of the signal at time t is compared with a copy/replica generated by the receiver, which can generate a replica of modulation codes of any satellite. The phase shift between the carrier and its replica is measured, meaning that we measure the cycle fraction that represents the offset between the two, rather than the total number of cycles that the carrier has achieved from its issuance from the satellite until it reaches the receiver.

The phase at time t is defined as:

$$\varphi(t) = \Delta\varphi(t) + n(t) + N \tag{II.14}$$

$\Delta\varphi(t)$ is the decimal fraction of the phase (phase shift), $n(t)$ is the integer number of cycles elapsed since the first correlation/measurement counted by the receiver's cycle counter and N is the integer ambiguity (satellite-receiver distance divided by the signal wavelength and from which we extract the integer part) that corresponds to the integer number of cycles from the satellite to the receiver. It is therefore understandable that observing distance between the receiver and the satellite is ambiguous of what is called integer ambiguity N. To get distance ρ_i^j [II.15] that separates the satellite j from receiver i will require subtracting the integer ambiguity N_i^j, the clock biases of satellite δ_{t_j} and receiver δ_{t^i}, tropospheric δ_{tropo} and ionospheric $\delta_{iono}(f)$ effects from the phase shift $\Delta\phi_i^j$. For this phase difference in meters and not in cycles, we will have to multiply the result by the wavelength λ:

$$\Delta\phi_i^j = \rho_i^j + c(\delta_{t_j} - \delta_{t^i}) + \delta_{iono}(f) + \delta_{tropo} + \varepsilon \tag{II.15}$$

Once is has been determined, the integer ambiguity N_i^j remains constant for satellite j throughout the continuous observation of i. This is what is called phase tracking. A simple cycle counter will show the number of cycles $n(t)$ since the first measurement. As a result, we do not create a new integer ambiguity at each observation, but the initial value is simply incremented. However, it may be that we lose the signal because of a receiver malfunction or under the effect of ionospheric scintillation, or even because of the presence of a mask (tree, wall) between the satellite and receiver: this is called a cycle slip. In this case, a new integer ambiguity must be determined (Duquenne et al., 2005).

The problem lies on determining the integer ambiguity. To solve this problem, one can use a second receiver with known coordinates (the base), this is called the Differential GPS or DGPS (Fig. II.7). A relative position is thus acquired by measuring the vector between the unknown coordinates of the receiver and the base. To get this relative position, we use a technique known as double differences phase measurement [II.16]. This is the combination of observations from two receivers that observe the same two satellites:

$$\nabla\Delta\phi_{i,k}^{j,l} = \nabla\Delta\rho_{i,k}^{j,l} + \lambda N_{i,k}^{j,l} + \nabla\Delta\delta_{iono}^{j,l,i,k}(f) + \nabla\Delta\delta_{tropo}^{j,l,i,k} + \nabla\Delta\varepsilon_{i,k}^{j,l} \tag{II.16}$$

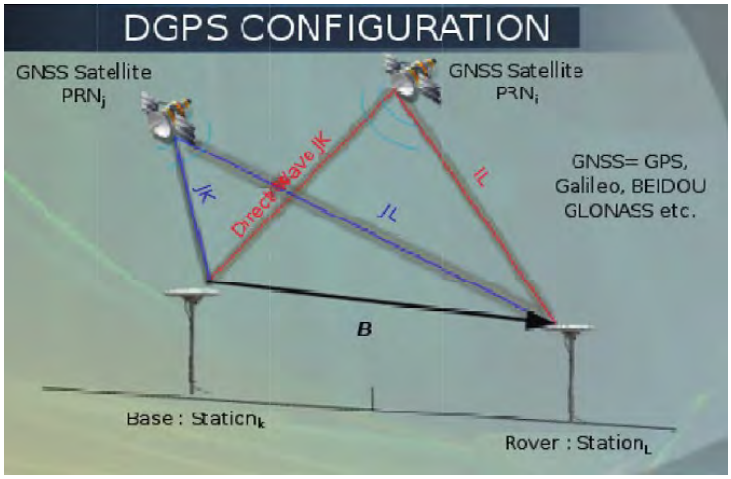

Figure II.7 – The DGPS configuration needed for a double differences phase measurement. Station k with known coordinates is the base, and station L or Rover represents the receiver, said to be "mobile", for which we wish to know the coordinates. Transmitter satellite are identified by their PRN: PRN_i and PRN_j. B is the baseline, that is to say the 3D vector connecting the two stations, which is measuring using the DGPS method.

The simple difference (two receivers, one common satellite) is usually done in two steps:

i. we consider that the integer ambiguities and coordinates of the receiver are unknown and we solve the approximate position and non-integer values of integer ambiguities by the least squares method. These solutions are said to be "floating";

ii. we fix ambiguities, meaning that we seek the nearest integer value that is injected into the linear system where we solve the new estimate of coordinates that is more accurate by the least squares method.

This accuracy depends on the time measurement and the base B (distance between the unknown receiver and the reference receiver: the "base"). It can be around a millimeter when B is less than 5 km and can reach $\sim$ 80 cm if $B \geq 100$ km.

II.1.7 Augmentation systems

These systems based on corrections from ground stations to improve the positioning accuracy in real time.

II.1.7.1 Local Based Augmentation System

The DGPS system involves the installation of a baseline with known coordinates. This real-time receiver performs measurements of the distance between the receiver and each of

the GNSS satellites in visibility. The measured distances include many errors which deteriorate the positioning accuracy, but the base, which has the actual coordinates as well as those of the satellites, can calculate the theoretical distance without error. The difference between the known and measured range for each satellite is the range error. This error is the amount that needs to be removed from each satellite distance measurement in order to correct for errors present in the system. The correction can be done in post-processing or in real time (link via GSM or Radio with the base). Positioning using corrections generated by DGPS radio-beacons for example, will provide a decimeter to centimeter horizontal accuracy with a 95% confidence depending on the quality of the GPS receiver used. Under the same principle, more sophisticated, short-range DGPS systems (10 to 15 km) can achieve centimeter-level accuracy using carrier phase. In this case, we commonly refer to such a system as "Real Time Kinematic" (RTK) instead of DGPS. These local corrections systems (Fig. II.8) are called the Local Based Augmentation System (LBAS).

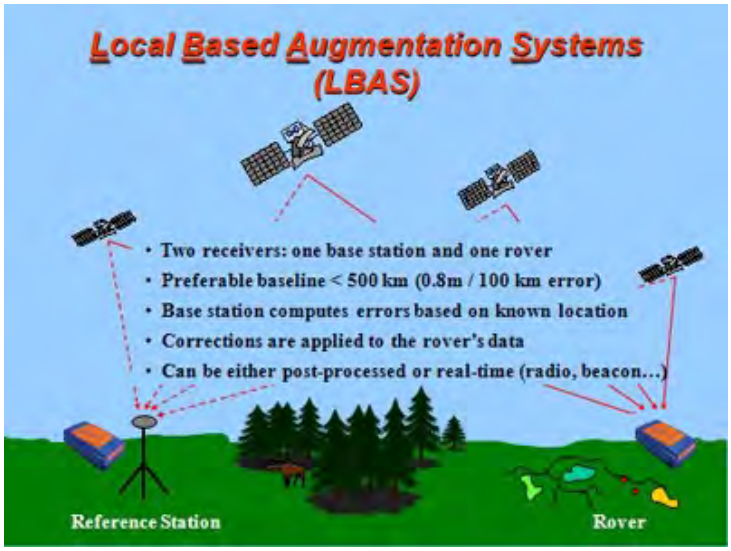

Figure II.8 – This is the predominant DGPS strategy used for a majority of real-time applications. The base station transmits the range error corrections to remote receivers in real-time. The remote receiver corrects its satellite range measurements using these differential corrections, yielding a much more accurate position (http://www.sxbluegps.com/technology/sbas-made-easy/#spacebased).

II.1.7.2 Space Based Augmentation Systems

Space Based Augmentation Systems (SBAS) incorporates a modular architecture, similar to GPS, comprised of a Ground Segment, Space Segment, and User Segment:

- The Ground Segment includes reference stations, processing centers, a communication network, and Navigation Land Earth Stations (NELS);

- The Space Segment includes geostationary satellites (For example, EGNOS uses Inmarsat transponders);
- The user segment consists of the user equipment, such as a SXBlue II GPS receiver and antenna.

SBAS uses a state-based approach in their software architecture. This means that a separate correction is made available for each error source rather than the sum effect of errors on the user equipment's range measurements. This more effectively manages the issue of spatial decor-relation than some other techniques, resulting in a more consistent system performance regardless of geographic location with respect to reference stations. Specifically, SBAS calculates separate errors for the following:

- The ionospheric error
- GPS satellite timing errors
- GPS satellite orbit errors

a) WAAS system

The US Federal Aviation Administration has developed a Wide Area Augmentation System (WAAS) for the purpose of providing accurate positioning to the aviation industry (Fig. II.9). In addition to providing a high quality and accurate service for this industry, this service is available free of charge to all other civilian users and markets in Central and North America. Land cover has been enhanced with monitoring stations in Canada and Mexico in September 2007. This service falls into the greater category of SBAS.

The ground segment consists of 38 Wide-area Reference Stations (WRS) and 3 Wide-area Master Stations (WMS), plus some stations in Mexico and Canada (I-WRS). Two types of corrections are provided. Fast corrections are errors that may change rapidly: instantaneous satellite positions, embedded clock errors. These corrections can be applied by any receiver in the WAAS coverage. Slow corrections are ephemeris and clock bias estimates, and errors related to ionospheric scintillation.

The spatial segment consists of two geostationary remote sensing satellites (Galaxy and Anik F1R), which broadcast the Ground Uplink Stations' (GUS) correction messages to the user segment. These satellites broadcast similar messages to the GPS messages, simulating additional GPS satellites (own PRNs).

The user segment consists of WAAS GPS receivers, which use the information provided by the GPS constellation to determine its position and the current time. They also receive WAAS messages on the L_1 carrier.

b) EGNOS system

Other agencies have developed SBAS for their respective geographical areas. In Europe, the ESA, the European Commission and EUROCONTROL have jointly developed

the European Geostationary Navigation Overlay Service (EGNOS). The EGNOS (Fig. II.9) is suitable for critical safety applications in air navigation and piloting of ships through narrow channels. The system uses 40 ground stations, which capture the GPS signals. Then they transmit these data to four European control centers, which refine the precision. The enhanced data are then sent to the EGNOS user receivers, for example airline pilots, via a constellation to three geostationary satellites. Furthermore, on June 28, 2007, the European Space Agency and the Agency for Security of Air Navigation in Africa and Madagascar have signed a cooperation agreement with the objective of using satellite navigation to improve air traffic safety over the African continent.

Japan has developed its own system by the Japan Civil Aviation Bureau (JCAB), the Multi-Functional Satellite-based Augmentation System (MSAS). The MSAS was commissioned on 27 September 2007.

In India, the Indian Space Research Organization (ISRO) and the Indian Airports Authority have set up the GPS Aided GEO Augmented Navigation System (GAGAN), which has been operational since December 2014.

China has a similar program, the service is called Chinese Satellite Navigation Augmentation System (SNAS) of which we have little information. Figure II.9 shows all of the existing augmentation systems and their geographic coverage.

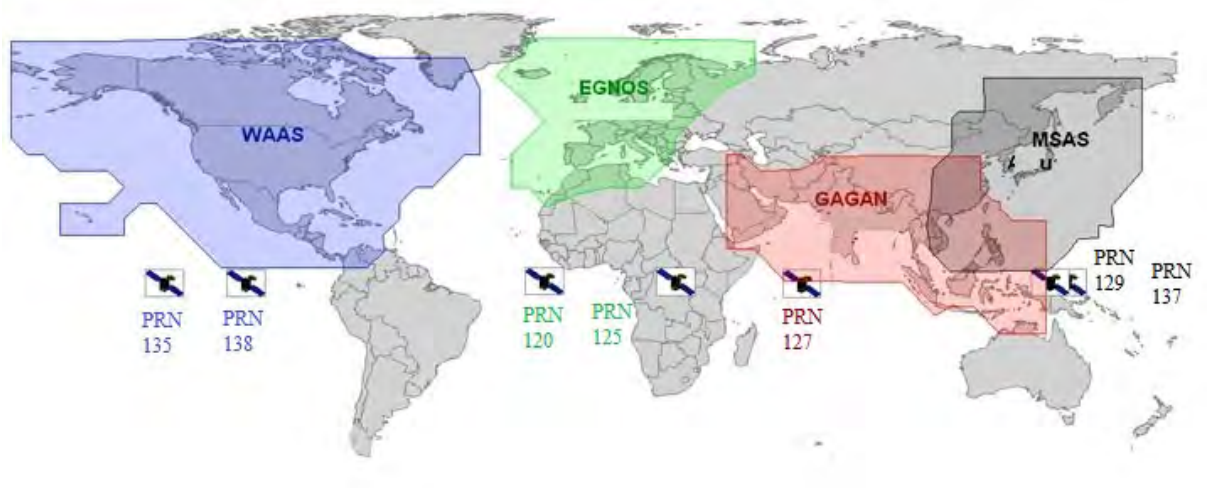

Figure II.9 – Geographical coverage of GNSS augmentation systems (modified from GENEQ Inc. © Copyrigth, 2013).

II.1.8 Perspective

The American GNSS constellations (GPS) and Russian (GLONASS) currently have over fifty operational satellites that emit permanently exploitable signals, and can be picked up anywhere in the world. When the Galileo and COMPASS/BeiDou constellations are

completed, more than 100 positioning satellites will gravitate around the Earth, not to mention the advent of other constellations.

TABLE II.2 – Characteristics of operational or most advanced GNSS constellations. The arrow indicates future developments. The set of GNSS frequency modulation codes is also presented: Binary Phase Shift Keying (BPSK: the most classic); Binary Offset Carrier (BOC); Multiplexed BOC (MBOC); Time Multiplexed BOC (TMBOC); Composite BOC (CBOC); Alternate BOC (AltBOC); Quadrature Phase Shift Keying (QPSK). Done on July 20, 2015, this table may therefore have evolved following the launches of the different satellites of the various constellations.

Constellation GNSS	GPS (USA)	GLONASS (RUSSIAN)	GALILEO (EUROPE)	COMPASS/ BeiDou (CHINA)
Operational satellites	32 MEO	24 MEO	4 IOV → 30 MEO	5 → 27 MEO, 3 → 5 GEO and 3 IGSO
Altitude (km)	20200	19100	IOV: 23222 MEO: 23616	21150
Orbital Plans	6	3	3	3
Orbital period	11 h 58 min	11 h 15 min	14 h 21 min	12 h 53 min
Angle	55°	64.8°	56°	55°
Multiple Access	CDMA	FDMA/CDMA	CDMA	CDMA
Carriers and Frequencies (MHz)	L1: 1575.42 L2: 1227.60 L5: 1176.45	L1: 1598.06 -1605.38 L2: 1242.94 -1248.63 L3: 1207.14 L5: 1176.45	E1: 1575.42 E5a: 1176.45 E5b: 1207.14 E6: 1278.75	B1: 1561.10 B1-2: 1589.74 B2: 1207.14 B3: 1268.52
Modulation	BPSK, BOC, TMBOC	BPSK, BOC	BPSK, BOC, CBOC, AltBOC	QPSK, BOC, MBOC, TMBOC
Status	OP	OP	VAL	~OP
OP: operational, ~OP: Quasi-operational, VAL: Validation phase				
Code Division Multiple Access: CDMA, Frequency DMA: FDMA				
MEO: Medium Earth Orbit, GEO: Geostationary, IOV: In Orbit Validation, IGSO: Inclined GeoSynchonous Orbit				

II.2 Reflection of GNSS signals

Natural elements (mountains, trees, etc.) and artificial (various constructions) on the surface of the Earth may impede electromagnetic signals transmitted by the satellites of different GNSS constellations. Depending on the nature of the obstacles encountered, they will then be absorbed, attenuated, reflected or refracted (Andréani, 2001). In the latter two cases, the reflected signals will change propagating direction (thus being reflected several times), creating well-known multipath. The signal thus takes longer to reach the antenna and be noisy and mitigated. In classical cases of GNSS positioning, the delay in the transmission time will result automatically by an error on the receiver-satellite

distance and hence the position deduced from observations. So, in classical positioning, multipaths are a source of error to remove.

GNSS reflectometry (or GNSS-R) offers an alternative vision: Reflected GNSS signals contain crucial information on reflective backgrounds. By isolating and analyzing these reflected signals, one can therefore trace back to the properties of the surroundings of the receiver. This opportunistic application in remote sensing is becoming more promising since the GNSS constellations are constantly developing with the sustainability and stability of the assured network.

This sector presents the process of reflection and analysis of electromagnetic waves in order to extract the characteristics of the reflective backgrounds.

II.2.1 Multipath

The multipath phenomenon occurs when the signal from the GNSS satellite arrives at the receiver after following another path than the direct path. This is the case of at least one reflection on a close surface (Figure II.10). This phenomenon is particularly present in urban areas, due to the presence of buildings. The reflected signals will then disrupt the total signal received by the antenna and in particular modify the pseudo-distance and phase measurements performed by the receiver. The perturbation associated with the multiple paths is both correlated with time and with respect to the various satellite signals. For this reason, we cannot associate this contribution with a simple white noise (random), which distorts the algorithms commonly used in classical positioning (Sutour et al., 2012).

Considering to the direct signal of amplitude A_d and phase φ_d in the form $A_d \cos(\varphi_d)$, the reflected signal will be:

$$\kappa A_d \cos(\varphi_d + \Delta\varphi_r) \tag{II.17}$$

where:

- κ: an attenuation factor ($0 \leq \kappa \leq 1$);
- $\Delta\varphi_r$: the phase shift due to the elongation of the path (Duquenne et al., 2005).

Regarding the measurement of pseudo-distance based on the code, lengthening the path can cause an error of up to 20m (depends on the distance between the antenna and the point of reflection). In order to minimize the impact of the multipath, it is understood that in geodetic positioning where precision is required, we have to minimize the maximum influence of the multipath. This can be done in several solutions:

- First, the measurement site solutions, take care to choose a more isolated measurement site possible, avoiding reflective surfaces too close.

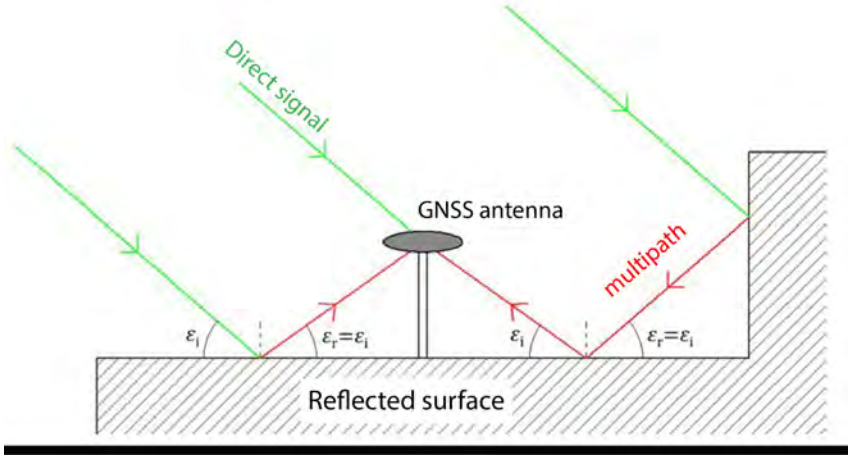

Figure II.10 – Multipath phenomenon on GNSS signals. ε_i: angle of incidence. ε_r: angle of reflection.

- Hardware solutions, it's possible to equip antennas with an absorbing plane on the lower hemisphere of the antenna to filter the signals picked up. This device equips most geodetic antennas.

- Solutions in the processing of observations including the possibility of filtering the waves received at the receiver to eliminate the waves of low incidence at the time of treatment (Andréani, 2001). For example, the multipath will be less effects if the acquisition time is long. In other words, the most sensitive techniques to multipath are those based on rapid observations; the extreme case being when a position is determined by time (kinematic) (Duquenne et al., 2005).

II.2.2 Specular and diffuse reflection

Multipath are the GNSS signals arriving at the antenna after reflection on nearby surfaces. Conceptually, it is possible to distinguish two contributions: the specular or coherent component and the diffuse or non-coherent component (Cardellach, 2001), as illustrated in figure II.11. The specular component comes from a reflection at a particular point (called the specular point in the remainder of this manuscript). This is the point of the reflective surface for which the reflected wave travels the shortest distance. This point obeys the Snell-Descartes law of reflection which stipulates that the angle of reflection r and the angle of incidence i are equal in absolute value. In other words (see § II.2.2.1): $i = r$.

The specular term is characterized by high orientation whereas the diffuse contribution spreads the signal over a wide range of reflected signals. In a purely specular reflection, it is possible to receive the signal only in one preferred direction, which is not the case

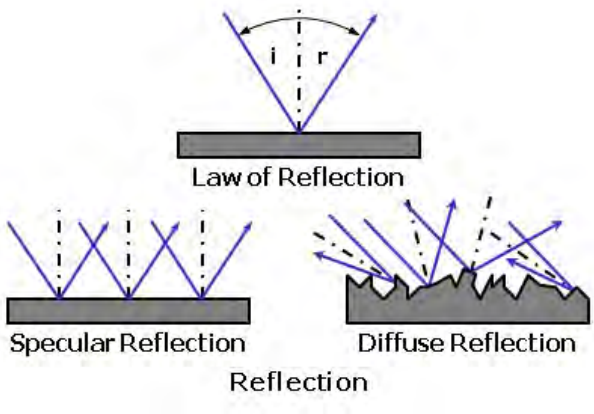

Figure II.11 – Specular and diffuse reflection.

for the diffuse component.

In practice, a reflected signal contains both a specular component and a diffuse component, in proportions depending on the angle of incidence and the roughness of the reflection surface.

II.2.2.1 Specular reflection

Specular reflection is generally described in geometrical optics, the electromagnetic propagation being modelled as a simple ray. A radius arriving on a perfectly flat surface with a certain angle of incidence generates another ray with an opposite azimuth and incidence angle in the plane defined by the incident ray and the normal to the surface at the point of incidence. Using this simple model, the specular point is the intersection of the two rays (incident and reflected) on the surface.

It is also possible to model specular reflection with a more realistic model using wave optics. Following the Huygens-Fresnel principles, each point of the incident wave front acts as a potential source of a secondary spherical wave. The reflected signal will then be the sum of all these secondary spherical waves and the major part of the energy will come from source points located on a surface surrounding the specular point: all these sources define the 2-D **Specular zone** or **Fresnel surface**.

Each point inside the Fresnel surface is at the origin of a signal whose phase shift is less than a certain proportion of the wavelength of the incident signal. The first Fresnel zone is thus defined as being the area on the reflection surface whose phase shift of the signal is less than half the wavelength of the incident signal.

The first Fresnel surface can then be described as an ellipse centered on the specular point and whose half-small axis r_b and half-major axis r_a are equal to (Larson and

Nievinski, 2013):

$$r_b = \sqrt{\frac{\lambda h}{\sin(\theta)} + (\frac{\lambda}{2\sin(\theta)})^2} \tag{II.18}$$

$$r_a = \frac{r_b}{\sin(\theta)} \tag{II.19}$$

with:

- λ the wavelength (m);
- h the height of the antenna (in m);
- θ the elevation angle of the satellite.

II.2.2.2 Diffuse reflection

A flat reflection surface is a purely theoretical case. When the reflecting surface has a non-zero roughness (real case), the reflection is no longer solely specular, but a diffuse component appears.

Like specular reflection, diffuse reflection can also be modelled in two ways: simple modelling in geometric optics, and a somewhat more complex modelling done in wave optics. In geometric optics, the reflective surface is constituted by a concatenation of small facets (scattering) of different size and orientation. Each of these facets acts as a mirror for the incident ray. Under these conditions, a receiver R receives reflections of each facet having an ideal orientation, namely an orientation such as the normal to the facet to the point of impact S of the incident ray is the bisector of the incident ray and the right (SR): See figure II.12. It is therefore understandable that for a wave incident on a surface modelled by facets, reflections no longer come only from the nominal specular point, but from multiple specular points, provided that the facets are well oriented.

We then define the flickering surface or glistening zone which is the zone in which it is possible to have well-oriented facets, respecting a defined probability threshold. More roughness of the reflecting surface, more the probability of having oriented facets and the nominal specular point, and consequently this area will be the glistening zone.

In an optical wave, the diffuse component reflected by the surface is equal to the sum of the spherical wave re-emitted by each point of the surface. A diffusion beam is thus defined. The signal received after a diffuse reflection can then be considered as the cumulative multiple individual contributions, each introducing a different phase shift.

II.2.2.3 Roughness of the reflective surface (The Rayleigh criterion)

As we have seen, if the surface of reflection were perfectly plane, there would be only specular reflection: diffuse reflection is due to the roughness of the surface (Beckmann and Spizzichino, 1987). The specular component dominates the signal when the reflecting

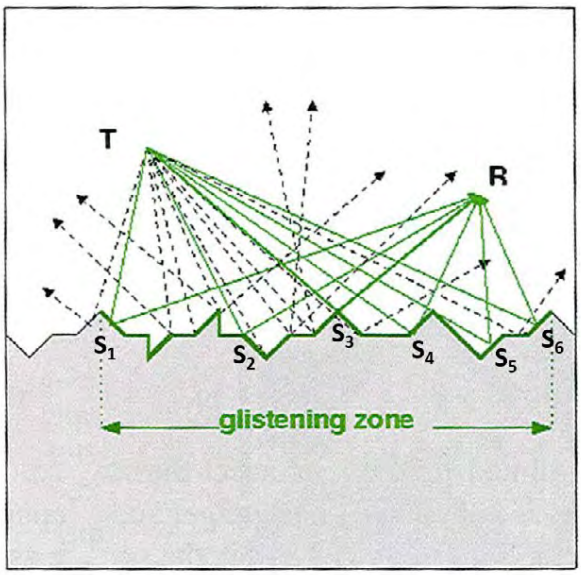

Figure II.12 – Glistening zone, decomposition of the reflective surface into multiple reflective facets. (Adapted from Shuanggen Jin (2014)).

surface is sufficiently smooth. In this case, the reflection process can be modelled by multiplying the incident wave by the Fresnel reflection coefficient and by an attenuation factor that depends on the surface roughness. Conversely, the diffuse (or incoherent) component dominates the signal when the reflective surface is sufficiently rough. When the diffuse component dominates, the diffusion coefficient and the phase are different for each facet. The total reflected power is the power of the sum of the electric fields coming from each facet (Alonso-Arroyo et al., 2015). This total power is less than that obtained when the coherent component dominates.

The **Rayleigh criterion** is generally used to distinguish a smooth surface from a rough surface (Beckmann and Spizzichino, 1987). A surface is considered smooth if:

$$\sigma_{rms} = \frac{\lambda}{8\sin(\theta)} \tag{II.20}$$

with:

- λ: the wavelength of the signal;
- θ: the elevation angle of the satellite;
- σ_{rms}: the RMS (Root Mean Square) roughness, which is the mean of the geometric deviation of the topographic surface from the mean line of the roughness.

This criterion is equivalent to the condition that the phase difference between each facet is less than $\pi/2$. It is possible to apply a more restrictive criterion by replacing

the factor 8 in equation II.20 by 16 or 32 (Beckmann and Spizzichino, 1987), which respectively means that the maximum phase difference between each facet will be $\pi/4$, or $\pi/8$. It is important to emphasize here that the roughness is therefore not a defined quantity from the point of the diffraction view, since the same surface can be judged to be very smooth at a given frequency and angle, and very rough for different frequency and angle.

II.3 GNSS Reflectometry (GNSS-R)

GNSS Reflectometry (GNSS-R) consist to recover the electromagnetic signals emitted continuously by the GNSS satellites (GPS, GLONASS, BEIDOU and GALILEO) currently in orbit and then reflected on the Earth surface: oceans, continental waters (rivers, lakes), and continental surfaces. The first application of using GNSS signals reflected off the Earth's surface for scatterometry purposes was proposed by Hall and Cordy (1988). Years after, one of the pioneer of this new science, Martin-Neira, show its applicability to estimate sea level (Martin-Neira, 1993). He used the correlation analysis of the phase delay between the direct and reflected signal of the same satellite to determine the position of the reflection point in time (geometric information) and to estimate parameters such as sea level or level of Inland Water (Treuhaft et al., 2001; Rius et al., 2002; Helm et al., 2007; Helm, 2008; Marchan-Hernandez et al., 2010). During the calibration phase of the SIR-C radar experiment on-board the U.S. Space Shuttle results gives the first reflection at steep incidence and were serendipitously discovered (Lowe et al., 2002b). With many similitudes to classical method of RADAR remote sensing, the GNSS-R can be applied to remote sensing of various types of natural covers, such as ocean, land, ice, snow, vegetation. The analysis of waveform gives access, meanwhile, to various parameters such as soil moisture (Kebiao et al., 2008; Larson et al., 2008b), surface roughness (Germain et al., 2004), the wind speed at the sea surface (Gleason et al., 2005), the thickness and structure of the snow cover on the northern plains (Larson et al., 2009), and the polar ice caps (Wiehl M. and R., 2003; Cardellach et al., 2012).

Although originally designed for navigation, GNSS has evolved using signal of opportunity in GNSS-R. GNSS-R can be used for a large variety of applications, and, particularly, for Earth remote sensing (Garrison J. L., 2014). The GNSSR remote sensing techniques could be divide into two main families:

1. The first family used a GNSS Bistatic Multi-Beam Radar and will analyse directly the GNSS waveform using specific receiver with two or more antennas. This technique is very promising due to is flexibility: it can be used for *in-situ*, aircraft and satellite applications. This methodology can be associated to aircraft/RPAS to develop mapping services for soil moisture and flooded area;

2. The second one uses a classical GNSS receiver and only one antenna, so it is designed as low-cost technique, it is also a promising technique but for *in-situ* and low elevation fly (RPAS, Aircraft). However due to the large amount of GNSS network existing worldwide it is possible to re-use some of these stations to make environmental system monitoring (soil moisture, biomass, flooded area etc.). This methodology can be used to validate aircraft and RPAS campaigns by appropriated ground measurements.

This section presents the principle of GNSS reflectometry and details the main applications of this opportunistic remote sensing technique. It summarizes no-limited to the main techniques and applications of GNSS-R in its two possible configurations: acquisition dual antenna system, or single antenna. In this thesis manuscript, I will focus mainly on the technique using a classical GNSS receiver with the single-antenna system and the "SNR" method which was the main object of my research (see § II.3.4).

II.3.1 GNSS-R Measurement Techniques

The first example of this type of measure was born in 1988 when Hall and Cordey proposed the concept of "Multistatic Diffusiometer" to estimate surface winds using a spatial radiometer measuring the signals of the GPS constellation reflected by the oceans (Hall and Cordy, 1988). In 1992, the French military detected from an aircraft the GPS interference caused by their reflections on the ocean surface (Auber et al., 1994). Since then, many acquisition systems for GNSS-R have been developed. These receivers can acquire GNSS waveforms (Fig. II.13 and II.14) and are quite different from conventional GNSS systems because they require a specific receiver that is capable of collecting the direct signal from satellite and the reflected signal from a reflective surface (rivers, lakes, vegetation, soil, ect.). This is therefore a double antenna device (Fig. II.15). Equation II.21 with correlation amplitude Y^c between the received signal and the replica of the carrier is given by the following expression:

$$Y^c(t_0, \tau, f_d) = \frac{1}{T_c} \int_{t_0}^{t_0+T_c} S_R(t) a^*(t-\tau) e^{-j2\pi(f_c+f_d)^t} dt \tag{II.21}$$

with t_0 is the time that marks the beginning of the integration, which is of duration T_c.

For the acquisition, there are two main families of receivers that carry out the complete acquisition of the waveform I and Q signals (§ II.1.2). These receivers are said to be “conventional” and “interferometric”.

Conventional waveform receptors or cGNSS-R (Fig. II.13) seek to coherently correlate, throughout a tile interval T_c (generally $1/f_c$, 1ms or even up to 19ms), the reflected signal $S_R(t)$ with a replica $a^*(t-\tau)$ of the code C/A generated locally by the receiver with a time $\log \tau$ and after Doppler frequency shift compensation f_d. However, as the

correlation amplitude Y^c has a low amplitude and suffers from significant noise known as speckle, in order to reduce it, it's essential to have incoherent average (N_i) to improve the Y^c signal:

$$\langle |Y^c(\tau, f_d)|^2 \rangle \approx \frac{1}{N_i} \sum_{n=1}^{N_i} |Y^c(t_n, \tau, f_d)|^2 \tag{II.22}$$

The width of the auto-correlation function is particularly important for applications in altimetry, which assumes that the overall noise is the sum of the thermal noise and speckle, both being totally uncorrelated. These receivers require a high bandwidth to achieve the root mean square (RMS) of Y^c and to have a good range resolution. This bandwidth is limited by the modulation required to code of the GNSS signal, and may be insufficient for certain applications. To solve this problem, recent receivers (since 2010) use the interferometric technique. **Interferometric** waveform receiver's iGNSS-R or

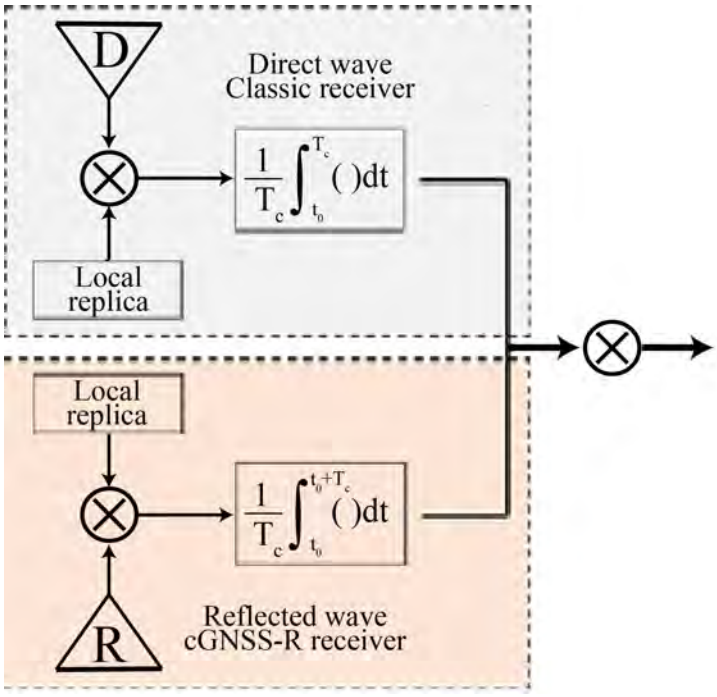

Figure II.13 – Principle of the cGNSS-R. The receivers record the waveform of the direct and reflected signals and correlate them with local replicas generated by the receivers.

PARIS (Fig. II.14) are the receivers in which the reflected signal (recorded by the LHCP antenna) is not correlated with a replica, but with the direct signal (recorded by the RHCP antenna [II.24]). We can retrieve the same equations for iGNSS-R if we replace the replica $a^*(t)$ in the equation [II.22, II.23] with the direct signal S_d, we will have:

$$Y^i(t_0, \tau, f_d) = \frac{1}{T_c} \int_{t_0}^{t_0+T_c} S_R(t) S_d * (t-\tau) exp^{-j2\pi(f_c+f_d)^t} dt \tag{II.23}$$

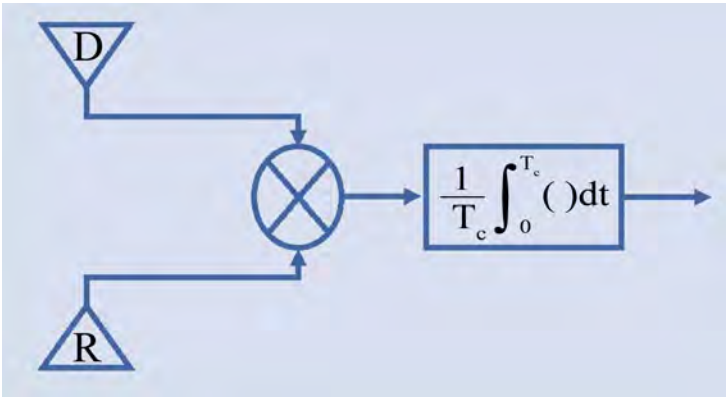

Figure II.14 – Principle of the iGNSS-R. The receiver records the reflected signal and correlates it with the direct signal recorded by the receiver. D and R mean direct and reflected paths.

$$\langle |Y^i(\tau, f_d)|^2 \rangle \approx \frac{1}{N_i} \sum_{n=1}^{N_i} |Y^i(t_n, \tau, f_d)|^2 \tag{II.24}$$

The comparison of the two technologies is not so simple and each one has its advantages

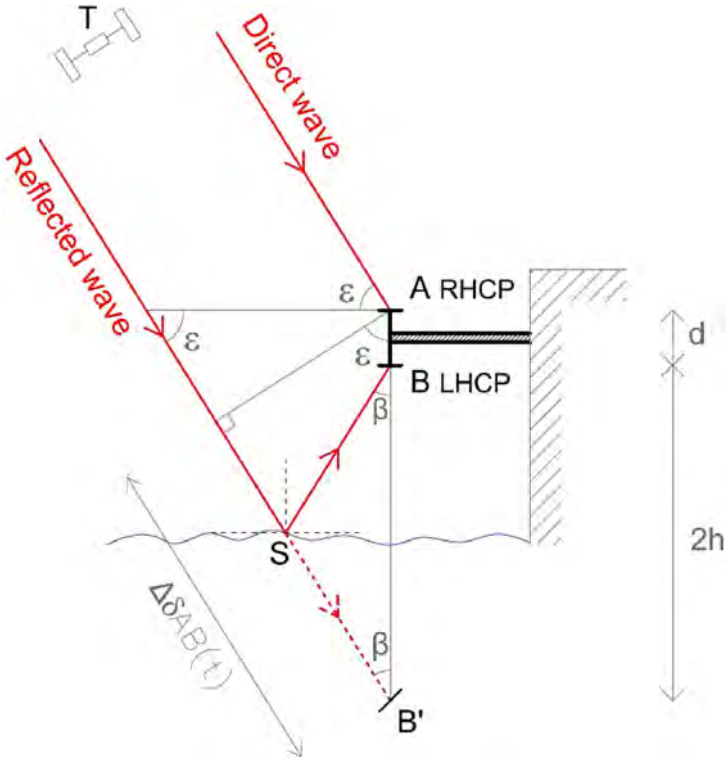

Figure II.15 – Geometry of an acquisition system in waveform. The geometry reflects the over-path caused by the reflected path (R) relative to the direct path (D), but also takes into account the phase shifts of the two-acquisition antenna center (Roussel et al., 2014).

and its defaults. From the perspective of the installation geometry of cGNSS-R or iGNSS-

R waveform receivers, it is identical and require two opposite polarization antennas: the RHCP for the direct signal from the antenna to the zenith and the LHCP for reflected signal from the antenna looking at the nadir (Fig. II.15), some experiment used also a horizontal and vertical polarizations for the antenna (Rodriguez-Alvarez et al., 2009).

For cGNSS-R, the code replica is generated locally, which provides the following pros and cons:

Advantages	**Downsides**
• It allows one to separate signals from different satellites by their specific code.	• Available public C/A codes for altimetry is not feasible due to their limited bandwidth which leads to a limited range resolution. But it could be promising in the future, when precise public codes will be widely available (Galileo E_5, GPS L_5). These precise codes would be needed at two frequencies for ionospheric corrections if not cGNSS-R will have limited performance for altimetric applications.
• It inherently has an infinite SNR.	• The delay and Doppler frequency dynamics for these codes are larger, and these values must be adjusted more frequently for proper operation (Park et al., 2014).
• Small size of antennas can be employed to track the reflected signals.	• The waveform is less detailed than those of the iGNSS receiver, and you have, in many case, more difficulties to identify the maximum pic which corresponds to the specular point (Fig. II.16).

This approach is the one used in all the GNSS-R experiments until 2010, and most of the campaigns between 2010 and 2013. It is also the receiver signal-processing approach to be implemented at the NASA recently approved CYGNSS Mission.

For iGNSS-R, the pros and cons are as follow:

Advantages	Downsides
• No need to know the code, since the direct signal itself is used instead. It allows to use also other signals of opportunity like satellite radio, satellite television, or any other sources with larger transmitted power, larger bandwidth, and better SNR, leading to potentially improved range resolution.	• The main drawbacks are the very large antenna size (directivity) required for the up-looking antenna, which leads to the use of beam-steering techniques, and/or multi-beam antennas (Zavorotny and Voronovich, 2000).
• The differential processing produced in the cross-correlation leads to slower delay and Doppler frequency dynamics (Park et al., 2014), which are, it seems, easier to track.	

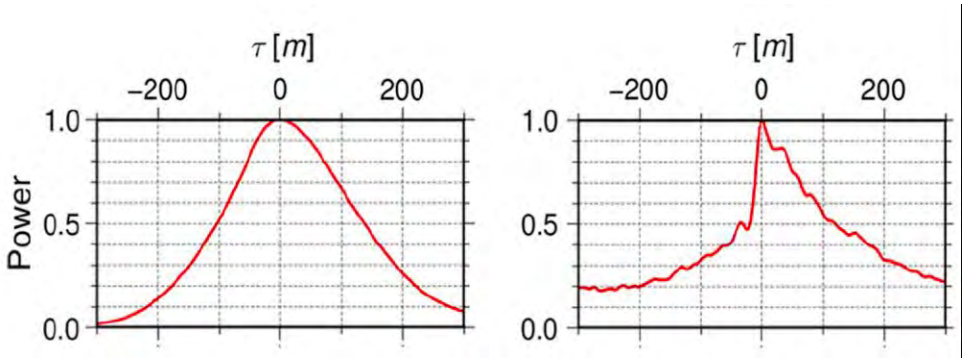

Figure II.16 – Normalized wave forms from measured data acquired over the Baltic Sea at ∼3km altitude using two receivers simultaneously. (Left) data from a cGNSS-R receiver working with C/A code (GOLD-RTR), and (right) data from a iGNSS-R receiver for a satellite transmitting C/A+P(Y)+M codes (PIR/A). Coherent integration time of 1ms and incoherent integration time of T_{in}=10s have been used in these examples. Here, the zero delay is set at the peak power, and the delay axis τ is given in units of length (in meters). From (Cardellach et al., 2011).

ESA consortium have designed and manufactured the only existing iGNSS-R receiver, and three experimental campaigns have been conducted, a ground-based and two airborne experiments. This technique is the one suggested for the ESA PARIS In Orbit Demonstrator mission (PARIS- IOD) (Martin-Neira et al., 2011), this technique provides altimetric estimates of at least twice precision than the cGNSS- R approach.
To overcome these limitations, newer approaches have been proposed:

TABLE II.3 – List of GNSS-R hardware or software solutions existed currently and future, modified from table of Cardellach et al. (2015).

Name	Hardware /software	Chan-nels	Bands	Band-width (MHz)	Sampling rate (MHz)	Output rate (Hz)	Architecture	Constellations
(gri)PAU	hardware	(1)2	L1	2.2	5.745	16.384	cGNSS-R (C/A)	GPS
BJ	software	4	L1+L2	18	20	20MHz	RAW	GPS
COMNAV	software	1	L1	5.7	-	-	RAW	GPS
COSMIC IIB 2018	hardware	6	L1 L2 L5 E1 E2 E5	-	-	-	Multiple steered beams	GPS, GALILEO, GLONASS
CyGNSS 2016	hardware	4	L1	-	-	-	unsteered	GPS L1C/A
DMR	hardware	-	L1+L2	-	-	-	-	GPS
GLORI	hardware	4	L1 L2 L5	-	160	-	iGNSS-R	GPS
GOLD-RTR	hardware	3	L1	8	20	1000	cGNSS-R (C/A)	GPS
GORS-1(2)	hardware	2(4)	L1+L2	-	-	-	cGNSS-R (C/A, L2)	GPS, GALILEO
GRAS	hardware	3	L1+L2	20	28.25	1000	cGNSS-R (C/A, P-semi-codeless)	GPS
GRIP-SAR-GO	hardware	2	L1+L5, E1+E5	52	≤150	1	cGNSS-R	GPS, GALILEO
NordNAV R30(Quad)	software	1(4)	L1	2	16.4	-	RAW	GPS
OceanPal/SAM	software	2	L1	4	16.367	1000	RAW	GPS
OceanPal MISTRALE	hardware	4	L1 L2 E5	>50	-	-	-	GPS, GALILEO
OpenGPS	hardware	2	L1	5.7	<100	-	cGNSS-R (C/A)	GPS
PIR/A	hardware	3	L1	12	80	1000	iGNSS-R	ANY at L1
POLITO-GNSS-R	software	1	L1	-	8.1838	-	RAW	GPS
PYCARO	hardware	2	L1+L2	20	20	-	cGNSS-R (C/A, P-semi-codeless), iGNSS-R (not full band width)	GPS
SMIGOL	hardware	1	L1	2.2	5.745	1	cGNSS-R (C/A)	GPS
SPIR	software	16	L1	80	40	40MHz	RAW	ANY at L1
SPIR-UAV	software	8	L1	80	40	40MHz	RAW	ANY at L1
STARGYM	software	-	-	-	-	-	Waveform, Bitstream, Interfero-metric, PARIS mode.	GPS, GLONASS
TR	software	2	L1+L2	-	-	-	RAW	GPS
TriG (extended)	hardware	8(16)	ANY 4 with L-Band	2-40	configurable	20/40	0.1-1000	ANY: software configurable GPS, GLONASS, FDMA, GALILEO, others 1-2 GHz
Ublox LEA-4T	hardware	1	L1	2	4	-	cGNSS-R (C/A)	GPS
Ingespace MISTRALE	hardware	4	L1 L2 L5	50	configurable	-	iGNSS-R	GPS, GALILEO, BeiDou
EAyard PRISM	hardware	4	L1+L2	20	configurable	-	iGNSS-R	GPS, GALILEO

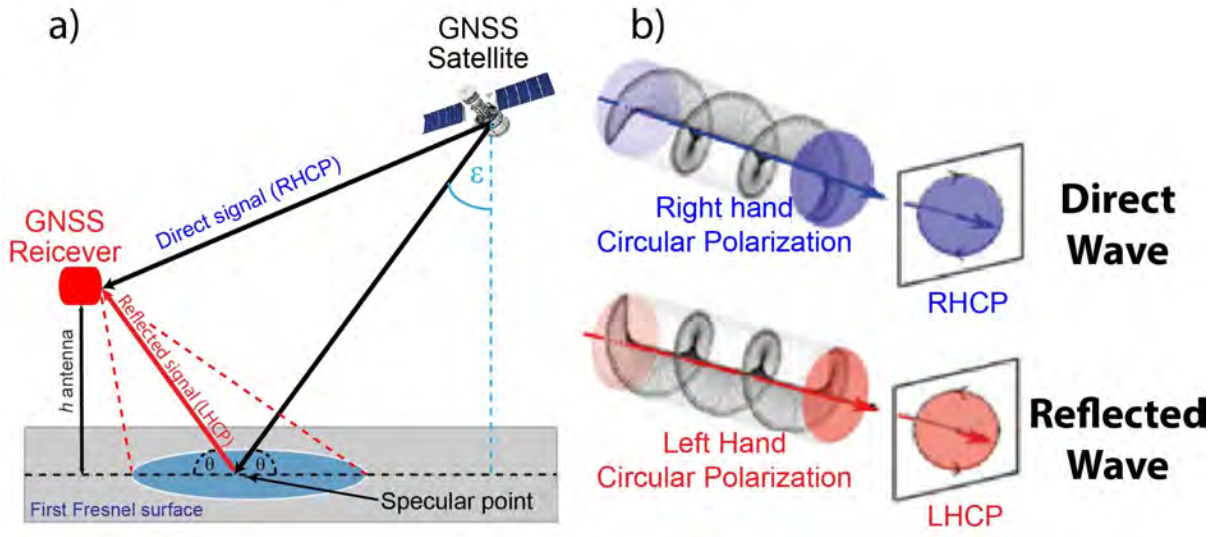

Figure II.17 – *In-situ* measurement scheme by the IPT method; a) geometry of the reflected multipath, position of the specular point that corresponds to the center of the first Fresnel surface (in blue); b) representation of the different polarizations recorded by an antenna "classic".

II.3.2 Opportunity of the signal reflectometry

II.3.2.1 Geometry of multi-static systems

There are therefore two types of geometry for multi-static systems, those dual antennas with specific receptors capable of acquiring the waveforms (cGNSS iGNSS-R or-R) and those single antennas using standard receivers and antennas omnidirectional able to acquire direct and reflected waves:

➢ Dual antenna device: to acquire the direct signal, use an antenna oriented at the zenith (towards the sky) and whose polarization is RHCP. For the signal reflected due to the change of sign related to the reflection, an LHCP antenna oriented towards the reflection surface will be used. The difference of path between the direct signal and the reflected signal can be found by simple geometric construction (Fig. II.17).

➢ Standard antenna device: in geometry with a standard antenna (Fig. II.17b, § II.3.4.1), the single antenna combines direct and indirect signals, producing constructive and destructive interference oscillations that are observable in the signal-to-noise ratio (SNR). The SNR data have a quasi-sinusoidal pattern whose dominant modulation frequency is proportional to the antenna height with respect to the reflective surface (Larson et al., 2009).

II.3.3 Observable obtained from airborne platforms

II.3.3.1 Delay-Doppler Map (DDM)

Figure II.18 shows the reflected waveform profiles for different surface conditions (§ II.3.1). There is a significant decrease in reflected signal power, which is accompanied by a strong asymmetry of the waveform with increasing surface roughness because the individual contributions are low and for some are very far from the specular point.

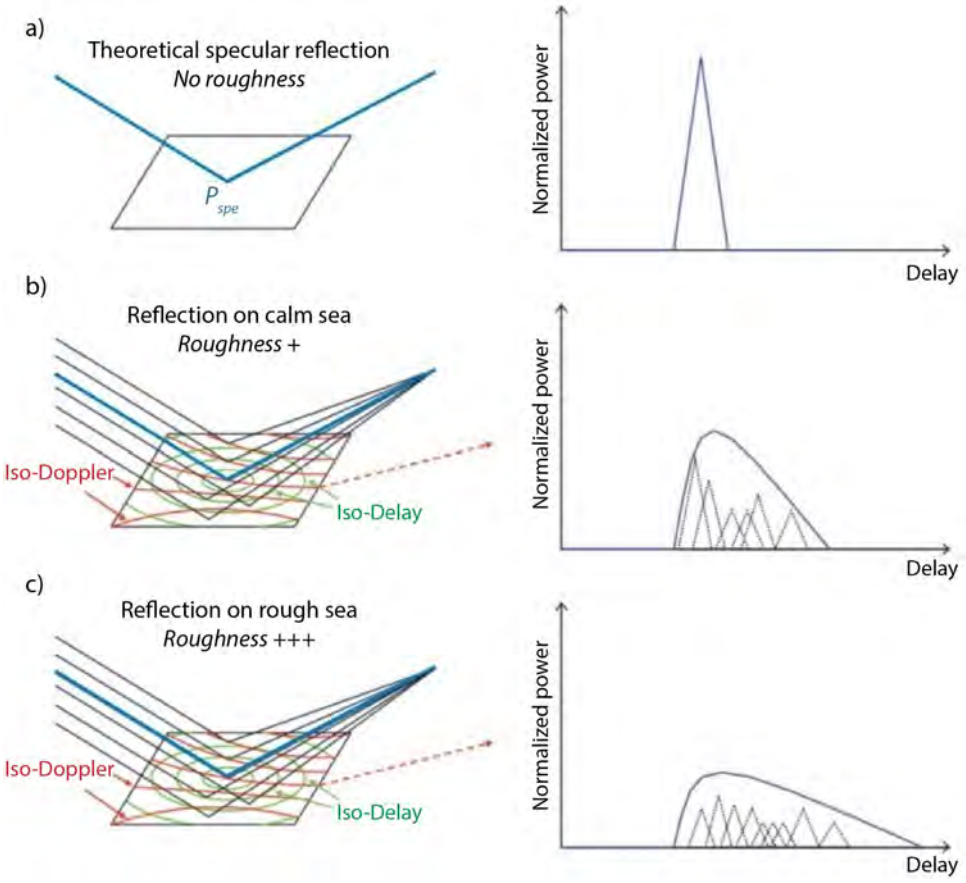

Figure II.18 – Waveform depending on the type of the scatter applied to a perfectly flat land surface (lake) and more or less rough ocean. For each profile, the blue curve shows the total waveform and the black curves show the individual reflections near the specular points, which are involved in the construction of the waveform. On the maps, the path in blue corresponds on the path of the specular point P_{spe}.

The shifts observed (Fig. II.18a and II.18b compared with II.18c) between reflected and direct signals are linked to the extension of the path of reflected signal, which passes through the reflective surface before reaching the receiver. The map that shows power versus delay and the Doppler is the DDM and it is the fundamental reflectometry observable. It reflects contributions of different pairs of delay and Doppler frequency (τ, f) from different cells of the observed surfaces. These cells are the intersections of iso-Delay

and iso-Doppler at any point on the surface, with a delay size determined by the satellite PRN code and the Doppler coherent integration time. The Map coordinates are relative to the specular point, which shows the delay and the Doppler as zero, and is therefore the point of origin of the DDM. The coordinates also pose the problem of ambiguity embodied.

By measuring this delay, the height [II.25] of the receiver can be estimated relative to the surface, and thus information related to the altimetry surface can be derived. For example, for a receiver installed *in-situ* on a mast, with the approximation of a flat surface, the convention equation of GNSS-R altimetry is written as:

$$c\tau_i = 2h\sin(\theta_i) + SB \tag{II.25}$$

Where τ_i is the measured delay between the direct and reflected waveform for satellite i, for a satellite elevation θ_i and h is the receiver height relative to the surface. SB is the system bias linked to the path difference between direct and reflected and which must also be considered.

For airborne or space receivers, the above equation cannot be used because of the non-applicability of the flat surface approximation and other disruptive effects on the delay that are linked to the troposphere and ionosphere.

The additional length of the reflected signal path can also be ascertained through the phase difference between direct and reflected electromagnetic fields, which can be measured through the complex cross-correlation waveform. This phase difference provides an estimation for surface altimetry, with increased accuracy that is theoretically around a centimeter. Finally, the waveform's downwards slope can be used to get information on the surface roughness.

II.3.3.2 The bi-static scattering coefficient

The bi-static scattering coefficient is particularly well analyzed for applications on ocean surfaces (roughness, surface wind) but here, we especially focus on land surfaces (soil moisture, plant cover biomass, etc.). To do this, we specifically look at the transmitter and receiver polarizations, the GNSS signal transmitted by the satellites is in RHCP polarization (Right Hand Circularly Polarized). Following its reflection on the earth's surface, the electromagnetic wave generally undergoes a reversal of the polarization sign and thus the majority of the scattered power passes in LHCP (Left Hand Circularly Polarized) polarization. However, the combined effects of the roughness, and geophysical parameters of the surface, means that the signal from the right polarization may be significant and thus be used for the determination of geophysical parameters of the surface. We thus obtain a more complex response which is dependent on the RHCP component

called co-polar τ_0, and LHCP component called cross-polar τ_χ:

$$\tau_0 = \frac{\tau_h + \tau_v}{2}, \quad \tau_\chi = \frac{\tau_h - \tau_v}{2} \tag{II.26}$$

These components are based on vertical reflection coefficients τ_v and τ_h horizontally that are dependent on parameters of the reflecting surface:

$$\tau_h = \frac{\sin(\theta) - \sqrt{\varepsilon - \cos^2(\theta)}}{\sin(\theta) + \sqrt{\varepsilon - \cos^2(\theta)}}, \quad \tau_v = \frac{\varepsilon \sin(\theta) - \sqrt{\varepsilon - \cos^2(\theta)}}{\varepsilon \sin(\theta) + \sqrt{\varepsilon - \cos^2(\theta)}} \tag{II.27}$$

where $\varepsilon = \varepsilon_r - j(\sigma/(\omega\varepsilon_0))$ is the complex dielectric constant, ε_r is the relative permittivity, σ is the electrical conductivity of the reflection surface and ε_0 is the permittivity of the vacuum. Figure II.19 gives some example of variation of reflection coefficients τ_v and τ_h (Fig. II.19a) and the corresponding co-polar τ_0 and cross-polar τ_χ coupled reflection coefficients (Fig. II.19b).

II.3.3.3 The reflectivity of the surface

The reflectivity of the surface [II.28] can be quantified by the ratio between direct and reflected waveforms in the case of signals not affected by thermal noise. For this purpose, it is considered that the frequency f is aligned with the Doppler shift of the direct signal, and applying the change of variable: $\tau' = \tau - R_d$, with R_d is the direct path. The reflectivity of the surface is described by the equation:

$$\Gamma'_{pq} = | < \frac{Y_{r,q}(\Delta\tau, f)}{Y_{d,p}(0, f)} > |^2 \tag{II.28}$$

with $< >$ is the operator of the mean, $\Delta\tau$ is the time between the direct and reflected paths; $Y_{d,p}$ corresponds to the correlation function of the direct incident polarization signal p, and $Y_{r,q}$ that of the reflected polarization signal q.

II.3.3.4 Interferometric complex field

Another observable, known as interferometric complex field (ICF), is defined by the temporal series of the maximal ratio of the reflected waveform to those of the direct waveform:

$$ICF(t) = \frac{Y_{r,q}(t, \Delta\tau, f)}{Y_{d,p}(t, 0, f)} = \frac{R(t)}{D(t)} = \frac{r(t)}{d(t)} e^{-i(\varphi_r(t) - \varphi_r(d))} \tag{II.29}$$

$R(t)$ and $D(t)$ are respectively the time series of the reflected and direct waveforms, with their associated amplitudes and phases$r(t)$, $d(t)$ and $\varphi_r(t)$, $\varphi_r(d)$.

With the ICF, the majority of common propagation effects for the direct and reflected

path can be eliminated in the condition of the antenna is close enough to the reflective surface. These are the ionospheric, tropospheric effects, the error of the receiver clock and the antenna radiation pattern only if the antennas for the direct and reflected signal are identical. This indicator contains information on the surface roughness and its dielectric properties. It also gives very good results to characterize soil moisture (Egido (2013)).

II.3.4 Interference Pattern Technical – Reflectometer with single antenna

This technique, known as the Interferometric Diagram (IPT), uses a single dual polarization antenna, one RHCP for the high-gain direct path, the other LHCP with a lower gain to measure the reflected signals (Fig. II.20). The direct and reflected signals are combined to obtain the visible interference pattern on the total SNR (SNR_t, Fig. II.21) resulting from the addition of direct SNR (SNR_d) and reflected SNR (SNR_r). This information is related to different geophysical parameters such as the moisture from the ground surface or the moisture from the vegetation cover if the plant density is too high. It is also possible to obtain information on the electrical conductivity σ, the relative permittivity ε_r, or the surface altimetry h.

II.3.4.1 Polarimetric measurements

In-depth knowledge of the characteristics of antenna radiation is essential. This is particularly the case for polarimetric systems, since small variations in the characteristics of the antenna could have significant impacts on the final measurement. Different aspects should be considered: the radiation pattern of antennas, polarization shift, isolation of cross-correlations and orientation of the antenna.

In general, the polarization of the incident wave does not coincide with the polarization plane of the receiving antenna, because of the fact that the plane of the antenna is typically not orthogonal to the direction of propagation of the electromagnetic wave. For linear polarizations, the orientation of the antenna and the incident field should be taken into account. The incident electric field is written as follows:

$$\vec{E_i} = \hat{\rho}_w E_i \tag{II.30}$$

Where, $\hat{\rho}_w$ is the unit vector of the wave polarization. The polarization of the receiving antenna is described by:

$$\vec{E_a} = \hat{\rho}_a E_a \tag{II.31}$$

$\hat{\rho}_a$ and E_a is the antenna polarization vector. For circular polarized antennas (the case for standard GNSS antennas), there is a loss of polarization that depends on the angle of incidence and the receiver wave. This is the polarization shift or the polarization loss

factor (PLF [II.32]). The PLF is written as the product of two squared polarization vectors:

$$PLF = |\hat{\rho}_w \hat{\rho}_a|^2 \tag{II.32}$$

Another key parameter for the performance of polarimetric measurement is the inter-polarization isolation of the receiving antenna: the lower the leakage between the two polarizations, the better the measurement.

The portion of power received by the orthogonal polarization relative to the antenna polarization is called the cross-polarization isolation. The direction of the antenna, the opening of its lobe, the model that simulates the diagram or measurement of the antenna pattern are essential to establish the adjustments necessary to restore the relationship between the GNSS-R observations and geophysical parameters.

In the case of a single antenna, the linear coefficients of horizontal and vertical reflection [II.27] add up to give the coupled polarization. The coupled polarization from the reflective surface is elliptical in shape when the vertical component is different from the horizontal one. It is circular when they are equal and linear when the vertical component is zero. The nature of the final polarization is determined by the relationship between the linear component of the reflection surface, the incidence angle of the satellite and the antenna gain pattern (Fig. II.19). This information is valuable for calculating the total SNR (SNR_t, [II.33]) as measured by the center of the antenna phase. At every moment, SNR_t is the sum of the SNR from the direct signal SNR_d and that of the reflected signal SNR_r:

$$SNR_t^2 = A_d^2 + A_r^2 + 2A_d A_r \cos(\Delta\Phi) \tag{II.33}$$

Where A_r and A_d are the amplitudes of reflected and direct signals and $\Delta\Phi$ is the phase difference between the two signals. As the direct signal is the signal that is most amplified by the antenna gain, one can assume that $A_d \gg A_r$. Then we get a simplified formulation of SNR_t:

$$SNR_t^2 \approx A_d^2 + 2A_d A_r \cos(\Delta\Phi) \tag{II.34}$$

SNR_t is dominated by a high amplitude and low frequency signal, which is mainly driven by the direct signal. The reflected signal SNR_r changes the SNR_t by producing high and medium frequencies for medium to low satellite elevations, which is where SNR_t disturbances are most sensitive and visible (Fig. II.21, green ellipse).

In order to analyze the reflected component (Fig. II.21, SNR_m), we must first remove the contribution of the SNR_d in the SNR_t curve. We can remove the direct signal effect by modelling the antenna gain pattern. However, this method requires knowledge of the antenna gain patterns of the receiver and the transmitter satellite.

Since this information is difficult to obtain, for patent reasons, Larson et al. (2008b) suggested using a second order polynomial for the SNR_d which is then subtracted from

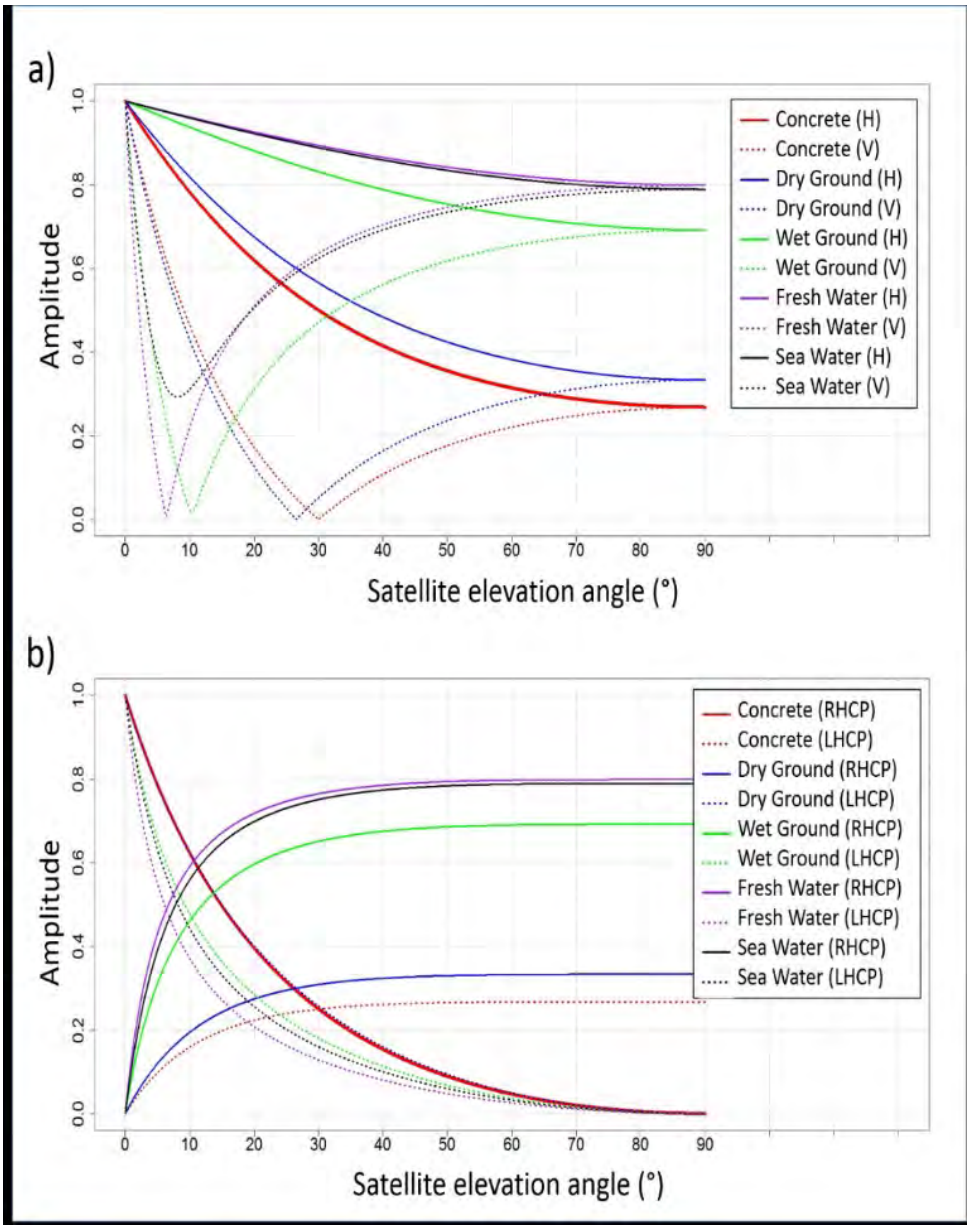

Figure II.19 – A representation for different grounds and based on the satellite elevation angle, (a) amplitude of the reflection coefficient for the horizontal (H) and vertical (V) components, and (b) the amplitude of the coupled reflection coefficients of the co-polar component (RHCP) and the cross-component (LHCP).For a frequency of $\sim$ 1.5GHz: The relative permittivity ε_r and the conductivity σ chosen for different grounds are: natural ground consisting of a mixture clay, limestone and sand ($\varepsilon_r = 15$ $s.u, \sigma = 2.10^{-3} S/m$), Dry Ground ($\varepsilon_r = 4, \sigma = 1.10^{-4} S/m$), Wet Ground ($\varepsilon_r = 30, \sigma = 2.10^{-2} S/m$), Fresh Water ($\varepsilon_r = 80, \sigma = 2.10^{-3} S/m$), Sea Water ($\varepsilon_r = 70, \sigma = 4.10^{-2} S/m$).

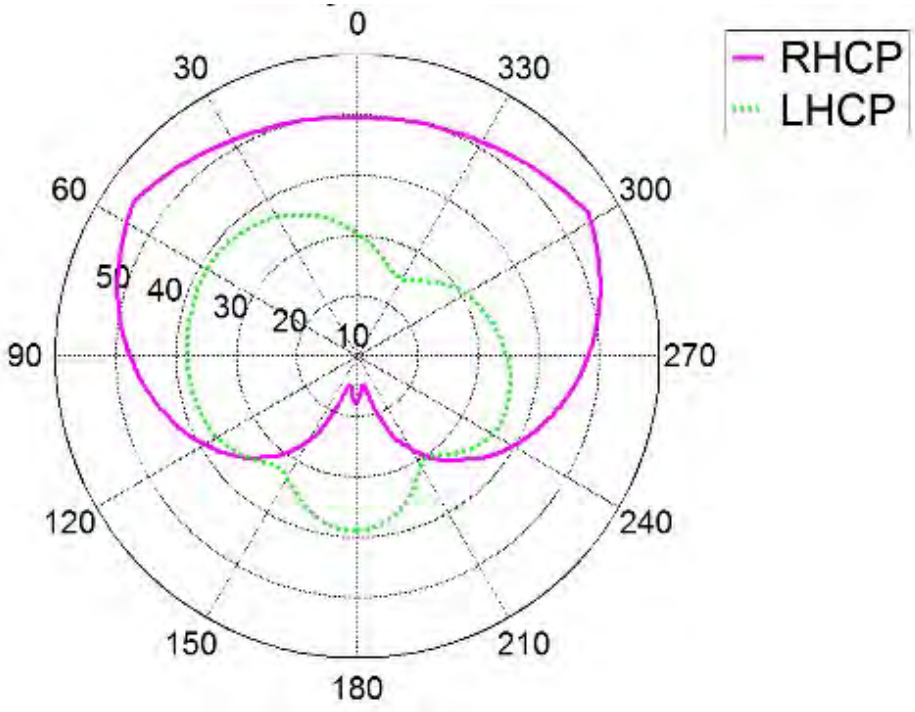

Figure II.20 – Diagram 2D of the Leica AR10 antenna. In pink (solid line) are the direct signal gains after antenna amplification (overestimated manufacturer's data); in green (dotted line), those of the reflected signal. This antenna has the advantage of providing good measurements in conventional GNSS and GNSS-R.

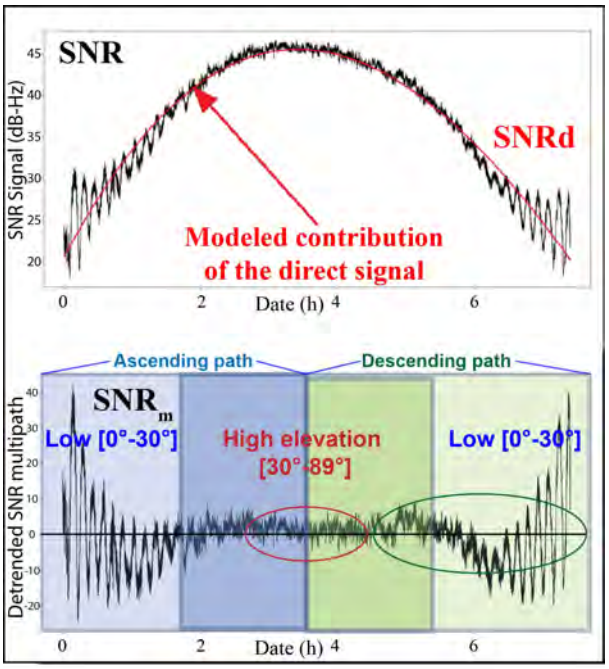

Figure II.21 – A representation of the different normalized powers of SNR for PNR12 satellite in the GPS constellation versus time (s): SNR_t (blue) is measured by the receiver, SNR_d (green) is modeled by a polynomial of degree 2 (Larson et al. (2008b)) and SNR_r (red) is obtained by subtracting the previous two. For low satellite elevations (green ellipse), the SNR_r has medium to high frequencies, but for which the amplitude is greater than the noise (speckle thermal noise); for satellites with high elevations (red ellipse), the SNR_r disappears in the noise measurement.

the SNR_t data to thereby isolate the SNR_r variations. Since this method gives results comparable to the modelling of the real signal, it will be preferred to obtain the SNR_r. As this latter method yields to better results than the modelling one, many studies among others have adopted the second one and removed a second-order polynomial function to their SNR time series, have presented a complete modelling, from the satellite to the antenna, of the SNR for altimetry but it is, for the time, not useful for *in-situ* applications

Nevertheless, modelling integrating satellite and receptor parameters offers promising prospects for solving the inverse problem that leads to the resolution of the geophysical parameters associated with the reflected surface (Frappart et al. (2015)).

II.3.4.2 The interferometric metrics of the IPT technique

➢ *Effective antenna height above the reflecting surface*

According to Bishop et al. (1985); Georgiadou and Kleusberg (1988), and assuming a planar reflector, the phase difference between the direct and reflected signals can be derived geometrically from the path delay δ of the reflected signal [II.35]:

$$\Delta = \frac{2\pi}{\lambda}\delta = \frac{4\pi h}{\lambda}\sin(\theta) \tag{II.35}$$

where θ the elevation of the satellite (rad), h the height (m) of the antenna phase center with respect to the reflection surface S (for examples: surface of an ocean, lake, and landslide). From [II.35], we can derive the frequency oscillations of the SNR_r with respect to time:

$$f_t = \frac{d\psi}{dt} = \frac{4\pi h}{\lambda}(h\cos(\theta)\dot{\theta} + \dot{h}\sin(\theta)) \tag{II.36}$$

where $\dot{\theta} = d\theta/dt$ is the elevation velocity of the satellite in rad.s^{-1}, $\dot{h} = dh/dt$ is the vertical velocity of the antenna height in m.s^{-1}. Variation of $\dot{h}$ maybe important when looking at ocean or inland waters (waves, height of the water line for river). Equation [II.36] can be simplified by making a variable change $x = \sin(\theta)$. We thus obtain f, the frequency of the multipath oscillations with respect to the sinus of the satellite elevation:

$$f = \frac{d\psi}{dx} = \frac{4\pi h}{\lambda}(\frac{\dot{h}\tan(\theta)}{\dot{\theta}} + h) \tag{II.37}$$

For ground application, soil moisture content has an influence on the penetration depth of the GNSS waves into the ground (Georgiadou and Kleusberg, 1988), hence slight variations with time of the effective height h of the antenna above the reflecting surface. Variations of h with time, retrieved from the measurement of $f(t)$, are thus an indicator of soil moisture variation. Equation [II.37] shows that, if $\dot{h}$ is approximated to zero, the frequency of the multipath oscillation is constant and directly proportional to the antenna height h above the reflecting surface. Unluckily, if $\dot{h}$ is not neglected, the

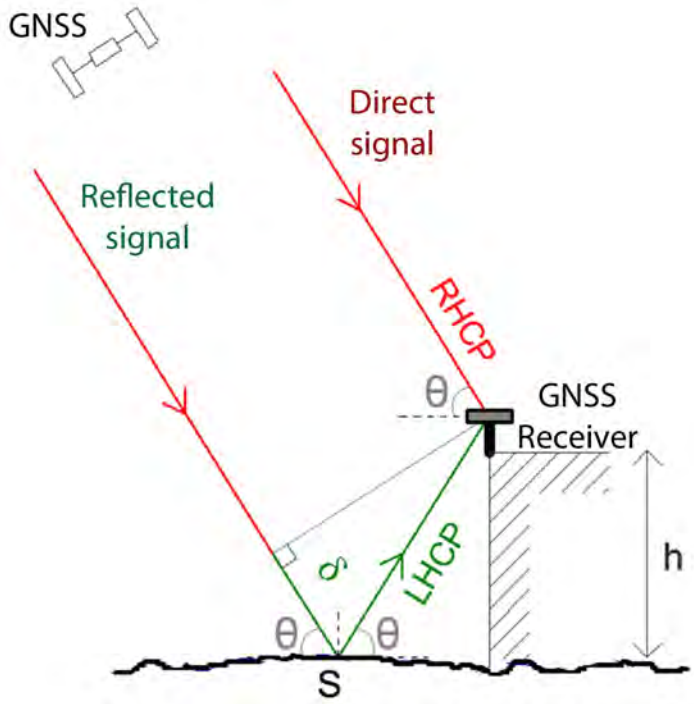

Figure II.22 – Multipath geometry of the reflected signal for a conventional GNSS receiver with its omnidirectional antenna and the equation of the phase difference ψ between direct and reflected signals.

frequency also depends on the satellite elevation θ, the satellite elevation velocity $\dot{\theta}$, and the variations of the effective antenna height over time $\dot{h}$. The two former terms are known but not $\dot{h}$. That is why many studies neglect the term $\dot{h}\frac{\tan(\theta)}{\dot{\theta}}$ while estimating the time series $h(t)$.

➢ *Amplitude and phase of the reflected signal*

For a given height h of the antenna above the reflecting surface, the SNR_r is a periodic function with a carrier phase given by can be formalized as:

$$SNR_r = A_r \cos(\frac{4\pi h}{\lambda} \sin(\theta) + \Phi_r) \tag{II.38}$$

Where A_r scales with the intensity of ground reflections, and Φ_r is the phase. A_r combines the gain pattern and the reflected intensity, which, both, depend on the satellite elevation.

Field observations show that these responses in terms of phase and amplitude are strongly correlated with soil moisture level. Furthermore, these observations show that the effects of humidity are more sensitive to the phase Φ_r than to amplitude A_r, as demonstrated by Larson et al. (2008b) and Roussel et al. (2016). A_r, Φ_r and h which are derived from f, are thus three metrics which can be inverted to retrieve soil moisture content.

➢ *Retrieving interferometric metrics*

This section presents simple methods to recover, over time, the three SNR_r metrics:

- effective antenna height h;
- amplitude A_r;
- phase Φ_r.

The time series that can be analyzed by IPT are assumed to be dependent on soil moisture variations and satellite elevation θ. As shown in figure II.21, for high elevations [30°,70°], the SNR_r has low amplitude variations. Moreover, beyond ($\theta > 70°$), SNR_r is buried in noise. Conversely, for low elevations [2°,30°], the RHCP component becomes dominant and the SNR_r has higher amplitudes, which is why we generally define two classes of elevation that are studied independently. The elevation and azimuth, at any instant, are derived from the satellite coordinates obtained from the IGS ephemeris final SP3 products which provide GNSS orbits with a centimetric precision and clock offset data with a temporal resolution of 15 minutes for the past epochs. In France, the IGN (National Geographical Institute) provides IGS products (`ftp://igs.ensg.ign.fr/pub/igs/products/`) just like the VLS/CNES (*Collect Localization Satellites*, a subsidiary of the French space research center CNES).

The oscillation frequency of the multipath is defined by the equation [II.36]. Two cases have been developed according to the objectives of the analysis by chosen IPT:

- the static case is typically used from soil moisture measurement;
- the dynamic case that deals with elevation changes and is therefore more suitable for measuring continental and/or ocean water levels.

a) Static case

The slight variations of soil moisture during the considered portion of the satellite pass (i.e., satellite elevation ranging either between [2°, 30°] or [30°, 70°]) are neglected, and h (and so f) is thus assumed to be constant during this time period and $\dot{h} = dh/dt$ tends towards zero . Larger time-scale soil moisture fluctuations are estimated by comparing the antenna height retrieved from a portion of the satellite passage with its counterpart of the following passes. During the considered time period, the height of the antenna above the reflecting surface is defined as:

$$h \approx \frac{\lambda f}{4\pi} \tag{II.39}$$

where the frequency oscillations f of the SNR_r is determined using a Lomb Scargle Periodogram LSP (Lomb, 1976; Scargle, 1982) and λ is the considered wavelength for GNSS frequency band.

b) Dynamic case

In the dynamic case, $\dot{h}$ is supposed high enough to be taken into account during the considered portion of satellite pass. h (and so f) is thus likely to change during this time period. That is why a windowing of this portion is mandatory to correctly estimate the variations of f over this time period. In this case, Roussel et al. (2015b) developed the method LSM which provides a single time series $h(t)$ combining all satellites. Nevertheless, the temporal resolution of the static consideration is limited by the repeat-ability of the GNSS constellations (i.e.), a maximum of four estimations, one during the descending phase, one during the ascending phase with twice passes per day per satellite for the GPS constellation, whereas the dynamic case provides a far better temporal resolution (details of this case will be present in chapter III,section § IV.2.1).

II.3.5 Platforms and constraints

One of the undeniable advantages of the GNSS-R technique in remote sensing is that it can be used at different spatial scales depending on the vector on which the antenna/receiver pair is installed. This ranges from the square meter scale for ground-based systems to the average scale of a few hectares for drones (less than a few hundred meters) to a few tens of square kilometers for aircraft ($h < 4$ km), or even higher to cover much larger areas of several hundred square kilometers when the vector is an airliner (h from 4 to 8 km) or a satellite (LEO: $h \sim 450 - 2000$ km to MEO: $h \sim 8000 - 20000$ km). Historically, it's the mobile vectors, mostly aircraft, which were first used (Auber et al., 1994; Martin-Neira, 1993; Garrison and Katzberg, 2000). Since then, with the explosion of the GNSS-R potential, many other vehicles have been used and will be presented under three main families:

- fixed vectors suitable for *in-situ* measurements;
- airborne systems for fine mapping of environmental parameters;
- satellite systems that should ultimately allow global monitoring of the Earth's system, whether its atmosphere (ionosphere and troposphere), its hydrological compartment (oceans, continental waters, snow and ice) or its continental compartment (Soil, biomass, superficial movements). For more information on the other domains that are the oceans and atmosphere, the "tutorial" developed by Zavorotny et al. (2014) will be a valuable source of information.

II.3.5.1 Fixed / in-situ

Initially, *in-situ* measurement sites were largely oriented to the study of moisture by using the IPT method (Larson et al., 2008b). Then a number of *in-situ* studies were started using both the waveforms and the IPT measure:

- Snow depth (Larson et al., 2009; Ozeki and Heki, 2012);
- Growth of vegetation (Rodriguez-Alvarez et al., 2011b)
- Monitoring ocean tides from a terrestrial observation point by measuring waveforms (Caparrini et al., 2007; Löfgren, 2014; Hobiger et al., 2014) or by measuring IPT (Larson et al., 2013; Roussel et al., 2015b).

This resulted in the development of simulators (Fig. II.23, the green lines correspond to the direct path and the red lines represent the reflected path of the GNSS signals) to better identify sites suitable for continental GNSS reflectometry. Indeed, contrary to oceanic surfaces (Fig. II.23a), in the continental area, the reflection points are dictated by land topography and the masks it causes (in the yellow, blue dashed line, Fig. II.23b).

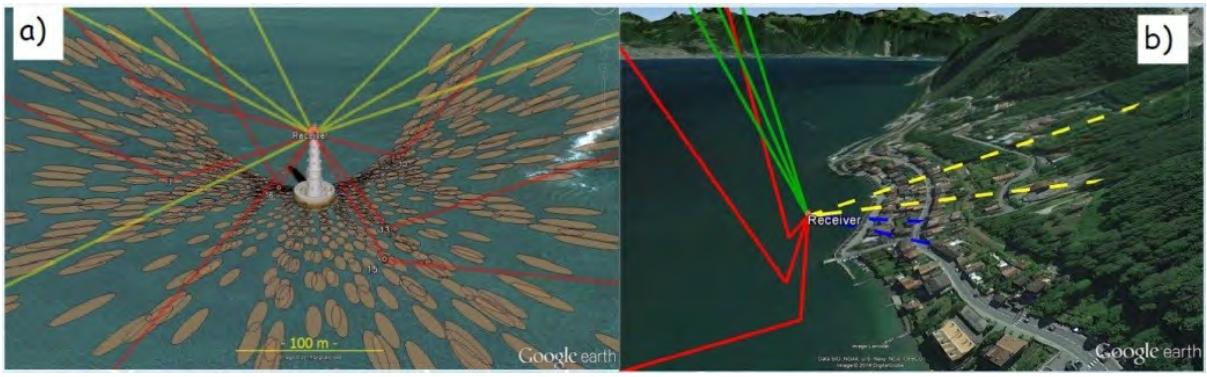

Figure II.23 – Example of *in-situ* simulation of associated reflection points and Fresnel surfaces. (a) in a coastal environment (Cordouan lighthouse, France), (b) in a continental environment (Lake Geneva, Switzerland) where the topography influences not only the position of the reflection points but also the existence of these points (Mask phenomena) (Modified from Roussel et al. (2014)).

II.3.5.2 Airborne

This is certainly the most used carriers by scientists to test their hypothesis whether it is from drones or "Remotely Piloted Aircraft Systems" (RPAS) as in the framework of the MISTRALE project funded by the "European GNSS Agency" (Fig. II.24), or balloons (Figure II.25) have, for manned balloons low flight altitude, the big advantage of having slow speeds which contributes to the stability of the measurements.

Tests with fast balloons in the upper troposphere were also carried out in 1999 as part of the MEBEX experiment, the balloon had a flight altitude of 37 km. The objective of this experiment was to study the surface roughness of the sea in order to determine the wind speed (Cardellach et al., 2003).

The receiver "$P(Y)$ and C/A Reflectometer" (Pycaro) should be embarked on satellite, it has also performed stratospheric balloon tests during the assignments of BEXUS 16 and 19 (funded by the German Aerospace Center - DLR and Swedish National Space Board – SNSB). It acquired for the first time the constellations GPS, GLONASS, and GALILEO in polarization LHCP and RHCP. Finally, planes in the widest sense (ULM, Piper aztec, ATR42...) are one of the most used transport carriers and France, with its fleet of SAFIRE aircraft, plays an important international role. Thus, an ATR-42 of this platform was used to perform one of the first cGNSS-R missions using the GLORI receiver (Motte et al., 2016).

II.3.5.3 Satellite

As the Earth's surface is 70% water, it is easy to understand that remote sensing applications are primarily interested in ocean altimetry, sea state and weather phenomena.

Figure II.24 – H2020 MISTRALE project to facilitate farming and monitoring of flooded areas from an iGNSS-R on board a RPAS (www.mistrale.eu), first results of the Scamandre air Campaign (South France) over a flooded pound, in red airplane trajectory, light blue to dark blue power ratio between reflected and direct waves which corresponds to moisture changes.

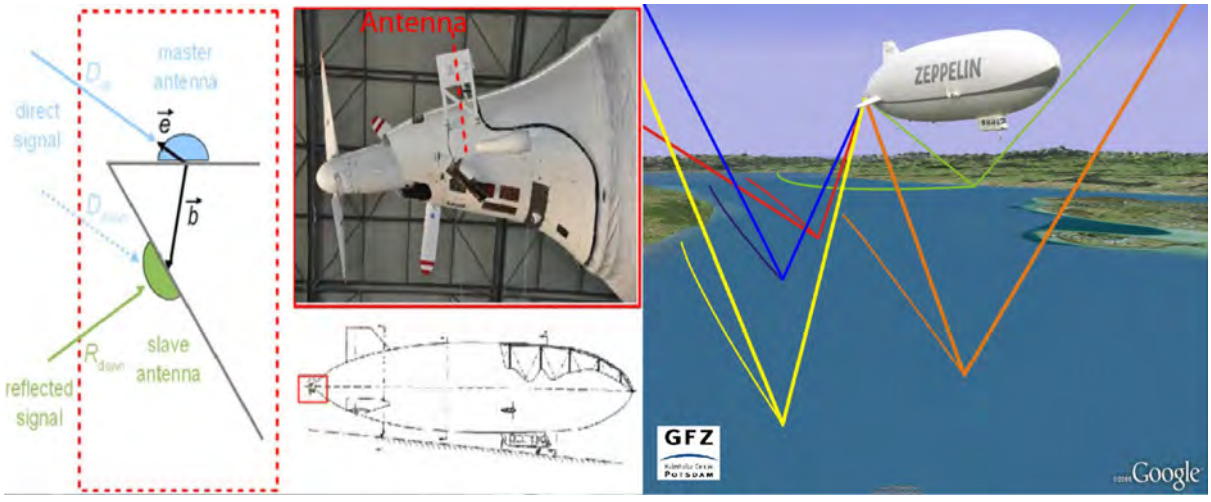

Figure II.25 – GNSS-R system on board of Zeppelin balloon, which carried out a measurement campaign over Lake Constance (German: Bodensee). Modified from Semmling et al. (2013).

TABLE II.4 – Main European airborne campaigns carried out since 2005, in green iGNSS-R receptors, orange cGNSS-R receptors and yellow GNSS conventional receptors (modified according to the website http://www.ice.csic.es/research/gold_rtr_mining).

Campaign	Year	Financed by	Location	Air/sol	Applications	Reflection LHCP + RHCP	Receiver
GOLD Test	2005	IEE/ICC	NO of the Mediterranean Sea (Spain)	Air (3 vols)	ocean continent	yes	cGNSS-R
CoSMOS-OS	2006	ESA	North Sea (Norway)	Air (12 vols)	ocean	yes	cGNSS-R
CoSMOS-OS	2007	ESA	Baltic Sea (Finland)	Air (2 vols)	ocean	no	cGNSS-R
CAROLS	2007	CNES	Bay of Biscay, South of France	Air (3 vols)	ocean continent	yes	cGNSS-R
SMOS calibration	2008	ESA	Finland to Valencia (Europe)	Air (12 vols)	ocean continent	no	cGNSS-R
CAROLS	2009	CNES	Bay de Biscay, South of France, Valencia (Spain)	Air (11 vols)	ocean continent	yes	cGNSS-R
GPS-SI	2008-2009	ESA	Bay of Disko (Greenland)	Sol (7 months)	ocean ice snow	yes	cGNSS-R
GPS-DS	2009	ESA	Dome-C (Antarctic)	Sol (10 days)	snow	yes	cGNSS-R
PIT-POC2	2011	ESA	Baltic Sea (Finland)	Air (2 vols)	ocean	yes	Pira iGNSS-R
BEGUR	2012	ESA	NO of the Mediterranean Sea (Spain)	Sol (3 days)	ocean	yes	Paris-MB iGNSS-R
SAPHIRE	2015	RTRA PRISM	SO of France	Air (5 vols)	ocean continent	yes	GLORY iGNSS-R
Lamasquère	2013-2015	RTRA PRISM	Midi-Pyrénées	Sol (30 months)	Sol humidity	yes	LEICA GNSS
Pech Rouge	2015	ESA H2020 MISTRALE	Aude	Sol (1 months)	Sol humidity	yes	LEICA GNSS
Pech Rouge	2015	ESA H2020 MISTRALE	Aude	Air (2 vols)	ocean continent	yes	OceanPal 2
Beach Volley	2015	ESA H2020 MISTRALE	Midi-Pyrénées	Sol (5 days)	Sol humidity	yes	LEICA GNSS

However, as these missions pass over continents, they will also improve techniques for measuring moisture level and identifying the properties of ice, as well as other continental applications:

- *TechDemoSat-1 (TDS 1)*: it follows the English UK-DMC experiment, which was a big success. The SGR-ReSi receiver on board the TechDemoSat-1 satellite was launched on July 8, 2014 (Foti et al., 2015; Unwin et al., 2016); it should be the basic device of future CYGNSS missions (NASA) dedicated to monitoring cyclones and others storms. It works on dual-frequency L_1 (C/A code) and L_2 bands and directly feeds the DDM. Its flights altitude is ∼700 km, with a period of 93 mins.

- *Cyclone Global Navigation Satellite System (CYGNSS)*: a constellation of 8 LEO satellites in equatorial orbit, which was launched on Dec. 15, 2016, at 8:37 a.m. EST into a low-inclination, low-Earth orbit over the tropics. CYGNSS also provide DDM from the equatorial zone with a time interval of five hours. The purpose of these missions is to study the tropical belt in the formation region of most cyclones. It should look at the variations in wind speeds and surface states of oceans in detail, and should also provide data for the global climate models of the Earth. This constellation will also provide information on the continent to estimate soil moisture.

- *Cube CAT-2 (^{3}CAT 2)*: this is a CubeSat or nano-satellite multi-constellations GNSS, dual frequencies and dual polarizations based on the PYCARO receiver, which uses a cGNSS-R for the C/A code and a rGNSS-R for the $P(Y)$ code. This receiver has been tested on stratospheric flights (Bexus 17 and 19 flights). It should focus on ocean altimetry, the characteristics of land surface and the cryosphere.

- *Passive Reflectometry and Interferometry System In Orbit Demonstrator (PARIS-IoD)*: PARIS-IoD is a means to carry out the ocean altimetry along large swaths (Martin-Neira et al., 2011). In Phase A (2013), the receiver was tracking four satellites for an expected altimetric accuracy of 15 cm. During the operational phase, the receiver will be able to track 20 satellites for an expected accuracy of 5 cm.

- *GNSS Reflectometry, Radio Occultation and Scatterometry on the International Space Station (GEROS ISS)*: this ambitious project funded by ESA aims to be introduced to the international station in 2019 (Fig. II.26), the project is currently in the feasibility study phase (phase A). The main objectives of the project are to use the recorded signals to make GNSS-R, radio occultation, and scatterometry to study the oceans, Earth's atmosphere and continents.

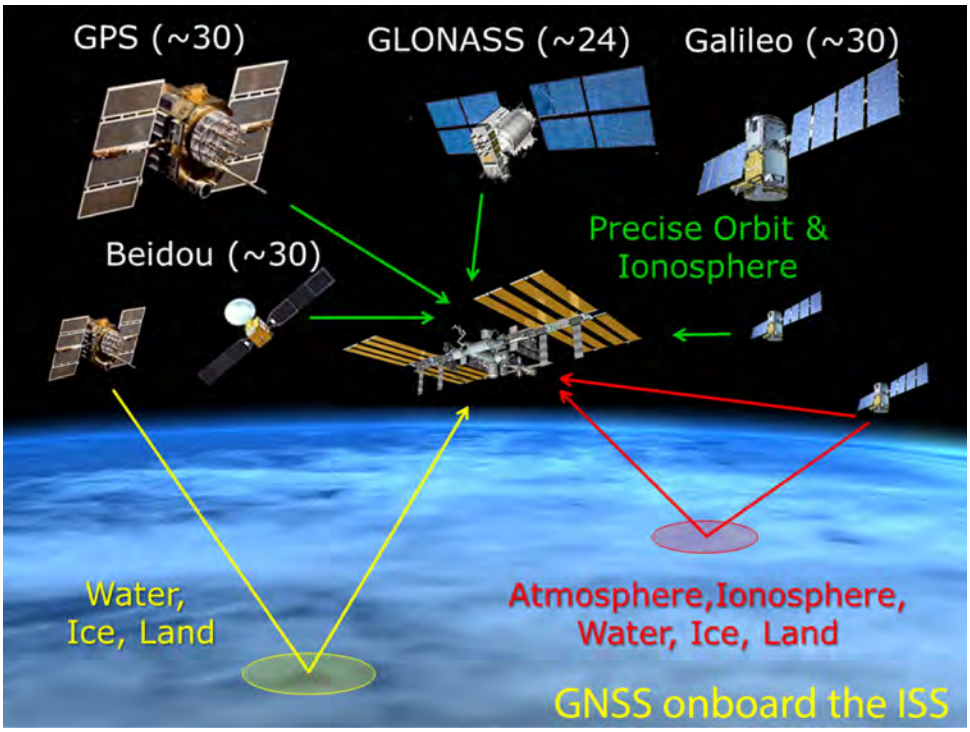

Figure II.26 – Principle of the GEROS multi-constellation receiver onboard the International Space Station (modified from Wickert et al. (2016)).

II.4 Efficiency of GNSS-R

We present here a compilation of remote sensing applications of the GNSS-R technique, some of their retrieval algorithms and performance. GNSS-R is a new science so most of these applications have been developed in the last decade. Historically, GNSS-R applications starts with the ocean altimetry (sea-surface height) and the scatterometric (sea winds and surface roughness) (Marchan-Hernandez et al. (2010) and Gleason et al. (2005), respectively). One can find accounts of various GNSS-R Environmental applications in Komjathy et al. (2000a); Fabra et al. (2012); Germain et al. (2004); Elfouhaily et al. (2002). Only the basic measurement principles are given to a complete review see the tutorial developed by Garrison J. L. (2014). The section is first organized in four sub-sections, each one devoted to a particular application:

- Ocean altimetry;
- Waves and wind;
- Cryosphere characterization;
- Soil moisture and/or biosphere characterization.

One important parameter which determines the feasibility of these different applications is the elevation height of the antenna, so different receiving system like, satellite, aircraft, RPAS or mast cannot have the same applications. Tables II.5 and II.5 gives you a good idea of the different receiving system and the possible applications associated to these platforms.

TABLE II.5 – Application feasibility in function of receiving platform for "waveform" receiver ((Modified from (Darrozes et al., 2016)).

Applications	*In-situ* (from 0 to few hundred m)	Aircraft/Rpas	Spaceborne>LEO
Ocean altimetry			
Waves and Winds		Roughness / permittivity	
Cryosphere		Sea ice / snow	
Soil moisture			
Biosphere			
Atmosphere (Tropo. and Iono.)			

(= not possible, = maybe, = ok)

TABLE II.6 – Application feasibility in function of receiving platform for "classical" GNSS receiver for ITP method (Modified from (Darrozes et al., 2016)).

Applications	*In-situ* (from 0 to few hundred m)	Aircraft/Rpas 0-290m or >290m	Spaceborne>LEO
Ocean altimetry			
Waves and Winds			
Cryosphere			
Soil moisture			
Biosphere			
Atmosphere (Tropo. and Iono.)			

(= not possible, = maybe, = ok)

II.5 Conclusions

We have seen that the GNSS-R, with the recent evolution of the different GNSS constellations, is and will be one of the fundamental tools for the monitoring of environmental phenomena. With the launch of TechDemoSat-1 it is the space segment that opens up to reflectometry applications. Recently, with the launch of CYGNSS, CAT-2, and the introduction of a receiver on the international station in future years, are expected to increase the interest of scientists and professionals in the private sector such as storms, tsunamis, the evolution of droughts, the monitoring of rivers, and ice sheets. These applications are now accessible via industrial receivers developed by young startups who have seen the potential of the GNSS-R technique and the many markets they can conquer.

There are still many methodology and technical leaps to be made:

- accuracy needs to be improved, recently studies have shown that by using the signal phase, we could easily achieve altimetry precision to the centimeter (airborne tests in France, Lestarquit et al. (2016)) and an accuracy of about 2-3% (Egido et al., 2014) in terms of volumetric water is already available. Can we, as in conventional GNSS, achieve superior quality information? This will include, as in conventional GNSS, better resolution of integer ambiguities, through improved antennas and an indispensable acquisition of all the constellations in dual-, or better, tri-frequency;

- the corollary of this increased flow of data acquired in real time is that it will fill the bottleneck imposed by the transfer rate between the waveform acquisition sys-

tem and storage systems on disks. Currently, these systems allow us, with great difficulty, to track multiple satellites with multiple frequencies while retaining the shapes of waves as completely as possible (here we mean GB/min). Another problem for satellite solutions is energy consumption: real-time systems used advanced processors which are highly energy-consuming;

- finally, for satellite and unmanned platforms, the weight of the device and antennas and their miniaturization are also fundamental points to be improved.

From this chapter we realized that:

1. GNSS-R is an opportunistic science that feeds off GNSS signal backscattered on the surface of oceans and continents. There are two large families of instrumentation for reflectometry: waveform acquisition (cGNSS-R and iGNSS-R) and SNR acquisition (conventional GNSS receiver).

2. It is important to use the signal's right (RHCP) and left (LHCP) polarization, either by combining them (conventional receivers) or through RHCP and LHCP acquisitions in separate channels.

3. Conventional receivers (cGNSS-R) use code replicas while interferometric receivers (iGNSS-R) directly use the direct signal to enslave the reflected signal.

4. The DDM (Delay Doppler Map) is a representation of the signal strength at any point in the Doppler Delay space and the maximum power point materializes the specular reflection point.

Chapter III

GNSS-R for soil moisture estimation using Unwrapping SNR phase for sandy soil

Contents

III.1 Introduction

Soil moisture measurements are very important observations for conducting climate studies, weather predictions, flood zone analyses, sustainable agriculture and aquifer recharge. In a farming environment, a real-time analysis of soil moisture conditions would enable the farmer to optimize the management of his plots (tillage, treatments, irrigation, etc.). The different current measurement techniques *e.g.* InSAR satellite measurement, *in-situ* probe, thermal imagery all have different characteristics in terms of spatial resolution (i.e., the ability of a sensor to discern a detail, or, in other words, the smallest area represented by a measurement), resolution (i.e., the repeatability of the measurement) and precision (i.e., the quality of the measurement performed). The optimization of one of these three parameters is unfortunately often to the detriment of the other two.

Thus, the conventional moisture probes provide only punctual measurements (few cm^3) and very heterogeneous, not representative of a whole plot. On the other hand, the precision is rather good (for example, for Theta probes, the predicted accuracy is 2% soil moisture volume with soil-specific standards), and measurements can be made continuously. With the advent of remote sensing techniques, soil moisture can be measured on a global scale, but this time to the detriment of temporal and spatial resolution. For example, even with the SMOS mission: Soil Moisture and Ocean Salinity satellite (Kerr et al., 2010), the repeatability is 3 days maximum at the equator and the side of a surface element is on average 43 km, for active radar satellite like COSMO-SkyMed the ground resolution is close to few meters (depending on acquisition mode) with a temporal resolution of 12h to few days.

Alternatively, recent studies suggested to take advantage of opportunity signals like the electromagnetic waves, continuously emitted by the Global Navigation Satellite System (GNSS) satellite constellations (GPS, GLONASS, Galileo, etc.), to retrieve different geophysical parameters of the Earth surface, which presents an excellent compromise between spatial, temporal and precision resolutions. This opportunistic remote sensing technique, known as GNSS Reflectometry (GNSS-R), is based on the analysis of the GNSS waves that are received by an antenna after reflection on the Earth's surface so-called multipath signals (Darrozes et al., 2016; Roussel et al., 2015a). Most of these applications was applied for the studies of the soil with rich content of clay. For example, the using of the single antenna SMIGOL reflectometer, Rodriguez-Alvarez et al. (2011a) announce an accuracy of 2.0% - 3.2%. The spatial resolution is only a function of the antenna height above the reflection surface (for a given satellite constellation over a defined time interval). An area around the antenna from a few meters to several kilometers will be covered. As for temporal resolution, it depends very much on the computational algorithm used to estimate moisture variations, but it is usually several hours or even days (*e.g.*, Larson et al. (2008b); Chew et al. (2014)).

This technique has applied in many applications for retrieving soil moisture variations

with very good results such as: An algorithm for soil moisture estimation using GPS-interferometric reflectometry for bare and vegetated soil (Chew et al., 2016) and only for low elevation angle 2° until 40°; Detection of Soil Moisture Variations Using GPS and GLONASS SNR Data for Elevation Angles Ranging From 2° to 70° for agricultural plot (Roussel et al., 2016) that increase the continuity of the obtained time series where I start my first study; Use of reflected GNSS SNR data to retrieve either soil moisture or vegetation height from a wheat crop (Zhang et al., 2017) where I develop a new algorithm for vegetation growth. All these studies shown the good results for soil moisture retrieval, but mostly was for the study case of the agriculture plot, bare or the grounds with rich clay content.

In the US, PBO H20 network effectively implemented this SNR technique and daily processes a set of permanent GNSS stations to provide soil moisture estimates (and also vegetation or snowfall indices). This network (`http://xenon.colorado.edu/portal`) is fully operational and is currently analyzing more than 133 stations dedicated to the estimation of soil moisture (*The GPS Reflections Research Group* - Kristine M. Larson and Eric E. Small).

In my dissertation, I am especially interested in this GNSS-R algorithm with the incorporation of special unwrapping phase techniques to recover the surface soil moisture of a sandy area or for vegetation growing. It is very important to study the water cycle in general and to measure the soil moisture content of riverine areas (i.e. riversides, beaches, desert or arid) in particular. Therefore, I have experimented with this new method for volleyball ground experiments to test the feasibility of the method and to apply the sandy soil moisture study.

This combined algorithms will be applied in natural case of Dahra (Kolda region, Senegal) where one can find sandy soil associated with low vegetation cover. And it is also the subject of my article:

"Unwrapping SNR phase method for soil moisture retrieval: experimental (Toulouse) and study case of Dahra (Senegal)", (Minh-Cuong Ha, José Darrozes, Manuela Grippa, Eric Mougin, Guillaume Ramillien, Muriel Llubes, Frédéric Frappart, Grégory Dufréchou, Phuong-Lan Vu, Frédéric Baup and Laurent Kergoat).

This zone shows very substantial differences compared to usual sites due to the influence of the West African Monsoon (WAS) climate (Fig. III.2): the soil consists of a high content of sand (>80%), variation in soil moisture has a significant impact on precipitation dynamics, surface temperature, and groundwater supply. The area has two main seasons, the rainy season (June-October) with few hundred millimeters and dry season with high temperature (20°-45°) conducive to a strong evaporation. We demonstrate that, in this case, L wave penetrate deep into the ground during dry period and strongly reduce the interest of GNSS-R moisture measurements. But, thankfully, using phase unwrapping method, it is possible to retrieve a correct and efficient measurement

of the soil moisture and obtain a very good temporal monitoring for a spatial resolution directly correlated to the antenna height.

III.2 Objective

The objective is to demonstrate that previous GNSS-R algorithms based on a single geodetic antenna/receiver and a method of the unwrapping phase to recover the surface moisture in area where the observed surface height change i.e. i) on an area covered with vegetation (vegetation growing change the height of reflecting surface) in Lamasquere (near Toulouse city) or ii) on sandy soil (wave penetration depends on the soil moisture and induce a change in height) in an experimental volley playground (University Paul Sabatier, Toulouse) to validate the unwrapping technique and in a real complex case in Dahra (Sénégal). Results obtained from the total of the different GNSS constellations will be used for unwrapping, as well as combined into single time series, and comparing them to independent soil moisture records made by Theta Probe Sensors used as validation.

III.3 GNSS R - SNR data for detecting soil moisture

III.3.1 Observation Sites

III.3.1.1 The Lamasquère experiment

This site is located in the south-west of France (43°29'14.45"N; 1°13'44.11"E), close to the Toulouse city, where a Leica GR25 receiver and an AR10 antenna were installed in a soya/wheat field with rich clay content (Fig. III.1).The study was published in the Hydrology and Earth System Sciences Journal: *"Use of reflected GNSS SNR data to retrieve either soil moisture or vegetation height from a wheat crop"* (Sibo Zhang, Nicolas Roussel, Karen Boniface, Minh Cuong Ha, Frédéric Frappart, José Darrozes, Frédéric Baup, and Jean-Christophe Calvet (2017)).

III.3.1.2 Volley playground experiment

This simple experimental site was used to develop a specific algorithm for sandy soil where the physics of wave penetration is quite different than areas with rich clay content commonly used for GNSS-R. In this type of soil GNSS waves are strongly attenuate and don't penetrate in the ground. For clay soil, the retrieved moisture is superficial (less than 5cm of penetration depth). The experiment took place in the framework of the MISTRALE project. The soil contains 100% of sand. It consists of small grains ranging between 0.3 and 0.5 mm in diameter. To monitor soil moisture variations of the beach volley field, one ML3 Theta Probe Sensors (accuracy of ± 0.01 $m^3.m^{-3}$) were

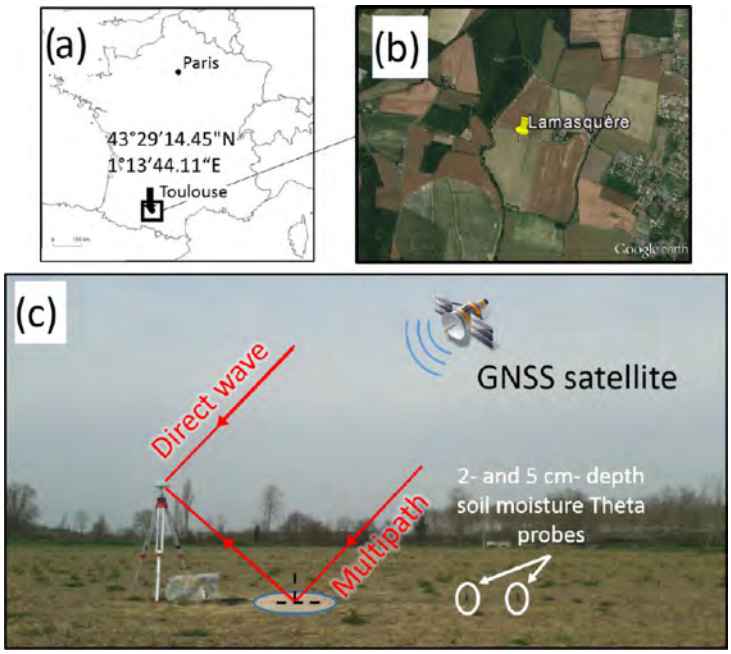

Figure III.1 – (a) Measurement site is located in Lamasquère, in the south-west of France. (b) Leica GR25 receiver and AR10 antenna were installed in a soya field in the country side (c) along with two theta probes. Note that during winter, the surface of the field is a bare soil.

installed at 7 cm depth, 1 meter away from the LEICA GR25 GNSS receiver (Fig. 4d, § III.4). Acquisitions were recorded every 5 minutes. These data have been used to validate SNR-based estimations of soil moisture fluctuations. The AR10 GNSS antenna was installed in the center of a 25x30 m² beach volley field (43°33'46.93" N; 1°28'16.57" E) at the University Paul Sabatier, located in Toulouse, France (Fig. 4a, § III.4). GPS L_1, L_2 (S1C, S2W) and GLONASS L_1 (S1C) frequencies were continuously acquired during 3 days of rainy weather, from 25th to 27th April 2015 at 1 Hz sampling frequency. Antenna height above the ground surface, determined with a tape meter, was 4 m. The 3D geometry was determined during a survey by Ground Penetrating Radar (GPR) with a 500 MHz antenna: mean sand thickness is $\sim$ 70 cm, and depth ranges between 35 cm and 1.10 m (see Fig. 4b, § III.4).

III.3.1.3 Dahra Experiment

This zone of the Dahra experiment is located in Senegal (Western Africa), under the influence of the West African Monsoon (WAS) climate (Fig. III.2): the soil consists of a high content of sand (>80%), variation in soil moisture has a significant impact on precipitation dynamics, surface temperature, and groundwater supply. The area has two main seasons, the rainy season (June-October) with few hundred millimeters and dry season with high temperature (20°-45°) conducive to a strong evaporation. The station

is equipped with two soil temperature sensors T_1 (5 cm depth), T_2 (10 cm depth) and three ML3 Theta Probe Sensors (moisture accuracy of ± 0.01 $m^3.m^{-3}$), installed at 5 cm, 10 cm and 100 cm depth (Fig. 7 in § III.4). Acquisitions were recorded with a sampling frequency of 15 min. Figure 7b (see § III.4) shows the evolution of soil moisture measured during the transition between wet to dry season in October, which corresponds to the SNR acquisition, the 5 cm depth soil moisture ranged from 2,91% to 4,38% VSM, the 10 cm ranged from 3,68% to 4,75% VSM and the 1 m ranged from 5,50% to 5,64% VSM. A Leica GR25 receiver with an AR10 antenna, were installed in a grazed range land in Dahra, Senegal (15°24'5.36"N; 15°26'0.13"W; see Figure 5a, b in § III.4). The antenna height H0 above the ground surface, determined with a tape measurement, is equal to 1.61 m. The ground around the antenna is considered as flat with a very low roughness. The soil moisture measurements for validation purpose is monitored by a soil moisture station, located 600 m from the antenna (15°23'48.79"N, 15°26'9.35"W; see Figure 5b in § III.4). L_1, L_2, L_5, and GLONASS L_1 and L_2 frequencies were continuously acquired from the 1st of October 2016 to the 31th of December 2016 at a 1-Hz frequency, in the transition period from rainy to dry season. In our study, we use all SNR signal strength on L_1, L_2 and L_5 C/A channels. We demonstrate that, in this case, L wave penetrate deep into the ground during dry period and strongly complicate the GNSS-R moisture measurements. But, thankfully, using phase unwrapping method, it is possible to retrieve a correct and efficient measurement of the soil moisture and obtain a very good temporal monitoring for a spatial resolution directly correlated to the antenna height (see § III.4).

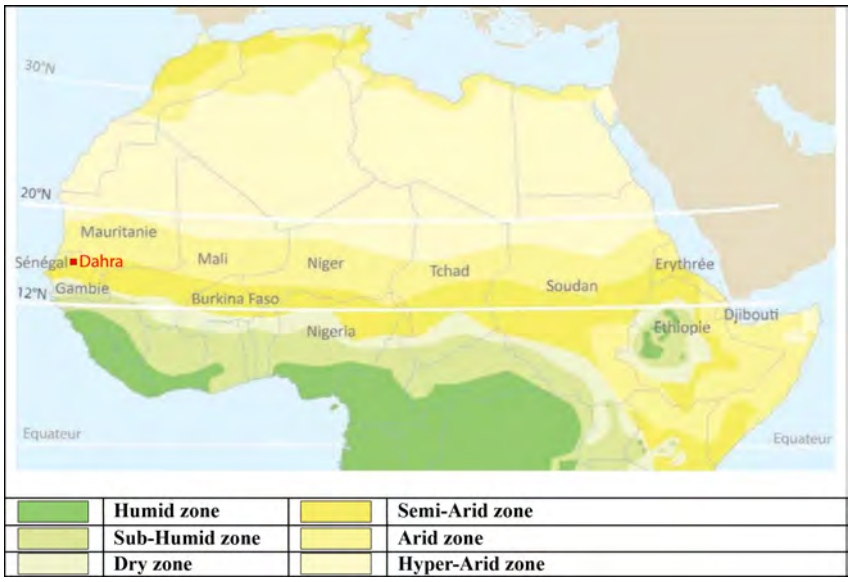

Figure III.2 – West African Monsoon climate and location of Dahra (Senegal) experiment in the Arid zone, western part of Sahelian region (Africa).

III.3.2 Soil moisture retrieval

During my thesis, we experimented the GNSS-R methodology to prove that it is adapted to other types of surface: i) area covered by vegetation; ii) soils with rich sand content. Results of Lamasquère experiment was published in the IEEE Journal of Selected Topics in Applied Earth Observations and Remote Sensing (JSTARS):

"Detection of Soil Moisture Variations Using GPS and GLONASS SNR Data for Elevation Angles Ranging From 2° to 70°", (Nicolas Roussel, Frédéric Frappart, Guillaume Ramillien, José Darrozes, Frédéric Baup, Laurent Lestarquit, and Minh Cuong Ha (2016)).

The aim of this study is to demonstrate that previous GNSS-R algorithms based on a single geodetic antenna and receiver to recover the surface moisture of a bare soil can significantly be improved for new environments and can be used to monitor vegetation growth (Zhang et al., 2017). Three different parameters can be computed from the multipath contribution to SNR: the amplitude A_m, the phase Φ_m, and the frequency f. The frequency f is used to retrieve the vertical height h of the antenna above the reflecting surface (eq. II.37,II.38). Results obtained from the different GPS satellites will be compared between them, as well as combined into single time series. Previous studies (*e.g.* Larson et al. (2008a); Chew et al. (2014)) filtered out SNR data from high satellite elevation angles (>30°) as they considered the respective multipath contribution to SNR insufficient to be detected. In the present study, two ranges of satellite elevation angles are tested: the first one from 2° to 30° (noted I_{2_30}) and the second one from 30° to 70° (noted I_{30_70}). We avoid satellites with high elevations because in this case the multipath is highly mitigated by the antenna and cannot be measured with our method. Results of both ranges of elevation angle will be compared and then combined into a single observable.The independent soil moisture records made by ML3 ThetaProbe Sensors used as validation.

$A^i_m(t)$, $\Phi^i_m(t)$, and $h^i(t)$ were computed for each GPS satellite i more than 1.5 months differentiating the two ranges of elevation angles I_{2_30} and I_{30_70}, as well as the ascendant and descendant phases of the satellite passages. Theoretically, for different time series of A^i_m, Φ^i_m, and h^i can thus be derived from each satellite i over the whole period of measurement. Linear correlation coefficients R are estimated between each SNR-based time series and the variations of soil moisture (P_{2cm} and P_{5cm} depth). Variations of soil moisture are scaled with respect to the minimum and maximum of the SNR-based time series A_m, Φ_m, and h that they are compared with.

As for the results:

- Satellite GPS-PRN32 was the one giving the best correlation, R equal to 0.97 with P_{2cm} and 0.95 with P_{5cm} (Fig. III.3a). $\Phi^{PRN32}_{m-I_{30\_70}}(t)$ has the inverse relationship with soil moisture, R equal to -0.87 with P_{2cm} and -0.84 with P_{5cm} (Fig. III.3b).

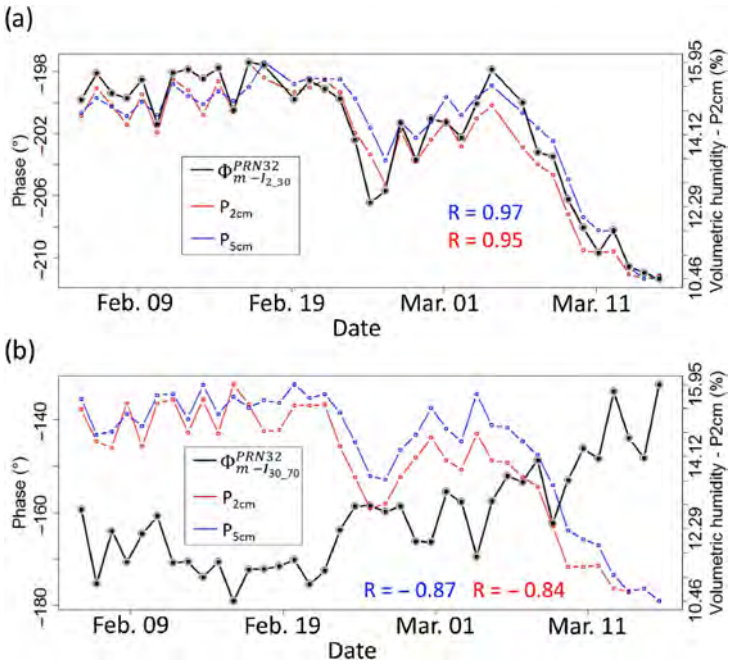

Figure III.3 – Evolution of Φ_m time series estimated from GPS constellation on PRN 32 for (a) low satellite elevation I_{2_30} and (b) high satellite elevation I_{30_70} with respect to volumetric soil moisture recorded by Theta probe at the depth of 2 cm (P_{2cm})and 5 cm (P_{5cm})time series. Note the inverse relationship between $\Phi^{PRN32}_{m-I_{30\_70}}(t)$ and soil moisture (b).

- Best results are obtained with $\Phi^{i}_{m-I_{2\_30}}$, computed from all the GPS satellites i, with a mean value of R ranging from 0.81 (P_{5cm}) to 0.84 (P_{2cm}). $A^{i}_{m-I_{2\_30}}$ gives the worst results with a mean value of R ranging from -0.32 (2cm depth) to -0.37 (5cm depth) and results for $h^{i}_{I_{2\_30}}$ are equal to -0.57 for both 2cm and 5cm. As already mentioned by Chew et al. (2014), $A^{i}_{m-I_{2\_30}}$ and $h^{i}_{I_{2\_30}}$ are anti-correlated with soil moisture, while $\Phi^{i}_{m-I_{2\_30}}$ is correlated.

To conclude:

⇒ SNR based on the IPT with a single geodetic antenna can perfectly be used to retrieve the main periods of the moisture variations of the surrounding rich clay content soil consist. The accuracy of estimated variations in surface soil moisture is equal to $\sim$ 6% of the soils consists of 18% of sand, 41% of clay, and 41% of silt (according to averages of five samples taken around the antenna), and field capacity is 48%.

⇒ Φ_m is well correlated with volumetric soil moisture (%) when A_m and h gives bad correlation due to the fact that it's disturb by vegetation content, ground roughness.

⇒ The soil moisture determination using IPT can be applied not only base on the low satellite elevation angles θ, but it's also possible to include high satellite elevation

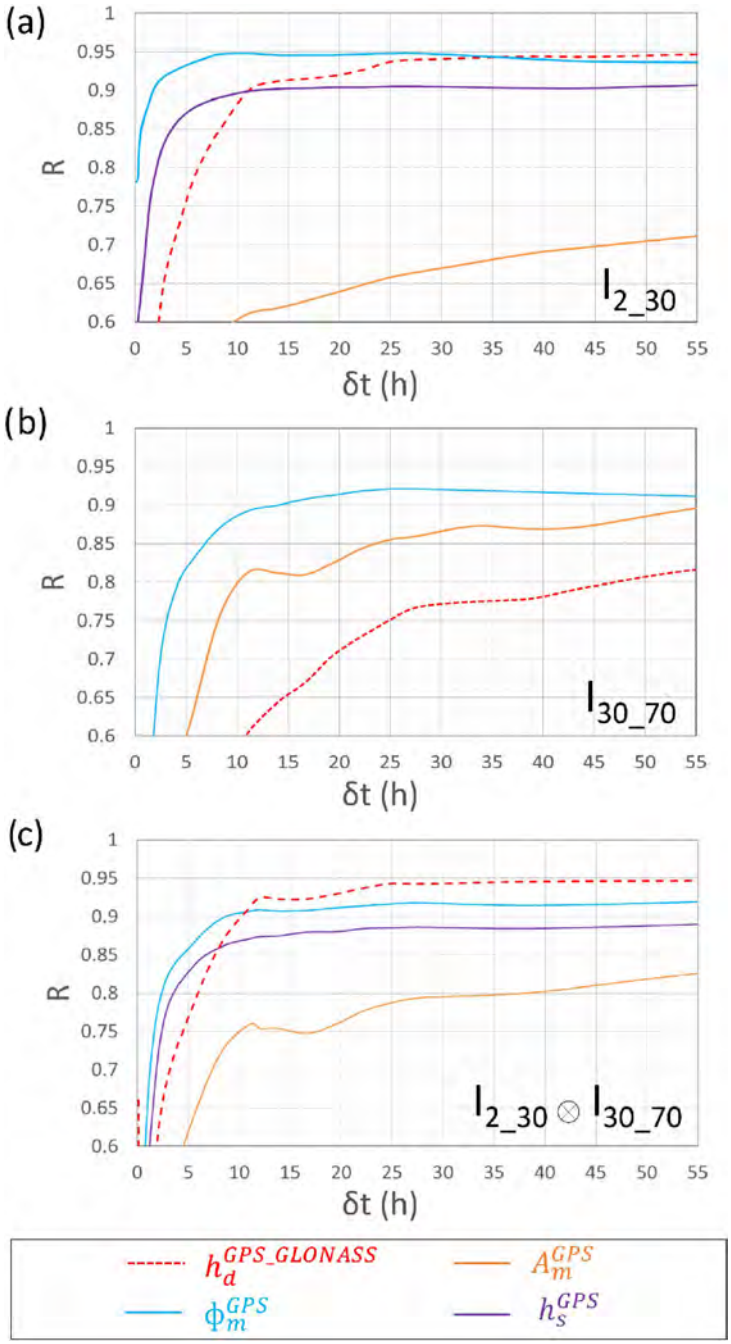

Figure III.4 – (Absolute) Linear correlation coefficient R between A_m^{GPS}, Φ_m^{GPS}, h^{GPS}, and $h^{GPS+GLONASS}$ vs Theta probe P_{2cm}, considering (a) low satellite elevation I_{2_30}, (b) high satellite elevation I_{30_70}, and the combination of $I_{2\_30} \otimes I_{30\_70}$.

angles θ in the computation, with attention to the sign of the correlation with soil moisture. The sign of the correlations is reversed when considering high satellite elevation angles. The cut-off angle where the sign of the correlation between the three metrics and soil moisture variations changes seems to be $\sim$30°. This can be explained by the combined effect of 1) the reflection coefficients of the RHCP and LHCP components (which depends on the satellite elevation angles) and 2) the antenna gain pattern which will reject, at some level, the RHCP and LHCP components (also depending on the satellite elevation angles).

III.3.3 Relation between soil moisture and vegetation height retrieval

In the previous section, we have shown the potential of GNSS-R and SNR technique for detecting soil moisture for bare soil consist of rich clay content. But if the ground is under significant vegetation effects, can soil moisture be retrieved? What is the relation between soil moisture and vegetation height retrieval? The subsequent modeling studies Chew et al. (2015) showed that the vegetation canopies affected the SNR modulation pattern. They showed that vegetation growth tended to trigger a decrease in the SNR amplitude. Because the vegetation effects tended to perturb the soil moisture retrieval, Chew et al. (2016) proposed an improved algorithm for soil moisture retrieval in vegetated environments, which used the amplitude decrease extent to decide when vegetation influence was too large. They used a model database for the SNR of the L2C signal to remove the most significant vegetation effects for the sites they considered in western USA. Small et al. (2016) further compared different algorithms of GNSS-IR soil moisture retrieval in the presence of vegetation. Using data from a field study, Wan et al. (2015) showed that the amplitude of the SNR data presented a good linear relationship with the vegetation water content (VWC), but it was restricted to VWC values of less than $\sim 1 kg.m^{-2}$.In addition to the amplitude of the SNR data, it was also possible to infer VWC by the $MP1_{rms}$ index, which is a linear combination of L1 and L2 carrier phase data and L1 pseudo-range data (Small et al., 2010), and by the NMRI (Normalized Microwave Reflection Index) which is derived from the $MP1_{rms}$ (Small et al., 2014; Larson and Small, 2014).

Following those studies, we also have an experiment to see the potential of GNSS-R and SNR data to retrieve either soil moisture or vegetation height from a wheat crop in the same field in Lamasquère. In this study, The least square estimation method proposed by Larson et al. (2008a) is used to estimate the multipath amplitude (A_m) and multipath phase (Φ_m) from the multipath SNR data. Then, Φ_m can be used to estimate the soil moisture changes (Chew et al., 2016). A vegetation-height retrieval algorithm is proposed using the SNR-dominant period (the peak period in the average power spectrum derived from a wavelet analysis of SNR). Soil moisture and vegetation height are retrieved at different time periods (before and after vegetation's significant growth). The retrievals are compared with two independent reference data sets: *in-situ* observations of soil moisture and vegetation height, and numerical simulations of soil moisture, vegetation height and above-ground dry biomass from the ISBA (Interactions between Soil, Biosphere and Atmosphere) land surface model. In this study, the SNR GNSS-IR technique was used to analyze GNSS SNR data obtained with a single classical geodetic antenna receiver over an intensively cultivated wheat field in Lamasquère. The data were used to retrieve either soil moisture or relative vegetation height during the growing period of the wheat crop. The method proposed by Chew et al. (2016) was used to retrieve soil moisture. Moreover, we performed a wavelet analysis in order to

extract the dominant period of the SNR. We investigated to what extent vegetation height influenced the dominant period resulting from the wavelet analysis. The main justification for investigating the impact of vegetation height was that it impacted the relative antenna height (the distance from the antenna to the reflecting surface). Vegetation growth tended to decrease the relative antenna height and broke up the constant height assumption used in soil moisture retrieval algorithms. In this context, key objectives of this study were to (1) assess the soil moisture retrieval technique in either short or tall vegetation conditions and (2) retrieve vegetation height H along the wheat growth cycle.

TABLE III.1 – Soil moisture scores from 16 January to 5 March 2015. MAE is the mean absolute error, RMSE is the root mean square error and SDD is the standard deviation of differences.

	GPS vs. in situ	GPS vs. ISBA	GPS vs. in situ	GPS vs. ISBA	GPS (ϕ_{index}) vs. in situ	GPS (ϕ_{index}) vs. ISBA	ISBA vs. in situ
S ($m^3\ m^{-3}\ o{-}1$)	0.0148	0.0148	0.0033	0.0033	–	–	–
N	47	43	47	43	47	43	43
MAE ($m^3\ m^{-3}$)	0.036	0.034	0.011	0.018	0.007	0.009	0.009
RMSE ($m^3\ m^{-3}$)	0.046	0.041	0.014	0.022	0.009	0.012	0.010
SDD ($m^3\ m^{-3}$)	0.036	0.037	0.009	0.012	0.008	0.011	0.006
Mean bias ($m^3\ m^{-3}$)	0.029	0.019	−0.010	−0.018	0.003	−0.005	0.008
R^2	0.73	0.63	0.73	0.63	0.74	0.65	0.88

Main results:

- Soil moisture retrieval: The surface soil moisture retrievals obtained from 16 January to 5 March 2015, together with independent *in-situ* VSM observations and ISBA simulations (III.5). The GPS and ISBA scores are given in table III.1. The mean soil moisture values during the experimental period are 0.27, 0.28, 0.31, 0.26, and 0.28 m^3m^{-3} for *in-situ* VSM measurements, ISBA simulations, GPS retrievals with S=0.0148 m^3m^{-3o-1}, GPS retrievals with S=0.0033 m^3m^{-3o-1}, and GPS retrievals from the scaled soil wetness index, respectively. The adjusted S value is the mean of slope values obtained for satellite tracks whose phase presented a linear correlation with *in-situ* soil moisture higher than 0.9. This occurred for the ascending tracks of GPS 13, 21, 24 and 30 and for the descending tracks of GPS 05, 09, 10, 15 and 23.

  The GPS VSM daily mean retrievals based on the Chew et al. (2016) method present a good agreement with both *in-situ* observations and ISBA simulations: MAE (mean absolute error) and RMSE (root mean square error) are lower than 0.05 m^3m^{-3}, and SDD (standard deviation of differences) does not exceed 0.04 m^3m^{-3}

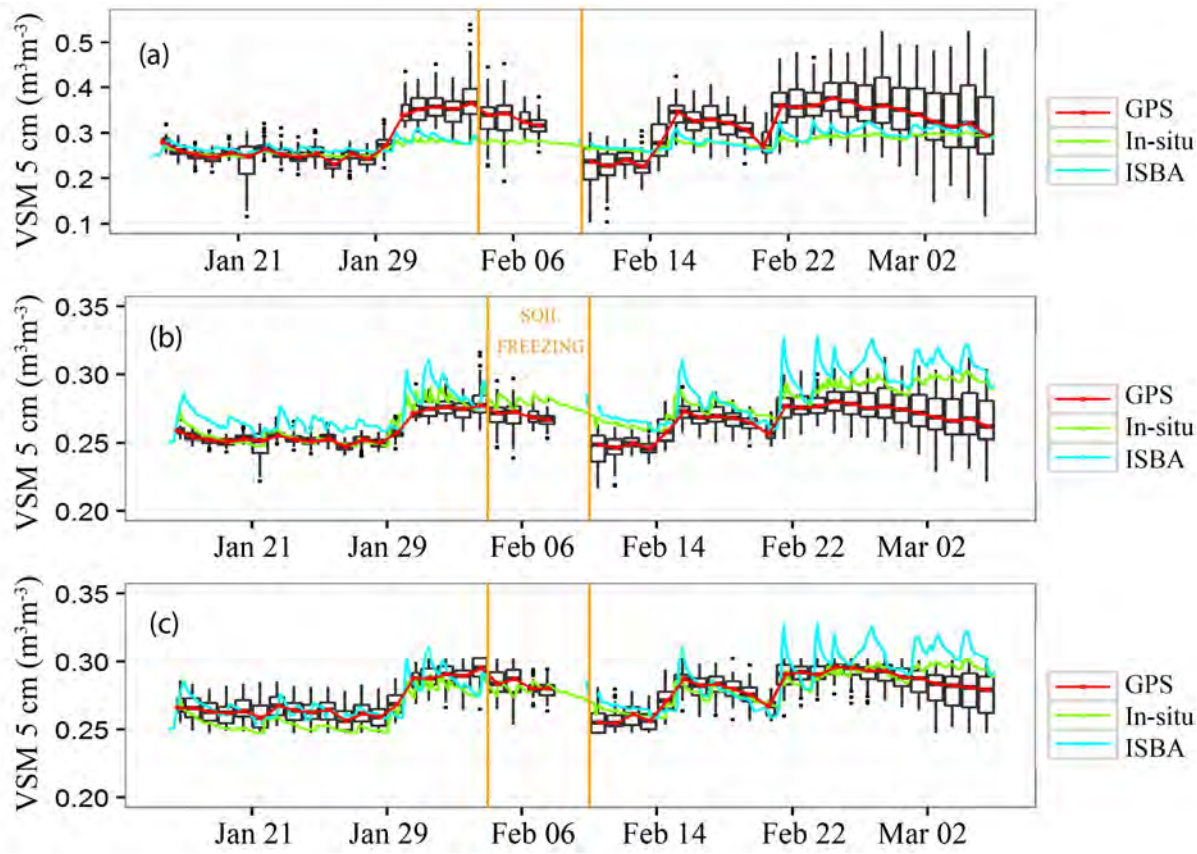

Figure III.5 – *In-situ* surface volumetric soil moisture (VSM) observations at 5 cm depth (green line), ISBA simulations (blue line) and median of the daily GPS retrievals (a) with the a priori slope (S=0.0148 m^3m^{-3o-1}) (red line), (b) with a locally adjusted slope (S=0.0033 m^3m^{-3o-1}) (red line) and (c) from scaled soil wetness index (red line), and their daily statistical distribution (black box plots) for all available satellite tracks from 16 January to 5 March 2015. Boxes: 25–75% percentiles; bars: maximum (minimum) values below (above) 1.5 IQR (Inter Quartile Range, corresponding to the 25–75% percentile interval); dots: data outside the 1.5 IQR interval. The ISBA simulations indicate soil freezing (i.e., the presence of ice in the top soil layer) from 4 to 9 February.

(Table III.1). The errors are reduced by at least 50% when the local adjusted slope is used. When the scaled soil wetness index is used, the errors are further reduced.

We also compared the retrievals with the independent ISBA simulations. The ISBA model VSM simulations present a better agreement with the *in-situ* VSM observations than the GPS retrievals, for all the scores, as shown by Table III.1 (last column) and figure III.5. In particular, R^2=0.88 for ISBA simulations, against R^2=0.74 for GPS retrievals. This shows that the ISBA simulations can be used as a reference to assess local GPS retrievals for this site. The statistical scores resulting from the comparison between the GPS retrievals and the simulations are similar to those based on *in-situ* observations.

- Vegetation height retrieval: The retrieved vegetation height obtained from 16 January to 15 July 2015, together with seven *in-situ* vegetation height measurements, the moving average of the GPS height retrievals computed using a centered gliding window of 21 days, and daily vegetation height simulations by ISBA (Fig. III.6). The differences between the relative vegetation height retrievals and *in-situ* height observations is shown in table III.2.

  In the figure III.6 shows that the retrieved vegetation height is related to the simulated above-ground dry biomass of the wheat (dark red line). We found a linear relationship between the moving average height from GPS retrievals and the above-ground dry biomass simulated by the ISBA model from 10 March to 29 May 2015 (when the maximum vegetation height, 1 m, was measured), during the time period from tillering to flowering. The correlation coefficient R between the moving average height and the above-ground dry biomass, with 81 observations, was equal to 0.996.

From the obtained results, we demonstrated that:

⇒ Changes in soil moisture mainly affect the multipath phase of the SNR data (assuming the relative antenna height is constant) with little change in the dominant period of the SNR data, whereas changes in vegetation height are more likely to modulate the SNR-dominant period.

⇒ Over a wheat field the vegetation gradually replaces the soil as the dominant reflecting surface when plant height becomes comparable to, or larger than, one wavelength. Or, we can say that the surface volumetric soil moisture can be estimated (R^2 = 0.74, RMSE = 0.009 m^3m^{-3}) when the wheat height is smaller than one wavelength (∼19cm on GNSS band L_1).

⇒ The quality of the estimates markedly decreases when the vegetation height increases. This is because the reflected GNSS signal is less affected by the soil. When

TABLE III.2 – Vegetation height retrievals from GPS and simulations from ISBA, and their relative deviations for each *in-situ* height observation. The phenological statuses are derived from the GDD (Growing Degree Days) model.

Dates (year 2015)	Phenological status	In situ height (cm)	GPS height (cm)	ISBA height (cm)	In situ–GPS (cm)	In situ–ISBA (cm)
20 January	–	10	18.4	15.4	−8.4	−5.4
10 March	–	20	15.7	14.5	4.3	5.5
12 March	tillering	–	15.5	15.6	–	–
30 March	–	35	40.4	24.6	−5.4	10.4
24 April	–	55	65.3	70.0	−10.3	−15.0
19 May	–	97	102.9	100.0	−5.9	−3.0
29 May	–	100	101.7	100.0	−1.7	0.0
31 May	flowering	–	102.4	100.0	–	–
3 June	ripening	–	101.9	100.0	–	–
18 June	–	39	40.5	100.0	−1.5	−61.0

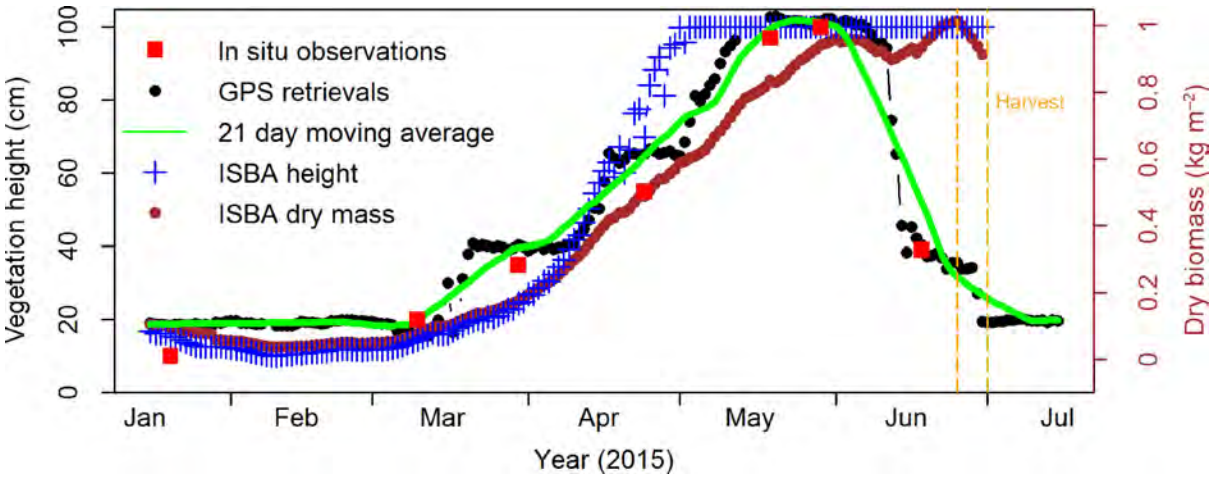

Figure III.6 – Wheat canopy height from 16 January to 15 July 2015 derived from GPS SNR data (black dots), from *in-situ* observations (red squares), and from ISBA simulations (blue crosses). The green line represents the moving average of the GPS retrievals, computed using a centered gliding window of 21 days. Wheat above-ground dry biomass simulated by the ISBA model is indicated by dark red dots.

vegetation replaces soil as the dominant reflecting surface, a wavelet analysis provides an accurate estimation of the wheat crop height (R^2=0.98, RMSE=6.2cm). The vegetation height retrievals are sensitive to changes in plant height of at least one wavelength.

⇒ Wheat growth gradually raised the reflecting surface of the GNSS signal, from the soil surface to the vegetation surface, which significantly modulated the dominant period of the multipath SNR data. In these conditions, vegetation effects could not be ignored and soil moisture could not be retrieved.

III.4 Article - Monitoring of soil moisture dynamics in sandy areas using the unwrapping phase of GNSS-R

Following two previous experiments in section III.3, GNSS-R algorithms based on a single geodetic antenna/receiver appear as a powerful tool for retrieving soil moisture variations and even vegetation height in the case of rich clay content. In this section, I would like to propose the new algorithm which allow to detect soil moisture for sandy soil using GNSS-R SNR data called Unwrapping SNR phase method. And this is also the title of the article I am preparing to post on the journal of the Remote Sensing :

"Monitoring of soil moisture dynamics in sandy areas using the unwrapping phase of GNSS-R", (Minh-Cuong Ha, José Darrozes, Manuela Grippa, Eric Mougin, Guillaume Ramillien, Muriel Llubes, Frédéric Frappart, Grégory Dufréchou, Phuong-Lan Vu, Idrissa Guiro, Håkan Torbern Tagesson, Frédéric Baup and Laurent Kergoat).

The aim of this article is to demonstrate that previous GNSS-R algorithms based on a single geodetic antenna/receiver and a method of the unwrapping phase to recover the surface moisture of a sandy soil. The method is based on the analysis of the SNR data routinely collected by a geodetic antenna. SNR data incorporate both direct and reflected signals. These latter interact with the ground while reflecting. Variations of the nature of the surface is likely to modify the properties of the reflected waves, hence dependence of SNR on soil moisture content. Three different parameters are under study: the phase, and the frequency of the multipath contribution to SNR which is directly linked to the antenna height above the reflecting surface (Löfgren, 2014). Results obtained from the total of the different GNSS satellites will be used for unwrapping, as well as combined into single time series, and comparing them to independent soil moisture records made by Theta Probe Sensors used as validation.

Monitoring of soil moisture dynamics in sandy areas using the unwrapping phase of GNSS-R

*Minh-Cuong Ha[1], José Darrozes[1], Manuela Grippa[1], Eric Mougin[1], Guillaume Ramillien[1], Muriel Llubes[1], Frédéric Frappart[1], Grégory Dufréchou, Phuong-Lan Vu[1], Idrissa Guiro[2], Håkan Torbern Tagesson[3], Frédéric Baup [1]and Laurent Kergoat[1].

1- Géosciences Environnement Toulouse, 14 avenue Edouard Belin, 31400 Toulouse, France.
2- Institut de Sciences de l'Environnement, UCAD, Dakar, Sénégal.
3- Department of Geography and Geology, University of Copenhagen, Denmark.

*Corresponding author: Minh-Cuong Ha, Géosciences Environnement Toulouse, 14 avenue Edouard Belin, 31400 Toulouse, France (cuonghm.rsc@gmail.com).

Key Points

- Global Navigation Satellite System Reflectometry (GNSS-R) based on a single geodetic antenna/receiver and a method to unwrap SNR phase is efficient to retrieve surface moisture on sandy soils.
- Opportunistic remote sensing technique, Interference Pattern Technique (IPT), for analyzing Signal-to-Noise Ratio (SNR) of the GNSS-R allows monitoring small surface soil moisture variations

Abstract

With population growth, water demand is expected to tremendously increase in the next decades. The optimization of water allocation for agriculture requires soil moisture monitoring. Recent studies suggested to take advantage of continuously emitted navigation signals by the Global Navigation Satellite System (GNSS) constellations, to retrieve soil moisture variations. This active remote sensing technique, known as GNSS Reflectometry (GNSS-R), consists in comparing the interference of reflected waves by the ground and those which come directly from satellites. It offers a wide range of applications in Earth sciences and particularly in soil moisture monitoring, this technique has shown their efficiency for soil with high clay content. It namely presents the advantage of sensing a whole surface around a reference GNSS antenna. In this article, we focus on soil moisture monitoring in sandy areas. The first study site, the soil

contains 100% of sand in the beach volley field, located at the University Paul Sabatier in Toulouse, France. And the second one is the Dahra field site in the Ferlo region, Senegal, located in the Sahelian ecoclimatic zone. The soil is sandy luvenic aerosol with 95 % sand. We demonstrated that, in Dahra, the waves of the GNSS signals penetrate deep into the ground surface during dry period and strongly reduce the interest of GNSS-R moisture measurements. But, thankfully, using a phase unwrapping method, it is possible to retrieve a correct (comparing to the *in situ* measurements, the correlation R can reach up to 0.86 on the experimental beach volley field and up to 0.91 in Dahra field) and efficient estimate of the soil moisture at 0.1m ÷ 0.5m depth and obtain a very good temporal monitoring with the benefit of a spatial resolution directly correlated to the antenna height.

Keywords: GNSS-R, SNR, IPT, Unwrapping phase, Soil moisture

1. Introduction

Water resource management is a key issue worldwide as water resources become increasingly vulnerable as a result of escalating demand arising from population growth, the need for increased food production, expanding industrialization due to rising living standards, pollution due to various anthropogenic activities, and climate change impacts. It is also important for irrigation management [Zhang et al., 2017] and flood prediction [Rodriguez-Iturbe and Porporato, 2007]. In the Sahelian regions, where the water resources are limited, it's management is of prime importance [McDonald, et al., 2014]. In many Sahelian countries like Mali, Chad, or Senegal, water resources essentially come from groundwater reservoirs that are either low- or non-renewable. There is no clear consensus whether this groundwater is or is not heavily dependent on soil moisture (SM) variations (Lopez et al. 2016; Mougin, et al., 2009; Lebel, et al., 2009; Fatras, et al., 2012) partly due to lack of SM data and a partly because it is a very complex hydrological phenomenon.

Soil moisture measurements are very important observations for conducting climate studies, weather predictions, flood zone analyses, sustainable agriculture and aquifer recharge. In a farming environment [Roussel et al., 2016; Zhang et al., 2017; Zhang et al., 2018], a real-time analysis of SM conditions would enable the farmer to optimize the management of his plots (tillage, treatments, irrigation, etc.). The existing measurement techniques (e.g. InSAR satellite measurement, in situ probe, thermal imagery) all have different characteristics in terms of spatial resolution (i.e., the ability of a sensor to discern a detail, or, in other words, the smallest area represented by a measurement), temporal resolution (i.e., the repeatability of the

66 measurement) and precision (i.e., the quality of the measurement performed by the sensor).
67 Unfortunately, the optimization of one of these three parameters is often to the detriment of the
68 other two.
69 Thus, conventional moisture probes provide only punctual measurements (few cm^3) and
70 very heterogeneous, not representative of a whole plot/region. On the one hand, *in situ*
71 observations of soil moisture are accurate, have a high temporal resolution, but have a very low
72 spatial representativeness (e.g., Mougin et al., 2009). On the other hand, the precision is rather
73 good (for example, for Theta probes, the predicted accuracy is 2% soil moisture volume with
74 soil-specific standards), and measurements can be made continuously. With the advent of
75 remote sensing techniques, SM can be measured on a global scale, but this time to the detriment
76 of the temporal sampling (from a few measurements per day to a few per month) and spatial
77 resolution (from tens of m^2 to tens of km^2). For example, for the Soil Moisture Ocean Salinity
78 Satellite (SMOS) mission [Kerr et al., 2010], the repeatability is 3 days maximum at the equator
79 and the side of a surface element is on average 43 km. For active microwave sensors like
80 COSMO-SkyMed the ground resolution is close to a few meters (depending on the acquisition
81 mode) but the temporal resolution ranges from 12 h to a few days. In order to have a sustainable
82 water resource management, it is essential to improve our understanding of soil moisture
83 dynamics and how the surface soil moisture (SSM) is related with the ground water [*e.g.*
84 Archambault 1960; Aranyossy and Ndiaye 1993]. An important factor to improve this
85 understanding is through an improvement of moisture monitoring at local to intermediate scales
86 associated to high temporal resolution.
87 Alternatively, recent studies have suggested to take advantage of "opportunity signals"
88 like the electromagnetic waves, continuously emitted by the Global Navigation Satellite System
89 (GNSS) satellite constellations (GPS, GLONASS, Galileo, etc.). Different geophysical
90 parameters of the Earth surface can be retrieved, with an excellent compromise between spatial,
91 temporal and accuracy resolutions. This opportunistic remote sensing technique, known as
92 GNSS Reflectometry (GNSS-R), is based on the analysis of the GNSS waves that are received
93 by an antenna after reflection on the Earth's surface so-called "multipath signals" [Darrozes et
94 al., 2016; Roussel et al., 2015], and offers a wide range of applications in Earth sciences and
95 particularly in soil moisture monitoring. To date, these techniques have been mostly used to
96 retrieve the soil moisture of soils with rich content of clay. For example, using of the single
97 antenna SMIGOL reflectometer, Rodriguez-Alvarez et al. (2011) announce an accuracy of
98 2.0% - 3.2%. The spatial resolution is a function of the antenna height above the reflection
99 surface (for a given satellite constellation over a defined time interval). An area around the

antenna of a few meters to several kilometers will be covered by EM wave reflections. The temporal resolution strongly depends on the computational algorithm used to estimate moisture variations, but it is typically of several hours or days [*e.g.* Larson et al., 2008; Chew et al., 2014]. The technique is based on the interaction of GNSS signals that reflect on the ground and thus contain information on the characteristics of the reflective surface, particularly the water content in the first centimeters (2-5 cm) of soil. Antenna interference between the direct wave and the reflected wave is particularly noticeable in the Signal-to-Noise Ratio (SNR) recorded by the receiver. The variations in the nature of the surface and its properties modify the reflected GNSS signal, and therefore the SNR, which can then be analyzed to estimate soil moisture content. This estimation method has the major advantage of being easily applicable using any conventional GNSS antenna (especially those of existing permanent networks), without any new hardware modification.

This technique was successfully applied for soil moisture retrieval in a wide range of environmental conditions for bare and vegetated soil [Chew et al., 2015]. SNR from several constellations such as GPS and GLONASS have been used with satellite elevation angles ranging from 2° to 70° [Roussel et al., 2016]. Both soil moisture and vegetation height from a wheat crop have been derived by Zhang et al. (2017). All these studies were successful in retrieving soil moisture, but uniquely for the case of plots either 'bare soil' or with a rich clay content.

The aim of this study is to demonstrate that previous GNSS-R algorithms based on a single geodetic antenna/receiver and a method of the unwrapping phase can be used to recover the surface moisture of a sandy soil. The method is based on the analysis of the SNR data continuously collected by the geodetic antenna. SNR data incorporate both direct and reflected signals. Variations of the nature of the surface is likely to modify the properties of the reflected waves, hence dependence of SNR on soil moisture content. Two different parameters are under study: the phase, and the frequency of the multipath contribution to SNR which is directly linked to the antenna height above the reflecting surface [Löfgren, 2014]. Results obtained from the total of the different GNSS satellite constellation will be used for phase unwrapping and will be evaluated using independent soil moisture records made by Theta Probe Sensors.

Our study presents results from GNSS-R experiments performed in at the beach volley field in Toulouse (France) and the Dahra field site in the Ferlo region (Senegal) with a classical one antenna GNSS receiver over local area. These data sets, which provides the behavior of different parameters of the so-called Interference Pattern Technique (IPT) based on multipath Signal Noise Ratio (SNR). These different parameters correspond to Soil Moisture (SM), and

Effective Antenna Height (EAH). Section 2 highlights GNSS-R theory, Interference Pattern technic (IPT) and unwrapping method. Section 3 methodology. Section 4 presents the two experiments set-up. Section 5 shows main results of two experimental plots. Section 6 provides final discussions, and Section 7 points out the main conclusions.

2. Theory of GNSS-R

2.1 Recovery of soil moisture from SNR

a) GNSS direct and reflected wave polarization

The GNSS-R is generally considered as an opportunistic remote sensing technique based on the analysis of the electromagnetic waves continuously emitted by the GNSS constellations that are received by an antenna after reflection on the Earth's surface so-called MulTiPath (MTP) signals [Darrozes et al., 2016; Roussel et al., 2015; Figure 1a]. While major part of the emitted GNSS signal is received directly in the zenith-looking hemisphere of a geodetic antenna, a minor part of it comes from below the horizon, after one or several reflections in the surrounding environment (Figure 1c). These MTP signals interfere with the direct wave and affect the GNSS measurements recorded by the receiver by adding new intermediate frequencies known as MTP frequencies. Geodetic GNSS antenna use the polarization properties of the GNSS signals to filter out part of the reflected waves and reduce the contribution of the MTP which degrade the accuracy of the position determination [Braasch, 1996]. The Right-Hand Circular Polarization (RHCP; Figure 1c) of the GNSS direct waves is likely to change upon reflection depending on the nature of the reflector characterized by reflection coefficient and the incidence angle θ that corresponds to the satellite elevation (SE) angle. The reflected signal can be considered as the sum of these two circularly polarized signals; one that maintains the co-polarized (RHCP) component, and a cross-polarized characterized by a Left-Hand Circular Polarization: (LHCP in Figure 1a) one. For SE angle below a threshold value known as the Brewster angle [Brewster, 1815], the predominant signal component after reflection becomes cross-polar (LHCP), and hence the reflected wave is mainly LHCP with less RHCP content. Conversely, for elevation angles greater than the Brewster angle, the predominant signal component is the co-polar (RHCP), and hence the reflected wave has right-hand elliptical polarization [Alonso-Arroyo et al., 2014].

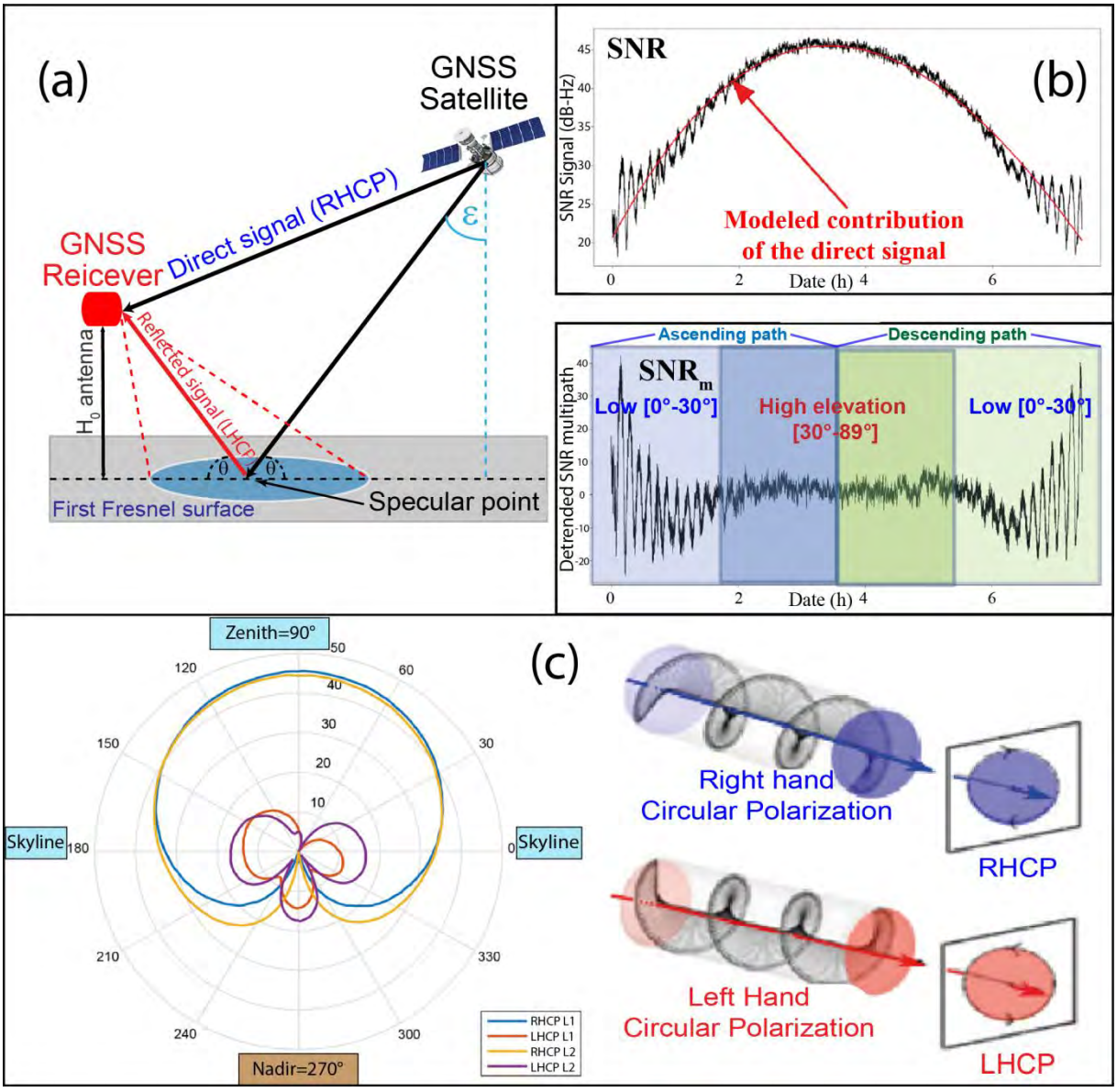

Figure 1 a) Interactions between GNSS electromagnetic waves and reflecting surface: GNSS measurements recorded by the receiver showing the direct path with RHCP of the GNSS waves and the reflected path with LHCP; b) SNR related to the addition of the powerful direct and weaker reflected GNSS signals in the receiving antenna and SNRm (multipaths) with the direct signal contribution is removed from the raw SNR profile, modified from [Roussel et al., 2015]; c) Antenna gain pattern for RHCP and LHCP for Leica AR10; modified from [Darrozes et al., 2016].

Following its reflection on the Earth's surface, the electromagnetic wave usually undergoes a polarization sign inversion and thus the majority of the scattered power goes into LHCP. However, the combined effects of roughness and geophysical properties of the surface are such as the signal from the right polarization can be significant and thus be used to determine geophysical properties of the surface. This results in a complex response that depends upon the RHCP components that are co-polar τ_0, and the LHCP cross-polar τ_x:

$$\tau_0 = \frac{\tau_h + \tau_v}{2}, \tau_x = \frac{\tau_h - \tau_v}{2} \quad (1)$$

These components (1) are based on vertical τ_v and horizontal τ_h reflection coefficients (2), which are functions of the surface reflection parameters:

$$\tau_h = \frac{sin(\theta)-\sqrt{\varepsilon-cos^2(\theta)}}{sin(\theta)+\sqrt{\varepsilon-cos^2(\theta)}} \ , \ \tau_v = \frac{\varepsilon sin(\theta)-\sqrt{\varepsilon-cos^2(\theta)}}{\varepsilon sin(\theta)+\sqrt{\varepsilon-cos^2(\theta)}} \qquad (2)$$

with the complex dielectric constant $\varepsilon = \varepsilon_r - j\frac{\sigma}{\omega\varepsilon_0}$, where ε_r is the relative permittivity, σ is the electrical conductivity of the reflection surface and ε_0 is the vacuum permittivity.

Classical GNSS geodetic antenna have a reduced LHCP gain (Figure 1b) to remove multipath effects for positioning application. GNSS antenna radiation pattern focuses the antenna gain for RHCP signals towards zenith and decreases the gain with decreasing elevation angle (Fig. 1c). These filtering techniques of GNSS antenna based on signal polarization affect the total received signal by reducing the amplitude of the reflected signals with respect to the direct signal amplitude. Fortunately for GNSS-R methods, real antenna quality is less than perfect and the energy of the reflected signal is not completely dampened [Roussel et al., 2016].

b) Interference Pattern Technique - IPT

The effect of multipath reflection clearly appears in the SNR measurements recorded by GNSS receivers on the different frequencies *i.e.* L1, L2, and L5 (Figure 1b). This interference creates oscillations whose frequency $\tilde{f}$ (Eq. 3) is a function of the sine of the SE angle, and can be modeled as follows [Roussel et al., 2015]:

$$\tilde{f} = \frac{4\pi}{\lambda}\left(\dot{h}\frac{\tan(\theta)}{\dot{\theta}} + h_{eff}\right) \qquad (3)$$

with h_{eff} being the effective antenna height above the reflecting surface. The term "effective" means the antenna height is measured with a part of penetration in the soil, θ the SE angle and λ the signal wavelength, $\dot{h} = dh/dt$ is the vertical velocity of the reflecting surface in m/s and $\dot{\theta} = d\theta/dt$ the elevation angle velocity. When h changes are negligible ($|\dot{h}|<1.10^{-5}$ m/s) Eq. (3) can be approximated by:

$$\tilde{f} = \frac{4\pi}{\lambda}h_{eff} \qquad (4)$$

The Eq. 4 shows that the frequency $\tilde{f}$ of the multipath oscillations is proportional to the effective antenna height h_{eff}. Our method is based on the analysis of the multipath signature present in the SNR data constantly collected by a single geodetic receiver and its associated antenna (Figure 1) with an acquisition frequency of 1 second. The reflected signal will affect the SNR by producing an intermediate (i.e. low satellite elevation - LSE) to high frequency (i.e.

high satellite elevation - HSE) oscillations amplitude smaller than the one of the direct signal, which depends on the SE angle. Since the direct signal is preferred to the reflected signal by the antenna gain pattern by construction and as the reflected signal energy is attenuated upon reflection, the direct signal dominates the main shape of the SNR time series (Figure 1b, parabolic low frequency in red line). In order to analyze the multipath component, the direct signal contribution must be removed from the raw SNR profile. The common way to proceed is to fit and remove a simple parabolic polynomial to the raw SNR time series [Larson et al., 2008; Figure 1b] to consequently obtain the residual SNR multipath (SNR_m).

$\tilde{f}$ is commonly estimated from SNR_m time series using the Lomb-Scargle Periodogram [Lomb, 1976; Scargle, 1982], based on harmonic Fourier decomposition. Due to the fact that $\dot{h}$ tends toward 0, the frequency of the multipath oscillations is constant and directly proportional to the antenna height H_0 above the reflecting surface. From an electromagnetic point of view, the antenna height, even for a non-moving surface and known as effective antenna height (h_{eff}) has some variations. These variations are due to radar wave penetration into the vegetation layer and the soil, and depends on soil moisture, soil type (*e. g.* a clayed soil is characterized by a low radar wave penetration, whereas penetration depth is larger in sandy soil) and vegetation type. Following [Larson et al., 2008] and given a quite constant antenna height: h_{eff}, SNR_m can be expressed as a function of three metrics h_{eff}, A_m and Φ_m:

$$SNR_m = A_m \cos\left(\frac{4\pi h_{eff}}{\lambda}\sin(\theta) + \Phi_m\right) \quad (5)$$

where A_m scales the backscattering intensity of ground reflections, and Φ_m is the phase. A_m includes both the gain pattern and multipath intensity, which both depend on the SE angle. Field observations show that these responses in terms of phase and amplitude are strongly correlated with soil moisture level [Larson, et al., 2010]. Furthermore, these observations show that the effects of moisture are more sensitive to the phase Φ_m than to amplitude A_m, as previously observed in Chew et al. (2015) and Roussel et al. (2016). The backscattering A_m, Φ_m and h_{eff} which are derived from $\tilde{f}$, are the three observations which can be considered to estimate soil moisture variations of the soil surface, for soils with high clay content.

2.2 Phase unwrapping method

a) Unwrapping SNR phase method

The penetration depth of the GNSS waves into the soil around the antenna depends on the soil moisture content, on the dielectric properties of the soil [Njoku, 1996] and on SE (Figure 2a).

Following Njoku (1996) and Behari (2006), the penetration depth P_d for a signal coming from the zenith can be expressed as:

$$P_d = \frac{\lambda\sqrt{R_e(\varepsilon_r)}}{2\pi I_m(\varepsilon_r)} \quad (6)$$

with $R_e(\varepsilon_r)$ and $I_m(\varepsilon_r)$ are the real and imaginary parts of the relative permittivity of the reflecting surface.

For most applications using SNR_m and IPT technique with a single geodetic antenna, over clayed soils, the penetration depth of the wave is smaller than the wavelength in the L1, L2 and L5 bands of the GNSS constellations. In these conditions, soil moisture at 2-5 cm depth can be accurately retrieved. However, if the soil is mostly sandy, the penetration of the wave can exceed the GNSS wavelength and induces cyclic wrapping (or repetitions) of the phase. In that case, no correlation is found between the three parameters estimated from SNR_m and the soil moisture. Therefore, in sites that are rich of sand, we propose to use an additional processing called "phase unwrapping" to solve this problem. The main point of this algorithm is to re-calculate the "wrong" gradient phase or the phase cycle slip appears in the Phase multipath estimated from SNR_m using IPT technique to obtain continuous variations of Phase.

Let's consider a discrete signal $\varphi(x)$ of phase exceeding the range [-π, π] (modulus 2 π). We can assume the wrapping process as $\psi = W(\varphi)$ by calculating the four-quadrant arctangent (atan2) of $sin(\varphi)$ and $cos(\varphi)$, where $W(\varphi)$ is the phase unwrapping operation and ψ is the wrapped phase. As the signal is discrete, this is an ill-conditioned problem as phase cycle slip with 2π jumps, as seen in the example of the wrapped phase (Figure 2c). For example, if $\psi_{i-1} = 3\pi/4, \; and \; \psi_i = -3\pi/4$ we obtain $\Delta\psi = -6/4\,\pi$ we correct it into $W(\Delta\psi) = -6/4\pi + 2\pi = \pi/2$ (Figure 2b). The 2π jumps must be removed in order to restore the phase variation $\varphi(x)$ to get rid of the phase cycle slip ("wrong" gradient). This process is known as "phase unwrapping", it is classically used in many InSAR studies [Zebker et al., 1998; Smith et al., 2002; Hooper et al., 2007], and it consists in restoring a wrapped phase signal to a continuous one that is free from 2π jumps.

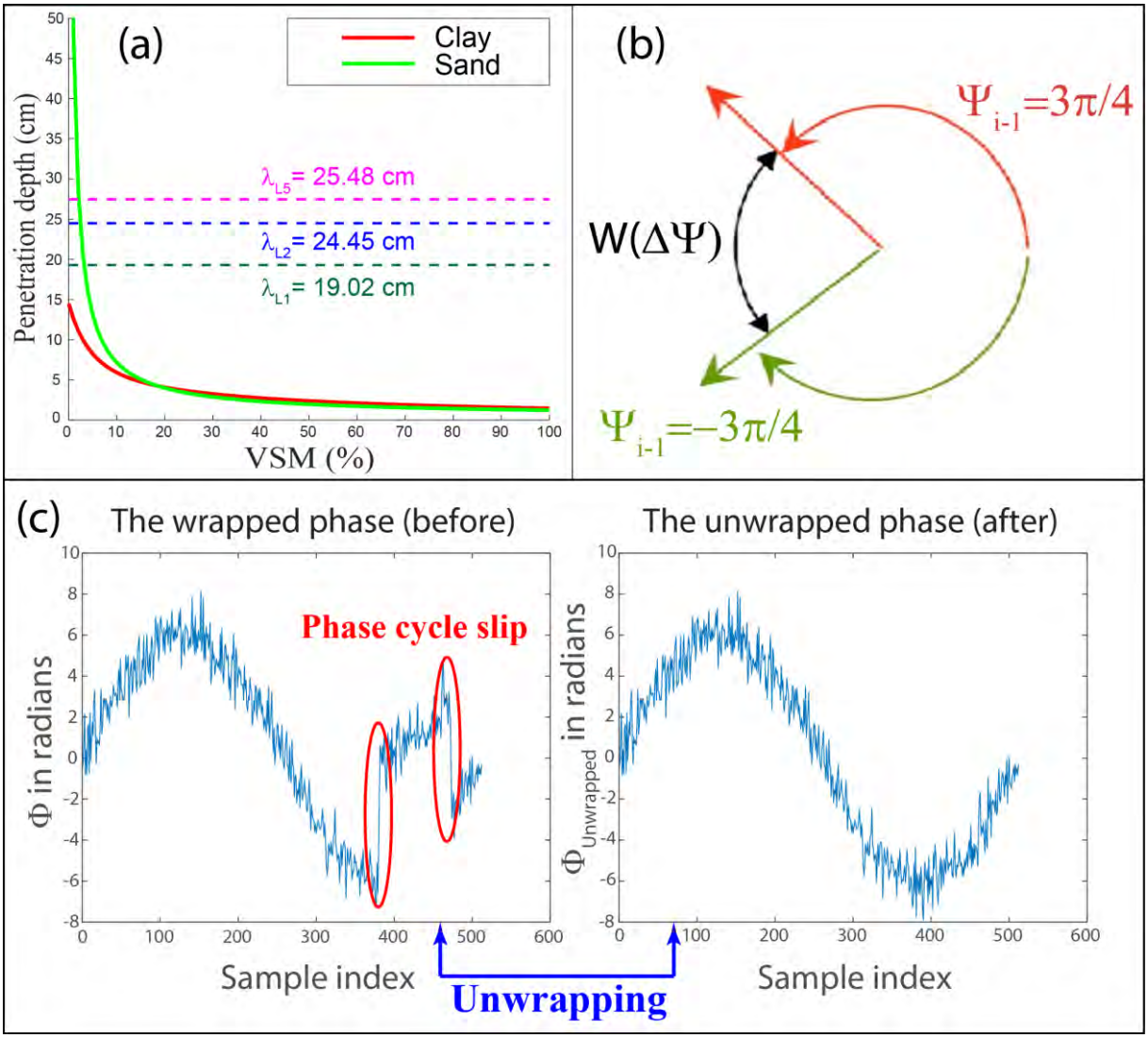

Figure 2 a) Theoretical penetration depth of the GNSS waves when the ground consists of 100% clay (red) and 100% sand (green); b) Example for the phase wrapping operation to correct of the "wrong" gradient (red arrow when phase slope is positive, green arrow when phase slope is negative); c) The simulation of the unwrapping phase process.

We can express the unwrapping process mathematically as:

$$\varphi_{unw}(x) = U[\psi] = \psi + 2k\pi \quad (7)$$

with $U[\psi]$ is the phase unwrapping operation, $\varphi_{unw}(x)$ is the unwrapped phase signal and $k \in Z$ is a relative integer corresponding to the number of cycle slips. In order to perform the phase unwrapping process, the difference between two consecutive samples (directly adjacent on its left) is calculated. When this difference is larger than +π in amplitude, or smaller than -π, a phase wrap is detected. Once a phase wrap is detected, the value of 2π is either added (phase slope is positive k>0) or subtracted (phase slope is negative k<0), from this sample and also from all the further samples to the right-hand side of it (Figure 2c).

b) New metrics

Following Eq. 5, the three SNR three metrics h_{eff}, A_m and Φ_m can be estimated from *SNR* and IPT technique for each GNSS satellite. We differentiate the two ranges of LSE angles and HSE angles, as well as the ascendant and descendant phases of the satellite passages. Due to the change of phase after using unwrapping phase function Φ_{unw}, the obtained effective antenna height h_{eff} is proportional to the frequency $\tilde{f}$ (Eq. 3), A_m is constant (as its depend on gain pattern and multipath intensity), it is necessary to re-calculate the new effective height. The height effective h_{eff}^{unw} after using unwrapping phase can be determined as:

$$h_{eff}^{unw} = \left(\cos^{-1}\left(\frac{SNR_m}{A_m}\right) - \Phi_{unw}\right) \times \frac{\lambda}{(4\pi \times \sin(\theta))} \quad (8)$$

3. Methodology

Following the theory of GNSS-R present in the section above, we propose a complex processing chain for detection of surface soil moisture (SSM) in sandy area using IPT technique and unwrapping phase method (Figure 3). Variations of soil moisture are scaled with respect to the minimum and maximum of the new calculated time series of Φ_{unw} and h_{eff}^{unw} that they are compared with. Pearson correlation coefficient R is a measure of the linear correlation between each of these time series and the volumetric soil moisture (VSM) measured with Theta probe. Total root-mean-squared error ($RMSE_{total}$), the differences between normalized phase of Φ_m, Φ_{unw} and *in situ* measurements (VSM), can be written as:

$$RMSE_{total} = RMSE_{rp} + RMSE_{SE} + RMSE_{spatial} \quad (9)$$

where $RMSE_{rp}$ is the error of difference between retrieved moisture estimated from SNR_m and the Theta probe reference measurement, $RMSE_{SE}$ is the instrumental error that depends on SE, soil roughness, and the penetration depth (frequency) of the wave, and $RMSE_{spatial}$ is the error caused by the spatial variations of moisture in the observed area.

R, BIAS and RMSE statistics are powerful tools in research, but its cannot express all the correlations in the study of the wave field. Thus, we propose to use another statistical method known as wavelet analysis *i.e.* Wavelet transform coherence (WTC) and Cross-wavelet transform (XWT) (Figure 3). WTC, XWT are the methods for analyzing the coherence and phase lag between two time series (time series of Φ_{unw} /h_{eff}^{unw} - X, *in situ* SM measurements - Y) as a function of both time and frequency (Grinsted et al., 2004). XWT permits the detection of phase angle (cross-magnitude), phase differences (= lag time), non-stationarity, and

coherency between X, Y. Phase angle statistics can be used to gain confidence in causal relationships and test geophysical relationships between the time series, the directions of the arrows indicate the relative phase relationship. Phase arrows pointing to the right: positive correlation (indicates 0 lag), left: anti-correlation, pointing to down: leading between them by 90 degrees; up: Y leading X by 90 degrees (Figure 10b, Figure 11b). Following Torrence and Webster (1998), wavelet coherence M^2 of two time series can be defined as:

$$M_n^2(s) = \frac{\left|S\left(s^{-1}V_n^{XY}(s)\right)\right|^2}{S\left(s^{-1}\left|V_n^X(s)\right|^2\right).S\left(s^{-1}\left|V_n^Y(s)\right|^2\right)} \quad (10)$$

where S is a smoothing operator (Morlet wavelet given by Torrence and Webster, 1998), $s = \sqrt{-2\ln(Z/n)}$ is the circular standard deviation ($Z = \sqrt{(X^2 + Y^2)}$), V is the wavelet power (see detail in Torrence and Compo, 1998). We have to notice that this definition closely resembles that of a traditional correlation coefficient, and it is useful to think of the wavelet coherence as a localized correlation coefficient in time frequency space.

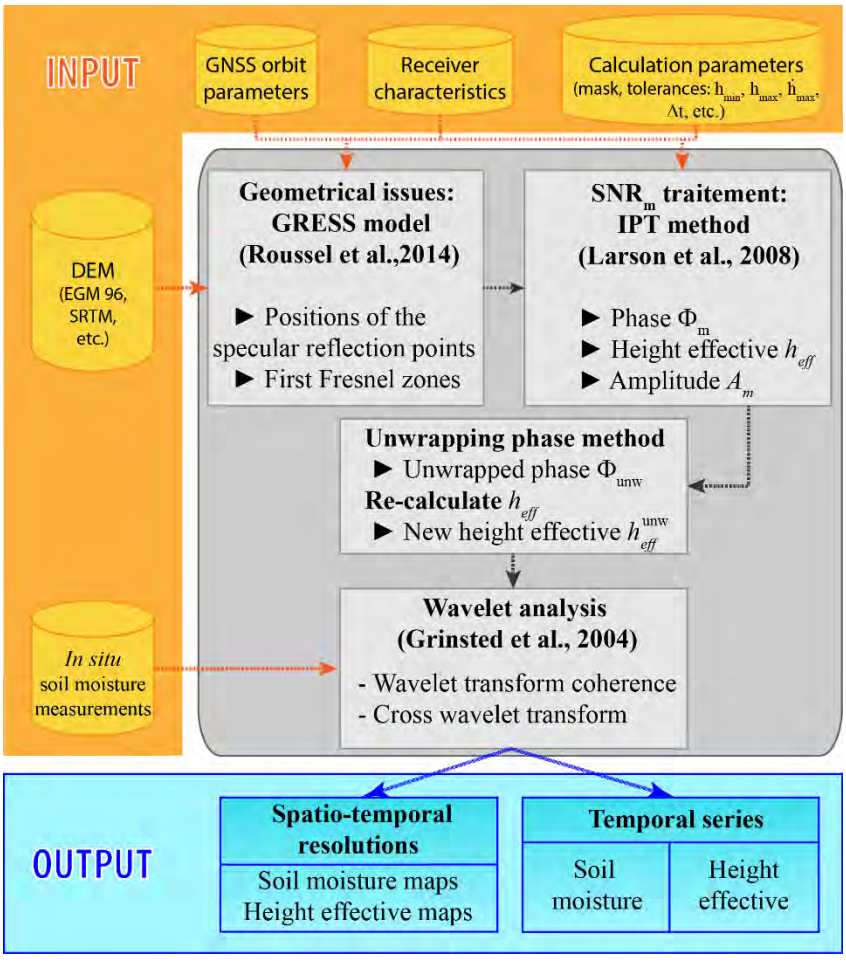

Figure 3 Flow chart presenting complex processing chain for detection/monitoring of surface soil moisture in sandy area using IPT technique and unwrapping phase method: the input, the different steps of the processing, and the output.

4. Applications to experimental plots

4.1 Beach Volley sandy ground

a) Measurement site

A Leica GR25 receiver with an AR10 antenna was installed in the center of a 25x30 m² beach volley field (43°33'46.93" N; 1°28'16.57" E) at the University Paul Sabatier, located in Toulouse, southwest of France (Figure 4a). The experiment took place in the framework of the MISTRALE project. The soil contains 100% of sand. It consists of small grains ranging between 0.3 and 0.5 mm in diameter. GPS L1, L2 (S1C, S2W) and GLONASS L1 (S1C) frequencies were continuously acquired during 3 days of rainy weather, from 25th to 27th April 2015 at 1 Hz sampling frequency. Antenna height above the ground surface, determined with a tape meter, was 4 m. The 3D geometry was determined during a survey by Ground Penetrating Radar (GPR) with a 500 MHz antenna: mean sand thickness is ~70 cm, and depth ranges between 35 cm and 1.10 m (see Figure 4b).

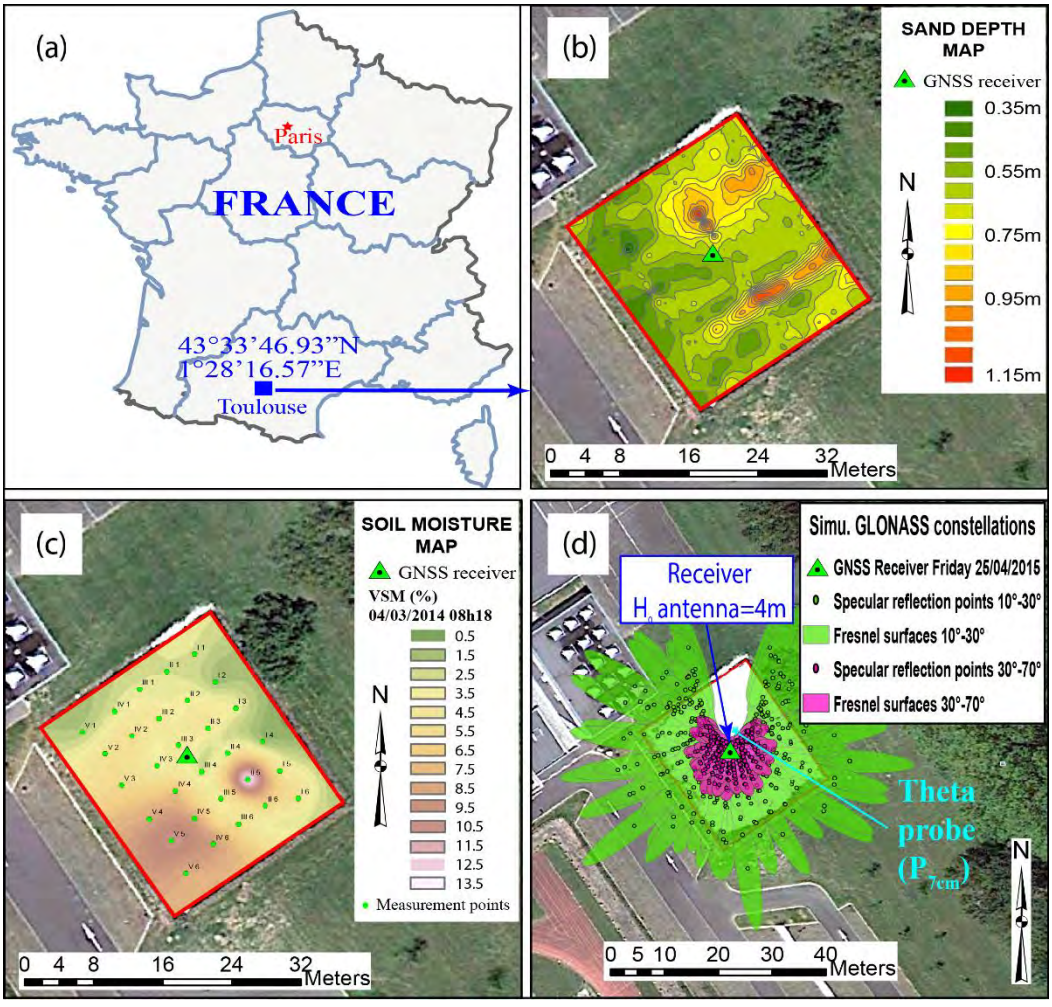

Figure 4 : Beach volley experiment; a) Location map of the beach volley field experiment at the University Paul Sabatier, Toulouse (France); b) map of sand layer depth done using Ground Penetrating Radar (GPR) with a 500 MHz antenna; c) Soil

moisture map of the sand layer created by interpolation of the measured points at 7 cm depth using Theta probe moisture sensors; d) location of GNSS receiver and of the Theta Probe sensors and map of the GLONASS specular reflection points and their first Fresnel surface, Simulations done on the 24th of April 2015 using GRESS [Roussel et al., 2014].

b) Data used for validation

To monitor soil moisture variations of the beach volley field, one ML3 Theta Probe Sensors (accuracy of ±0.01 m^3/m^{-3}) were installed at 7 cm depth (P_{7cm}), 1 meter away from the GNSS receiver (Figure 4d). Acquisitions were recorded every 5 minutes. These data have been used to validate SNR-based estimations of soil moisture fluctuations.

4.2 Dahra (heterogeneous soil)

a) Measurement Site

Following the methodology firstly applied to the beach volley field experiment to quantify soil moisture variations in case of a rich sand content, we want to apply this algorithm on a natural case study located near Dahra in the Ferlo region, Senegal, (western part of the Sahel). The annual rainfall 2016 was 367 mm and it fell during the rainy season from mid-July to end of September. The mean annual temperature 2016 was 29ºC. For a closer description of the field site we refer to Tagesson et al (2015).

The same instrument (Leica GR25 receiver and an AR10 antenna), were installed in a grazed rangeland in Dahra, Senegal (15°24'5.36"N; 15°26'0.13"W; see Figure 14a, b). GPS L1, L2, L5, and GLONASS L1 and L2 frequencies were continuously acquired from the 1st of October 2016 to the 31th of December 2016 at a 1-Hz frequency, in the transition period from rainy to dry season. In our study, we use all SNR signal strength on L1, L2 and L5 C/A channels.

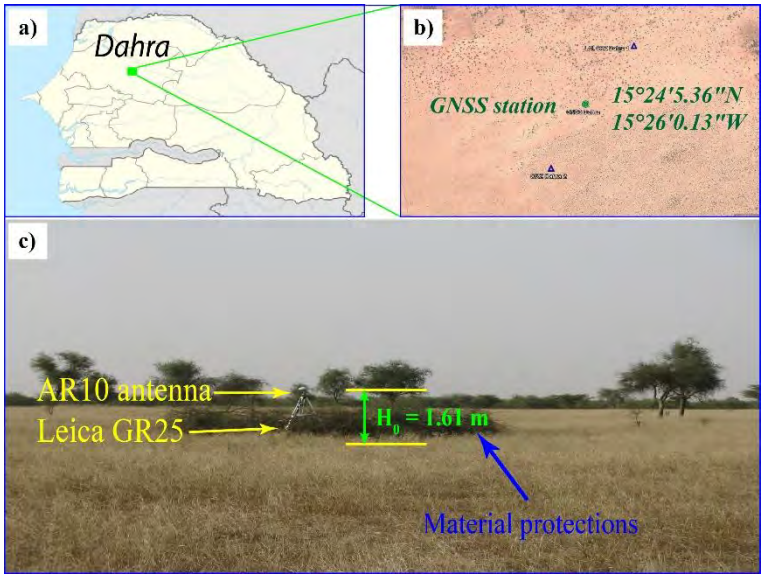

Figure 5 The experiment site of Dahra (Senegal), with a Leica GR25 receiver and an AR10 antenna installed on sandy soil (15°24'5.36"N; 15°26'0.13"W).

b) GNSS Reflectometry and parameters used for IPT

The antenna height H_0 above the ground surface, determined with a tape measurement, is equal to 1.61 m. The ground around the antenna is considered as flat. There are no structures in the close environment around the antenna which would act as a mask between the GNSS satellites and the antenna. A fence made of spiny shrub branches, was set up around the antenna to protect the GNSS station from cattle. This fence can disturb specular reflection of HSE (Figure 5c). For this reason, only satellites with elevation angles from 2° to 70° were considered (SE angles more than 70° were not considered as the amplitude of the multipath contribution to SNR becomes too small to be analyzed).

The power of the received signal is mostly due to coherent reflection, and most of the scattering comes from the first Fresnel zone [Beckmann et al., 1987]. Accurate locations of the specular reflection points on the ground surface have been determined through direct modeling using GNSS reflected signals simulations (GRESS) [Roussel et al., 2014]. Figure 5a, b shows the locations of the specular reflection points and associated Fresnel zones for both GPS and GLONASS satellites for the 1st of October 2016 as simulated by GRESS. As the antenna height H_0 is 1.61 m above the reflecting surface, the farthest specular reflection points are a bit more than 3.5 m away from the receiver for SE angles above 30° and reach ~ 50 m for SE angles above 2°.

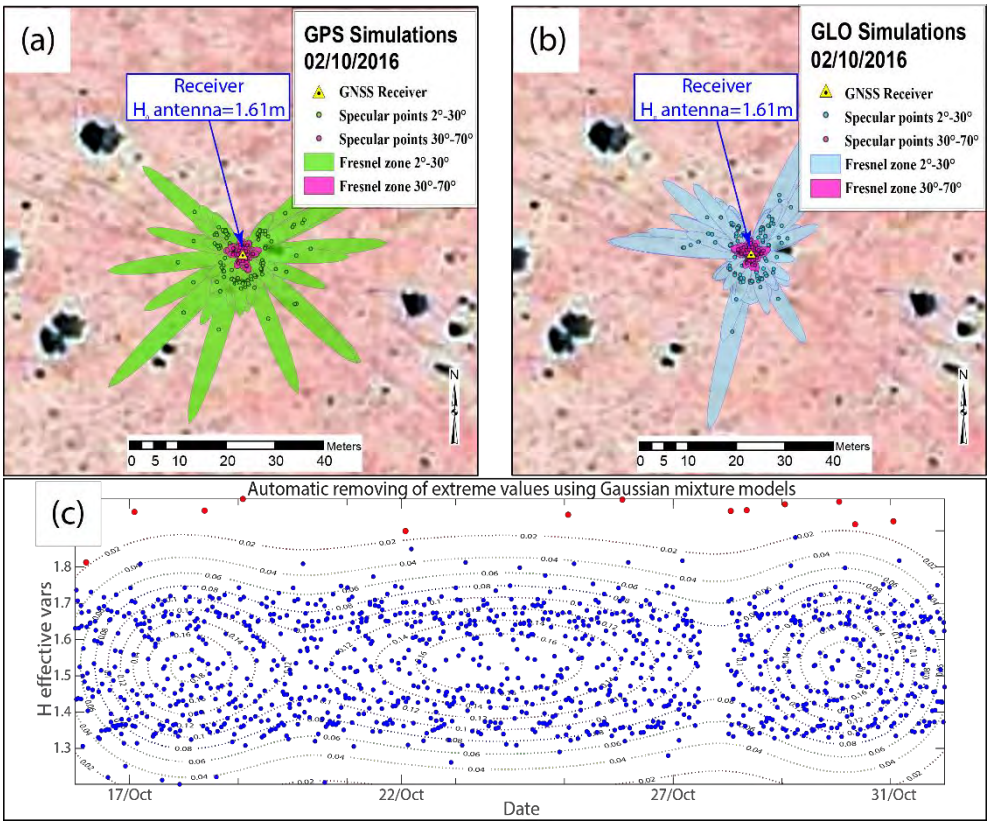

Figure 6 Locations of the GPS (a), GLONASS (b) specular reflection points and first Fresnel surfaces for a GNSS receiver at the Dahra experiment site. Simulations done for the 1st of October 2016. Satellite elevation angles range from 2° to 30° (green, cyan) and from 30° to 70°(magenta). Sampling rate is equal to 15 min (i.e., satellites positions are actualized every 15 min in the SP3 file that gives precise satellite orbits processed by the International GNSS Service). c) Clustering, Gaussian mixture model for removing extreme SNR data values (red dots).

To remove the elevation angle dependence of the three SNR parameters (A_m, Φ_m, and h_{eff}), two different ranges of SE angles are tested: the first one from 2° to 30° (referred to as SE_{2_30} in the following) and the second one between 30° and 70° (referred to as SE_{30_70}). As the effective reflection coefficient for an incident RHCP signal is negatively correlated with wetness of the soil for LSE angles, and positively correlated for HSE angles, the 30° cutoff was chosen as in, *e.g.*, Larson et al., (2008). The limit conditions in processing chain (Figure 3) were assumed to be: $h_{min} = 1.5$ m; $h_{max} = 2.62$ m; $\dot{h}_{max} = 1.10^{-5} m.s^{-1}$ (necessary assumption to compute the multipath frequency define by Eq.4). The number of observed maximal periods N was set to 4, which is the first number of observed periods above the 1% of error probability. Δt was set to 10 min for temporal resolution of the three SNR parameters [Roussel et al., 2016], close to sampling frequency of moisture measurements recorded by the probes (15 min).

c) Data used for validation

The soil moisture of the experiment site is monitored by a soil moisture station, located 600 m from the antenna (15°23'48.79"N, 15°26'9.35"W; see Figure 5b). The station is equipped with two soil temperature sensors T1 (5 cm depth), T2 (10 cm depth) and six soil moisture sensors ML3 Theta Probe Sensors (accuracy of ±0.01 $m^3.m^{-3}$), installed at 5 cm (Theta 1,3), 10 cm (Theta 2,4), 40 cm (Theta 5, out of order after few days) and 100-cm (Theta 6) depth (Figure 7). Acquisitions were recorded with a sampling frequency of 15 min. Figure 7b shows the evolution of soil moisture measured by those Theta Probes. During the wet to dry season transition period in October, which corresponds to the SNR acquisition, the 5 cm depth soil moisture (referred as P_{5cm}) ranged from 2,91% to 4,38% VSM, the 10 cm depth soil moisture (referred as P_{10cm} in the following) ranged from 3,68% to 4,75% VSM and the 1-m depth soil moisture (referred as P_{1m}) ranged from 5,50% to 5,64% VSM.

For these Theta Probes *i.e.* P_{5cm} and P_{10cm}, VSM shows as clear daily sinusoidal period (Figure 7b). This can be due to the impact on daily process of evapotranspiration (maximal in the midday) absorption (maximal dew deposition occurring at ~ 6 am), but also to the dependence of theta ML3 probe on soil temperature [Kaleita et al., 2005].

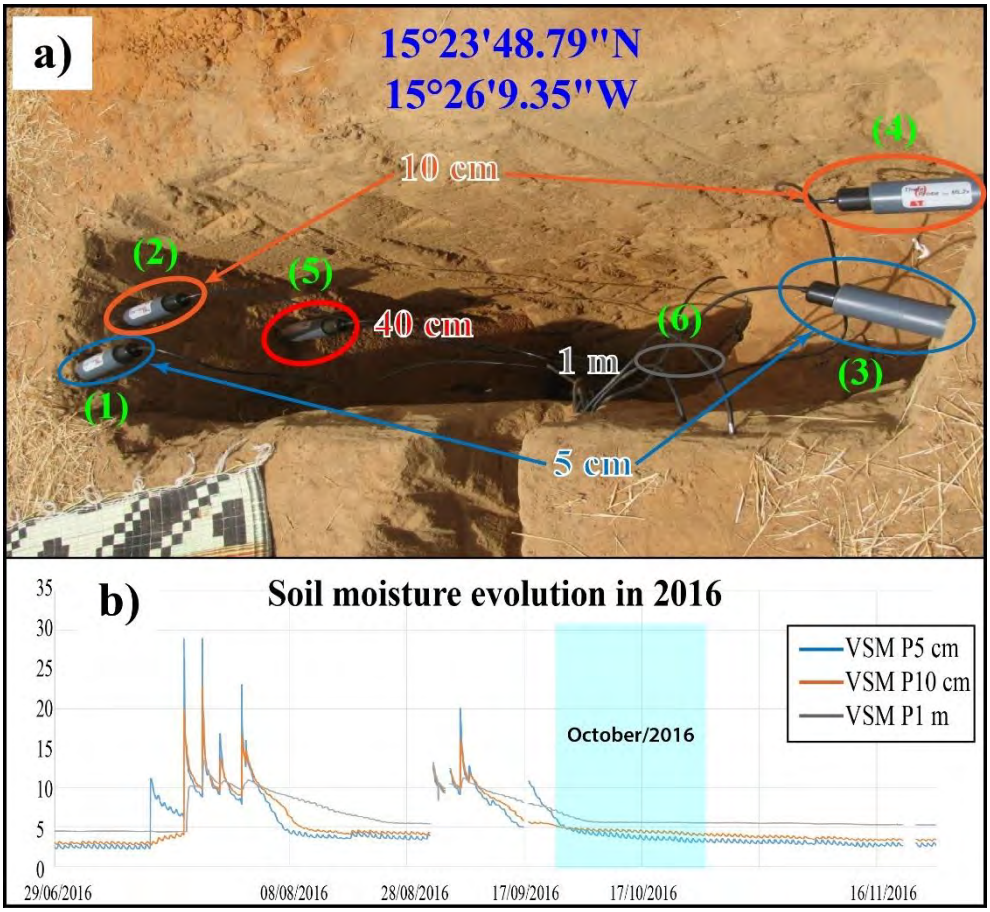

412

413 *Figure 7 a) Configurations of the Soil Moisture station (15°23'48.79"N, 15°26'9.35"W). The station equipped with 6 Theta*
414 *probes: TP1: 5 cm, TP2: 10 cm, TP3: 5 cm, TP4: 10 cm, TP5: 40 cm, TP6: 100 cm; b) VSM recorded by Theta probes in 2016.*

415

5. Results

5.1 Beach Volley field

During this period of SNR acquisitions, the Theta Probes record soil moisture that ranging between 2.68 % to 6.62 % of VSM. All the reflections occurring outside the beach volley field were removed from the analysis. Only SNR from HSE i.e. 30°-70° (Figure 4d) were processed.

Table 1 Linear correlation coefficient R between Phase Φ_m, unwrapped phase Φ_{unw} (estimating using IPT method with SE and soil moisture recorded by Theta probe P_{7cm} for different constellations on band L1.

Φ_m, $\Phi_{unwrapped}$ /VSM	**BIAS** (%Vol)	**RMS** (%Vol)	**RMSE** (%Vol)	**R** (%Vol)
For Ascending pass of satellites				
Φ_m (GPS) *	1.22	1.13	1.66	0.03
$\Phi_{unwrapped}$ (GPS) **	0.18	0.66	0.68	0.72
Φ_m (GLONASS) *	0.45	1.43	1.49	0.06
$\Phi_{unwrapped}$ (GLONASS) **	0.04	0.57	0.57	0.86
Φ_m (GPS+ GLONASS) *	0.96	1.22	1.55	0.03
$\Phi_{unwrapped}$ (GPS+ GLONASS) **	0.79	0.49	0.93	0.85
For Descending pass of satellites				
Φ_m (GPS) *	0.63	1.15	1.31	0.13
$\Phi_{unwrapped}$ (GPS) **	0.33	0.66	0.73	0.75
Φ_m (GLONASS) *	0.16	1.09	1.09	0.42
$\Phi_{unwrapped}$ (GLONASS) **	0.05	0.52	0.52	0.89
Φ_m (GPS+ GLONASS) *	0.63	1.05	1.22	0.24
$\Phi_{unwrapped}$ (GPS+ GLONASS) **	0.81	0.57	0.99	0.81
For Ascending and Descending pass of satellites				
Φ_m (GPS) *	0.98	1.13	1.49	0.08
$\Phi_{unwrapped}$ (GPS) **	0.36	0.63	0.72	0.74
Φ_m (GLONASS) *	0.47	1.22	1.30	0.12
$\Phi_{unwrapped}$ (GLONASS) **	0.04	0.54	0.54	0.86
Φ_m (GPS+ GLONASS) *	0.84	1.11	1.39	0.10
$\Phi_{unwrapped}$ (GPS+ GLONASS) **	0.85	0.52	1.00	0.82

Results for the beach volley field experiment (Table 1 and Figure 4) show that:

When reflecting ground contains 100% of sand, it is possible to retrieve variations of the VSM by using the unwrapping method. The unwrapping function is necessary to retrieve reliable estimates of SSM. The correlation R between SNR-based soil moisture estimation after using unwrapping function and the independent data (P_{7cm}) is above 0.80 over the 3-day period of acquisition (Figure 4). The results using the GLONASS constellation has better correlations and are more sensitive to soil moisture for this sand reflecting soil (R>0.85) than when using the GPS signals (Table 1).

Table 2 Statistics of spatial resolution using different methods: in situ with single Theta probe, map create from Theta probes measurements network and GNSS-R.

Method	Area (m^2)	Volume (m^3)	Mean VSM (%)	STD σ (%)	RMSE Γ (%)	Depth (cm)
Probe alone	0.03	0.00075	3.95	0.95	NaN	7±2.5
Map of the probes	0.03	0.00075	3.84	1.19	NaN	7±2.5
	189	17.955	4.82	0.69	1.28	7±2.5
GNSS-R	3.6	0.985	4.37	0.97	0.66	27.4±10
	189	51.786	4.21	0.91	0.54	27.4±10

We observe large variations (~14%) of soil moisture in the beach volley field depending on the location of the moisture sensor, as shown in the soil moisture map (Figure 4c). These variations are clearly dependent on the sand thickness/depth of the volley ground (Figure 4b). The sampling volume of ML3 Theta probe is ~0.00075 m^3, with an average moisture of 3.95% +/- 0.95%, the spatial resolution using GNSS-R technique covers an area of ≈ 189 m^2 (i.e. the range of SE from 30° to 70° - magenta zone, Figure 4d), which corresponds to a volume of ≈ 51.79 m^3 (estimated by multiplying the GNSS-R explored area by the average penetration depth of 0.27m +/- 0.1 m, Table 2). The average SM for the volley field measured by GNSS is ~6% +/- 3%. $RMSE_{total}$ obtained, in Figure 4, is still high, ~0.54% comparing with SM measured by probe that ranges between 2.68 % and 6.62 % of VSM (~4%). Thus, GNSS-R and unwrapping SNR phase method can be used to detect soil moisture changes (for both spatio-temporal resolutions) in the case of sandy soil. The unwrapping technique increases the accuracy of SM retrievals in comparison to phase measurements, and GNSS-R provides spatial information that are not provided by the moisture probe. Moisture probes, however, are necessary for calibration of GNSS-R moisture retrieval, which can also be achieved by gravimetric moisture measurements.

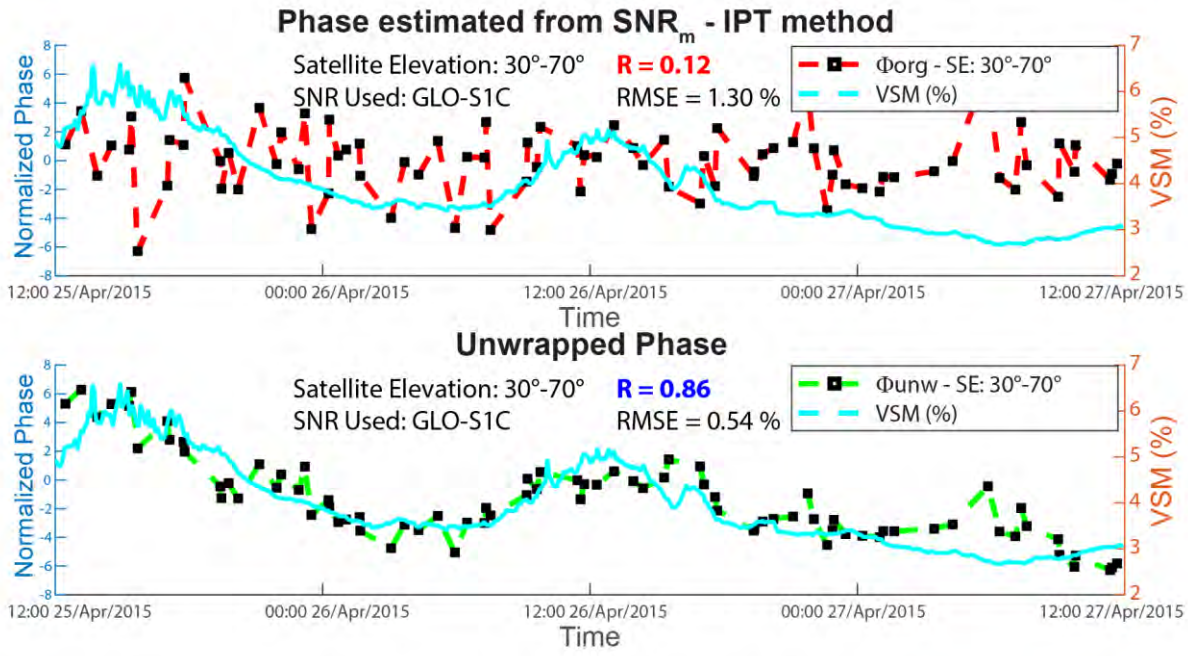

Figure 8 : Evolution of the unwrapped phase Φ_{unw} (green line) and independent soil moisture records (cyan line) at 7 cm depth in the beach volley field using SNRm on L1 band of GLONASS constellation.

5.2 Dahra

From Table 3 and Figure 9, we can see that Φ_{unw} and h_{eff}^{unw} have negative correlations. This can be explained by wave penetration. The strongest positive and negative R were found between Φ_{unw} and VSM_{10} (0.91) and between h_{eff}^{unw} and VSM_{10} (-0.93), respectively (Figure 9). The constellations generating the strongest results were with the GPS and the integration of GPS + GLONASS for HSE SE_{30_70}. We have stronger correlations during the rainy period than during the dry period due to larger variability. However, the VSM_{10} still only changed 2% in the whole study period (Figure 10a). VSM of P_{1m} has no correlation and display very small changes in moisture (0.14% VSM).

462 *Table 3 Linear correlation coefficient R between Φ_m, h_{eff}, unwrapped phase Φ_{unw}, new height effective h_{eff}^{unw} and VSM*
463 *measured by P_{5cm} and P_{10cm} probe for difference constellations in October 2016.*

GNSS	Band	SNR	Rainy period (01/10/2016-15/10/2016)				Dry period (16/10/2016-31/10/2016)			
			SE_{2_30}		SE_{30_70}		SE_{2_30}		SE_{30_70}	
			R_{P5cm}	R_{P10cm}	R_{P5cm}	R_{P10cm}	R_{P5cm}	R_{P10cm}	R_{P5cm}	R_{P10cm}
GPS	L1	Φ_m	0.06	0.08	0.11	0.04	0.00	-0.05	0.13	0.07
		H_{eff}	-0.03	-0.07	-0.17	-0.09	0.04	0.07	-0.08	0.03
		Φ_{unw}	0.67	0.68	0.76	0.74	0.73	0.89	0.37	0.66
		H_{eff}^{unw}	-0.69	-0.73	-0.68	-0.64	-0.68	-0.86	-0.37	-0.59
	L2	Φ_m	0.16	0.21	0.04	0.03	0.09	0.03	0.14	0.03
		H_{eff}	-0.10	-0.19	-0.07	-0.08	-0.07	-0.07	-0.13	-0.02
		Φ_{unw}	0.83	0.80	0.83	0.87	0.28	0.71	0.46	0.70
		H_{eff}^{unw}	-0.80	-0.81	-0.73	-0.78	-0.26	-0.69	-0.28	-0.60
	L5	Φ_m	0.06	0.06	0.11	0.15	0.10	0.04	0.36	0.33
		H_{eff}	-0.10	-0.10	-0.13	-0.14	-0.15	-0.08	-0.29	-0.31
		Φ_{unw}	0.79	0.83	0.72	0.73	0.61	0.79	0.27	0.70
		H_{eff}^{unw}	-0.68	-0.68	-0.70	-0.72	-0.11	-0.61	-0.15	-0.67
	L1+ L2+ L5	Φ_m	0.11	0.12	0.07	0.05	0.15	0.06	0.16	0.08
		H_{eff}	-0.07	-0.09	-0.10	-0.08	-0.14	-0.09	-0.14	-0.04
		Φ_{unw}	0.76	0.80	0.87	0.90	0.43	0.77	0.74	0.84
		H_{eff}^{unw}	-0.73	-0.76	-0.79	-0.79	-0.47	-0.79	-0.53	-0.73
GLO	L1	Φ_m	0.03	0.05	-0.10	-0.09	0.11	0.04	-0.03	-0.03
		H_{eff}	-0.05	-0.07	0.09	0.06	-0.18	-0.15	0.06	0.07
		Φ_{unw}	0.65	0.67	0.62	0.66	0.58	0.81	0.17	0.64
		H_{eff}^{unw}	-0.59	-0.62	-0.50	-0.53	-0.47	-0.77	-0.20	-0.64
	L2	Φ_m	-0.11	-0.05	0.11	0.14	0.06	0.08	0.08	0.15
		H_{eff}	0.06	0.02	-0.10	-0.15	-0.05	-0.08	-0.05	-0.12
		Φ_{unw}	0.72	0.76	0.65	0.70	-0.03	0.58	0.01	0.61
		H_{eff}^{unw}	-0.71	-0.74	-0.61	-0.65	-0.03	-0.58	-0.07	-0.55
	L1+ L2	Φ_m	-0.08	-0.04	0.04	0.07	0.07	0.05	0.03	0.08
		H_{eff}	0.03	0.00	-0.05	-0.09	-0.08	-0.05	-0.01	-0.05
		Φ_{unw}	0.67	0.74	0.82	0.87	0.15	0.68	0.42	0.78
		H_{eff}^{unw}	-0.71	-0.75	-0.75	-0.81	-0.14	-0.66	-0.30	-0.70
GPS+ GLO	All bands	Φ_m	-0.01	0.00	0.05	0.06	0.08	0.06	0.08	0.06
		H_{eff}	-0.02	-0.03	-0.07	-0.08	-0.07	-0.06	-0.07	-0.05
		Φ_{unw}	0.66	0.70	0.88	0.91	0.04	0.65	0.68	0.85
		H_{eff}^{unw}	-0.71	-0.73	-0.83	-0.88	-0.11	-0.63	-0.58	-0.80

464

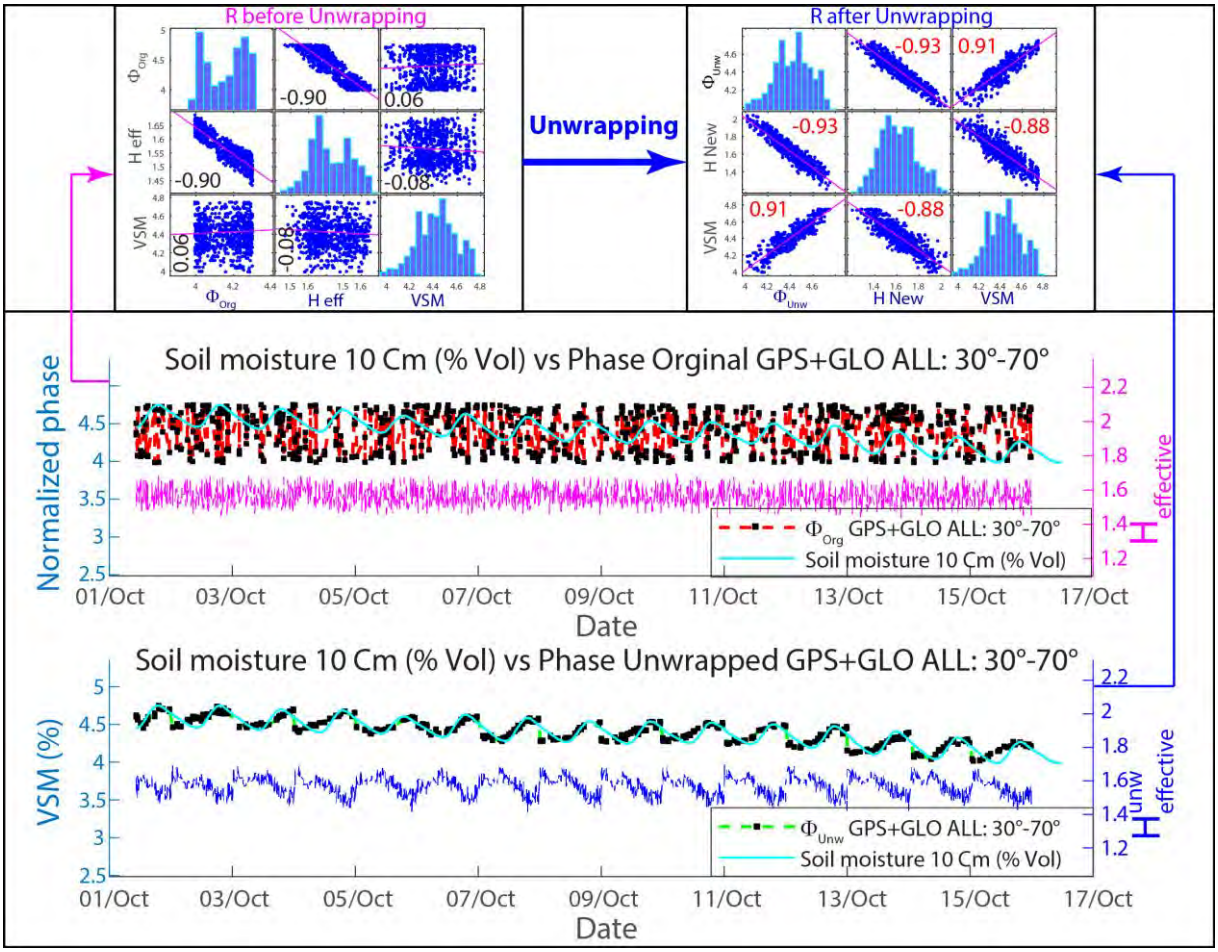

Figure 9 Results obtained with all GPS+GLONASS constellations for high satellite elevations from 30°-70° before and after Unwrapping phase vs VSM measured by P10 cm probe during rainy period and their linear correlations R.

For the final results - all series combined, including the transition period from rainy to dry season in October 2016 - are obtained by combining all the time series Φ_{unw}, h_{eff}^{unw}. The best results are obtained with all the GPS satellites, the correlation R between Φ_{unw} (green line for SE_{2_30} in Figure 10a, red line for SE_{30_70} in Figure 11a) and VSM P_{10cm} (blue line) is respectively: $R_{\mathrm{P10cm}}^{2-30} = 0.95$ and $R_{\mathrm{P10cm}}^{30-70} = 0.97$.

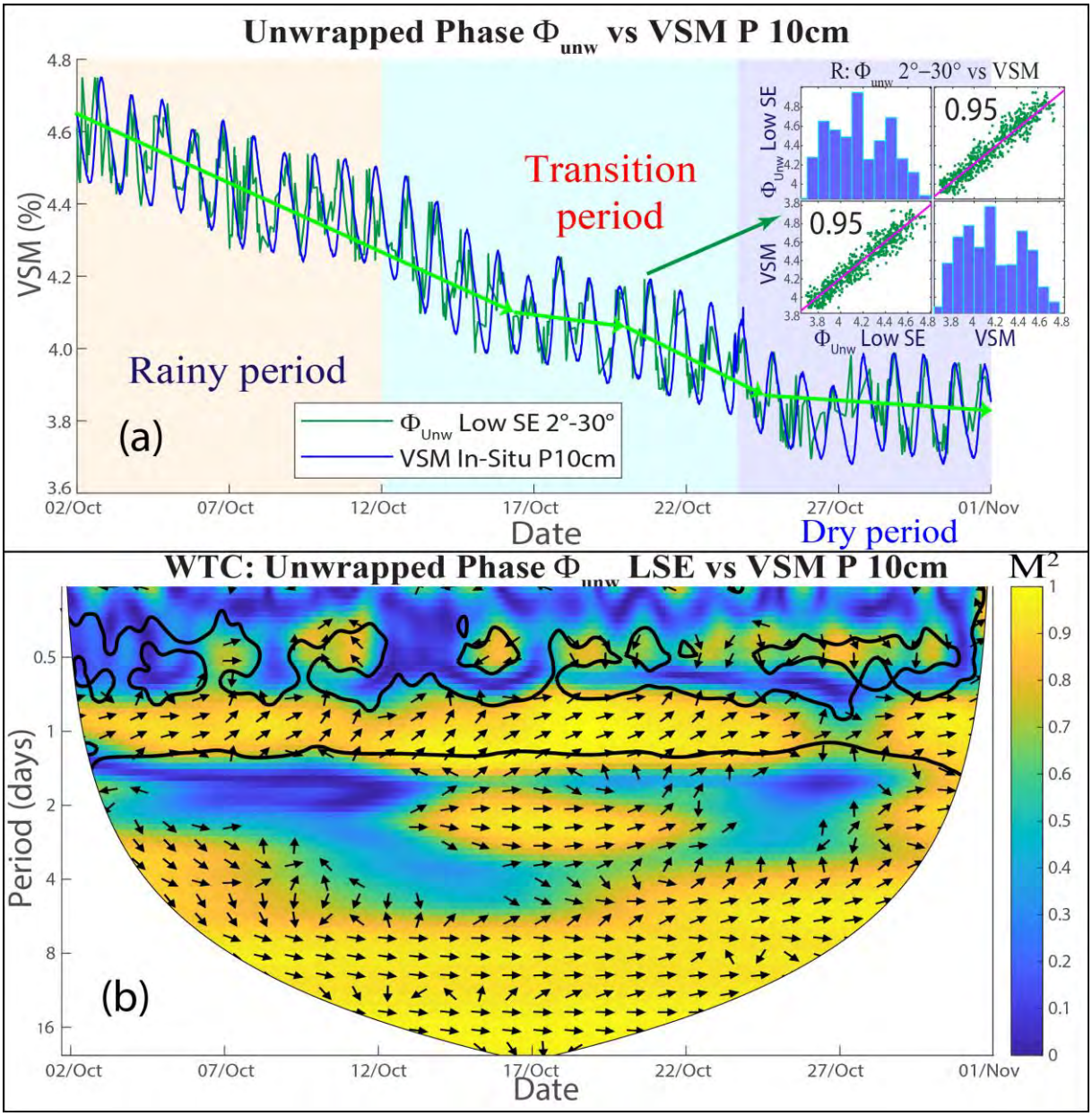

Figure 10 a) Evolution of the final results for all the time series Φ_{unw} – during transition period in October 2016 - obtained from SNR measurements and Unwrapping phase algorithm for all GPS satellites with low satellite elevations SE_{2_30} versus VSM measured by P_{10} cm. b) Wavelet coherence (M^2) of Wavelet transform coherence between Φ_{unw} and P_{10} cm (LSE is low elevation angle).

For the low SE, The Unwrapped phase $\Phi_{\mathrm{unw}}^{2-30}$ shows positive, *i.e.* in-phase correlation, with VSM, $M_{1-day}^2 \sim 0.95$ for the period of 1 day and has good correlation from the period of 1 week $M_{8-days}^2 \sim 0.98$ (Figure 10b). An inflexion of the trend, related to a transition between the end of the rainy period and the dry period is observed from 13/10/2016 till 22/10/2016 over two-days period of the WTC.

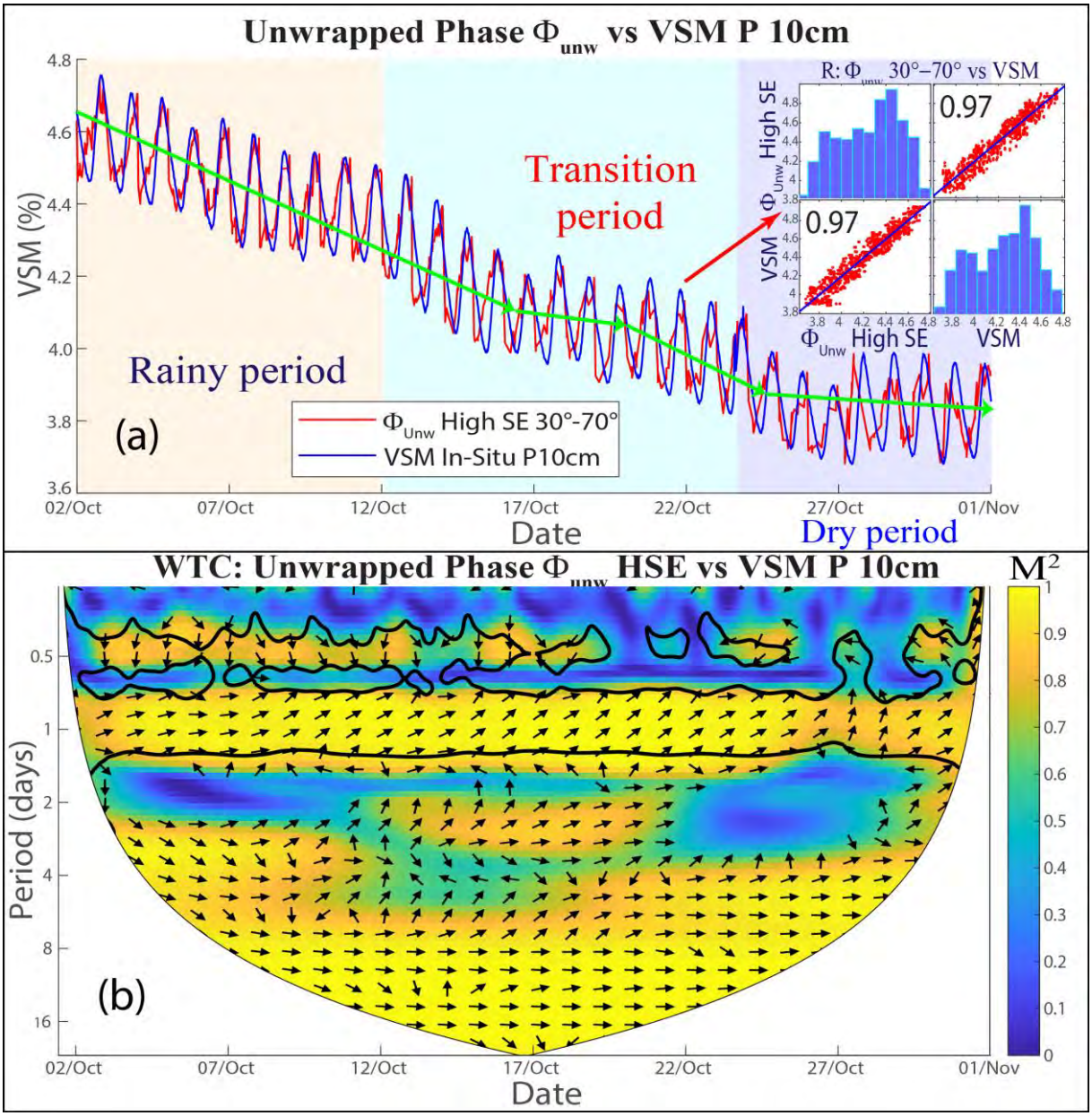

Figure 11 a) Evolution of the results for all the time series Φ_{unw} – during transition period in October 2016 - obtained from SNR measurements and Unwrapping phase algorithm for all GPS satellites with high satellite elevations SE_{30_70} versus VSM measured by P_{10} cm. b) Wavelet coherence (M^2) of Wavelet transform coherence between Φ_{unw} and P_{10} cm. (HSE means high elevation angle).

For the HSE (Figure 11b), the inflexion of the trend is also observed in the two-day period but this is 1 day earlier than for LSE. This 1-day difference in the start of the transition period in the two ranges of elevation may be related to the presence of the protective fence/barrier around the study area. (Figure 5, Figure 6). The fence of 3m from the antenna is included in the Fresnel zone for LSE simulated in Figure 6 (~100 m^2). Its presence likely affects the delay time of phase estimated from SNR_m.

To eliminate the effect of the daily evapotranspiration/absorption and soil temperature on the soil moisture content recorded by Theta probe, a daily average was applied to all-time series

(Figure 12a). Soil Moisture retrievals are again very good for both low and high incident angles (R=0.99). From wavelet coherence in the Figure 12b, we can see the change of the arrow direction to -45° of 2 days period from 22/10/2016 till 31/10/2016. Its mean SNR multipath detects soil moisture variations before VSM recorded by P_{10cm}. This also shows that the moisture in the soil is decreasing as it shifts to the dry period.

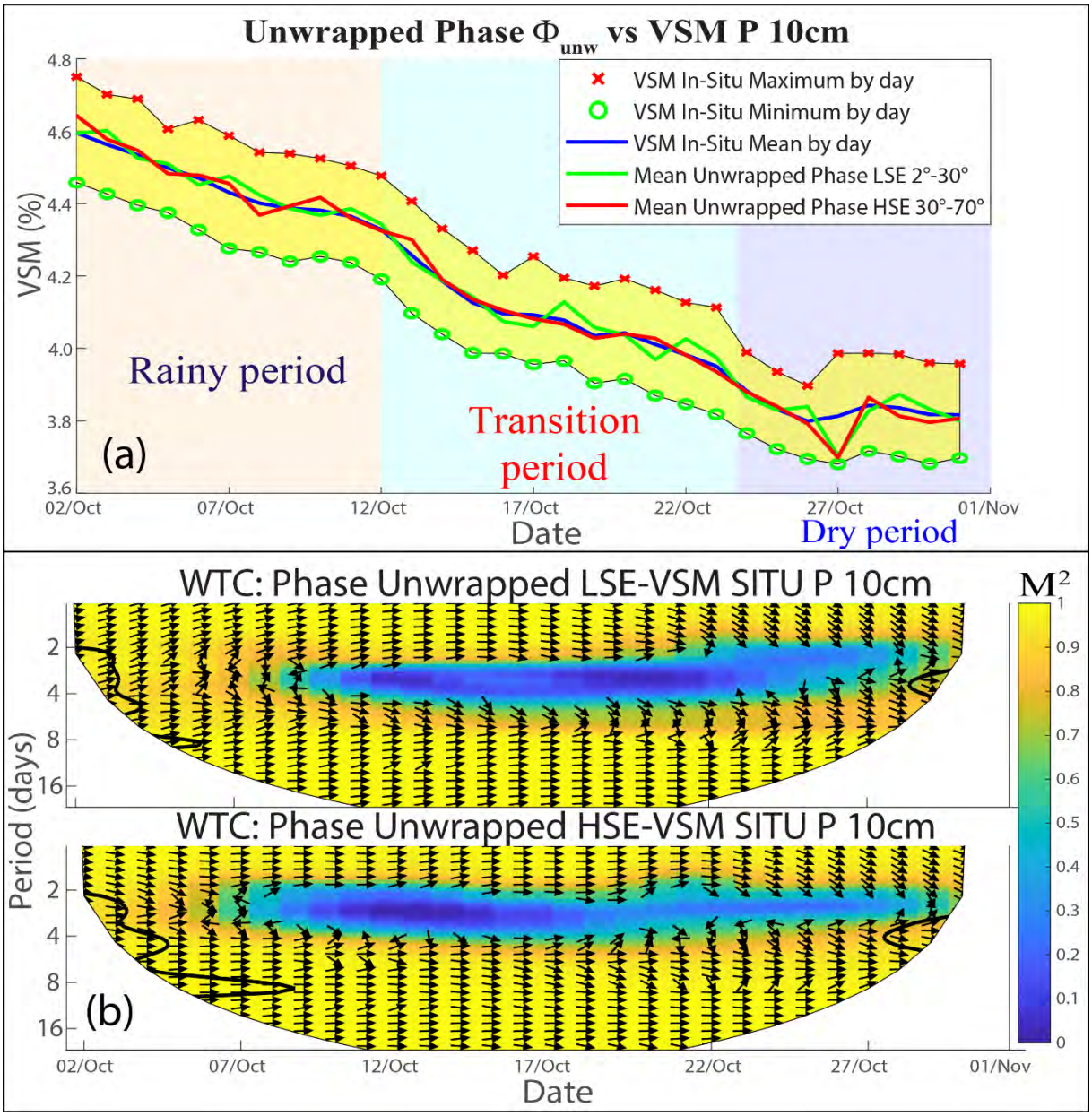

Figure 12 Average by day of the Φ_{unw} and VSM recorded by Theta probe P10 cm time series. ***O, X*** *are the minimum and maximum VSM measured by Theta probe by day.*

Another interesting point is the capability of this method to estimate spatio-temporal variability in SM (Figure 13). The spatial area covered depends on the antenna height and in our case with a height of 1.61 m the radius of the measured area is ~12 m. That represents an average area of 452 m^2 with a mean penetration depth of 0.2234 m (mean h_{eff}^{unw}) that gives a mean volume

of ~100 m^3. The time step to compute the spatial variability is set to 3 days and the same color scale for the moisture is used for the different dates (Figure 13). The soil moisture ranges from 3.68% to 4.75% and maps from Figure 13 indicate a slow drying of the soil around the antenna over the study period, slightly more important in the southern part. Soil moisture is very similar over the 100 m^2 mapped area with a spatial distribution smaller than 0.01% (Figure 13).

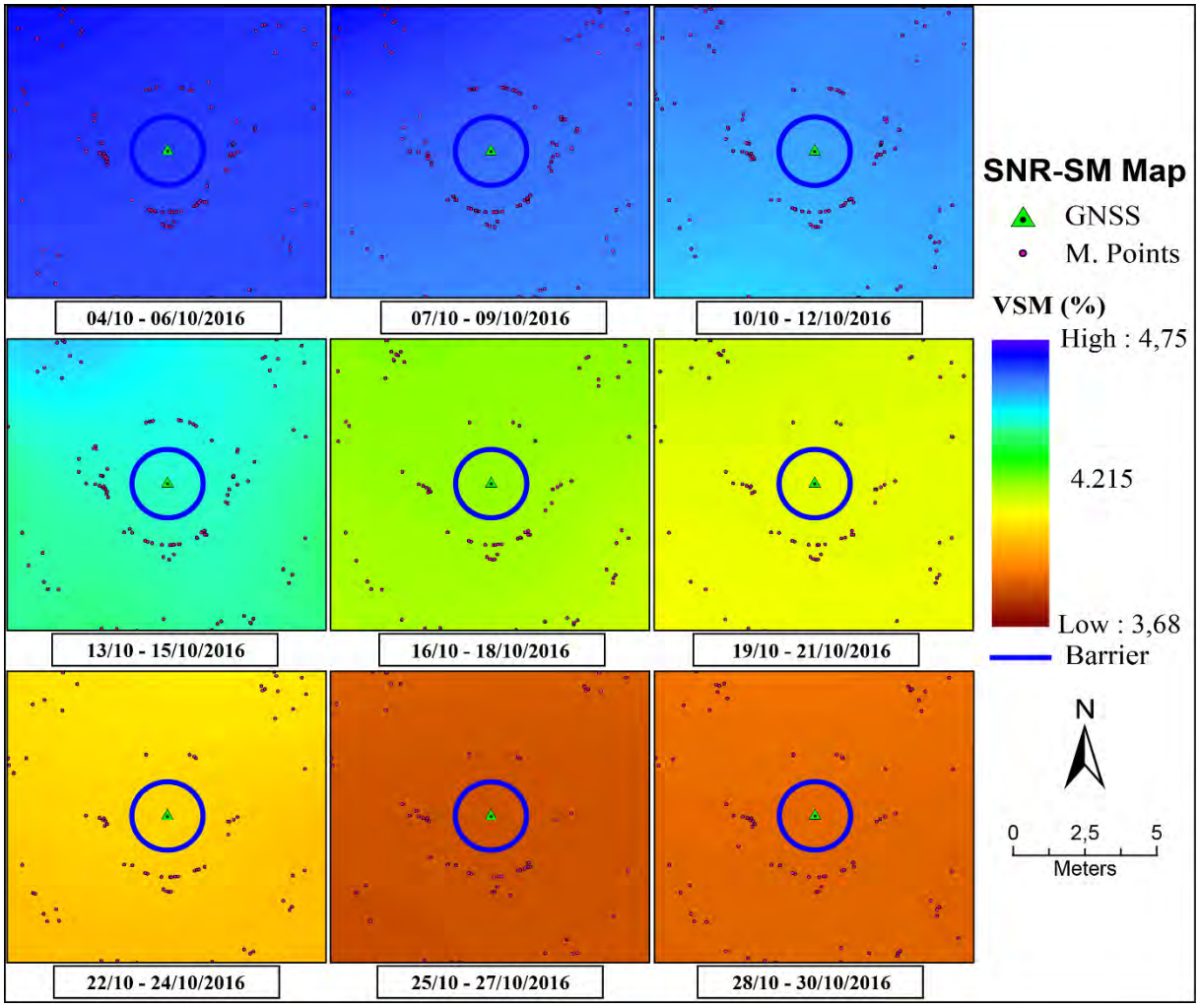

Figure 13 Series soil moisture maps created from results of Φ_{unw} for 3 days in October 2016 and the locations of the measured specular reflection points (M. points) on the ground surface around Dahra GNSS station (the surface around the antenna was considered as flat).

6. Discussions

As mentioned by Baghdadi et al. (2006), surface soil moisture represents the water content in the upper layer of the ground and is essential for the precipitation distribution and also for the separation between runoff and infiltration [Hossain & Easson, 2009]. Continuous and long soil moisture time series are crucial for climatic studies [Longobardi, 2008] and the characterization of the critical zone [Kirkby M. J., 2016; Cleverly et al., 2016]. Numerous automated techniques

for *in situ* and remote sensing measurements have been operational over few decades. We now present a discussion about these "conventional" techniques and GNSS-R.

6.1 GNSS-R versus *in situ* probes

The GNSS-R with the single-antenna system is an excellent alternative to the current *in situ* technique used for measuring soil moisture for different types of soil including for the plot where the GNSS penetration depth of the ground around the antenna is higher than the wavelength of the GNSS signal and the VSM is too low or rapidly changes (i.e. in case of the beach volley field, Desert regions or West Africa of sandy areas). All *in situ* techniques require reliable reference data sets, which have been calibrated using reference gravimetric technique under laboratory conditions [Walker et al., 2004]. Some sensors, like the Theta probe used in this study, show a clear dependence to daily temperature variations [Holzman et al., 2017] while other ones like TDR sensors are less sensitive to thermal artefacts [Walker et al., 2004]. GNSS-R is also sensitive to thermal effects. A daily period is clearly visible in the GNSS-R estimates as on Theta probe retrievals. However, GNSS-R integrates a larger volume and penetrate deeper and its answer seems more correlated to soil moisture at ground level when humidity rises as the temperature falls. Another possibility was pointed out by Roxy et al. (2010). These authors suggest that daily moisture variations correspond to daily variations of surface albedo. These variations decrease from the dew point until the maximum sun illumination and reversely from the maximum sun illumination to the dew point, and it's less correlated to the thermal diffusivity of the soil.

Another aspect was discussed by Coopersmith et al. (2016). He showed, that in many cases, the change of probe is responsible for discontinuities and biases in the time series. Obviously using GNSS-R, the change of receiver is also needed. But unlike for *in situ* sensors where the technology can evolve quickly and drastically, for GNSS-R, the source does not change. GNSS constellations improve over time, but the initial signals like L1 or L2 are retained, which allows to have longtime series, reaching up to two decades in some case with time steps as small a one second.

A key point of GNSS-R moisture retrieval is the existing unknown dataset; many users make continuous GNSS measurement for field observations for geological or ecological purposes but few use it for soil moisture monitoring. It should be possible to reuse these datasets to establish long-term time series worldwide. For example, GNSS networks exist in many countries and can be used easily for free. The International GNSS Service (IGS) has a worldwide network that has been working for more than two decades, but these IGS stations cannot be used due to

557 the used choke ring antenna, that reject the multipath signals by construction
558 (http://www.igs.org/network/information, 2018).

559 6.2 GNSS-R and remote sensing

560 Monitoring soil moisture dynamics has greatly improved with the launch of the dedicated soil
561 moisture satellite missions as well as with GNSS-R using UK TechDemoSat-1 with its
562 opportunistic moisture measurement over land surface [Chew et al., 2016]. To improve the
563 spatio-temporal information, one can use the combination of various missions: i) Sentinel 1 and
564 2 [Baghdadi et al., 2012; Paloscia et al., 2013; Gao et al., 2018]; ii) optical and radar images
565 [Faye et al., 2017]; iii) GRACE Gravimetric satellite and SMOS L band satellite [Tian et al.,
566 2016]; iv) thermal infrared images [Verstraeten et al., 2006] etc. The scientific paradigm of
567 remote sensing monitoring of soil moisture is to highlight global/worldwide changes with a
568 pinpoint accuracy associated to a revisiting period as small as possible, ideally few hours would
569 be perfect.

570 This is a challenging point to improve the spatio-temporal resolutions because, for example,
571 when we increase the accuracy of spatial resolution, we have lower temporal resolution with a
572 revisiting time of few weeks and reversely. Numerous studies have shown good results with the
573 method of moisture calibration of remote sensing using *in situ* probes in homogeneous soil
574 [Holzman et al., 2017; Koyama et al., 2017]. But if the soil is spatially heterogeneous with
575 strong moisture variations, in that case, a single *in situ* sensor is insufficient, one has to increase
576 drastically the number of sensors depending on the surface explored by remote sensing as
577 demonstrated in Figure 5. The GNSS-R allows with one sensor to monitor large area, it could
578 in that case reduce the monitoring cost and human resources needed for monitoring. It is also
579 well adapted to L band remote sensing (SMOS, ALOS, ALOS 2) because GNSS-R is less
580 sensitive to weather conditions, dust and vegetation effects than optical remote sensing sensors.

581 Another interesting property of GNSS receivers is their ability to quickly and efficiently change
582 of scale. The explored surfaces, sum of first Fresnel surface, is only dependent on the antenna
583 height (any user controls it), satellite elevation ε, that can be obtained from broadcast ephemeris
584 or precise one (2 weeks later), and the number of visible satellites at the time t. So, one can
585 define different scales just dividing the visible satellites in two sets: low elevations and high
586 elevations (Figure 8). We can then analyze surfaces of few m^2 for an antenna height close to 5
587 m with ε varying from 35° to 70° and the surfaces of 100 m^2 to 10000 m^2 for an antenna height
588 of 100 m with $\mathcal{E}$ <35°. However, there is a limitation due to the maximum antenna height

(Figure 14b) that have to be lower than C/A code wavelength *i.e.* 293m otherwise the interference pattern is not constructive (Ribot et al., 2016).

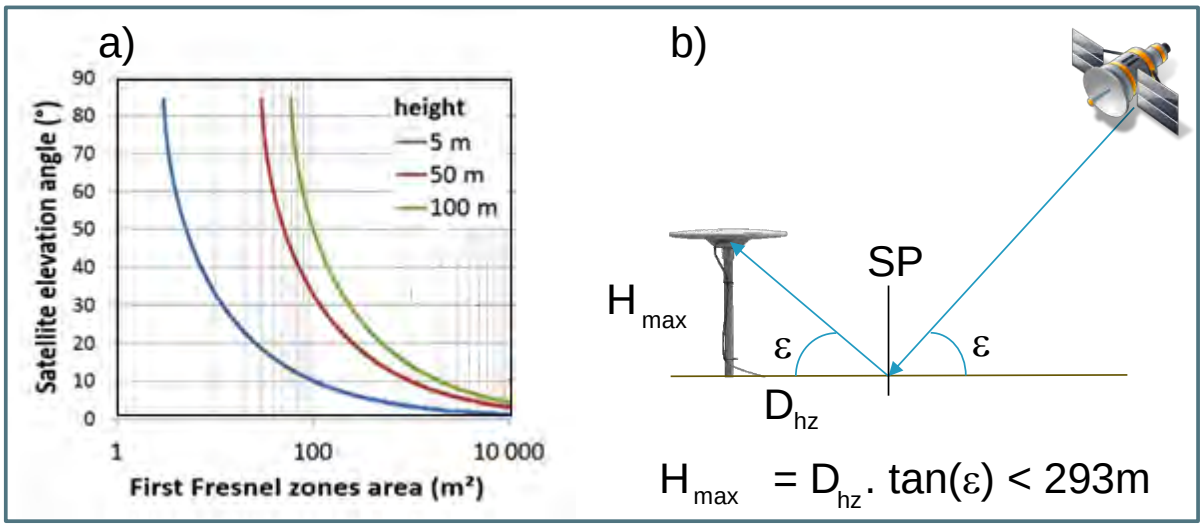

Figure 14: Evolution of explored scale for one satellite; a) First Fresnel area (log scale) as a function of antenna height and satellite elevation; b) IPT limitation, definition of the maximum antenna height depending on reflected path and ε.

7. Conclusion and perspectives

The classical IPT technique developed by Larson et al. (2008) provides a good retrieval of soil moisture for soils that are rich in clay as shown by previous studies [Chew et al., 2014; Vey et al., 2016; Zhang et al., 2017]. In the present study, we have demonstrated that this technique can also be used for sandy soils if we combine it with a phase unwrapping method to obtain a continuous phase measurement of the SNR multipath. In our case, the correlation, between soil moisture variations retrieved with our technique and VSM measured *in situ*, can reach up to 0.86 on an experimental beach volley field (100% of sand) and up to 0.97 on Dahra field (95% of sand).

Another attractive aspect revealed by this experiment is the ability of GNSS-R technique to map the spatial variability of the soil moisture, this cannot be done with neither a single nor few moisture probes. A detailed look at the three-observables computed by the IPT technique shows that the phase gives the best retrieval for the soil moisture, whereas the effective height has an important anti-correlation with VSM, the wave penetration increases in dry sand. The multipath amplitude gives poor results due to the parameters polluting amplitude of the reflected signal, *i.e.* ground roughness, soil heterogeneity. The explored surface is dependent on the antenna height and the satellite elevation, that is to say, we can explore local to intermediate spatial scales by increasing the antenna height: e.g. few square meters for an antenna height of ~1.5 m to more than 10000 m^2 for an antenna height of 50 m.

In the study case of Dahra, where the soil consists more than 95% sand, GNSS-R for detecting soil moisture using SNRm and IPT method to retrieve geophysical ground parameters represent a more complex observation of ground moisture: amplitude A_m gives only a trend it is probably disturbed by the presence of vegetation and ground roughness. The phase Φ_{unw} time series corrected by the unwrapping SNR phase method displays the best correlation with soil moisture. It seems less sensitive to the roughness and vegetation. The effective height h_{eff}^{unw} is well correlated but with a negative correlation, due to the wave penetration. This height increases when the water content decreases inside the soil. The combination of all GPS/GLONASS satellites in the processing of SNR data can be used to produce a complete sequence of time precision, which significantly improves the correlation with soil moisture, as well as the temporal resolution i.e. from 1 day to 10 min.

Using the methodology proposed in this paper, we can detect the change in soil moisture content from rainy to dry seasons in sandy soil.

We can also investigate soil moisture spatial variability, by creating series of the average soil moisture maps with temporal resolution of 6 hours, 12 hours or by-days periods for the ground surface around the GNSS receiver. The spatial resolution depends on the height of the antenna (Figure 13). GNSS-R has the potentiality of giving continuous and perennial time series during the next decades. Another interesting perspective is its capacity to give information at intermediate spatial scales which permit to better understand the scale enlargement from local/*in situ* to global/spatial ones.

Acknowledgements

The work of Minh-Cuong Ha and José Darrozes was performed within the GET laboratory (UMR CNRS 5563) in the framework of the MISTRALE H2020 and RTRA PRISM project. Authors would also like to thank M. Ndiobo Camara (ISE/UCAD Dakar) and the person who helped for collecting ground data.

638 References

639 Alonso-Arroyo, A., Camps, A., Aguasca, A., Forte, G., Monerris, A., Rüdiger, C., . . . Onrubia,
640 R. (2014, 12). Improving the Accuracy of Soil Moisture Retrievals Using the Phase
641 Difference of the Dual-Polarization GNSS-R Interference Patterns. *IEEE Geoscience*
642 *and Remote Sensing Letters, 11*, 2090-2094. doi:10.1109/LGRS.2014.2320052

643 Aranyossy, J., & Ndiaye, B. (1993). Étude et modélisation de la formation des dépressions
644 piézométriques en Afrique sahelienne. *Revue des sciences de l'eau, 6*, 81-96.

645 Archambault, J. (1960). *Les eaux souterraines de l'Afrique Occidental.* A. O. F. Hydraulic
646 Service.

647 Baghdadi, N., Cresson, R., El Hajj, M., Ludwig, R., & La Jeunesse, I. (2012). Estimation of
648 soil parameters over bare agriculture areas from C-band polarimetric SAR data using
649 neural networks. *Hydrology and Earth System Sciences, 16*, 1607-1621.
650 doi:10.5194/hess-16-1607-2012

651 Baghdadi, N., Holah, N., & Zribi, M. (2006). Soil moisture estimation using multi-incidence
652 and multi-polarization ASAR data. *International Journal of Remote Sensing, 27*, 1907-
653 1920. doi:10.1080/01431160500239032

654 Beckmann, P., & Spizzichino, A. (1987). *The Scattering of Electromagnetic Waves from Rough*
655 *Surfaces.* Artech House Radar Library.

656 Behari, J. (2006). *Microwave Dielectric Behavior of Wet Soils.* School of Environmental
657 SciencesJawaharlal Nehru UniversityNew DelhiIndia: Springer, Dordrecht.
658 doi:https://doi.org/10.1007/1-4020-3288-9

659 Braasch, M. S. (1996, 1). Multipath Effects. In P. Astronautics, & Aeronautics (Eds.). American
660 Institute of Aeronautics and Astronautics: Global Positioning System: Theory and
661 Applications. doi:10.2514/5.9781600866388.0547.0568

662 Brewster, D. (1815). On the Laws Which Regulate the Polarisation of Light by Reflexion from
663 Transparent Bodies. *Philosophical Transactions of the Royal Society of London, 105*,
664 125-159. Retrieved from http://www.jstor.org/stable/107362

665 Chan, S. K., Bindlish, R., O'Neill, P. E., Njoku, E., Jackson, T., Colliander, A., . . . Kerr, Y.
666 (2016, 8). Assessment of the SMAP Passive Soil Moisture Product. *IEEE Transactions*
667 *on Geoscience and Remote Sensing, 54*, 4994-5007. doi:10.1109/TGRS.2016.2561938

668 Chew, C. C., Small, E. E., Larson, K. M., & Zavorotny, V. U. (2014, 1). Effects of Near-Surface
669 Soil Moisture on GPS SNR Data: Development of a Retrieval Algorithm for Soil
670 Moisture. *IEEE Transactions on Geoscience and Remote Sensing, 52*, 537-543.
671 doi:10.1109/TGRS.2013.2242332

672 Chew, C. C., Small, E. E., Larson, K. M., & Zavorotny, V. U. (2015, 5). Vegetation Sensing
673 Using GPS-Interferometric Reflectometry: Theoretical Effects of Canopy Parameters
674 on Signal-to-Noise Ratio Data. *IEEE Transactions on Geoscience and Remote Sensing,*
675 *53*, 2755-2764. doi:10.1109/TGRS.2014.2364513

676 Chew, C., Small, E. E., & Larson, K. M. (2016, 7 01). An algorithm for soil moisture estimation
677 using GPS-interferometric reflectometry for bare and vegetated soil. *GPS Solutions, 20*,
678 525-537. doi:10.1007/s10291-015-0462-4

679 Cleverly, J., Eamus, D., Coupe, N. R., Chen, C., Maes, W., Li, L., . . . Huete, A. (2016). Soil
680 moisture controls on phenology and productivity in a semi-arid critical zone . *Science*
681 *of The Total Environment , 568*, 1227-1237.
682 doi:https://doi.org/10.1016/j.scitotenv.2016.05.142

683 Coopersmith, E. J., Cosh, M. H., & Jacobs, J. M. (2016). Comparison of In Situ Soil Moisture
684 Measurements: An Examination of the Neutron and Dielectric Measurements within the
685 Illinois Climate Network. *Journal of Atmospheric and Oceanic Technology, 33*, 1749-
686 1758. doi:10.1175/JTECH-D-16-0029.1

687 Darrozes, J., Roussel, N., & Zribi, M. (2016, 7). The Reflected Global Navigation Satellite
688 System (GNSS-R): from Theory to Practice. 50.

689 Doolittle, J. A., & Brevik, E. C. (2014). The use of electromagnetic induction techniques in
690 soils studies. *Geoderma, 223-225*, 33-45.
691 doi:https://doi.org/10.1016/j.geoderma.2014.01.027

692 Fatras, C., Frappart, F., Mougin, E., Grippa, M., & Hiernaux, P. (2012). Estimating surface soil
693 moisture over Sahel using ENVISAT radar altimetry. *Remote Sensing of Environment,*
694 *123*, 496-507. doi:https://doi.org/10.1016/j.rse.2012.04.013

695 Faye, G., Frison, P.-L., Diouf, A.-A., Wade, S., Kane, C. A., Fussi, F., . . . Mougin, E. (2017).
696 Soil moisture estimation in Ferlo region (Senegal) using radar (ENVISAT/ASAR) and
697 optical (SPOT/VEGETATION) data. *The Egyptian Journal of Remote Sensing and*
698 *Space Science*. doi:https://doi.org/10.1016/j.ejrs.2017.11.005

699 Fontaine, B., & Louvet, S. (2006). Sudan-Sahel rainfall onset: Definition of an objective index,
700 types of years, and experimental hindcasts. *Journal of Geophysical Research:*
701 *Atmospheres, 111*. doi:10.1029/2005JD007019

702 Gao, Q., Zribi, M., Escorihuela, M. J., & Baghdadi, N. (2017, 8). Synergetic Use of Sentinel-1
703 and Sentinel-2 Data for Soil Moisture Mapping at 100 m Resolution. *17*, 1966. doi:DOI:
704 10.3390/s17091966

705 Grinsted, A., Moore, J. C., & Jevrejeva, S. (2004, 11). Application of the cross wavelet
706 transform and wavelet coherence to geophysical time series. *{Nonlinear Processes in*
707 *Geophysics}, 11*, 561-566. Retrieved from https://hal.archives-ouvertes.fr/hal-
708 00302394

709 HA, C. M., Roussel, N., Darrozes, J., Frappart, F., Baup, F., Ramillien, G., & Llubes, M. (2015).
710 GNSS-R moisture quantification on a beach volley field: Single case or true benchmark?
711 *GNSS+R* . Potsdam, Germany.

712 Holzman, M., Rivas, R., Carmona, F., & Niclòs, R. (2017). A method for soil moisture probes
713 calibration and validation of satellite estimates. *MethodsX, 4*, 243-249.
714 doi:https://doi.org/10.1016/j.mex.2017.07.004

715 Hooper, A., & Zebker, H. A. (2007, 9). Phase unwrapping in three dimensions with application
716 to InSAR time series. *J. Opt. Soc. Am. A, 24*, 2737-2747.
717 doi:10.1364/JOSAA.24.002737

718 Hossain, A. K., & Easson, G. (2009, 10). *Microwave Remote Sensing of Soil Moisture in Semi-*
719 *arid Environment.* (I. Pei-Gee Peter Ho (Ed.), Ed.) Geoscience and Remote Sensing.
720 doi:DOI: 10.5772/8301

721 Kaleita, A., Heitman, J., & Logsdon, S. D. (2005, 9). Field calibration of the Theta Probe for
722 Des Moines lobe soils. *21*.

723 Kerr, Y. H., Waldteufel, P., Wigneron, J. P., Delwart, S., Cabot, F., Boutin, J., . . . Mecklenburg,
724 S. (2010, 5). The SMOS Mission: New Tool for Monitoring Key Elements ofthe Global
725 Water Cycle. *Proceedings of the IEEE, 98*, 666-687.
726 doi:10.1109/JPROC.2010.2043032

727 Kirkby, M. J. (2016). Water in the critical zone: soil, water and life from profile to planet. *SOIL,*
728 *2*, 631-645. doi:10.5194/soil-2-631-2016

729 Koyama, C., Liu, H., Takahashi, K., Shimada, M., Watanabe, M., Khuut, T., & Sato, M. (2017,
730 6). In-Situ Measurement of Soil Permittivity at Various Depths for the Calibration and
731 Validation of Low-Frequency SAR Soil Moisture Models by Using GPR. *Remote*
732 *Sensing, 9*, 580. doi:10.3390/rs9060580

733 Larson, K. M., Braun, J. J., Small, E. E., Zavorotny, V. U., Gutmann, E. D., & Bilich, A. L.
734 (2010, 3). GPS Multipath and Its Relation to Near-Surface Soil Moisture Content. *IEEE*
735 *Journal of Selected Topics in Applied Earth Observations and Remote Sensing, 3*, 91-
736 99. doi:10.1109/JSTARS.2009.2033612

737 Larson, K. M., Small, E. E., Gutmann, E. D., Bilich, A. L., Braun, J. J., & Zavorotny, V. U.
738 (2008). Use of GPS receivers as a soil moisture network for water cycle studies.
739 *Geophysical Research Letters, 35*, n/a--n/a. doi:10.1029/2008GL036013

740 Lebel, T., Cappelaere, B., Galle, S., Hanan, N., Kergoat, L., Levis, S., . . . Seguis, L. (2009).
741 AMMA-CATCH studies in the Sahelian region of West-Africa: An overview. *Journal*
742 *of Hydrology, 375*, 3-13. doi:https://doi.org/10.1016/j.jhydrol.2009.03.020

743 Leblanc, M., Razack, M., Dagorne, D., Mofor, L., & Jones, C. (2003). Application of Meteosat
744 thermal data to map soil infiltrability in the central part of the Lake Chad basin, Africa.
745 *Geophysical Research Letters, 30*, n/a--n/a. doi:10.1029/2003GL018094

746 Löfgren, J. S. (2014). *Local Sea Level Observations Using Reflected GNSS Signals.* phdthesis,
747 Department of Earth and Space Sciences, Chalmers University of Technology,
748 Gothenburg. Retrieved from
749 http://publications.lib.chalmers.se/records/fulltext/191472/191472.pdf

750 Lomb, N. R. (1976, 2). Least-squares frequency analysis of unequally spaced data. *Astrophysics*
751 *and Space Science, 39*, 447-462. doi:10.1007/BF00648343

752 Longobardi, A. (2008). Observing soil moisture temporal variability under fluctuating climatic
753 conditions. *Hydrology and Earth System Sciences Discussions, 5*, 935-969. Retrieved
754 from https://hal.archives-ouvertes.fr/file/index/docid/298941/filename/hessd-5-935-
755 2008.pdf

756 Lopez, T., Antoine, R., Kerr, Y., Darrozes, J., Rabinowicz, M., Ramillien, G., . . . Genthon, P.
757 (2016). Subsurface hydrology of the Lake Chad Basin from convection modelling and
758 observations. *Surveys in Geophysics, 37*, 471-502. doi:10.1007/s10712-016-9363-5

McDonald, R. I., Weber, K., Padowski, J., Flörke, M., Schneider, C., Green, P. A., . . . Montgomery, M. (2014). Water on an urban planet: Urbanization and the reach of urban water infrastructure. *Global Environmental Change, 27*, 96-105. doi:https://doi.org/10.1016/j.gloenvcha.2014.04.022

Mougin, E., Hiernaux, P., Kergoat, L., Grippa, M., Rosnay, P., Timouk, F., . . . Mazzega, P. (2009). The AMMA-CATCH Gourma observatory site in Mali: Relating climatic variations to changes in vegetation, surface hydrology, fluxes and natural resources. *Journal of Hydrology, 375*, 14-33. doi:https://doi.org/10.1016/j.jhydrol.2009.06.045

Njoku, E. G., & Entekhabi, D. (1996). Passive microwave remote sensing of soil moisture. *Journal of Hydrology, 184*, 101-129. doi:https://doi.org/10.1016/0022-1694(95)02970-2

Paloscia, S., Pettinato, S., Santi, E., Notarnicola, C., Pasolli, L., & Reppucci, A. (2013). Soil moisture mapping using Sentinel-1 images: Algorithm and preliminary validation. *Remote Sensing of Environment, 134*, 234-248. doi:https://doi.org/10.1016/j.rse.2013.02.027

Ribot, M. A., Botteron, C., & Farine, P.-A. (2016). Derivation of the Cramér-Rao Bound in the GNSS-Reflectometry Context for Static, Ground-Based Receivers in Scenarios with Coherent Reflection. *Sensors, 16*, 2063. doi:10.3390/s16122063

Rodriguez-Alvarez, N., Camps, A., Vall-llossera, M., Bosch-Lluis, X., Monerris, A., Ramos-Perez, I., . . . Sanchez, N. (2011, 1). Land Geophysical Parameters Retrieval Using the Interference Pattern GNSS-R Technique. *IEEE Transactions on Geoscience and Remote Sensing, 49*, 71-84. doi:10.1109/TGRS.2010.2049023

Rodriguez-Iturbe, I., & Porporato, A. (2007). *Ecohydrology of Water-Controlled Ecosystems: Soil Moisture and Plant Dynamics.* Cambridge University Press. Retrieved from https://books.google.fr/books?id=XERRFS6qT1kC

Roussel, N. (2015). *Application de la réflectométrie GNSS à l'étude des redistributions des masses d'eau à la surface de la Terre.* phdthesis, Université Paul Sabatier - Toulouse III, Toulouse.

Roussel, N., Frappart, F., Ramillien, G., Darrozes, J., Baup, F., Lestarquit, L., & Ha, M. C. (2016, 10). Detection of Soil Moisture Variations Using GPS and GLONASS SNR Data for Elevation Angles Ranging From 2° to 70°. *IEEE Journal of Selected Topics in*

790 *Applied Earth Observations and Remote Sensing, 9*, 4781-4794.
791 doi:10.1109/JSTARS.2016.2537847

792 Roussel, N., Frappart, F., Ramillien, G., Desjardins, C., Gegout, P., Pérosanz, F., & Biancale,
793 R. (2014, 1). Simulations of direct and reflected waves trajectories for in situ GNSS-R
794 experiments. *Geoscientific Model Development Discussions, 7*, 1001-1062.
795 doi:10.5194/gmdd-7-1001-2014

796 Roxy, M. S., Sumithranand, V. B., & Renuka, G. (2010, 8 01). Variability of soil moisture and
797 its relationship with surface albedo and soil thermal diffusivity at Astronomical
798 Observatory, Thiruvananthapuram, south Kerala. *Journal of Earth System Science, 119*,
799 507-517. doi:10.1007/s12040-010-0038-1

800 Scargle, J. D. (1982, 12). Studies in astronomical time series analysis. II - Statistical aspects of
801 spectral analysis of unevenly spaced data. *Astrophysical Journal, 263*, 835-853.
802 doi:10.1086/160554

803 Smith, L. C. (2002). Emerging Applications of Interferometric Synthetic Aperture Radar
804 (InSAR) in Geomorphology and Hydrology. *Annals of the Association of American*
805 *Geographers, 92*, 385-398. doi:10.1111/1467-8306.00295

806 Tian, S., Tregoning, P., Renzullo, L. J., Dijk, A. I., Walker, J. P., Pauwels, V. R., & Allgeyer,
807 S. (2017). Improved water balance component estimates through joint assimilation of
808 GRACE water storage and SMOS soil moisture retrievals. *Water Resources Research,*
809 *53*, 1820-1840. doi:10.1002/2016WR019641

810 Torbern, T., Rasmus, F., Idrissa, G., Olander, R. M., Silvia, H., Cheikh, M., . . . Jonas, A.
811 (2015). Ecosystem properties of semiarid savanna grassland in West Africa and its
812 relationship with environmental variability. *Global Change Biology, 21*, 250-264.
813 doi:10.1111/gcb.12734

814 Torrence, C., & Compo, G. P. (1998). A Practical Guide to Wavelet Analysis. *Bulletin of the*
815 *American Meteorological Society, 79*, 61-78. doi:10.1175/1520-
816 0477(1998)079<0061:APGTWA>2.0.CO;2

817 Torrence, C., & Webster, P. J. (1999). Interdecadal Changes in the ENSO–Monsoon System.
818 *Journal of Climate, 12*, 2679-2690. doi:10.1175/1520-
819 0442(1999)012<2679:ICITEM>2.0.CO;2

820 Verstraeten, W. W., Veroustraete, F., Sande, C. J., Grootaers, I., & Feyen, J. (2006). Soil
821 moisture retrieval using thermal inertia, determined with visible and thermal spaceborne
822 data, validated for European forests. *Remote Sensing of Environment, 101*, 299-314.
823 doi:https://doi.org/10.1016/j.rse.2005.12.016

824 Vey, S., Güntner, A., Wickert, J., Blume, T., & Ramatschi, M. (2016, 10 01). Long-term soil
825 moisture dynamics derived from GNSS interferometric reflectometry: a case study for
826 Sutherland, South Africa. *GPS Solutions, 20*, 641-654. doi:10.1007/s10291-015-0474-
827 0

828 Walker, J. P., Willgoose, G. R., & Kalma, J. D. (2004). In situ measurement of soil moisture: a
829 comparison of techniques. *Journal of Hydrology, 293*, 85-99.
830 doi:https://doi.org/10.1016/j.jhydrol.2004.01.008

831 Zebker, H. A., & Lu, Y. (1998, 3). Phase unwrapping algorithms for radar interferometry:
832 residue-cut, least-squares, and synthesis algorithms. *J. Opt. Soc. Am. A, 15*, 586-598.
833 doi:10.1364/JOSAA.15.000586

834 Zhang, S., Calvet, J.-C., Darrozes, J., Roussel, N., Frappart, F., & Bouhours, G. (2018).
835 Deriving surface soil moisture from reflected GNSS signal observations from a
836 grassland site in southwestern France. *Hydrology and Earth System Sciences, 22*, 1931-
837 1946. doi:10.5194/hess-22-1931-2018

838 Zhang, S., Roussel, N., Boniface, K., Ha, M. C., Frappart, F., Darrozes, J., . . . Calvet, J.-C.
839 (2017). Use of reflected GNSS SNR data to retrieve either soil moisture or vegetation
840 height from a wheat crop. *Hydrology and Earth System Sciences, 21*, 4767-4784.
841 doi:10.5194/hess-21-4767-2017

842

843

844

Figure caption

903

Chapter IV

GNSS-R for detection of extreme hydrological events: Red River Delta and Mekong Delta (Vietnam)

Contents

Accurate and continuous measurement of river water levels is a worldwide challenge to obtain continuous estimation of river discharge around the world. But it is quite difficult: in-situ gauges give continuous and punctual measurements whereas satellite altimetry closely monitoring vast territories but with orbital repeat cycle not too short to completely capture extreme and rapid hydrological events (flash flood, tidal bore etc.). We have applied this method on two user cases located in Vietnam. This two experiments monitored by the GET laboratory (UMR 5563) in the framework of the MISTRALE

H2020 project. For the first one we located the antenna/GNSS receiver couple of the delta of Red river (21° 2'44.04"N, 105°51'48.86"E) to identify flood events and morphological changes associated to these hydrological events. This measurements was done since the 27th july until 12th august 2016, during the period of the Mirinae and Nida storms. And the second one, during 23th-31th August 2016, is located close to the mouth of the Mekong river (9°31'38.63"N, 106°12'2.01"E) where continental water interacts with oceanic water. GNSS-R height retrieval is obtained from SNR multipath, and to increase the number of reflection point we used both GLONASS/GPS constellations. The results will be compared with in-situ tide/river gauge. We demonstrate that the assumption for obtaining useful continuous and spatial measurements of river level from GNSS-R is promising. We obtain not only the height river, but we also retrieve the local slope of the water surface, and flooded areas.

IV.1 Introduction

Global warming may result in intensifying many subsystems of the global water cycle. This can increase the flood magnitude as well as flood frequency, making weather less predictable and increase precipitation uncertainly. Over the past three decades, flooding and coastal storms increase and have been linked with climate change, and the number of disastrous floods and storms reported globally has tripled (Kunkel et al., 2013; Woodruff et al., 2013). Floods are difficult to monitor on large scales, because they are triggered by local conditions such as precipitation, slope of terrain, drainage network, protective structures, land cover, and other factors. Each river or coastal area must be monitored at different places along its course and/or its border. Some flood disasters happen annually, yet others can occur unexpectedly (Groeve, 2010; Harman et al., 2013).

The substantial sea level rise and more frequent storms predicted for the next 50–100 years would affect coastal cities and roads, coastal economic development, beach erosion control strategies, salinity of estuaries and aquifers, coastal drainage and sewage systems, and coastal wetlands (Doornkamp, 1998; Cazenave and Llovel, 2010; Cazenave and Cozannet, 2014). During flooding, timely and detailed situation reports are required by disaster management authorities to locate and identify the affected areas and to implement the required damage mitigation. This critical management function involves rescue operations and the safety of people and property (Haq et al., 2012; Ogashawara et al., 2013).

Traditionally, coastal flooding due to hurricanes has been estimated by measured water levels on buoys and coastal tide gauges. Although these monitoring networks provide good historical data for coastal flooding, they lack of spatial information because of the limited number of stations over many large areas. For the past few decades, optical and radar remote sensing systems on satellites and aircraft have been able to provide much of the required information for mapping the extent of a flood, assessing the damage, and feeding models that can evaluate the vulnerability to flooding of various inland and coastal areas. Conventional hydrological monitoring systems have limited use in flood forecasting, mapping, and emergency response. For adequate flood warning (ect. Red River, Mekong from China to Vietnam), countries need to be able to collect information across borders independently. Furthermore, gauging stations measure water height, but not the extent of the flood.

GNSS reflectometry thus appears as an excellent alternative to conventional space altimetry in the coastal domain, the lake or the river (See Fig. II.23) with an accuracy up to a few centimeters using ground or on-board systems (Lowe et al., 2002c; Ruffini et al., 2004; Löfgren et al., 2011; Semmling et al., 2011; Rius et al., 2012). In addition, the downstream processing chain is simpler, a large number of permanent GNSS stations are located on the coast in Europe and around the world, and using those on the seaside for altimetry measurements by GNSS-R would be quite feasible(Fig.IV.1). A whole net-

work would thus already be in place, and only the processing algorithm remains to be developed. This is particularly important at a time when it is a question of co-locating GNSS stations with tide gauges and sea/river/lake water surface's level.

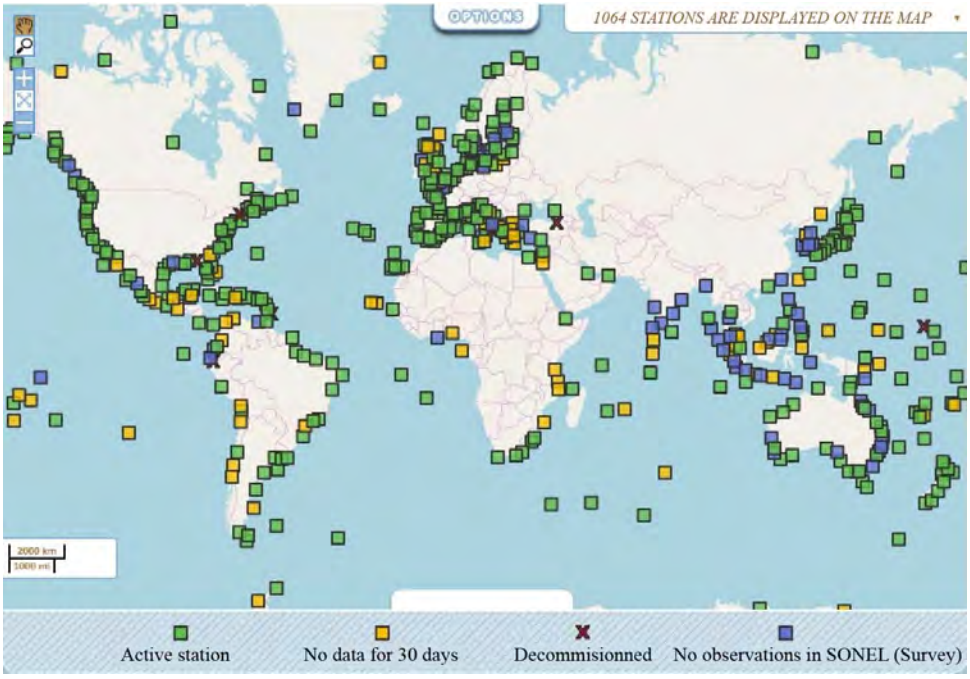

Figure IV.1 – GNSS Observations station for surveying water surface's level of the program GLOSS (Global Sea Level Observing System - `http://www.sonel.org/-GPS-.html`)

It is therefore of interest to study in detail the potential of GNSS-R for altimetry in hydrological environments, and particularly the single-antenna system based on the SNR method. In my thesis, I have mainly been interested in this promising technique for monitoring storms, flood areas and altimetry of river, and I propose to use both LSM and Larson methods (see next section) (Roussel et al., 2015b).

IV.2 Methodology

The objective is to estimate the variations of height h through the temporal variations deduced from the SNR measurements for each satellite in view base on the method IPT (SNR Static case, developed by Larson et al. (2008b), see § II.3.4, eq. II.38). And the method in the dynamic case of SNR, known as LSM (Roussel et al., 2015b), is based on the determination of the time series $f(t)$ of the frequency of the oscillations due to the multipath. By combining the time series $f_i(t)$ measured for each satellite i simultaneously visible, it is possible to construct an over-determined linear equation system based on equation [II.37] for a time period dt, with only two unknowns: h and $\dot{h}$. Such a system

of equations can be solved by applying the least squares criterion-based formalism. The main points of this method are presented in this section, and synthesized in figure IV.2.

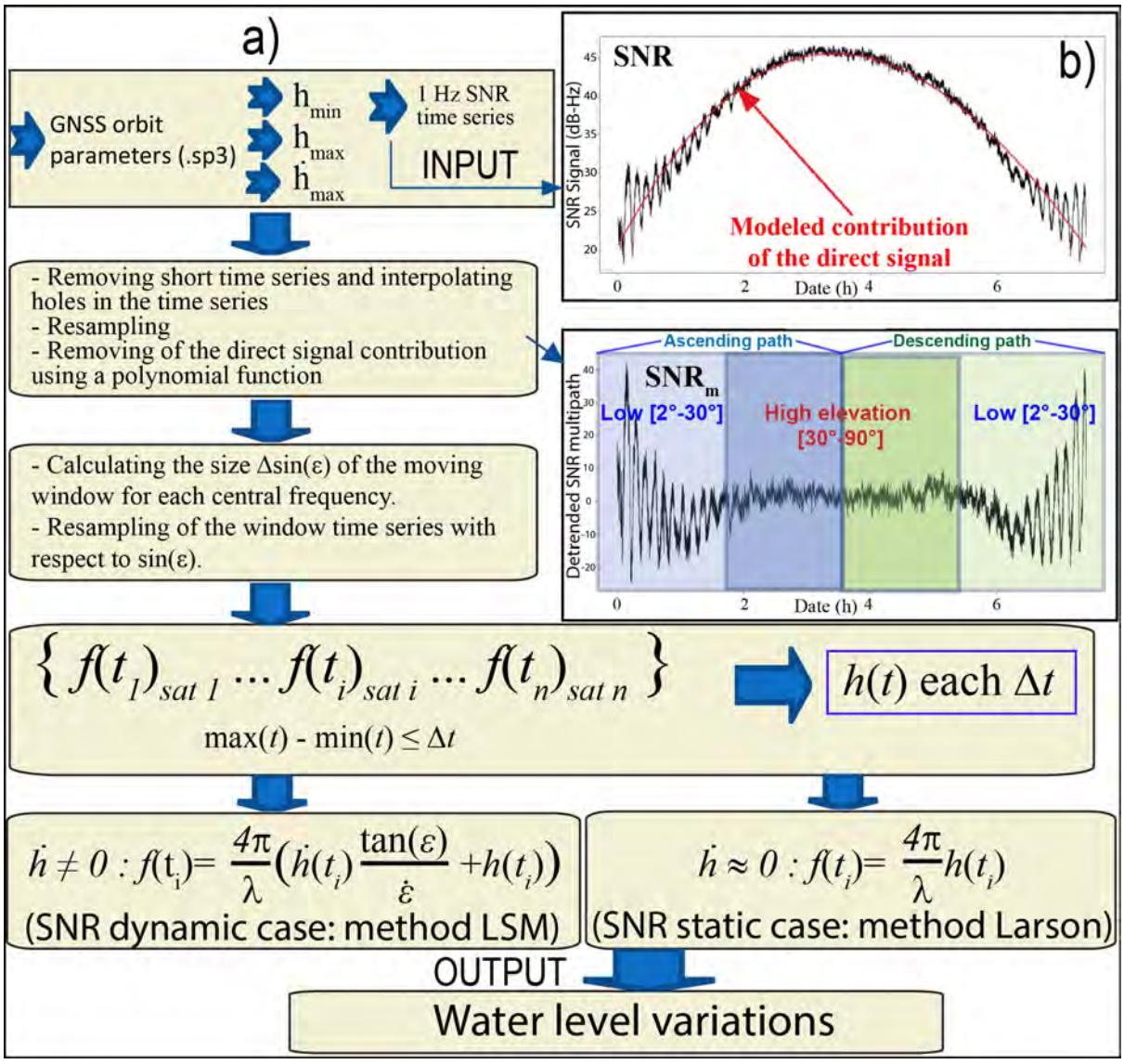

Figure IV.2 – SNR data processing chain used for altimetry of the water surface, based on a single antenna reflectometer. Time series are from the GPS satellite. a) Flow chart presenting the processing of the SNR data using Least Square Method (LSM) and Interference Pattern Technical method (IPT-method Larson): the input, the different steps of the processing, and the output; b) Example of a time series of SNR measured on L of the GPS constellation during August 2, 2017. SNR related to the addition of the powerful direct and weaker reflected GNSS signals in the receiving antenna and SNR_m with the direct signal contribution is removed from the raw SNR profile, modified from (Roussel et al., 2015b).

IV.2.1 SNR-Least Square Method for the estimation of the continental water level

As explained in section II.3.4, the direct signal and the reflected signal interfere at the antenna. The quasi-sinusoidal aspect of the time series of the SNR consists of a low frequency due to the direct signal and a high frequency due to the reflected signal, which is denoted SNR_m and very high frequencies correspond to white noise. The intermediate/high of the SNR oscillations due to the multipath (SNR_m) as a function of the sine of the elevation angle is expressed in this form (see §II.3.4, eq. II.37). Variation of $\dot{h}$ may be important when looking at ocean or continental waters (waves, height of the water line for river). In this case, $\dot{h}$ can not be neglected, f also depends on the elevation angle θ, the satellite elevation velocity $\dot{\theta}$, and the variations of the effective antenna height over time $\dot{h}$. If the first two parameters are known, the determination of h and $\dot{h}$ remains problematic because we have two unknowns for a single satellite observation of f (i.e., under-determined case).

Some proposals have been made to take account of this. For example, Löfgren (2014) suggested two iterations: the first approximates $h(t)$ by neglecting $\dot{h}$, and the second incorporates an estimate of $h(t)$ based on a theoretical sinusoidal function adjusted to $\dot{h}$ from the first iteration. The underlying idea is that during one day the change in water level is mainly due to the diurnal and semi-diurnal tides of known frequencies and it is therefore possible to predict a theoretical sinusoidal function. This two-step method improves the accuracy of the results, but requires prior knowledge of the phenomena likely to influence the antenna height in the study area.

(Larson and Nievinski, 2013) proposed a similar method, also based on two iterations. The first iteration determines an approximate value of $h(t)$ by neglecting $\dot{h}$. The temporal series $h(t)$ thus obtained is derived to calculate the time series $\dot{h}$. The second iteration will integrate these values of $\dot{h}$ to determine more precise values of $h(t)$. Unfortunately, this method only works for small values of $\dot{h}$ and can not be used in the sites of extreme hydrological events for example.

In my thesis, for the method Least Square Method (SNR dynamic case - LSM) I used the method proposed by Roussel et al. (2015b), which allowing h and $\dot{h}$ to be determined simultaneously using multiple satellites, we have an over-determined system of equations that can be solve.

IV.2.1.1 Determination of the time series SNR_m(t)

The goal is to measure $f(t)$, the frequency of SNR_m oscillations, in order to deduce the variations of the antenna height $h(t)$ based on the equation in SNR processing chain (Fig. IV.2a). Since the frequency f is not stationary, a windowing of the time series $SNR_m(\sin(\theta))$ is necessary to determine its variations over time intervals. The choice of

the sliding window is a critical parameter because it must meet antithetical requirements. The window must be large enough to be able to precisely identify the fundamental frequency of the oscillations, but it must not be too wide for the frequency variations to be quasi-constant over the considered temporal portion.

Let $\Delta\sin(\theta)$ be the size of the moving-average window. To obtain the suited size $\Delta\sin(\theta)$ corresponding to each central value, an a priori coarse knowledge of the parameters under determination is mandatory. Ones have to consider the following three parameters as known by the user:

- h_{min}(m): the minimum vertical distance that can be observed between the antenna (fixed) and the reflected surface (water level of the river);
- h_{max}(m): the maximum vertical distance that can be observed between the antenna (fixed) and the reflected surface (water level of the river);
- $\dot{h}_{max}$(m/s): the maximum vertical velocity of the reflecting surface.

The more precise the knowledge of these three values is, the faster the determination of f will be. From these values, we estimate expected f_{min} and f_{max} for each central value. In order to get the largest moving window through which the frequency could be considered as constant, and to include enough variations of f within the chosen window, the following two conditions (Roussel et al., 2015b) are considered:

$$\Delta\frac{F_{max}}{f} \leq x \tag{IV.1}$$

$$\frac{N_0}{f_{min}} < \Delta(\sin(\theta)) \tag{IV.2}$$

With x (in %) the maximal variation of f accepted within the moving window, N_0 the minimal number of observed periods within the moving window (needed to verify f, which is quite constant over the considered period), and f_{max} is the maximal variation over time of the frequency. Δf_{max} is computed from equation [IV.5] as follows:

$$\frac{df}{dt} = \frac{2}{\lambda}(\dot{h} + \frac{\ddot{h}\tan(\theta)}{\dot{\theta}} + \frac{\dot{h}}{\cos^2(\theta)} - \frac{\dot{h}\ddot{\theta}\tan(\theta)}{\dot{\theta}^2}) \tag{IV.3}$$

$$\frac{df}{d(\sin(\theta))} = \frac{df}{dt}\frac{dt}{d(\sin(\theta))} = \frac{df}{dt}\frac{1}{\dot{\theta}\cos(\theta)} \tag{IV.4}$$

Considering the maximal value $\dot{h} = \dot{h}_{max}$ ´ and $\ddot{h} = 0$ within the moving-average window, we have [IV.5]:

$$\frac{\Delta f_{max}}{d(\sin(\theta))} \leq |\frac{2}{\lambda\dot{\theta}\cos(\theta)}|(\dot{h}_{max} + |\frac{\dot{h}}{\cos^2(\theta)}| + |\frac{\dot{h}\ddot{\theta}\tan(\theta)}{\dot{\theta}^2}|) \tag{IV.5}$$

N_0 could be estimated using the SNR_m time-series, which means that a minimum of N_0 periods are required in the moving window to estimate correctly f. With regards to x (in %) empirically derived by "trial and error" and verifying the first condition [IV.1]; x gives the most numerous estimations of f for each satellite and the best significance result from LSP.

It is important to note that f_{min} and f_{max} will be different for each moving window because the mean elevation (in rad) and elevation rate ($rad.s^{-1}$) change for each window. We thus estimate an optimized size $\Delta(\sin(\theta))$ of moving-average window guaranteeing to have at least N_0 periods of a quasi-constant frequency. Thus, this size is not constant over the time-series and is re-estimated for each time increment.

IV.2.1.2 Determination of the frequency *f* of the SNR multipath oscillation

The main frequency f is estimated using Lomb-Scargle periodogram (LSP): Lomb (1976); Scargle (1982), which seems to be a suitable solution. The LSP is achieved for each moving window. Knowing the three considered parameters of h_{min}, h_{max} and $\dot{h}_{max}$, the theoretical value of f_{min} and f_{max} can be determined. It is thus not any more necessary to consider the whole spectra of the signal under study, but it is sufficient to only consider frequencies ranging from f_{min} to f_{max} to compute the LSP. Only periodogram peaks significant at 0.01 and presenting a unique local maximum in the interval between f_{min} and f_{max} are considered.

IV.2.1.3 Determination of the height *h* of the antenna with respect to the reflection surface

Once f is accurately estimated for each satellite in sight of the receiver, h can be obtained solving [II.38], with two unknowns' h and $\dot{h}$. The solution presented, in this study, consists in combining measurements from all the GNSS satellites in sight at a given time to define conjointly $h(t)$ and $\dot{h}(t)$. Using a classical LSM resolution as detailed hereafter.

Let $f = \frac{d\psi}{dt}$, $U = \frac{4\pi \tan(\theta)}{\lambda \dot{\theta}}$ and $V = \frac{4\pi}{\lambda}$, we obtain for a satellite i and for an instant t:

$$f_i(t) = U_i \dot{h}(t) + V_i h(t) \tag{IV.6}$$

with $f_i(t)$ being the frequency of the multipath oscillations, with respect to the sine of the satellite i. Combining all the visible satellites at each time t, we obtain an equation

system:

$$\begin{aligned} f_{i=1}(t) &= U_{i=1}\dot{h}(t) + V_{i=1}h(t) \\ f_{i=2}(t) &= U_{i=2}\dot{h}(t) + V_{i=2}h(t) \\ &\vdots \\ f_{i=2n}(t) &= U_{i=n}\dot{h}(t) + V_{i=n}h(t) \end{aligned} \tag{IV.7}$$

Or in matrix structure:

$$F = U\dot{h}(t) + Vh(t) = AX \tag{IV.8}$$

with $A = (U \quad V)$ and $X = \binom{\dot{h}(t)}{h(t)}$, [IV.8] solved with the Least Square Inversion Method (LSM, Fig. IV.3) at each time step, thus determining conjointly *h(t)* and $\dot{h}(t)$ as follows:

$$X = (A^t A)^{-1}(A^t F) \tag{IV.9}$$

All GNSS satellites from the different constellations (GPS, Galileo, GLONASS and others) are likely combined in this over-determined system.

The main challenge is to find the correct time interval Δt between each estimation and also the length δt of the moving window (Roussel et al., 2015b). Δt and δt must be chosen with attention to have a large enough temporal resolution for h and $\dot{h}$. The number of satellite observations available decreases with δt and so the accuracy of the determination of h and $\dot{h}$ using LSM. Yet, choosing a too large value for δt causes an inaccurate determination of the unknown parameters since the receiver height would have changed during this interval. Unlike the static case which provide an estimation of the time series $h_i(t)$ for each satellite i.

For the altimetry application, the LSM method provides a single time series $h(t)$ combining all satellites. Nevertheless, the temporal resolution of the static consideration is limited by the repeat-ability of the GNSS constellations (i.e.), a maximum of four estimations by day, one during the descending phase, one during the ascending phase with twice passes per day per satellite for the GPS constellation, whereas the dynamic case provides a far better temporal resolution (depending on the chosen δt).

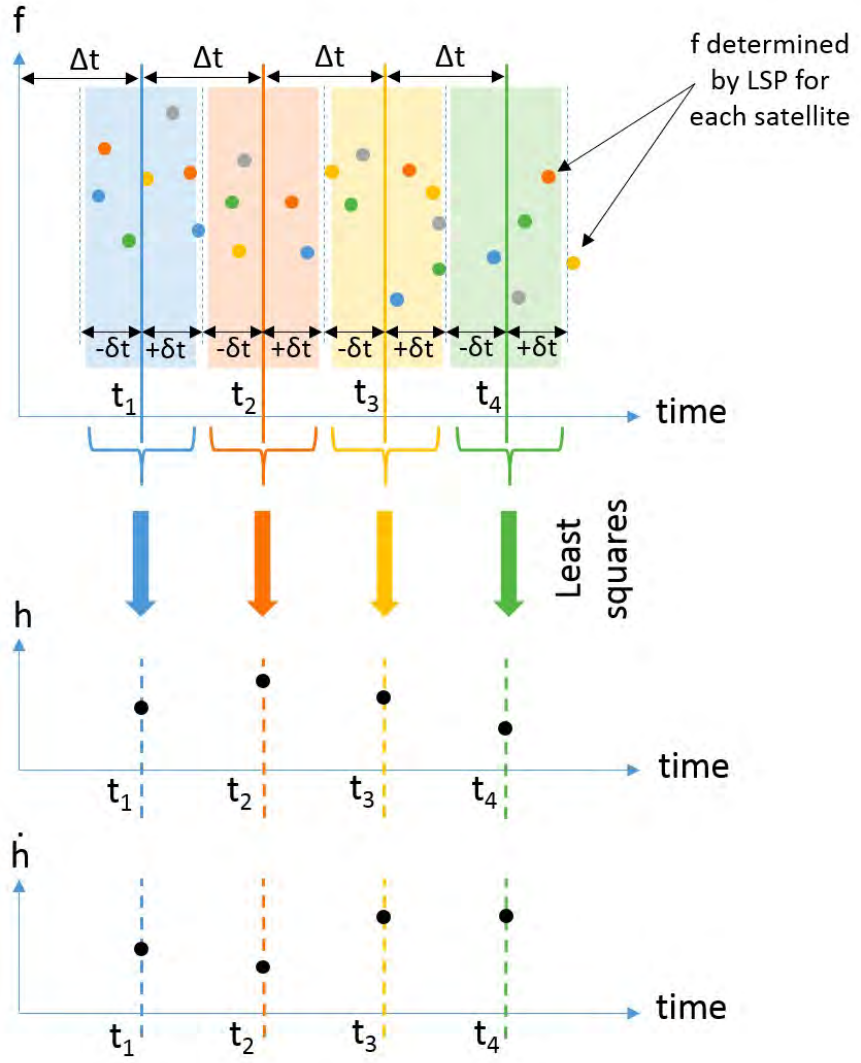

Figure IV.3 – Principle of Least Square Inversion Method used to determine h based on LSP estimates of f. For reasons of clarity, overlapping was not represented in this figure, even if our case $\delta t > \Delta t$. From Roussel et al. (2015b)

IV.3 Mekong Delta experiment (Vietnam)

IV.3.1 Presentation of the measurement site and experimental conditions

The experiment site was decided in Tran De district, Soc Trang province, Vietnam. This interesting site has show the competition between hydrological regime (continental waters of Mekong river and tides (oceanic ater) and may be during storm oceanic waves, are more stable with an average speed of 0.4-0.5 m/s. In winter, the flow direction has the same direction and under the influence of the north-east monsoon. Near the coast, flow orientation is more complex due to the influence of the estuaries and canals flowing into the sea. Coastal tides of the study area are semi-irregular, with a tidal amplitude in Hau river (Mekong River Delta) estuary at about 3m (tides) and 1.80m (low tide). Tidal amplitude decreases with the upstream distance . According to monitoring data in Vung Tau stations, the highest average tide peak of 4.43m (in months 10, 11) and the lowest is 0.58m in May, August. The highest tide feet - 0.24m (November) , the lowest tide feet - 3.0m (June).

To monitor this area we used a Leica GR25 receiver and an AR10 antenna was set up at $\sim$ 30 m above the ground surface, on the top of the Tran De water tower (106°12'10.17"E, 9°31'27.16"N). The Tran De water tower located in the Tran De port at 100 m from the Mekong River and at the same place of the Tran De hydrological station (Fig. IV.4). SNR data were acquired from 23th to 30th August 2016 at a 10 Hz frequency. The experiment monitored by the GET laboratory (UMR 5563) in the framework of the MISTRALE H2020 project and the ERGO project (Experience de mise en place d'un Reseau GNSS-R sur Rivière et Ocean au Vietnam-University Paul Sabatier).

The *in-situ* data used in this experiment consist in records of tide/river gauge from two hydrological stations over the period of acquisition: Tran De (106°12'10.17"E, 9°31'27.16"N), Dai Ngai (106°04'27.3" E, 9°44'4.4"N). The water level measurements are obtained at a 1h time sampling.

Positions of the specular reflection points on the surface have been determined through direct modeling using GRESS developed by Roussel et al. (2014). To remove the effect of the continent on the reflected signal, we used satellite elevation angles θ from 0° to 20° and an azimuth mask from 0° to 140° (Fig. IV.5).

Figure IV.4 – The GNSS receiver with a single antenna set up at about 30 m above sea level, on the top of the Tran De water tower (106°12'1.96"E; 9°31' 38.37"N, MeKong Delta - Vietnam).

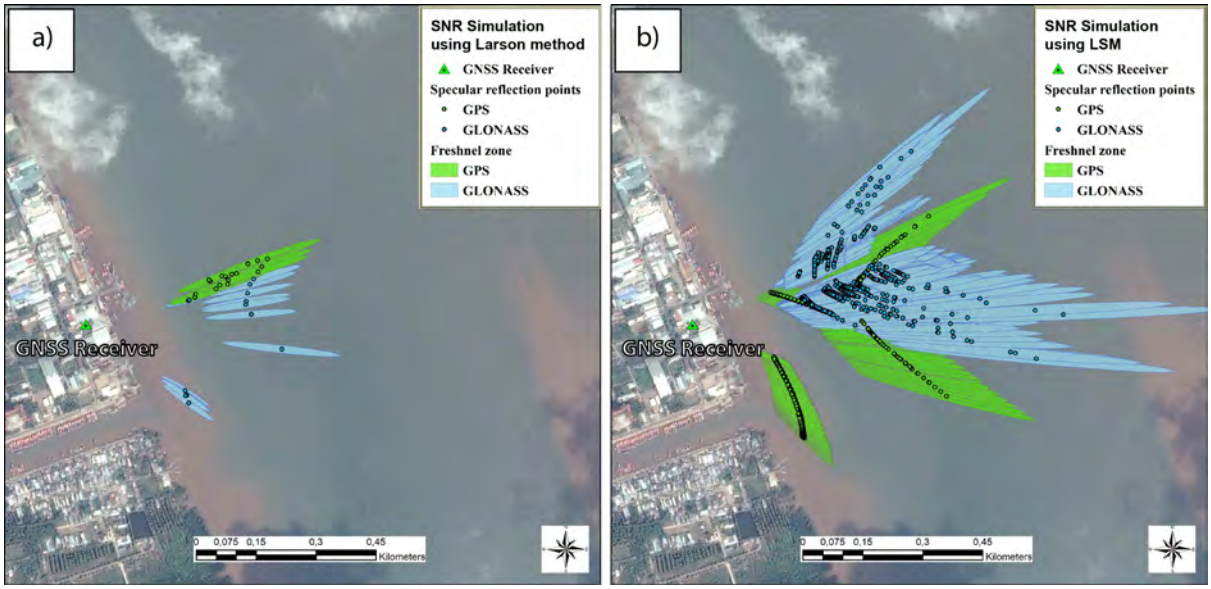

Figure IV.5 – Locations of the specular reflection points and fresnel surface for a GNSS receiver on the top of the Tran De water tower from 23th to 30th August 2016 (all satellites with elevation angles from 0° to 20°): a) Simulation of SNR multipath using IPT method of Larson et al. (2008b); b) Simulation of SNR multipath using LSM method of Roussel et al. (2015b).

IV.3.2 Parameters for SNR data analysing

The following two methods were tested:

- A static SNR method (IPT classic - Larson et al. (2013); § II.3.4): $\dot{h} \approx 0$, f is constant and directly proportional to the receiver height above the reflecting surface.
- A dynamic SNR method (Least Square Method - Roussel et al. (2015b); § IV.2.1): $\dot{h} \neq 0$, the time series $f(t)$ of the frequency of the multipath oscillations from the SNR data of each GNSS satellite. The input parameters chosen are: $h_{min} = 26m$, $h_{max} = 34m$ and $\dot{h}_{max} = 5 * 10^{-4} mm/h$ (i.e., $1,5 * 10^{-3} mm/h$).

IV.3.3 Comparison between the height derived from GNSS-R and *in-situ* gauge records

The water level height derived from SNR was compared to records obtained from a traditional Tran De tide gauge (located downstream at 450 m from GNSS station) and a Dai Ngai river gauge (located upstream at 26.7 km from GNSS station).The height h estimated from two applied methods gives good results with correlation coefficient more than 80% when compare with *in-situ* gauge. The dynamic case is less correlated, due to the fact the reflecting surface is relatively static and less affected by waves, but it has more accuracy than the static one (Figs. IV.5, IV.6 and Table IV.1).

The results in Tab. IV.1 shows that the water level is obtained when combined both GPS and GLONASS data is better than no combination. Time series variations of water level at the Tran De station over 23 to 30 August 2016 are showed in Fig. IV.6.

In this study, we demonstrated that SNR data from GNSS-R receivers allows estimating the water level with high accuracy in the estuarine areas impacted by different phenomenon of different characteristics such as hydrological regime, storm, waves and etc. The water level derived from SNR signal provides results of similar quality the classical gauges when using both GPS and GLONASS satellite (R reach ~ 0.85 in complex environment). So it can allow evaluating the performances of GNSS-R for monitoring river changes.

TABLE IV.1 – Comparison between the *in-situ* gauges with the raw SNR-based time series calculated with only the GPS and/or GLONASS constellation. (a) In Static case, (b) In Dynamic case.

a)	SNR Static case (method Larson)			
Hydrological station	GNSS constellations	Bias (m)	RMSE (m)	Corr. Coeff.
Tran De station	GPS	0.08	0.32	0.92
	GLONASS	0.01	0.52	0.83
	GPS+GLONASS	0.12	0.36	0.93
Dai Ngai station	GPS	0.09	0.41	0.78
	GLONASS	0.04	0.57	0.67
	GPS+GLONASS	0.14	0.45	0.82
b)	SNR Dynamic case (method LSM)			
Hydrological station	GNSS constellations	Bias (m)	RMSE (m)	Corr. Coeff.
Tran De station	GPS	0.02	0.49	0.83
	GLONASS	0.09	0.65	0.68
	GPS+GLONASS	0.13	0.5	0.85
Dai Ngai station	GPS	0.05	0.44	0.79
	GLONASS	0.1	0.56	0.62
	GPS+GLONASS	0.14	0.44	0.81

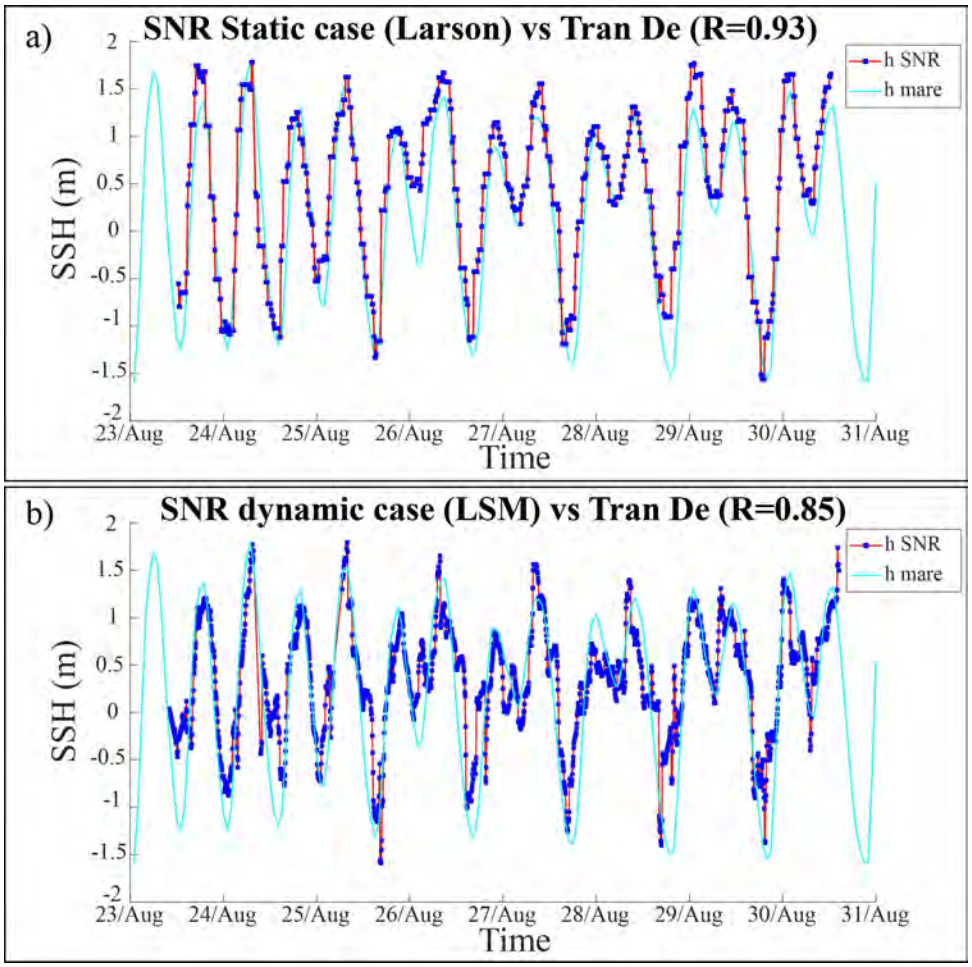

Figure IV.6 – Comparisons between height estimated from SNR measurements obtained with method LSM (a, 1989 measurements), method Larson (b, 369 measurements) vs Tran De tide gauge (cyan line), from 23th to 30th August 2016.

IV.4 Red River Delta experiment (Vietnam)

IV.4.1 Presentation of the study area and datasets available

The Red River Delta (RRD), which is located in the northern part of Vietnam, is a very complex hydrological network that has been heavily impacted by human activity. The area of the RRD covers $\sim$ 14,300 km^2 , entirely lying below three meters above sea level and much of it does not rise more than one meter above sea level. The RRD is limited landwards by the town of Son Tay in the north–west (150 km from the sea) and seawards by the coastline, which extends 360 km from Hai Phong province in the north-east to the Ninh Binh province in the south.

Every year the sea storms and south-west monsoon has caused heavy rains in the upstream region and northern plains. Due to the impact of weather volatility worldwide as waters of El Nino and La Nina, sea storms and heavy rains occur more violent than ever. Hurricane season usually from June to October, has an annual average number of 4 storms.These storms often come from the Philippines, South China Sea and the western Pacific and then 3-4 days later to the coast of Vietnam. Upstream terrain includes mountainous areas with steep slopes, rainwater quickly passed down to the plains. The majority of this major floods occurred in August, aimed at the height of the rainy season.

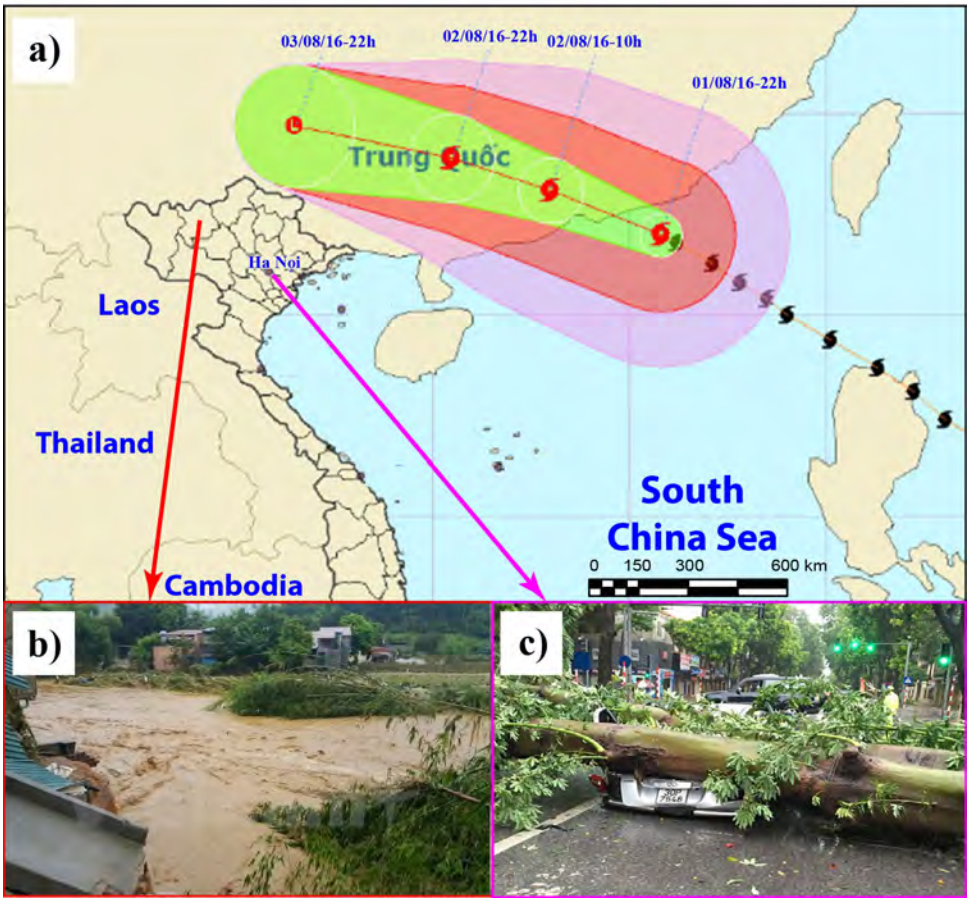

Figure IV.7 – a) Strong tropical storm that struck China and Northern Vietnam in late July 2016; b) Circulation impact of the storm Nida in some parts of the Lao Cai province caused severe flooding (4/8/2016); c) The Mirinae with heavy rain and intensive gusts in Hanoi caused serious accidents (28/07/2016).

IV.4.1.1 GNSS-R installation

The same equipment as for the previous station were installed on the top of the old bridge abutment (21° 2'44.04"N, 105°51'48.86"E) on the Red River in Hanoi, Vietnam (Fig. IV.8). GPS L1, L2 (S1C, S2W) and GLONASS L1 (S1C) frequencies were continuously acquired in rainy and windy conditions during the period of the Mirinae and Nida storms (Fig. IV.7), from the 27th July to 12th August 2016 at both sampling frequencies 1 Hz and 10 Hz.

Figure IV.8 – The GNSS receiver with a single antenna installed on the top of of the old bridge abutment (21° 2'44.04"N, 105°51'48.86"E) on the Red River in Hanoi, Vietnam from the 27th July to 12th August 2016.

IV.4.1.2 River gauge data

In-situ gauge collected with Hydrological Meter, located at the same place of the experiment site (Fig. IV.8), recorded from Hanoi Environmental Hydrology Station, National

Centre for Hydro-meteorological Forecasting. The water level measurements are obtained at a 1h time sampling. In the period of this campaign, the Mirinae storms caused heavy rains, large quantities of water from upstream (China) came to downstream (Red River Delta) and released into the sea, the water level recorded from hydrological station on the site measurement was therefore changing and increasing quickly (Fig. IV.7). As a result, many areas are flooded, in the figure IV.9 you can see large flooded area during this period in the mudflats/oasis of agricultural crops in the middle of the Red River. There are lots of those oasis were totally flooded.

IV.4.1.3 Site interest

Due to the safety of the instruments and the location of the GNSS station placed within the same location as gauging stations, on the top of the old bridge abutment (Fig. IV.8), the SNR multipath signals obtained will be disturbed in the south directions of the GNSS antenna by the Long-Bien bridge multipaths. Therefore, positions of the reflection points on the surface and their Fresnel zones have been determined using GRESS with azimuth mask from 0° to 70° (satellite elevation angles θ limited from 18° to 70°; north-east side of the antenna) and the azimuth from 240° to 360° with θ limited from 6° to 70° in the north-west side of the antenna (Fig. IV.9). The maximum of the Fresnel zones measured $\sim 1000m^2$ at the low satellite elevation and $\sim 10m^2$ at the high satellite elevation.

IV.4.2 Parameters for SNR data analysing

The following two methods and input parameters for SNR data analysing have been chosen:

- A static SNR method (§ II.3.4): $\dot{h} \approx 0$, f is constant and directly proportional to the receiver height above the reflecting surface.
- A dynamic SNR method (§ IV.2.1): $\dot{h} \neq 0$, the time series $f(t)$ of the frequency of the multipath oscillations from the SNR data of each GNSS satellite. The input parameters chosen are: $h_{min} = 14m$, $h_{max} = 20m$ and $\dot{h}_{max} = 5 * 10^{-4}$. $\dot{h}_{max}$ was chosen is approximately 3 times the maximum water level fluctuations observed by Hanoi hydrological station (= 4 m) during the floods period.

IV.4.3 Results

Unlike the Mekong Delta experiment, the Red river study area is located far from the estuary, so the water level is not influenced by tides. In this site, with the characteristics of GNSS location measurement stations, the two methods has applied for retrieving variations of water level h using two different ranges of satellite elevation (Fig. IV.9).

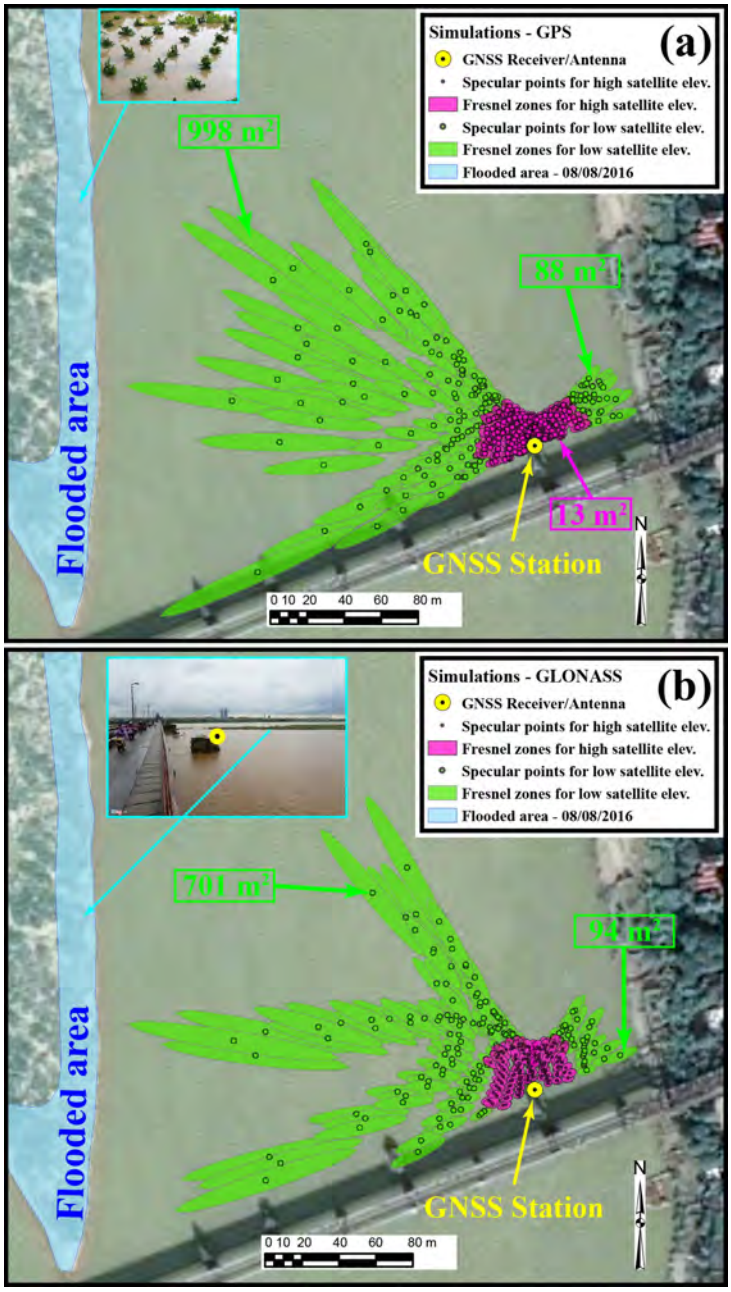

Figure IV.9 – Position of the GPS (a), GLONASS (b) specular reflection points and their first Fresnel surface for a GNSS receiver on Red River campaign. Simulations done the 08$^{\text{th}}$ of August 2016 with two range of Satellite elevation angles θ: High satellite elevation (in magenta; from 30° to 70°) and Low satellite elevation (in green; 6°-30° in the left side and 18°-30° in the right side). Sampling rate is equal to 15 mins (i.e., satellites positions are actualized every 15 mins);The cyan area shows flooded area during the storm event.

Comparing with the water level recorded by the Hydrological station, correlation coefficients obtained from both methods gives good results but the difference is in the number of solution computed : Larson gives accurate results but for a limited number of points whereas LSM gives a large number of accurate solutions (Fig. IV.10). The height h estimated with high satellite elevation gives accuracy of $\sim 10cm$ better than from low satellite elevation (6°-30° in the left side and 18°-30° in the right side of the GNSS station). Comparing between L_1 and L_2 frequencies, as it is known for GPS measurements, L_2 is more noisy but gives accurate measurements and for GLONASS constellation, L_2 is more accurate than L_1 with a RMSE $\leq$ 10 cm (Table IV.2).

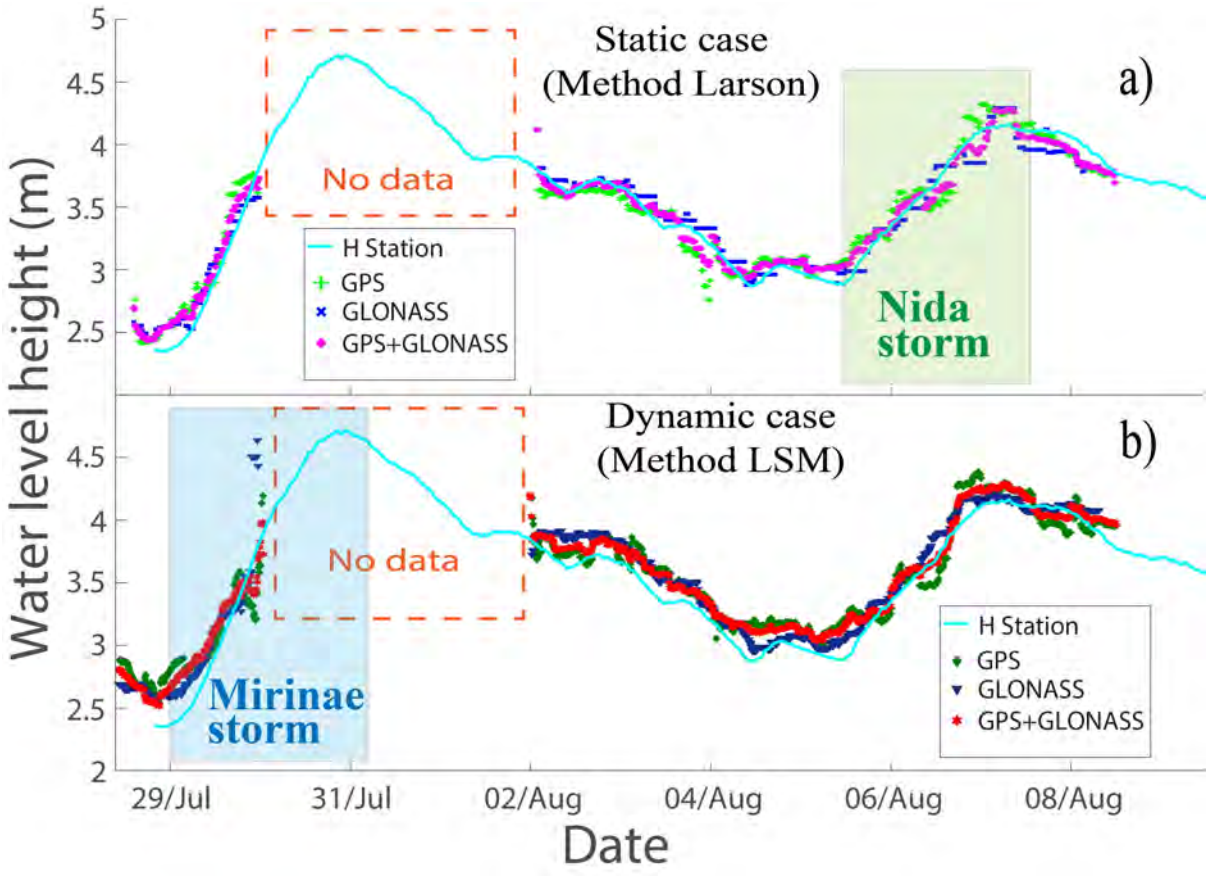

Figure IV.10 – Comparisons between height estimated from SNR measurements obtained using method LSM (a), method Larson (b) with only the GPS constellation /GLONASS constellation /both constellations versus height recorded from the hydrological station during the period of the Mirinae and Nida storms (from the 27th July to 12th August 2016).

The two main storms, Mirinae and Nida, have been well recorded, one can see a delay of 54 hours for Mirinae and 48 hours for Nida between storms and GNSS-R answers due to the water transit time of the watershed (Fig. IV.10).

We have also compared the difference among PRN of GPS and GLONASS constellations. The correlation coefficients R, between the height h station and the estimated

TABLE IV.2 – Comparison between the *in-situ* gauges with the raw SNR-based time series calculated using different ranges of satellite elevation with only the GPS and/or GLONASS constellation. (a) In Static case, (b) In Dynamic case.

LARSON / GNSS	Band	Low Sat. elev.			High Sat. elev.		
		Bias (m)	RMSE (m)	Corr. Coeff.	Bias (m)	RMSE (m)	Corr. Coeff.
GPS	L1	-0.22	0.25	0.89	-0.13	0.18	0.97
	L2	-0.17	0.25	0.89	-0.07	0.15	0.96
	L1+L2	-0.15	0.24	0.93	-0.01	0.13	0.96
GLO	L1	-0.23	0.24	0.96	0.03	0.25	0.88
	L2	-0.23	0.29	0.90	-0.12	0.18	0.96
	L1+L2	-0.20	0.25	0.95	-0.03	0.10	0.98
GPS+GLO	All bands	-0.15	0.22	0.95	-0.01	0.09	0.98
LSM / GNSS	Band	Low Sat. elev.			High Sat. elev.		
		Bias (m)	RMSE (m)	Corr. Coeff.	Bias (m)	RMSE (m)	Corr. Coeff.
GPS	L1	-0.17	0.26	0.93	-0.18	0.22	0.96
	L2	-0.30	0.39	0.90	0.02	0.20	0.87
	L1+L2	-0.26	0.32	0.93	-0.07	0.16	0.94
GLO	L1	-0.15	0.24	0.94	-0.09	0.18	0.93
	L2	-0.30	0.49	0.80	-0.07	0.09	0.99
	L1+L2	-0.25	0.38	0.87	-0.11	0.13	0.99
GPS+GLO	All bands	-0.22	0.26	0.96	-0.08	0.12	0.98

height h from different PRN, are ≈ 0.9 (Fig. IV.11). The best correlations are with observed GNSS constellations: i) GPS PRNs: 06, 10, 12, 14, 17, 19, 20, 21, 22 and 30; ii) GLONASS: 01, 04, 08, 10, 11, 14, 15, 16, 21 and 24.

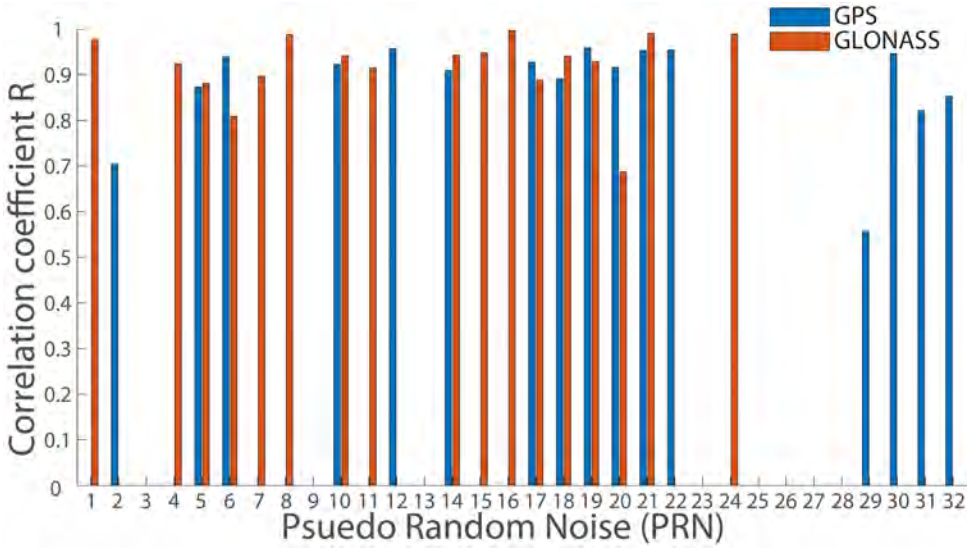

Figure IV.11 – Chart of the correlation coefficients between the h recorded from the hydrological station and the estimated h from different GPS and GLONASS constellations.

In this study, we demonstrated that SNR data from GNSS-R receivers allows estimating the water level with an accuracy ∼10cm. In the literature, the two methods, method Larson and method LSM, are set down depending on the height variations of the GNSS-R antenna, if we have no variations or very small ones that is to say we are in the static case we used Larson method otherwise we are in the dynamic case and we used LSM.

IV.5 Conclusion

From the two studies presented in this chapter, we demonstrated that the SNR from GNSS-R receivers allows estimating the water level with quite good accuracy ∼10cm. LSm and Larson methods can be applied not only in the coastal area e.g. Roussel et al. (2015b), but also for continental waters (river, lake, etc.) and even in the estuarine areas where has impacts of different characteristics such as hydrological regime, coastal oceanographic and so on. In the literature, two methods are set down depending on the height variations of the GNSS-R antenna, if we have no variations or very small ones that is to say we are in the static case we used Larson method otherwise we are in the dynamic case and we used LSM. Both method gives good results but the difference is in the number of solution computed: Larson gives accurate results but for a limited number of points whereas LSM gives a large number of accurate solutions. Multi-constellation increases the accuracy of the solutions and the number of computed points. We have also compared L_1 and L_2 frequencies. As it is known for GPS measurements, L_2 is noisier but gives also accurate measurements. For GLONASS constellation, L_2 is more accurate than L_1 with a RMSE <=10cm. The accuracy of GNSS-R, in many cases, is not obstacle for Red river or Mekong measurements because reference gauges record have water variations upper than 20cm. The main storm i.e. Mirinae was not completely recorded due to the technical problem when Nida have been well recorded, one can see a delay of 54 hours for Mirinae and 48 hours for Nida between storms and GNSS-R answers due to the water transit time of the watershed.

In the Mekong river experiment, GNSS antenna was installed at the Tran De water tower (high 30 m), 100 m from the river. In this site, we can use only SNR data with low satellite elevation and it gives lower correlations. Comparisons with in-situ gauge data have a correlation coefficient of 0.92 with Larson method and 0.85 with LSM method. The results of Larson method are better than the LSM method can be explained by the reflecting surface is relatively static, less affected by waves. The water level derived from SNR signal provides results of similar quality the classical gauges when using both GPS and GLONASS satellite. So, it can allow evaluating the performances GNSS-R for monitoring river changes and the possibility to use this technique for calibration/validation of altimetry data (SARAL, Jason-2, 3, Sentinel 3A etc.).

So, GNSS-R base on SNR analysing is the promising tool for obtaining useful continuous and spatial measurements of river level. We obtain not only the river water level, but we can also retrieve the local slope of the water surface, and flooded areas. So, it can be use for detection of extreme hydrological events.

Chapter V
Conclusion and perspectives

V.1 Conclusion

En français:

Nous avons vu que le GNSS-R, avec l'évolution récente des différentes constellations GNSS, est et sera l'un des outils fondamentaux pour la surveillance de nombreux phénomènes environnementaux. Avec le lancement de TechDemoSat-1, c'est le segment spatial qui s'est ouvert aux applications de réflectométrie. Récemment, avec le lancement de la constellation CYGNSS, du cubesat ^{3}CAT-2, et l'introduction d'un récepteur GNSS-R sur la station internationale dans les années à venir, l'intérêt des scientifiques et des professionnels du secteur privé devraient augmenter notamment pour les tempêtes, les tsunamis, l'évolution des sécheresses, la surveillance des rivières et des calottes glaciaires. Ces applications sont aussi accessibles via des récepteurs géodésiques classiques pour des mesures *in-situ* jusqu'à des échelles intermédiaires ($\sim$ 40 km^2 pour une antenne à 60 m de hauteur).

La technique IPT développée par Larson et al. (2008a)pour les récepteurs classiques a démontré une bonne qualité de mesure de l'humidité du sol pour les sols riches en argile. Mais nos travaux mettent en évidence l'efficacité de cette méthodologie pour les sols sableux. Dans ce cas, nous devons combiner la technique IPT avec le déroulement de la phase pour obtenir une série temporelle de la phase du SNR_m continue. Si l'on compare la même série temporelle de phase en utilisant IPT seul et l'"IPT + unwrapping" on peut voir une très nette amélioration: le facteur de corrélation entre la sonde *in-situ* et la phase SNR_m passe ainsi d'une valeur proche de 0 à une valeur proche de 0,7, pour le terrain synthétique du « Beach volley» composé de 100% de sable puis d'une géomembrane avant de retrouver dessous la molasse de la Garonne. Un autre atout majeur mis en évidence par cette expérience est la capacité de la technique GNSS-R à cartographier la distribution spatiale de l'humidité du sol sur une zone qui dépend de la hauteur de l'antenne et des classes d'élévation des satellites. Sur le «Terrain de Beach volley», pour couvrir l'ensemble du terrain, nous avons utilisé uniquement des satellites de haute altitude (habituellement non utilisés) avec une empreinte de quelques mètres carrés et une hauteur d'antenne de 4m. Cette variabilité spatiale ne peut pas être que difficilement réalisée avec une

ou plusieurs sondes d'humidité *in-situ*. Cet exemple montre que des échelles locales à intermédiaires peuvent être explorées simplement en augmentant la hauteur de l'antenne: quelques mètres carrés pour une hauteur d'antenne de $\sim$ 1,5 m et à plus de 10.000 m^2 pour une hauteur d'antenne de 50 m. On peut aussi regarder simultanément deux échelles spatiales juste en séparant les satellites de hautes élévations et de basses élévations. Dans le cas de l'étude du site naturel de Dahra, où la concentration de sable dans le sol est supérieure à 80%, nous avons comparé les trois métriques obtenues à l'aide de l'IPT: la phase Φ_{unw}, l'amplitude A_m de $\mathrm{SNR_m}$ et la hauteur effective h_{eff}. L'humidité du sol restituée à partir de ces paramètres a une qualité variable en fonction du paramètre regardé:

- A_m ne donne qu'une tendance due à sa forte sensibilité à la végétation et à la rugosité de la surface du sol.

- La phase Φ_{unw} donne une bien meilleure corrélation avec les sondes d'humidité. De plus, elle montre aussi une certaine aptitude à pénétrer plus profondément dans certains types de sols notamment ceux qui sont riches en sables. On constate aussi que Φ_{unw} elle est nettement moins sensible aux effets de la rugosité et de la végétation de surface. Enfin, elle montre une excellente qualité de mesure même lorsque le taux d'humidité dans le sol est très faible (<5%) ceci pour une précision approchant les 0,5%.

- Le dernier paramètre, la hauteur effective h_{eff}^{unw} se traduit par une claire anti-corrélation avec les sondes d'humidité car la pénétration de l'onde augmente lorsque l'humidité diminue.

La surface couverte dans le cas de Dahra est de quelques dizaines de mètres autour de l'antenne ($\mathrm{H_{antenne}}$ = 1.61m), mais il est possible d'augmenter la surface explorée en augmentant la hauteur de l'antenne ou en déplaçant/ajoutant des récepteurs pour couvrir une zone plus large. La combinaison de toutes les constellations existantes GPS/GLONASS/GALILEO/BEIDOU dans le traitement du SNR permet d'augmenter le nombre de points spéculaires et de produire des séries temporelles plus complètes et plus précises ce qui améliore significativement la détermination de l'humidité du sol, ainsi que la résolution temporelle. La fréquence d'échantillonnage passe de 10 minutes à 1 minute voire 1 seconde et fournit une analyse détaillée des séries temporelles. On peut alors identifier à la fois des signaux basses fréquences (pluriannuels) et hautes fréquences (variation quotidienne de l'humidité liées à l'activité solaire). Avec la méthodologie proposée dans cette thèse, nous pouvons construire de longues séries chronologiques continues d'humidité du sol qui sont/seront très utiles pour cartographier les effets du changement climatique sur le long terme ou les changements saisonniers tels que la transition saison des pluies à saison sèche. Par exemple, en octobre 2016, en créant une série de cartes

d'humidité moyenne du sol avec une résolution temporelle de 6 heures, 12 heures ou journalière pour une aire explorée autour de l'antenne GNSS de ∼300m² (pour dans le cas de Dahra, un rayon ∼ 10m et $H_{antenne}$ ∼ 1.60m). Une autre contribution importante est sa capacité à fournir des séries chronologiques continues et durables pour, au moins, les décennies à venir (les constellations GNSS étant pérennes).

De nombreuses applications utilisent les mesures d'humidité : i) la météorologie, ii) l'agriculture, iii) l'hydrologie etc. mais pour avoir de bons suivis il est important que les mesures d'humidité répondent à trois critères important : a) un pas de suivi temporel le plus fin possible surtout si l'on désire voir les interactions sols/plantes englobés dans les phénomènes d'évapotranspiration, si l'on vaut suivre l'évolution diurne et nocturne du point de rosée jusqu'au maximum d'ensoleillement ; b) différentes échelles d'analyse (global à *in-situ* avec aussi les échelles intermédiaires) ; c) une précision importante pour pouvoir suivre de très faibles variations des conditions de saturation (ou non saturation) du milieu ; d) la mesure doit correspondre à une mesure de surface (les premiers centimètre, décimètres de sol. L'utilisation de la télédétection permet d'avoir une couverture globale avec des pas temporels qui s'affinent de plus en plus, ainsi en une trentaine d'année on est passé de données mensuelles (SPOT, LANDSAT) à hebdomadaires (constellations SENTINEL) voire journalières (MODIS). Elles permettent aussi d'obtenir de nombreuses échelles intermédiaires puisque leur résolution va de moins de 50km (e. g. SMOS, Sánchez et al. (2016); Wigneron et al. (2000)) en passant par quelques centaines de mètres (e.g. MODIS, Wang et al. (2007); Zhang et al. (2014)) à moins d'une centaine de mètre (e. g. RADARSAT-2, Baghdadi et al. (2012); SENTINEL 1, Paloscia et al. (2013); SWIR hyperspectral airplane sensor, Finn et al. (2011)).
Cependant, toutes ces missions nécessitent une phase de calibration s'appuyant sur des capteurs au sol qui vont permettre de d'inverser la réflectivité du sol en contenu en eau du sol. Sur ce point le GNSS-R nécessite aussi cette phase de calibration il ne permet donc pas de s'affranchir des données *in-situ* par contre du fait de son exploration spatiale relié à la hauteur d'antenne il est beaucoup plus intéressante de calibrer les données satellitaires et aéroportées avec cette méthode car les corrélations locales avec les sondes d'humidité sont de très bonne qualité avec $R^2 > 0.9$ et une prise en compte de l'hétérogénéité locale (de quelques m² pour $H_{antenne}$ ∼1m à un millier d'hectare pour $H_{antenne}$ ∼50m) voire régionale (si on installe un réseau de capteurs). Autre point important c'est la résolution temporelle qui peut être adaptée au phénomène étudié et peut atteindre un pas temporel inférieur à la minute. De plus, les échelles globales peuvent aussi être exploitées en utilisant non plus l'analyse du SNR mais en utilisant les formes d'ondes (directes et réfléchies) acquises par des récepteurs spécifiques embarqués dans les satellites de la constellation CYGNSS (Chew and Small (2018)) ou de la mission SMAP (Carreno-Luengo et al. (2017)).
Les analyses *in-situ* que ce soit par méthode gravimétrique qui est la référence puisqu'elle

mesure directement la quantité d'eau dans le sol (Schmugge et al. (1980)) mais qui est longue à mettre en œuvre car elle nécessite une phase de séchage de l'échantillon d'une douzaine d'heures au moins ce qui nuit à sa résolution temporelle. Les méthodes indirectes que sont les méthodes nucléaire (sonde neutrons, ou sonde gamma-ray) électromagnétique (sonde TethaProbe, sonde capacitive Sentek, etc.) ou tensiométrique (bougie poreuse qui mesure la capillarité ou l'énergie de tension Richards and Gardner (1936)) permettent d'avoir des pas temporels plus précis proche de quelques minutes généralement. L'inconvénient majeur de ces techniques est quelles sont ponctuelles et ne représentent que de très faibles surfaces par rapports aux techniques de télédétection classiques. Bien sûr on peut utiliser des réseaux de capteurs *in-situ* pour calibrer et valider les données spatiales comme l'ont démontré Sánchez et al. (2010) avec un réseau de 23 stations couvrant une surface de 1300 km^2 dans le bassin du Duro en Espagne qui donnent de bonne corrélation pour les parcelles agricoles non irriguées avec cependant une sous-estimation systématique pour les zones de céréales et de vignes. Si l'on compare cela aux résultats obtenus sur Lamasquère avec le GNSS-R on ne constate pas de sous-estimation systématique ce qui est plutôt en faveur du GNSS-R. De plus, on a pu suivre la croissance des céréales avec le même instrument ce qui réduit fortement l'instrumentation de terrain, les problèmes d'énergie et de maintenance.

Dans les études du delta du fleuve Rouge et de celui du Mékong, nous avons montré que le $\mathrm{SNR_m}$ permet d'estimer le niveau de l'eau avec une précision de $\sim$ 10cm. Dans la littérature, deux méthodes sont définies en fonction de la hauteur de l'antenne. Si nous sommes dans le cas statique, non-déplacement ou très faible déplacement de la surface et/ou de l'antenne, nous pouvons utiliser la méthode IPT qui dépend de la fréquence du signal et de sa longueur d'onde (Larson et al., 2008b). Autrement, lorsque nous sommes dans le cas dynamique, c'est-à-dire que l'on regarde une surface mobile (mer, surface de la rivière) et/ou que l'antenne est embarquée sur un avion ou un satellite, nous utilisons la méthode LSM. LSM est une solution plus complexe pour calculer le h_{eff} il faut tenir compte de la vitesse verticale de l'antenne, de la vitesse angulaire et de l'élévation du satellite. Les deux méthodes donnent de bons résultats mais la différence réside dans le nombre de solutions calculées: Larson donne des résultats précis mais pour un nombre limité de points alors que LSM donne un grand nombre de solutions précises. La combinaison des constellations augmente aussi la précision de la solution et le nombre de points calculés. Nous avons également comparé les différentes fréquences GNSS *i.e.* L_1 et L_2 (L_5 n'a pas été pris en compte car trop peu de satellites l'utilisent). Comme il est classiquement admis pour les mesures GPS, L_2 est la plus bruitée mais donne des mesures précises car sa période est plus courte que celle de L_1. Pour la constellation GLONASS, L_2 est plus précis que L_1 avec un RMSE <= 10cm. La précision de h_{eff} est, dans de nombreux cas pour les deux méthodes, satisfaisante pour de nombreuses rivières comme les deltas du fleuve Rouge et du Mékong car les jauges de référence ont généralement des

variations d'eau significativement supérieures à 20cm puisque l'on a à la fois les effets des crues continentales et des marées océaniques.

Pour le site du delta du Mékong, une antenne GNSS a été installée à la tour d'eau de Tran De haute de 30 m, et à 100 m du fleuve. Dans ce site, nous pouvons utiliser uniquement les données SNR_m provenant des satellites à faible élévation. Dans ces conditions, en comparant avec le capteur fluvial *in-situ*, la méthode LSM donne une corrélation plus faible ($R \sim 0{,}85$) que la méthode de Larson ($R \sim 0{,}92$) comme le montre dans la figure IV.6. Les résultats de la méthode de Larson sont meilleurs que ceux de la méthode LSM et cela peuvent s'expliquer par une surface réfléchissante relativement statique où seules des variations à basses fréquences ont été enregistrées, à savoir les marées (période de 12h) et les inondations (plusieurs heures à plusieurs jours). Cette zone est moins affectée par les ondes qui génèrent des oscillations à hautes fréquences qui conduisent à des variations verticales importantes et rapides de la surface de l'eau. Mais en termes de séries temporelles, LSM (1989 points) donne six fois plus de mesures que Larson (369 points) et permet donc un bien meilleur suivi temporel.

Sur le fleuve Rouge, deux fortes tempêtes ont été enregistrées, à savoir Mirinae (phase de crue descendante tronquée) et Nida (complète), on peut observer un retard de 54 heures pour Mirinae et de 48 heures pour Nida entre l'évènement climatique – la tempête et réponses hydrologique mesurée par le GNSS-R ; ce retard est due temps de transit des eaux de ce grand bassin versant.

Avec le développement de système d'alerte aux crues comme le Global Flood Monitoring System de plus en plus de données sont utilisées pour contrainte les modèles de prévision en temps réel : généralement il s'agit de données satellitaire comme l'analyse multi-satellite des précipitations, données qui permettent de prédire les hauteurs dans les prochaines heures cependant ces modèles sont aussi corrigés en temps réel en s'appuyant sur de la télémétrie *in-situ* des hauteurs d'eau et des débits dans les différents points clés du bassin-versant, ainsi on s'appuie sur une mesure ponctuelle proche d'une confluence ou d'une ville, où l'on développe des systèmes spécifique aux milieux urbains (Henonin et al. (2013)). Avec le GNSS-R on peut encore améliorer la compréhension de l'évolution des crues car elle nous donne une carte de la topographie de surface des eaux mais aussi une vision des zones inondées même sous couvert végétal, là où par exemple les images optiques ne voient que la canopée. Les premières application GNSS-R appliquée au « monitoring des rivières » ont été réalisées dans le cadre du projet WISDOM (germano-vietnamien, Beckheinrich et al. (2014)) où il a été montré la faisabilité d'un tel système mais où il a aussi été montré la difficulté d'avoir des mesures continues et précises. Cependant avec l'augmentation du nombre de satellites et surtout l'intégration de la vitesse de déplacement vertical de la rivière/fleuve/lac on a maintenant des mesures beaucoup plus fines comme l'ont montré les études sur le delta du Mékong et du fleuve Rouge faites dans cette thèse. L'utilisation d'une cartographie sur des rivières assez larges (il faut

avoir suffisamment de points de réflexion pour pouvoir résoudre le système par moindre carré) doit permettre i) de mieux comprendre l'hydrologie des zones de confluence (effet de barrage de la rivière principale qui peut induire une inondation régressive (vers l'amont) dans le tributaire ; ii) mieux comprendre la dynamique fluviale dans les zones urbaines où les phénomènes de ruissellement sont amplifiés, iii) mieux suivre les zones humides des grands bassins versants (Nghiem et al. (2017)) et enfin iv) mieux appréhender la compétitions entre les eaux océaniques et les eaux continentales au niveau des embouchures des fleuves.

In English:

We have seen that GNSS-R, with the recent evolution of different GNSS constellations, is and will be one of the fundamental tools for monitoring environmental phenomena. With the launch of TechDemoSat-1, the space segment is opening up to reflectometry applications. Recently, with the launch of CYGNSS, ^{3}CAT-2, and the introduction of a receiver on the international station in the coming years, are expected to increase the interest of scientists and professionals in the private sector such as storms, tsunamis, the evolution of droughts, the monitoring of rivers, and ice sheets. These applications are now accessible via classical geodetic receivers for *in-situ* measurements up to intermediate scales ($\sim$ 40 km^2 for an antenna at 60 m height).

The IPT technique developed by Larson et al. (2008a) for the classical receiver demonstrated good soil moisture retrieval for rich clay soil content. But our works highlight the efficiency of this methodology for sandy soil. In this case, we need to combine the IPT technique with an unwrapping of the phase to obtain a continuous phase time series of the $\mathrm{SNR_m}$. If you compare the same phase time series using IPT alone and "IPT + unwrapping" one can see the improvement: the correlation factor between near surface *in-situ* probe and $\mathrm{SNR_m}$ phase increase from a value close to 0 to a value close to 0.7 for the synthetic field "Beach volleyball" composed of 100% sand and a geomembrane before returning below the sandstone ("molasse") of the Garonne. Another major asset highlighted by this experiment is the ability of GNSS-R technique to map the spatial distribution of soil moisture over an area that depend on the antenna height and the satellite elevation class. In the beach volley playground, to cover the entire playground, we used only high elevation satellites with a footprint of a few square meters and an antenna height of 4m. This spatial variability cannot be difficult to achieve with a single or few *in-situ* moisture probes. This example shows that local to intermediate scales can be explored simply by increasing the height of the antenna: few square meters for an antenna height of $\sim$1.5 m to more than 10.000 m^2 for an antenna height of 50 m or just separating satellites from high elevations and low elevations. In the case of Dahra's natural study, where the sand concentration in the soil is greater than 80%, we compared the three metrics obtained using the IPT i.e. phase Φ_{unw}, amplitude A_m of $\mathrm{SNR_m}$, and effective height h_{eff}. The soil moisture restored from these parameters has a variable quality depending on the parameter used:

- A_m give only a trend due to a high level of sensitivity to vegetation and ground roughness.

- The phase Φ_{unw} gives a much better correlation with the humidity probes. In addition, it also shows a certain ability to penetrate deeper into certain types of soils especially those which are rich in sands. We also note that Φ_{unw} is much less sensitive to the effects of roughness and surface vegetation. Finally, it shows

excellent measurement quality even when the soil moisture content is very low (<5%) for a precision approaching of 0.5%.

- The last parameter, the effective height h_{eff}^{unw} results in a clear anti-correlation with the humidity probes because the wave penetration increases when the humidity decreases.

The covered surface is a few tens of meters around the antenna ($H_{antenna}$ = 1.61m), but it is possible to improve the explored surface by varying the height of the antenna or by moving/adding receiver to cover a wide region. The combination of all GPS/GLO/GELLILEO/BEIDOU satellites in the treatment of SNR to produce a complete sequence of time precision significantly improves the correlation with soil moisture, as well as the temporal resolution of the time series. The sampling frequency increases from daily to 10 min or even to 1s and provides a detailed analysis of the time series and one can identified at the same time low (multi-year) and high frequency signals (daily moisture variation due to the sun activity). With the methodology demonstrated in this paper, we can build long continuous soil moisture time series that are very useful for recording and mapping long-term climate change or seasonal changes such as the transition from the rainy season to the dry season in the Dahra study case. For example, during October 2016, by creating a series of the average soil moisture maps with a temporal resolution of 6 hours, 12 hours or by-days period for an area explored around GNSS antenna of $\sim$ 300m^2 (for in the case of Dahra, radius $\sim$10m for $H_{antenna} \sim$ 1.60m). Another contribution is its potentiality to provide continuous and sustainable time series for, at least, the coming decades. Many applications use soil moisture measurements: i) meteorology, ii) agriculture, iii) hydrology, etc. but to have good follow-up it is important that the moisture measurements meet three important criteria: a) a time step for tracking the finest possible events especially if one wishes to see the interactions between soils/plants included in the phenomena of evapotranspiration, or if one is to follow the diurnal and nocturnal evolution from the dew point to the maximum of sunshine; b) different scales of analysis (global to *in-situ* with intermediate scales as well); c) an important precision to be able to monitor very small variations of the saturation conditions (or undersaturation) of the medium; d) the measurement must correspond to a surface measurement (the first centimeters, decimeters of soil) The use of remote sensing makes it possible to have an overall coverage with time steps which are refined more and more, thus in about thirty year this time step has passed from monthly data (SPOT, LANDSAT) to weekly (SENTINEL constellations) or even daily data (MODIS). They also allow to obtain many intermediate scales since their resolution is range between less than 50km (eg SMOS, Sánchez et al. (2016); Wigneron et al. (2000)) through a few hundred meters (eg MODIS, Wang et al. (2007); Zhang et al. (2014)) within a hundred meters (eg RADARSAT-2 , Baghdadi et al. (2012); SENTINEL 1, Paloscia et al. (2013); SWIR hyperspectral airplane sensor, Finn et al. (2011)).

However, all these missions require a calibration, validation phases based on ground sensors that will allow to reverse the reflectivity of soil into the soil moisture content. On this point, the GNSS-R also requires this calibration/validation phases, so it is not possible to dispense with *in-situ* data, but due to its spatial exploration related to the antenna height it is much more interesting to calibrate/validate the remote sensing (satellite and airborne) data with this method because the local correlations with the humidity probes are of very good quality with $R^2 > 0.9$ and taking into account the local heterogeneity (from a few m^2 for $H_{antenna} \sim 1m$ to a thousand of hectare for $H_{antenna} \sim 50m$) even regional (if we install a network of GNSS-R sensors). Another important point is the temporal resolution that can be adapted to the studied phenomenon and can reach a time step less than one minute. Worldwide scale can also be explored not using GNSS-R SNR analysis but using waveform analysis of direct and reflected signals of specific waveform receiver embedded the recent constellation like CYGNSS (Chew and Small, 2018) or SMAP mission (Carreno-Luengo et al., 2017).
In-situ analyses whether by gravimetric method which is the reference since it directly measures the quantity of water in the soil (Schmugge et al., 1980) but which takes a long time to implement because it requires a drying phase sample of a dozen or more hours which is detrimental to its temporal resolution. Indirect methods such as electromagnetic (neutron probe, or gamma-ray probe) electromagnetic (TethaProbe probe, Sentek capacitive probe, etc.) or tensiometric probe (porous candle that measures capillarity or tension energy Richards and Gardner (1936)) allow to have more precise time steps close to a few minutes generally. The major disadvantage of these techniques is that they are punctual and represent only very small areas compared to conventional remote sensing techniques. Of course, *in-situ* sensor networks can be used to calibrate and validate spatial data as demonstrated by Sánchez et al. (2010) with a network of 23 stations covering an area of 1300 km^2 in the Duro Basin in Spain which give a good correlation for non-irrigated agricultural plots with however a systematic underestimation for cereal and vineyard areas. Comparing this with the results obtained on Lamasquère with GNSS-R, there is no systematic underestimation, which is rather in favour of GNSS-R. In addition, it was possible to follow the growth of cereals with the same instrument, which greatly reduces field instrumentation, energy and maintenance problems.

Our studies of Red river and Delta Mekong have shown that the SNR_m allows estimating the water level with a quite good accuracy ∼10cm. In the literature, two methods are set down depending on the height antenna. If we are in the static case, *i.e.* non-moving surface and antenna, we can use IPT method that depend on the frequency of the signal and its wavelength (Larson et al., 2008a). Otherwise, when we are in the dynamic case, *i.e.* moving surface (sea, river surfaces) and/or moving antenna embedded on an aircraft or a satellite, we used LSM method. LSM is a more complex solution to compute the h_{eff} that depend on vertical velocity of the antenna, satellite angular velocity and elevation.

Both methods gives good results but the difference is in the number of solution computed: Larson gives accurate results but for a limited number of points whereas LSM gives a large number of accurate solutions. The combination of Multi-constellation increase the solution accuracy and the number of computed points. We have also compared L_1 and L_2 frequencies (L_5 have too few visible satellites). As it is known for GPS measurements, L_2 is more noisy but gives accurate measurements and for GLONASS constellation, L_2 is more accurate than L_1 with a RMSE <=10cm. The accuracy of h_{eff} is, in many cases for both methods, satisfactory for many rivers as Red river or Mekong delta measurements because reference gauges have usually water variations significantly higher than 20cm. For the Mekong river experiment, GNSS antenna was installed at the Tran De water tower (height of 30m) and 100m from the river. In this site, we can use only SNR_m data from low satellite elevation. Under this condition, comparing with *in-situ* river gauge, LSM method give lower correlation (R∼0.85) than Larson method (R∼0.92) as shown in figure IV.6. The results of Larson method are better than the LSM method and can be explained by a relatively static reflecting surface where only low frequency variations have been recorded i.e. tides and floods. This area is less affected by waves that generate high frequency oscillations that lead to important and quick vertical variations of the water surface. But in terms of time series, LSM (1989 points) gives six time more measurements than Larson (369 points). For Red river, two main storms i.e. Mirinae (descending flood phase is truncated) and Nida have been well recorded, one can see a delay of 54 hours for Mirinae and 48 hours for Nida between storms and GNSS-R answers due to the water transit time within the watershed.

With the development of flood warning systems such as the Global Flood Monitoring System, more and more data are being used to constrain real-time forecasting models: generally it is satellite data such as multi-satellite analysis of precipitation data that are used to predict river height in the next few hours, however, these models are also corrected in real time using *in-situ* telemetry/gauge of water heights and flows in the different key points of the watershed. Thus, we rely on a measure point close to a confluence or a city, where we develop systems specific to urban environments (Henonin et al. (2013)). With GNSS-R we can further improve the understanding of the evolution of floods because it gives us a map of the surface topography of the waters but also a vision of the flooded areas even under/without vegetation cover, where for example the optical images ray tracing is blocked by the canopy. The first GNSS-R application applied to river monitoring was carried out within the framework of the WISDOM project (German-Vietnamese, Beckheinrich et al. (2014)) where it was shown the feasibility of this system but where it was also shown the difficulty of having continuous and accurate measurements. However, with the increase in the number of satellites and especially the integration of the vertical velocity of the river/lake surface, we now have much finer measures as shown by the studies on the Mekong Delta and the Red river made in this

thesis. The use of a cartography on rather large rivers (it is necessary to have enough points of reflection to be able to solve the system by least squares) must allow i) to better understand the hydrology of the zones of confluence (effect of dam due to the main river that can induce headward (upstream) flooding in the tributary ii) better understand river dynamics in urban areas where runoff phenomena are magnified; iii) better understanding of wetland and flooded areas (Nghiem et al. (2017)) and iv) finally better understand the competitions between oceanic and inland waters at the mouths of the rivers.

V.2 Perspectives

En français:

Environ 70% de l'eau continentale dans le monde entier est utilisée pour l'agriculture. Avec l'augmentation drastique de la population dans un avenir proche (jusqu'à 2 milliards de personnes de plus d'ici 2030), la demande en eau devrait augmenter considérablement. Les agriculteurs sont mis au défi de produire « plus de grains par goutte ». Afin d'optimiser la gestion des ressources en eau, il est crucial d'améliorer la connaissance de la situation hydrique du sol. Fondamentalement, cela implique l'amélioration de la résolution temporelle et spatiale des mesures d'humidité du sol pour développer la recherche d'un système d'alerte dédié aux agriculteurs pour une meilleure irrigation de leurs champs et pour développer la prochaine génération de l'agriculture durable.

Nous avons démontré que la méthode SNR_m peut surveiller les grands deltas ou lacs (nous avons besoin de nombreux points de réflexion) mais les futurs travaux de recherche peuvent être améliorés pour surveiller les zones inondées même dans des conditions complexes comme les zones inondées sous la forêt. Cela peut conduire à une meilleure estimation des flux d'eau continentaux pendant les événements extrêmes tels que les sécheresses, par ex. celles observées en France au cours de l'année 2003 ou les inondations éclairs ou les phénomènes de Mascaret. Un point intéressant est la disponibilité de récepteurs multi-constellations à bas coût comme les Ublox qui ont une fréquence d'échantillonnage supérieure à 10 Hz qui autorisent l'installation de grands réseaux et l'exploration des très hautes fréquences nécessaires pour caractériser certains phénomènes hydrologiques extrêmes et rapides comme le mascaret (quelques dizaines secondes) et des inondations brutales (heures).

Un autre type d'application développée dans ce travail et corrélée à la variation de la hauteur de l'eau peut être appliquée à la surveillance côtière (par exemple, la hauteur des marées, la compétition entre les eaux océaniques et continentales dans les estuaires, les changements de salinité, système d'alerte pour les ondes de tsunami avant qu'elles n'atteignent le rivage, etc.) où l'antenne est située à quelques dizaines de mètres voire centaine de mètres au-dessus des eaux océaniques. Ce type de récepteur peut fournir une résolution spatiale et temporelle plus précise que les récepteurs embarqués sur des avions ou des satellites. Pour les échelles locales à intermédiaires, certaines campagnes expérimentales côtières ont été faites (Roussel et al., 2015b; Löfgren et al., 2014). Les résultats obtenus sont plus précis, avec de meilleures résolutions spatiales et temporelles que prévu et beaucoup plus précises que les données de télédétection, même si l'utilisation de cette technique pour une couverture mondiale semble assez difficile. Mais l'existence de réseaux GNSS nationaux dans le monde entier peut être utilisée pour générer des séries temporelles mondiales et améliorer l'intérêt de cette technique pour les zones côtières.

Toutes ces raisons font que cette méthode peut devenir incontournable pour les travaux futurs. Les niveaux d'eau, dérivés des signaux SNR_m, fourniront des résultats de

qualité similaire à celles des jauges fluviales / marégraphiques classiques lorsque toutes les constellations GNSS actuelles et futures seront utilisées conjointement. De plus, cette méthode peu couteuse peut et pourra être utilisé pour l'étalonner/valider des données altimétriques des missions spatiales (SARAL, Jason-2, 3, Sentinel 3A, etc.).

La autre perspective de ce travail est la surveillance de la contamination par les métaux lourds. Pour ce faire, nous avons réalisé une étude préliminaire dans la Sierra Minera (Espagne). Des décennies d'activité minière (principalement du Zn et du Pb) dans la zone des villes de Cartagena et La Union ont généré une grande quantité de bassin de résidus miniers et la plupart abandonnés sans mesures de sécurité particulières. Ils sont composés de déchets miniers malsains et de risques environnementaux en raison de leur forte susceptibilité aux processus de lixiviation et d'érosion (par exemple, inondations brutales, phénomène de diffusion de talus, de transport aérien). Notre étude préliminaire se concentre sur le bassin de résidus miniers remédiés du bassin versant de l'Avenque près de Carthagène, qui a été « assaini » localement en y ajoutant du lisier de porc/du fumier ainsi que des résidus de marbre. Cette réhabilitation a été réalisée pour améliorer les conditions physico-chimiques et biologiques du sol afin de garantir l'immobilisation des métaux lourds et le développement de plantes essentielles à l'évolution de ces sols. Les mesures géophysiques préliminaires (EM38, susceptibilimètre) et des analyses du sol géochimiques réalisées (Xref) pour caractériser cette zone et les propriétés profondes d'un bassin de résidus miniers partiellement remis en état. Nous avons aussi regardé également le potentiel du GNSS-R pour cartographier la contamination des sols en métaux lourds. La contamination du sol de la zone minière affecte la composition du sol qui peut être quantifiée avec GNSS-R en mesurant les changements de conductivité électrique et de la permittivité relative dus à l'augmentation ou la diminution de la concentration en métaux lourds. Nos premiers résultats indiquent une augmentation d'A_m lorsque la susceptibilité magnétique et le Fe total augmentent, alors que le Cd et le Cu voient leur concentration diminuer dans le même temps. De futurs travaux devraient tenter d'améliorer cette méthodologie en effectuant une modélisation inverse pour extraire la permittivité relative et la conductivité électrique réelles des sols afin de mieux estimer leur concentration de métaux lourds.

In English: Around 70 percent of worldwide continental water feeds agriculture. With the drastic increase of population in a foreseeable future (up to 2 billion people by 2030), water demand is expected to increase tremendously. Farmers are challenged to produce "more crop per drop". In order to optimize water resource management, it is crucial to improve soil moisture situation awareness. Basically, this implies the improvement of both temporal and spatial resolution of soil moisture measurements to develop research for helpful warning system dedicated to farmers for a better field irrigation and to produce the next generation of sustainable agriculture.

We have demonstrated the SNR_m method can monitor large river delta or lake (we need of numerous reflecting points) but future research works can be improved for monitoring of flooded area even in complex condition like flooded area below the forest. This can lead to a better estimation of continental water fluxes during extreme evens like droughts, e.g. those observed in France during the year 2003 or flash floods or Mascaret phenomenon (Tidal bore). An interesting point is the availability of low cost multi-constellation receiver like Ublox with a sampling frequency upper than 10 Hz that authorize the installation of large networks and the exploration of very high frequency needed to characterize some extreme hydrological phenomenon like tidal bore (few ten seconds) and flash floods (hours).

Another type of application developed in this work correlated to water height variation can be applied for coastal surveillance (*e.g* tidal height, competition between oceanic and continental waters, salinity changes, warning system for tsunami waves before it reaches shore etc.) where the antenna is located a few ten meters above oceanic waters. This kind of receiver can provide more accurate spatial and temporal resolution than air-borne or space based receivers. For local to intermediate scales, some coastal experimental campaigns were done (Roussel et al., 2015b; Löfgren et al., 2014). The obtained results are more accuracy, with better spatial and temporal resolutions, than expected and much more accurate than remote sensing data even if the worldwide coverage seems quite difficult using with this technique. But the existence of national GNSS networks all around the world can be used to generate worldwide long time series and improve the interest of this technique for coastal areas. That is the reason why this way of water surface can become decisive for the future works. The water levels, derived from SNR_m signals, provide results of similar quality than the classical river/tide gauges when using all the existing and future GNSS constellations. So, it can allow evaluating the performances GNSS-R for monitoring river changes and the possibility to use this technique for calibration/validation of altimetry data (SARAL, Jason-2, 3, Sentinel 3A etc.).

Last perspective of our work is the monitoring of heavy metal contamination. For that purpose, we have done a preliminary study in the Sierra Minera (Spain). Decades of mining activity (mainly Zn and Pb) in the area of Cartagena-La Union cities generated a large amount of mine tailings ponds and most of them were abandoned without

particular safety measure. They are composed of unhealthy mining wastes and environmental hazards due to their high susceptibility to leaching and erosional processes (*e.g.* flash floods, slope diffusion, aerial transport). Our preliminary study focuses on the mine tailings pond in the Avenque watershed close to Cartagena, which was locally remediated by adding pig slurry/manure and marble residue (sand). Such rehabilitation was done to improve physical, chemical, and biological conditions of the soil to guarantee the immobilization of heavy metals, and the development of plants essential for the formation and evolution of such soils. We present preliminary geophysical measurements and geochemical soil analysis performed to characterize the surface and deep properties of a partially remediated mine tailings pond. We used an EM38 electromagnetic induction meter to measure the apparent electrical conductivity of soil and field portable X-ray fluorescence spectrometers to map and estimate the surface contamination of remediate and common mining wastes. For these, we also investigate the potential of GNSS-Reflectometry. The ground contamination in mining area affects the soil composition that can be quantified with GNSS-R by measuring electrical conductivity and correlated relative permittivity changes due to the increase or decrease of heavy metal concentration. Our first results indicate an increase of A_m when both magnetic susceptibility and the Fe total increased, while Cd and Cu decreased in its concentration. Future works may attempt to improve this methodology by making inverse modelling to retrieve the real relative permittivity and electrical conductivity to better estimate heavy metal concentration in soil.

List of Figures

List of Tables

Bibliography

Alonso-Arroyo, A., Camps, A., Park, H., Pascual, D., Onrubia, R., and Martín, F. (2015). Retrieval of significant wave height and mean sea surface level using the gnss-r interference pattern technique: Results from a three-month field campaign. *IEEE Transactions on Geoscience and Remote Sensing*, 53(6):3198–3209.

Alonso-Arroyo, A., Zavorotny, V. U., and Camps, A. (2017). Sea ice detection using u.k. tds-1 gnss-r data. *IEEE Transactions on Geoscience and Remote Sensing*, 55(9):4989–5001.

Andréani, A. (2001). *Le GPS : une révolution - lack of GPS christopher columbus never found the Indies*. Number 160p. Sciences et Tec, Paris, jean jarry edition. Langue : Français.

Auber, J.-C., Bibaut, A., and Rigal, J.-M. (1994). Characterization of multipath on land and sea at gps frequencies," proceedings of the 7th international technical meeting of the satellite division of the institute of navigation. *Proceedings of the 7th International Technical Meeting of the Satellite Division of The Institute of Navigation (ION GPS 1994) September 20 - 23, 1994 Salt Palace Convention Center Salt Lake City, UT*, pages 1155–1171.

Azmani, M. (2010). *Fusion non-linéaire appliquée aux voies pilote et données du signal GPS L2C*. phdthesis, l'Université du Littoral Côte d'Opale, 50 rue Ferdinand Buisson – B.P. 719, 62228 Calais Cedex, France. ULCO 2010.30.

Baghdadi, N., Cresson, R., El Hajj, M., Ludwig, R., and La Jeunesse, I. (2012). Estimation of soil parameters over bare agriculture areas from c-band polarimetric sar data using neural networks. *Hydrology and Earth System Sciences*, 16(6):1607–1621.

Beckheinrich, J., Hirrle, A., Schön, S., Beyerle, G., Semmling, M., and Wickert, J. (2014). Water level monitoring of the mekong delta using gnss reflectometry technique. In *2014 IEEE Geoscience and Remote Sensing Symposium*, pages 3798–3801.

Beckmann, P. and Spizzichino, A. (1987). *The Scattering of Electromagnetic Waves from Rough Surfaces*. Artech House Radar Library.

Bernhard Hofmann-Wellenhof, Herbert Lichtenegger, J. C. (2001). *Global Positioning System - 2001 - Theory and Practice*. Springer, Vienna.

Biancamaria, S., Frappart, F., Leleu, A.-S., Marieu, V., Blumstein, D., Desjonquères, J.-D., Boy, F., Sottolichio, A., and Valle-Levinson, A. (2017). Satellite radar altimetry

water elevations performance over a 200m wide river: Evaluation over the garonne river. *Advances in Space Research*, 59(1):128 – 146.

Birkett, C. M. and Beckley, B. (2010). Investigating the performance of the jason-2/ostm radar altimeter over lakes and reservoirs. *Marine Geodesy*, 33(sup1):204–238.

Bishop, G. J., Klobuchar, J. A., and Doherty, P. H. (1985). Multipath effects on the determination of absolute ionospheric time delay from gps signals. *Radio Science*, 20(3):388–396.

Blanchet, J. and Lehning, M. (2010). Mapping snow depth return levels: smooth spatial modeling versus station interpolation. *Hydrology and Earth System Sciences*, 14(12):2527–2544.

Blanchet, J., Marty, C., and Lehning, M. (2009). Extreme value statistics of snowfall in the swiss alpine region. *Water Resources Research*, 45(5):n/a–n/a. W05424.

Blumberg, D. G. and Freilikher, V. (2001). Soil water-content and surface roughness retrieval using ers-2 sar data in the negev desert, israel. *Journal of Arid Environments*, 49(3):449 – 464.

Caparrini, M., Egido, A., Soulat, F., Germain, O., Farres, E., Dunne, S., and Ruffini, G. (2007). Oceanpal ®: Monitoring sea state with a gnss-r coastal instrument. In *2007 IEEE International Geoscience and Remote Sensing Symposium*, pages 5080–5083.

Cardellach, E. (2001). *Sea Surface Determination Using GNSS Reflected Signals.* PhD thesis, Universitat Politecnica de Catalunya (UPC).

Cardellach, E., Fabra, F., Nogués-Correig, O., Oliveras, S., Ribó, S., and Rius, A. (2011). Gnss-r ground-based and airborne campaigns for ocean, land, ice, and snow techniques: Application to the gold-rtr data sets. *Radio Science*, 46(6):n/a–n/a. RS0C04.

Cardellach, E., Fabra, F., Rius, A., Pettinato, S., and D'Addio, S. (2012). Characterization of dry-snow sub-structure using gnss reflected signals. *Remote Sensing of Environment*, 124(0):122–134. 0034-4257.

Cardellach, E., Ruffini, G., Pino, D., Rius, A., Komjathy, A., and Garrison, J. L. (2003). Mediterranean balloon experiment: ocean wind speed sensing from the stratosphere, using gps reflections. *Remote Sensing of Environment*, 88(3):351 – 362.

Cardellach, E., Tomás, S., Oliveras, S., Padullés, R., Rius, A., de la Torre-Juárez, M., Turk, F. J., Ao, C. O., Kursinski, E. R., Schreiner, B., Ector, D., and Cucurull, L. (2015). Sensitivity of paz leo polarimetric gnss radio-occultation experiment to precipitation events. *IEEE Transactions on Geoscience and Remote Sensing*, 53(1):190–206.

Carreno-Luengo, H., Lowe, S., Zuffada, C., Esterhuizen, S., and Oveisgharan, S. (2017). Spaceborne gnss-r from the smap mission: First assessment of polarimetric scatterometry over land and cryosphere. *Remote Sensing*, 9:362.

Cazenave, A. and Cozannet, G. L. (2014). Sea level rise and its coastal impacts. *Earth's Future*, 2(2):15–34.

Cazenave, A. and Llovel, W. (2010). Contemporary sea level rise. *Annual Review of Marine Science*, 2(1):145–173. PMID: 21141661.

Chelton, D. B., Ries, J. C., Haines, B. J., Fu, L.-L., and Callahan, P. S. (2001). Chapter 1 satellite altimetry. In Fu, L.-L. and Cazenave, A., editors, *Satellite Altimetry and Earth SciencesA Handbook of Techniques and Applications*, volume 69 of *International Geophysics*, pages 1 – ii. Academic Press.

Chew, C., Small, E. E., and Larson, K. M. (2016). An algorithm for soil moisture estimation using gps-interferometric reflectometry for bare and vegetated soil. *GPS Solutions*, 20(3):525–537.

Chew, C. C. and Small, E. E. (2018). Soil moisture sensing using spaceborne gnss reflections: Comparison of cygnss reflectivity to smap soil moisture. *Geophysical Research Letters*, 45(9):4049–4057.

Chew, C. C., Small, E. E., Larson, K. M., and Zavorotny, V. U. (2014). Effects of near-surface soil moisture on gps snr data: Development of a retrieval algorithm for soil moisture. *IEEE Transactions on Geoscience and Remote Sensing*, 52(1):537–543.

Chew, C. C., Small, E. E., Larson, K. M., and Zavorotny, V. U. (2015). Vegetation sensing using gps-interferometric reflectometry: Theoretical effects of canopy parameters on signal-to-noise ratio data. *IEEE Transactions on Geoscience and Remote Sensing*, 53(5):2755–2764.

Clarizia, M. P. and Ruf, C. S. (2017). Bayesian wind speed estimation conditioned on significant wave height for gnss-r ocean observations. *Journal of Atmospheric and Oceanic Technology*, 34(6):1193–1202.

Clifford, S. F., Tatarskii, V. I., Voronovich, A. G., and Zavorotny, V. U. (1998). Gps sounding of ocean surface waves: theoretical assessment. In *Geoscience and Remote Sensing Symposium Proceedings, 1998. IGARSS '98. 1998 IEEE International*, volume 4, pages 2005–2007 vol.4.

Corenblit, D., Baas, A. C. W., Bornette, G., Darrozes, J., Delmotte, S., Francis, R. A., Gurnell, A. M., Julien, F., Naiman, R. J., and Steiger, J. (2011). Feedbacks between geomorphology and biota controlling earth surface processes and landforms: A

review of foundation concepts and current understandings. *Earth-Science Reviews*, 106(3â€“4):307–331. 0012-8252.

Corenblit, D., Tabacchi, E., Steiger, J., and Gurnell, A. M. (2007). Reciprocal interactions and adjustments between fluvial landforms and vegetation dynamics in river corridors: A review of complementary approaches. *Earth-Science Reviews*, 84(1â€“2):56–86. 0012-8252.

CP Scott, RB Lohman, T. J. (2017). Insar constraints on soil moisture evolution after the march 2015 extreme precipitation event in chile. *Scientific Reports*, 7:4903.

Darrozes, J., Roussel, N., and Zribi, M. (2016). 7 - the reflected global navigation satellite system (gnss-r): from theory to practice. In Baghdadi, N. and Zribi, M., editors, *Microwave Remote Sensing of Land Surface*, pages 303 – 355. Elsevier.

Doornkamp, J. (1998). Coastal flooding, global warming and environmental management. *Journal of Environmental Management*, 52(4):327 – 333.

Dorigo, W., Wagner, W., Albergel, C., Albrecht, F., Balsamo, G., Brocca, L., Chung, D., Ertl, M., Forkel, M., Gruber, A., Haas, E., Hamer, P. D., Hirschi, M., Ikonen, J., de Jeu, R., Kidd, R., Lahoz, W., Liu, Y. Y., Miralles, D., Mistelbauer, T., Nicolai-Shaw, N., Parinussa, R., Pratola, C., Reimer, C., van der Schalie, R., Seneviratne, S. I., Smolander, T., and Lecomte, P. (2017). Esa cci soil moisture for improved earth system understanding: State-of-the art and future directions. *Remote Sensing of Environment*, 203(Supplement C):185 – 215. Earth Observation of Essential Climate Variables.

Dorsey, J. H. (2015). The ballona wetlands: Nature's water treatment system. phdthesis, Loyola Marymount University.

Duquenne, F., Botton, S., Peyret, F., Bétaille, D., and Willis, P. (2005). *GPS : Localisation et navigation par satellites.* Hermes Science Publications, 2nd edition revised and expanded edition. Langue : Français.

D'Addio, S., Martín-Neira, M., di Bisceglie, M., Galdi, C., and Alemany, F. M. (2014). Gnss-r altimeter based on doppler multi-looking. *IEEE Journal of Selected Topics in Applied Earth Observations and Remote Sensing*, 7(5):1452–1460.

Egido, A. (2013). *GNSS Reectometry for Land Remote Sensing Applications.* phdthesis, Starlab Barcelona, Universitat Politecnica de Catalunya, Signal Theory and Communications Dpt., Barcelona.

Egido, A., Paloscia, S., Motte, E., Guerriero, L., Pierdicca, N., Caparrini, M., Santi, E., Fontanelli, G., and Floury, N. (2014). Airborne gnss-r polarimetric measurements for

soil moisture and above-ground biomass estimation. *IEEE Journal of Selected Topics in Applied Earth Observations and Remote Sensing*, 7(5):1522–1532.

Eisen, O., Frezzotti, M., Genthon, C., Isaksson, E., Magand, O., van den Broeke, M. R., Dixon, D. A., Ekaykin, A., Holmlund, P., Kameda, T., Karlöf, L., Kaspari, S., Lipenkov, V. Y., Oerter, H., Takahashi, S., and Vaughan, D. G. (2008). Ground-based measurements of spatial and temporal variability of snow accumulation in east antarctica. *Reviews of Geophysics*, 46(2):n/a–n/a. RG2001.

Elfouhaily, T., Thompson, D. R., and Linstrom, L. (2002). Delay-doppler analysis of bistatically reflected signals from the ocean surface: theory and application. *IEEE Transactions on Geoscience and Remote Sensing*, 40(3):560–573.

Enderle, W. (2009). Galileo/egnos. the international symposium on global navigation satellite systems. techreport 33-36, Space-Based and Ground-Based Augmentation Systems and Applications, Berlin, Germany.

Fabra, F., Cardellach, E., Rius, A., Ribo, S., Oliveras, S., Nogues-Correig, O., Rivas, M. B., Semmling, M., and D'Addio, S. (2012). Phase altimetry with dual polarization gnss-r over sea ice. *IEEE Transactions on Geoscience and Remote Sensing*, 50(6):2112–2121.

Ferrazzoli, P., Guerriero, L., Pierdicca, N., and Rahmoune, R. (2011). Forest biomass monitoring with gnss-r: Theoretical simulations. *Advances in Space Research*, 47(10):1823–1832. 0273-1177.

Ferrazzoli, P., Guerriero, L., and Solimini, D. (2000). Simulating bistatic scatter from surfaces covered with vegetation. *Journal of Electromagnetic Waves and Applications*, 14(2):233–248.

Finn, M. P., Lewis, M. D., Bosch, D. D., Giraldo, M., Yamamoto, K., Sullivan, D. G., Kincaid, R., Luna, R., Allam, G. K., Kvien, C., and Williams, M. S. (2011). Remote sensing of soil moisture using airborne hyperspectral data. *GIScience & Remote Sensing*, 48(4):522–540.

Foti, G., Gommenginger, C., Jales, P., Unwin, M., Shaw, A., Robertson, C., and Roselló, J. (2015). Spaceborne gnss reflectometry for ocean winds: First results from the uk techdemosat-1 mission. *Geophysical Research Letters*, 42(13):5435–5441. 2015GL064204.

Frappart, F., Roussel, N., Gay, A., Ramillien, G., Darrozes, J., Lestarquit, L., and Perosanz, F. (2015). Modeling of gnss multipath signals for altimetry applications using signal to noise ratio data. In *2015 IEEE International Geoscience and Remote Sensing Symposium (IGARSS)*, pages 1598–1601.

Garrison, J. L. and Katzberg, S. J. (1997). Detection of ocean reflected gps signals: theory and experiment. In *Southeastcon '97. Engineering new New Century., Proceedings. IEEE*, pages 290–294.

Garrison, J. L. and Katzberg, S. J. (2000). The application of reflected gps signals to ocean remote sensing. *Remote Sensing of Environment*, 73(2):175–187.

Garrison, J. L., Komjathy, A., Zavorotny, V. U., and Katzberg, S. J. (2002). Wind speed measurement using forward scattered gps signals. *IEEE Transactions on Geoscience and Remote Sensing*, 40(1):50–65.

Garrison J. L., Camps A., C. E. (2014). Remote sensing with reflected global navigation satellite system (gnss-r) signals. In *IGARSS*, pages FD–05.

Georgiadou, P. and Kleusberg, A. (1988). On carrier signal multipath effects in relative gps positioning. *Journal of Geodesy*, 13(3):172–179.

Germain, O., Ruffini, G., Soulat, F., Caparrini, M., Chapron, B., and Silvestrin, P. (2004). The eddy experiment: Gnss-r speculometry for directional sea-roughness retrieval from low altitude aircraft. *Geophysical Research Letters*, 31(21):n/a–n/a. L21307.

Gleason, S. (2005). Space reflected gnss signals detected off an ice sheet in an alaskan sound and from a diverse land surface in the plains of north america. In *GNSS-R Workshop, University of Surrey.*

Gleason, S., Hodgart, S., Sun, Y., Gommenginger, C., Mackin, S., Adjrad, M., and Unwin, M. (2005). Detection and processing of bistatically reflected gps signals from low earth orbit for the purpose of ocean remote sensing. *IEEE Transactions on Geoscience and Remote Sensing*, 43(6):1229–1241.

Gornitz, V., Rosenzweig, C., and Hillel, D. (1997). Effects of anthropogenic intervention in the land hydrologic cycle on global sea level rise. *Global and Planetary Change*, 14:147–161.

Grimm, A. M. and Tedeschi, R. G. (2009). Enso and extreme rainfall events in south america. *Journal of Climate*, 22(7):1589–1609.

Groeve, T. D. (2010). Flood monitoring and mapping using passive microwave remote sensing in namibia. *Geomatics, Natural Hazards and Risk*, 1(1):19–35.

Grünewald, T., Schirmer, M., Mott, R., and Lehning, M. (2010). Spatial and temporal variability of snow depth and ablation rates in a small mountain catchment. *The Cryosphere*, 4(2):215–225.

Gutmann, E. D., Larson, K. M., Williams, M. W., Nievinski, F. G., and Zavorotny, V. (2012). Snow measurement by gps interferometric reflectometry: an evaluation at niwot ridge, colorado. *Hydrological Processes*, 26(19):2951–2961.

Hajj, G. A. and Zuffada, C. (2003). Theoretical description of a bistatic system for ocean altimetry using the gps signal. *Radio Science*, 38(5):n/a–n/a. 1089.

Hall, C. and Cordy, R. (1988). Multistatic scatterometry. In *In Proceedings of the IEEE International Geoscience and Remote Sensing Symposium*, Edinburgh, Scotland.

Haq, M., Akhtar, M., Muhammad, S., Paras, S., and Rahmatullah, J. (2012). Techniques of remote sensing and gis for flood monitoring and damage assessment: A case study of sindh province, pakistan. *The Egyptian Journal of Remote Sensing and Space Science*, 15(2):135 – 141.

Harman, B., Heyenga, S., M. Taylor, B., and Fletcher, C. (2013). Global lessons for adapting coastal communities to protect against storm surge inundation. *Journal of Coastal Research*, 31(4):790–801.

Helm, A. (2008). *Ground-based GPS altimetry with the L1 OpenGPS receiver using carrier phase-delay observations of reflected GPS signals*. Phd thesis, (scientific technical report str ; 08/10), Potsdam : Deutsches GeoForschungsZentrum GFZ.

Helm, A., Stosius, R., Beyerle, G., Montenbruck, O., and Rothacher, M. (2007). Status of gnss reflectometry related receiver developments and feasibility studies within the german indonesian tsunami early warning system. In *2007 IEEE International Geoscience and Remote Sensing Symposium*, pages 5084–5087.

Henonin, J., Russo, B., Mark, O., and Gourbesville, P. (2013). Real-time urban flood forecasting and modelling – a state of the art. *Journal of Hydroinformatics*, 15(3):717.

Hobiger, T., Haas, R., and Löfgren, J. (2014). Glonass-r: Gnss reflectometry with an fdma based satellite navigation system. *Radio Science*, 49(4):271–282.

ILRS (2012). Compass. In *International Laser Ranging Service - A service of the International Association of Geodesy*, Technical University Vienna. International Association of Geodesy (IAG).

JA, A.-R. (2008). *On generalized signal waveforms for satellite navigation*. phdthesis, Department of Aerospace Engineering, University FAF Munich, Munich.

Jackson, T. J. (2001). Multiple resolution analysis of l-band brightness temperature for soil moisture. *IEEE Transactions on Geoscience and Remote Sensing*, 39(1):151–164.

Jackson, T. J., Gasiewski, A. J., Oldak, A., Klein, M., Njoku, E. G., Yevgrafov, A., Christiani, S., and Bindlish, R. (2002). Soil moisture retrieval using the c-band polarimetric scanning radiometer during the southern great plains 1999 experiment. *IEEE Transactions on Geoscience and Remote Sensing*, 40(10):2151–2161.

Jin, S. and Komjathy, A. (2010). Gnss reflectometry and remote sensing: New objectives and results. *Advances in Space Research*, 46(2):111–117. 0273-1177.

Jin, S. and Najibi, N. (2014). Sensing snow height and surface temperature variations in greenland from gps reflected signals. *Advances in Space Research*, 53(11):1623–1633. 0273-1177.

Jin, S., Park, J., Wang, J., Choi, B., and Park, P. (2006). Electron density profiles derived from ground-based gps observations. *Journal of Navigation*, 59(3):395–401.

Jin, S., Park, J.-U., Cho, J.-H., and Park, P.-H. (2007). Seasonal variability of gps-derived zenith tropospheric delay (1994–2006) and climate implications. *Journal of Geophysical Research: Atmospheres*, 112(D9):n/a–n/a. D09110.

Katzberg, S. J. and Dunion, J. (2009). Comparison of reflected gps wind speed retrievals with dropsondes in tropical cyclones. *Geophys. Res. Lett.*, 36(17):n/a–n/a.

Katzberg, S. J. and Garrison, James L., J. (1996). Utilizing gps to determine ionospheric delay over the ocean. Technical Report NASA-TM-4750, NAS 1.15:4750, L-7575, NASA Technical Reports Server (NTRS), NASA Langley Research Center; Hampton, VA United States.

Katzberg, S. J., Torres, O., and Ganoe, G. (2006a). Calibration of reflected gps for tropical storm wind speed retrievals. *Geophysical Research Letters*, 33(18):n/a–n/a. L18602.

Katzberg, S. J., Torres, O., Grant, M. S., and Masters, D. (2006b). Utilizing calibrated gps reflected signals to estimate soil reflectivity and dielectric constant: Results from smex02. *Remote Sensing of Environment*, 100(1):17 – 28.

Kebiao, M., Mengyang, Z., Jianming, W., Huajun, T., and Qingbo, Z. (2008). The study of soil moisture retrieval algorithm from gnss-r. In *2008 International Workshop on Education Technology and Training 2008 International Workshop on Geoscience and Remote Sensing*, volume 1, pages 438–442.

Kerr, Y. H., Waldteufel, P., Wigneron, J. P., Delwart, S., Cabot, F., Boutin, J., Escorihuela, M. J., Font, J., Reul, N., Gruhier, C., Juglea, S. E., Drinkwater, M. R., Hahne, A., Martin-Neira, M., and Mecklenburg, S. (2010). The smos mission: New

tool for monitoring key elements ofthe global water cycle. *Proceedings of the IEEE*, 98(5):666–687.

Komjathy, A., Armatys, M., Masters, D., Axelrad, P., Zavorotny, V., and Katzberg, S. (2004). Retrieval of ocean surface wind speed and wind direction using reflected gps signals. *Journal of Atmospheric and Oceanic Technology*, 21(3):515–526.

Komjathy, A., Maslanik, J., Zavorotny, V. U., Axelrad, P., and Katzberg, S. J. (2000a). Sea ice remote sensing using surface reflected gps signals. In *IGARSS 2000. IEEE 2000 International Geoscience and Remote Sensing Symposium. Taking the Pulse of the Planet: The Role of Remote Sensing in Managing the Environment. Proceedings (Cat. No.00CH37120)*, volume 7, pages 2855–2857 vol.7.

Komjathy, A., Zavorotny, V. U., Axelrad, P., Born, G. H., and Garrison, J. L. (2000b). Gps signal scattering from sea surface: Wind speed retrieval using experimental data and theoretical model. *Remote Sensing of Environment*, 73(2):162 – 174.

Kostelecký, J., Klokočník, J., and Wagner, C. (2005). Geometry and accuracy of reflecting points in bistatic satellite altimetry. *Journal of Geodesy*, 79(8):421–430.

Kunkel, K. E., Karl, T. R., Brooks, H., Kossin, J., Lawrimore, J. H., Arndt, D., Bosart, L., Changnon, D., Cutter, S. L., Doesken, N., Emanuel, K., Groisman, P. Y., Katz, R. W., Knutson, T., O'Brien, J., Paciorek, C. J., Peterson, T. C., Redmond, K., Robinson, D., Trapp, J., Vose, R., Weaver, S., Wehner, M., Wolter, K., and Wuebbles, D. (2013). Monitoring and understanding trends in extreme storms: State of knowledge. *Bulletin of the American Meteorological Society*, 94(4):499–514.

Kursinski, E. R. and Gebhardt, T. (2014). A method to deconvolve errors in gps ro-derived water vapor histograms. *Journal of Atmospheric and Oceanic Technology*, 31(12):2606–2628.

Kursinski, E. R., Healy, S. B., and Romans, L. J. (2000). Initial results of combining gps occultations with ecmwf global analyses within a 1dvar framework. *Earth, Planets and Space*, 52(11):885–892.

Larson, K. M. (2015). Gnss h2o: Expanding reflection research to the global gnss network. In *GNSS+R 2015, Potsdam, Germany.*

Larson, K. M., Braun, J. J., Small, E. E., Zavorotny, V. U., Gutmann, E. D., and Bilich, A. L. (2010). Gps multipath and its relation to near-surface soil moisture content. *IEEE Journal of Selected Topics in Applied Earth Observations and Remote Sensing*, 3(1):91–99.

Larson, K. M., Gutmann, E. D., Zavorotny, V. U., Braun, J. J., Williams, M. W., and Nievinski, F. G. (2009). Can we measure snow depth with gps receivers? *Geophysical Research Letters*, 36(17):n/a–n/a. L17502.

Larson, K. M., Löfgren, J. S., and Haas, R. (2013). Coastal sea level measurements using a single geodetic gps receiver. *Advances in Space Research*, 51(8):1301–1310. 0273-1177.

Larson, K. M. and Nievinski, F. G. (2013). Gps snow sensing: results from the earthscope plate boundary observatory. *GPS Solutions*, 17(1):41–52.

Larson, K. M., Ray, R. D., and Williams, S. D. P. (2017). A 10-year comparison of water levels measured with a geodetic gps receiver versus a conventional tide gauge. *Journal of Atmospheric and Oceanic Technology*, 34(2):295–307.

Larson, K. M. and Small, E. E. (2014). Normalized microwave reflection index: A vegetation measurement derived from gps networks. *IEEE Journal of Selected Topics in Applied Earth Observations and Remote Sensing*, 7(5):1501–1511.

Larson, K. M., Small, E. E., Gutmann, E., Bilich, A., Axelrad, P., and Braun, J. (2008a). Using gps multipath to measure soil moisture fluctuations: initial results. *GPS Solutions*, 12(3):173–177.

Larson, K. M., Small, E. E., Gutmann, E. D., Bilich, A. L., Braun, J. J., and Zavorotny, V. U. (2008b). Use of gps receivers as a soil moisture network for water cycle studies. *Geophysical Research Letters*, 35(24):n/a–n/a. L24405.

Larson, K. M., Wahr, J., and Munneke, P. K. (2015). Constraints on snow accumulation and firn density in greenland using gps receivers. *Journal of Glaciology*, 61(225):101–114.

Lehning, M. and Fierz, C. (2008). Assessment of snow transport in avalanche terrain. *Cold Regions Science and Technology*, 51(2):240 – 252. International Snow Science Workshop (ISSW) 2006.

Leite, S. M. and Peixoto, J. P. (1995). Spectral analysis of climatological series in duero basin. *Theoretical and Applied Climatology*, 50:157–167.

Lestarquit, L., Peyrezabes, M., Darrozes, J., Motte, E., Roussel, N., Wautelet, G., Frappart, F., Ramillien, G., Biancale, R., and Zribi, M. (2016). Reflectometry with an open-source software gnss receiver: Use case with carrier phase altimetry. *IEEE Journal of Selected Topics in Applied Earth Observations and Remote Sensing*, 9(10):4843–4853.

Lin, B., Katzberg, S. J., Garrison, J. L., and Wielicki, B. A. (1999). Relationship between gps signals reflected from sea surfaces and surface winds: Modeling results and

comparisons with aircraft measurements. *Journal of Geophysical Research: Oceans*, 104(C9):20713–20727.

Liu, J. (2013). Beidou - chinas rapidly emerging gnss. *Inside GNSS*.

Liu, W., Beckheinrich, J., Semmling, M., Ramatschi, M., Vey, S., Wickert, J., Hobiger, T., and Haas, R. (2017). Coastal sea-level measurements based on gnss-r phase altimetry: A case study at the onsala space observatory, sweden. *IEEE Transactions on Geoscience and Remote Sensing*, 55(10):5625–5636.

Livingstone, C. E., Onstott, R. G., Arsenault, L. D., Gray, A. L., and Singh, K. P. (1987). Microwave sea-ice signatures near the onset of melt. *IEEE Transactions on Geoscience and Remote Sensing*, GE-25(2):174–187.

Lomb, N. R. (1976). Least-squares frequency analysis of unequally spaced data. *Astrophysics and Space Science*, 39:447–462.

Lowe, S. T., Kroger, P., Franklin, G., LaBrecque, J. L., Lerma, J., Lough, M., Marcin, M. R., Muellerschoen, R. J., Spitzmesser, D., and Young, L. E. (2002a). A delay/doppler-mapping receiver system for gps-reflection remote sensing. *IEEE Transactions on Geoscience and Remote Sensing*, 40(5):1150–1163.

Lowe, S. T., LaBrecque, J. L., Zuffada, C., Romans, L. J., Young, L. E., and Hajj, G. A. (2002b). First spaceborne observation of an earth-reflected gps signal. *Radio Science*, 37(1):7–1–7–28.

Lowe, S. T., Zuffada, C., Chao, Y., Kroger, P., Young, L. E., and LaBrecque, J. L. (2002c). 5-cm-precision aircraft ocean altimetry using gps reflections. *Geophysical Research Letters*, 29(10):13–1–13–4.

Löfgren, J. S. (2014). *Local Sea Level Observations Using Reflected GNSS Signals*. phdthesis, Department of Earth and Space Sciences, Chalmers University of Technology, Gothenburg, Sweden.

Löfgren, J. S., Haas, R., and Hobiger, T. (2015). The gnss-r tide gauge at the onsala space observatory. In *GNSS+R 2015, Potsdam, Germany.*

Löfgren, J. S., Haas, R., and Johansson, J. M. (2011). Monitoring coastal sea level using reflected gnss signals. *Advances in Space Research*, 47(2):213–220. 0273-1177.

Löfgren, J. S., Haas, R., and Scherneck, H.-G. (2014). Sea level time series and ocean tide analysis from multipath signals at five gps sites in different parts of the world. *Journal of Geodynamics*, (0). 0264-3707.

Mancini, M., Hoeben, R., and Troch, P. A. (1999). Multifrequency radar observations of bare surface soil moisture content: A laboratory experiment. *Water Resources Research*, 35(6):1827–1838.

Marchan-Hernandez, J. F., Valencia, E., Rodriguez-Alvarez, N., Ramos-Perez, I., Bosch-Lluis, X., Camps, A., Eugenio, F., and Marcello, J. (2010). Sea-state determination using gnss-r data. *IEEE Geoscience and Remote Sensing Letters*, 7(4):621–625.

Martin-Neira, M. (1993). A passive reflectometry and interferometry system (paris): Application to ocean altimetry. *ESA Journal*, 17:331–355.

Martin-Neira, M., Caparrini, M., Font-Rossello, J., Lannelongue, S., and Vallmitjana, C. S. (2001). The paris concept: an experimental demonstration of sea surface altimetry using gps reflected signals. *IEEE Transactions on Geoscience and Remote Sensing*, 39(1):142–150.

Martin-Neira, M., D'Addio, S., Buck, C., Floury, N., and Prieto-Cerdeira, R. (2011). The paris ocean altimeter in-orbit demonstrator. *IEEE Transactions on Geoscience and Remote Sensing*, 49(6):2209–2237.

Masters, D., Axelrad, P., and Katzberg, S. (2004). Initial results of land-reflected gps bistatic radar measurements in smex02. *Remote Sensing of Environment*, 92(4):507 – 520. 2002 Soil Moisture Experiment (SMEX02).

Masters, D., Zavorotny, V., Katzberg, S., and Emery, W. (2000). Gps signal scattering from land for moisture content determination. In *IGARSS 2000. IEEE 2000 International Geoscience and Remote Sensing Symposium. Taking the Pulse of the Planet: The Role of Remote Sensing in Managing the Environment. Proceedings (Cat. No.00CH37120)*, volume 7, pages 3090–3092 vol.7.

Maurer, E. P., O'Donnell, G. M., Lettenmaier, D. P., and Roads, J. O. (2001). Evaluation of the land surface water budget in ncep/ncar and ncep/doe reanalyses using an off-line hydrologic model. *Journal of Geophysical Research: Atmospheres*, 106(D16):17841–17862.

McCabe, M. F., Gao, H., and Wood, E. F. (2005). Evaluation of amsr-e-derived soil moisture retrievals using ground-based and psr airborne data during smex02. *Journal of Hydrometeorology*, 6(6):864–877.

McLaughlin, D. (2002). An integrated approach to hydrologic data assimilation: interpolation, smoothing, and filtering. *Advances in Water Resources*, 25(8):1275 – 1286.

Melling, H. (1998). Detection of features in first-year pack ice by synthetic aperture radar (sar). *International Journal of Remote Sensing*, 19(6):1223–1249.

Mitchell, K. E., Lohmann, D., Houser, P. R., Wood, E. F., Schaake, J. C., Robock, A., Cosgrove, B. A., Sheffield, J., Duan, Q., Luo, L., Higgins, R. W., Pinker, R. T., Tarpley, J. D., Lettenmaier, D. P., Marshall, C. H., Entin, J. K., Pan, M., Shi, W., Koren, V., Meng, J., Ramsay, B. H., and Bailey, A. A. (2004). The multi-institution north american land data assimilation system (nldas): Utilizing multiple gcip products and partners in a continental distributed hydrological modeling system. *Journal of Geophysical Research: Atmospheres*, 109(D7):n/a–n/a. D07S90.

Motte, E., Zribi, M., Fanise, P., Egido, A., Darrozes, J., Al-Yaari, A., Baghdadi, N., Baup, F., Dayau, S., Fieuzal, R., Frison, P.-L., Guyon, D., and Wigneron, J.-P. (2016). Glori: A gnss-r dual polarization airborne instrument for land surface monitoring. *Sensors*, 16(5).

Nghiem, S. V., Zuffada, C., Shah, R., Chew, C., Lowe, S. T., Mannucci, A. J., Cardellach, E., Brakenridge, G. R., Geller, G., and Rosenqvist, A. (2017). Wetland monitoring with global navigation satellite system reflectometry. *Earth and Space Science*, 4(1):16–39.

Njoku, E. G. and Entekhabi, D. (1996). Passive microwave remote sensing of soil moisture. *Journal of Hydrology*, 184(1):101 – 129. Soil Moisture Theories and Observations.

Ogashawara, I., Curtarelli, M., and Ferreira, C. (2013). The use of optical remote sensing for mapping flooded areas. *International Journal of Engineering Research and Application*, 3(5):1–5.

Ozeki, M. and Heki, K. (2012). Gps snow depth meter with geometry-free linear combinations of carrier phases. *Journal of Geodesy*, 86(3):209–219.

Paloscia, S., Pettinato, S., Santi, E., Notarnicola, C., Pasolli, L., and Reppucci, A. (2013). Soil moisture mapping using sentinel-1 images: Algorithm and preliminary validation. *Remote Sensing of Environment*, 134:234 – 248.

Pan, M. and Wood, E. F. (2006). Data assimilation for estimating the terrestrial water budget using a constrained ensemble kalman filter. *Journal of Hydrometeorology*, 7(3):534–547.

Pan, M., Wood, E. F., Wójcik, R., and McCabe, M. F. (2008). Estimation of regional terrestrial water cycle using multi-sensor remote sensing observations and data assimilation. *Remote Sensing of Environment*, 112(4):1282 – 1294. Remote Sensing Data Assimilation Special Issue.

Park, H., Pascual, D., Camps, A., Martin, F., Alonso-Arroyo, A., and Carreno-Luengo, H. (2014). Analysis of spaceborne gnss-r delay-doppler tracking. *IEEE Journal of Selected Topics in Applied Earth Observations and Remote Sensing*, 7(5):1481–1492.

Pascual, D., Camps, A., Martin, F., Park, H., Arroyo, A. A., and Onrubia, R. (2014a). Precision bounds in gnss-r ocean altimetry. *IEEE Journal of Selected Topics in Applied Earth Observations and Remote Sensing*, 7(5):1416–1423.

Pascual, D., Park, H., Camps, A., Arroyo, A. A., and Onrubia, R. (2014b). Simulation and analysis of gnss-r composite waveforms using gps and galileo signals. *IEEE Journal of Selected Topics in Applied Earth Observations and Remote Sensing*, 7(5):1461–1468.

Paustian, K., h ravindranath, n., and Van Amstel, A. (2006). *2006 IPCC Guidelines for National Greenhouse Gas Inventories. Volume 4 Agriculture, forestry and other land use*. IPCC.

Ramillien, G., Frappart, F., and Seoane, L. (2014). Application of the regional water mass variations from grace satellite gravimetry to large-scale water management in africa. *Remote Sensing*, 6:7379–7405.

Richards, L. and Gardner, W. (1936). Tensiometers for measuring the capillary tension of soil water. *Journal of the American Society of Agronomy*, 28(5):352–358.

Rius, A., Aparicio, J. M., Cardellach, E., Martín-Neira, M., and Chapron, B. (2002). Sea surface state measured using gps reflected signals. *Geophysical Research Letters*, 29(23):37–1–37–4. 2122.

Rius, A., Nogués-Correig, O., Ribó, S., Cardellach, E., Oliveras, S., Valencia, E., Park, H., Tarongí, J. M., Camps, A., van der Marel, H., van Bree, R., Altena, B., and Martín-Neira, M. (2012). Altimetry with gnss-r interferometry: first proof of concept experiment. *GPS Solutions*, 16(2):231–241.

Rivas, M. B., Maslanik, J. A., and Axelrad, P. (2010). Bistatic scattering of gps signals off arctic sea ice. *IEEE Transactions on Geoscience and Remote Sensing*, 48(3):1548–1553.

Roads, J., Lawford, R., Bainto, E., Berbery, E., Chen, S., Fekete, B., Gallo, K., Grundstein, A., Higgins, W., Kanamitsu, M., Krajewski, W., Lakshmi, V., Leathers, D., Lettenmaier, D., Luo, L., Maurer, E., Meyers, T., Miller, D., Mitchell, K., Mote, T., Pinker, R., Reichler, T., Robinson, D., Robock, A., Smith, J., Srinivasan, G., Verdin, K., Vinnikov, K., Vonder Haar, T., Vörösmarty, C., Williams, S., and Yarosh, E. (2003). Gcip water and energy budget synthesis (webs). *Journal of Geophysical Research: Atmospheres*, 108(D16):n/a–n/a. 8609.

Rodriguez-Alvarez, N., Aguasca, A., Valencia, E., Bosch-Lluis, X., Camps, A., Ramos-Perez, I., Park, H., and Vall-llossera, M. (2012). Snow thickness monitoring using gnss measurements. *IEEE Geoscience and Remote Sensing Letters*, 9(6):1109–1113.

Rodriguez-Alvarez, N., Bosch-Lluis, X., Camps, A., Aguasca, A., Vall-llossera, M., Valencia, E., Ramos-Perez, I., and Park, H. (2011a). Review of crop growth and soil moisture monitoring from a ground-based instrument implementing the interference pattern gnss-r technique. *Radio Science*, 46(6):n/a–n/a. RS0C03.

Rodriguez-Alvarez, N., Bosch-Lluis, X., Camps, A., Vall-llossera, M., Valencia, E., Marchan-Hernandez, J. F., and Ramos-Perez, I. (2009). Soil moisture retrieval using gnss-r techniques: Experimental results over a bare soil field. *IEEE Transactions on Geoscience and Remote Sensing*, 47(11):3616–3624.

Rodriguez-Alvarez, N., Camps, A., Vall-llossera, M., Bosch-Lluis, X., Monerris, A., Ramos-Perez, I., Valencia, E., Marchan-Hernandez, J. F., Martinez-Fernandez, J., Baroncini-Turricchia, G., Perez-Gutierrez, C., and Sanchez, N. (2011b). Land geophysical parameters retrieval using the interference pattern gnss-r technique. *IEEE Transactions on Geoscience and Remote Sensing*, 49(1):71–84.

Ropelewski, C. F. and Yarosh, E. S. (1998). The observed mean annual cycle of moisture budgets over the central united states (1973–92). *Journal of Climate*, 11(9):2180–2190.

Roussel, N., Frappart, F., Ramillien, G., Darrozes, J., Baup, F., and Ha, C. (2015a). Detection of soil moisture content changes by using a single geodetic antenna: The case of an agricultural plot. In *2015 IEEE International Geoscience and Remote Sensing Symposium (IGARSS)*, pages 2008–2011.

Roussel, N., Frappart, F., Ramillien, G., Darrozes, J., Baup, F., Lestarquit, L., and Ha, M. C. (2016). Detection of soil moisture variations using gps and glonass snr data for elevation angles ranging from 2° to 70°. *IEEE Journal of Selected Topics in Applied Earth Observations and Remote Sensing*, 9(10):4781–4794.

Roussel, N., Frappart, F., Ramillien, G., Desjardins, C., Gegout, P., Pérosanz, F., and Biancale, R. (2014). Simulations of direct and reflected waves trajectories for in situ gnss-r experiments. *Geoscientific Model Development Discussions*, 7:1001–1062.

Roussel, N., Ramillien, G., Frappart, F., Darrozes, J., Gay, A., Biancale, R., Striebig, N., Hanquiez, V., Bertin, X., and Allain, D. (2015b). Sea level monitoring and sea state estimate using a single geodetic receiver. *Remote Sensing of Environment*, 171(Supplement C):261 – 277.

Rubashkin S.G., Pavelev A.G., Y. O. (1993). Reflection of radar waves by the ocean surface for bistatic radar using two satellites. *Journal of Communications Technology and Electronics*, 38(9):156–17464–70.

Ruffini, G., Soulat, F., Caparrini, M., Germain, O., and Martín-Neira, M. (2004). The eddy experiment: Accurate gnss-r ocean altimetry from low altitude aircraft. *Geophysical Research Letters*, 31(12):n/a–n/a. L12306.

Sahagian, D. (2000). Global physical effects of anthropogenic hydrological alterations: sea level and water redistribution. *Global and Planetary Change*, 25(1):39 – 48.

Salati, E. and Vose, P. B. (1986). The water cycle in tropical forests, with special reference to the amazon. In Marini-Bettòlo, G., editor, *Chemical Events in the Atmosphere and their Impact on the Environment*, volume 26 of *Studies in Environmental Science*, pages 623 – 648. Elsevier.

Scargle, J. D. (1982). Studies in astronomical time series analysis. ii - statistical aspects of spectral analysis of unevenly spaced data. *Astrophysical Journal*, 263:835–853.

Schiavulli, D., Frappart, F., Ramillien, G., Darrozes, J., Nunziata, F., and Migliaccio, M. (2017). Observing sea/ice transition using radar images generated from techdemosat-1 delay doppler maps. *IEEE Geoscience and Remote Sensing Letters*, 14(5):734–738.

Schirmer, M., Schweizer, J., and Lehning, M. (2010). Statistical evaluation of local to regional snowpack stability using simulated snow-cover data. *Cold Regions Science and Technology*, 64(2):110 – 118. International Snow Science Workshop 2009 Davos.

Schmidt, T., Heise, S., Wickert, J., Beyerle, G., and Reigber, C. (2005). Gps radio occultation with champ and sac-c: global monitoring of thermal tropopause parameters. *Atmospheric Chemistry and Physics*, 5(6):1473–1488.

Schmidt, T., Wickert, J., Beyerle, G., and Heise, S. (2008). Global tropopause height trends estimated from gps radio occultation data. *Geophysical Research Letters*, 35(11):n/a–n/a. L11806.

Schmugge, T. J., Jackson, T. J., and McKim, H. L. (1980). Survey of methods for soil moisture determination. *Water Resources Research*, 16(6):961–979.

Seeber, G. (1993). *Satellite geodesy: foundations, methods, and applications*. W. de Gruyter.

Semmling, A. M., Beyerle, G., Stosius, R., Dick, G., Wickert, J., Fabra, F., Cardellach, E., Ribó, S., Rius, A., Helm, A., Yudanov, S. B., and d'Addio, S. (2011). Detection of arctic ocean tides using interferometric gnss-r signals. *Geophysical Research Letters*, 38(4):n/a–n/a. L04103.

Semmling, A. M., Wickert, J., Schön, S., Stosius, R., Markgraf, M., Gerber, T., Ge, M., and Beyerle, G. (2013). A zeppelin experiment to study airborne altimetry using specular global navigation satellite system reflections. *Radio Science*, 48(4):427–440.

Serreze, M. C., Clark, M. P., Armstrong, R. L., McGinnis, D. A., and Pulwarty, R. S. (1999). Characteristics of the western united states snowpack from snowpack telemetry (snotel) data. *Water Resources Research*, 35(7):2145–2160.

Shah, R. and Garrison, J. L. (2014). Application of the icf coherence time method for ocean remote sensing using digital communication satellite signals. *IEEE Journal of Selected Topics in Applied Earth Observations and Remote Sensing*, 7(5):1584–1591.

Shokr, M. E. (1998). Field observations and model calculations of dielectric properties of arctic sea ice in the microwave c-band. *IEEE Transactions on Geoscience and Remote Sensing*, 36(2):463–478.

Shuanggen Jin, Estel Cardellach, F. X. (2014). *GNSS Remote Sensing. Theory, Methods and Applications.* Springer.

Small, E. E., Larson, K. M., and Braun, J. J. (2010). Sensing vegetation growth with reflected gps signals. *Geophysical Research Letters*, 37(12).

Small, E. E., Larson, K. M., Chew, C. C., Dong, J., and Ochsner, T. E. (2016). Validation of gps-ir soil moisture retrievals: Comparison of different algorithms to remove vegetation effects. *IEEE Journal of Selected Topics in Applied Earth Observations and Remote Sensing*, 9(10):4759–4770.

Small, E. E., Larson, K. M., and Smith, W. K. (2014). Normalized microwave reflection index: Validation of vegetation water content estimates from montana grasslands. *IEEE Journal of Selected Topics in Applied Earth Observations and Remote Sensing*, 7(5):1512–1521.

Spellman, F. (2017). *The Science of Environmental Pollution, Third Edition.* Taylor & Francis.

Stacheder, M., Königer, F., and Schuhmann, R. (2009). New dielectric sensors and sensing techniques for soil and snow moisture measurements. *Sensors*, 9:2951–67.

Sutour, C., Émilie Darrin, Giremus, A., and Pereira, V. (2012). Étude d'une nouvelle modélisation des erreurs de multitrajets en navigation gps. Rapport de projet, Université Bordeaux 1 - Sciences Technologies.

Sánchez, N., González-Zamora, , Piles, M., and Martínez-Fernández, J. (2016). A new soil moisture agricultural drought index (smadi) integrating modis and smos products: A case of study over the iberian peninsula. *Remote Sensing*, 8(4).

Sánchez, N., Martínez-Fernández, J., Calera, A., Torres, E., and Pérez-Gutiérrez, C. (2010). Combining remote sensing and in situ soil moisture data for the application

and validation of a distributed water balance model (hidromore). *Agricultural Water Management*, 98(1):69 – 78.

Talib, A. and Randhir, T. (2017). Climate change and land use impacts on hydrologic processes of watershed systems. *Journal of Water and Climate Changej*, 8:jwc2017064.

Tapley, B. D., Bettadpur, S., Ries, J. C., Thompson, P. F., and Watkins, M. M. (2004). Grace measurements of mass variability in the earth system. *Science*, 305(5683):503–505.

Thomas Yunck, C. M. and Lenz, C. (2007). The cicero project: A community initiative for continuing earth radio occultation. In *Second FORMOSAT-3/COSMIC Data Users Workshop*, pages 22–24, Boulder, Colorado, USA.

Thompson, D. R., Elfouhaily, T. M., and Garrison, J. L. (2005). An improved geometrical optics model for bistatic gps scattering from the ocean surface. *IEEE Transactions on Geoscience and Remote Sensing*, 43(12):2810–2821.

Trenberth, K. E. and Hoar, T. J. (1996). The 1990–1995 el niño-southern oscillation event: Longest on record. *Geophysical Research Letters*, 23(1):57–60.

Treuhaft, R. N., Lowe, S. T., Zuffada, C., and Chao, Y. (2001). 2-cm gps altimetry over crater lake. *Geophysical Research Letters*, 28(23):4343–4346.

Ulaby, F. T., Dubois, P. C., and van Zyl, J. (1996). Radar mapping of surface soil moisture. *Journal of Hydrology*, 184(1):57 – 84. Soil Moisture Theories and Observations.

Unwin, M., Jales, P., Tye, J., Gommenginger, C., Foti, G., and Rosello, J. (2016). Spaceborne gnss-reflectometry on techdemosat-1: Early mission operations and exploitation. *IEEE Journal of Selected Topics in Applied Earth Observations and Remote Sensing*, 9(10):4525–4539.

van der Ent, R. J., Savenije, H. H. G., Schaefli, B., and Steele-Dunne, S. C. (2010). Origin and fate of atmospheric moisture over continents. *Water Resources Research*, 46(9):n/a–n/a. W09525.

Vergados, P., Mannucci, A., O. Ao, C., H. Jiang, J., and Su, H. (2015). On the comparisons of tropical relative humidity in the lower and middle troposphere among cosmic radio occultations and merra and ecmwf data sets. *Atmospheric Measurement Techniques*, 8.

Vergados, P., Mannucci, A. J., and Ao, C. O. (2014). Assessing the performance of gps radio occultation measurements in retrieving tropospheric humidity in cloudiness: A comparison study with radiosondes, era-interim, and airs data sets. *Journal of Geophysical Research: Atmospheres*, 119(12):7718–7731. 2013JD021398.

Vergados, P., Mannucci, A. J., and Su, H. (2013). A validation study for gps radio occultation data with moist thermodynamic structure of tropical cyclones. *Journal of Geophysical Research: Atmospheres*, 118(16):9401–9413.

Vey, S., Güntner, A., Wickert, J., Blume, T., and Ramatschi, M. (2016a). Long-term soil moisture dynamics derived from gnss interferometric reflectometry: a case study for sutherland, south africa. *GPS Solutions*, 20(4):641–654.

Vey, S., Güntner, A., Wickert, J., Blume, T., Thoss, H., and Ramatschi, M. (2016b). Monitoring snow depth by gnss reflectometry in built-up areas: A case study for wettzell, germany. *IEEE Journal of Selected Topics in Applied Earth Observations and Remote Sensing*, 9(10):4809–4816.

Vu, P. L., Frappart, F., Darrozes, J., Marieu, V., Blarel, F., Ramillien, G., Bonnefond, P., and Birol., F. (2018). Multi-satellite altimeter validation along the french atlantic coast in the southern bay of biscay from ers-2 to saral. *Remote Sensing*, 10(1).

Wagner, C. and Klokočník, J. (2003). The value of ocean reflections of gps signals to enhance satellite altimetry: data distribution and error analysis. *Journal of Geodesy*, 77(3):128–138.

Wan, W., Larson, K. M., Small, E. E., Chew, C. C., and Braun, J. J. (2015). Using geodetic gps receivers to measure vegetation water content. *GPS Solutions*, 19(2):237–248.

Wang, L., Qu, J. J., Zhang, S., Hao, X., and Dasgupta, S. (2007). Soil moisture estimation using modis and ground measurements in eastern china. *International Journal of Remote Sensing*, 28(6):1413–1418.

Wickert, J., Cardellach, E., Martín-Neira, M., Bandeiras, J., Bertino, L., Andersen, O. B., Camps, A., Catarino, N., Chapron, B., Fabra, F., Floury, N., Foti, G., Gommenginger, C., Hatton, J., Høeg, P., Jäggi, A., Kern, M., Lee, T., Li, Z., Park, H., Pierdicca, N., Ressler, G., Rius, A., Roselló, J., Saynisch, J., Soulat, F., Shum, C. K., Semmling, M., Sousa, A., Xie, J., and Zuffada, C. (2016). Geros-iss: Gnss reflectometry, radio occultation, and scatterometry onboard the international space station. *IEEE Journal of Selected Topics in Applied Earth Observations and Remote Sensing*, 9(10):4552–4581.

Wiehl M., L. B. and R., D. (2003). Potential of reflected gnss signals for ice sheet remote sensing. *Progress In Electromagnetics Research*, 40:177–205.

Wigneron, J.-P., Waldteufel, P., Chanzy, A., Calvet, J.-C., and Kerr, Y. (2000). Two-dimensional microwave interferometer retrieval capabilities over land surfaces (smos mission). *Remote Sensing of Environment*, 73(3):270 – 282.

Wirz, V., Schirmer, M., Gruber, S., and Lehning, M. (2011). Spatio-temporal measurements and analysis of snow depth in a rock face. *The Cryosphere*, 5(4):893–905.

Woodruff, J., L Irish, J., and Camargo, S. (2013). Coastal flooding by tropical cyclones and sea-level rise. *Nature*, 504:44–52.

You, H., Garrison, J. L., Heckler, G., and Zavorotny, V. U. (2004). Stochastic voltage model and experimental measurement of ocean-scattered gps signal statistics. *IEEE Transactions on Geoscience and Remote Sensing*, 42(10):2160–2169.

Yu, K., Rizos, C., Burrage, D., Dempster, A. G., Zhang, K., and Markgraf, M. (2014). An overview of gnss remote sensing. *EURASIP Journal on Advances in Signal Processing*, 2014(1):134.

Zavorotny, V. and Zuffada, C. (2002). A novel technique for characterizing the thickness of first-year sea ice with the gps reflected signal. In *Fall Meeting 2002; San Francisco, CA; United States*, number 20060030417. Jet Propulsion Lab., California Inst. of Tech.; Pasadena, CA, United States.

Zavorotny, V. U., Gleason, S., Cardellach, E., and Camps, A. (2014). Tutorial on remote sensing using gnss bistatic radar of opportunity. *IEEE Geoscience and Remote Sensing Magazine*, 2(4):8–45.

Zavorotny, V. U. and Voronovich, A. G. (2000). Scattering of gps signals from the ocean with wind remote sensing application. *IEEE Transactions on Geoscience and Remote Sensing*, 38(2):951–964.

Zhang, F., ZHANG, L.-W., SHI, J.-J., and HUANG, J.-F. (2014). Soil moisture monitoring based on land surface temperature-vegetation index space derived from modis data. *Pedosphere*, 24(4):450 – 460.

Zhang, S., Roussel, N., Boniface, K., Ha, M. C., Frappart, F., Darrozes, J., Baup, F., and Calvet, J.-C. (2017). Use of reflected gnss snr data to retrieve either soil moisture or vegetation height from a wheat crop. *Hydrology and Earth System Sciences*, 21(9):4767–4784.